

Exploring high density nuclear matter with dimuons & hadrons at FAIR energies

By

EKATA NANDY

PHYS04201704002

Variable Energy Cyclotron Centre, Kolkata

A thesis submitted to

The Board of Studies in Physical Sciences

In partial fulfillment of requirements

for the Degree of

DOCTOR OF PHILOSOPHY

of

HOMI BHABHA NATIONAL INSTITUTE

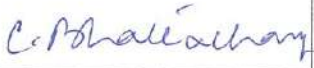




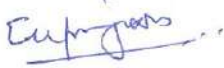


January, 2023

Homi Bhabha National Institute¹

Recommendations of the Viva Voce Committee

As members of the Viva Voce Committee, we certify that we have read the dissertation prepared by Ekata Nandy entitled "Exploring high density nuclear matter with dimuons & hadrons at FAIR energies" and recommend that it may be accepted as fulfilling the thesis requirement for the award of Degree of Doctor of Philosophy.

Chairman	Dr. Chandana Bhattacharya		Date: 23.6.23
Guide/Convener	Dr. Subhasis Chattopadhyay		Date: 23/6/23
Examiner	Dr. Lokesh Kumar		Date: 23.6.23
Member 1	Dr. Sourav Sarkar		Date: 23.6.23
Member 2	Dr. Zubayer Ahamad		Date: 23.6.23
Member 3	Dr. Supriya Das		Date: 23/6/2023

Final approval and acceptance of this thesis is contingent upon the candidate's submission of the final copies of the thesis to HBNI.

I hereby certify that I/we have read this thesis prepared under my direction and recommend that it may be accepted as fulfilling the thesis requirement.

Date: 23/6/23

Place: NECC Kolkata

Guide 

¹This page is to be included only for final submission after successful completion of viva voce.

STATEMENT BY AUTHOR

This dissertation has been submitted in partial fulfillment of requirements for an advanced degree at Homi Bhabha National Institute (HBNI) and is deposited in the Library to be made available to borrowers under rules of the HBNI.

Brief quotations from this dissertation are allowable without special permission, provided that accurate acknowledgement of source is made. Requests for permission for extended quotation from or reproduction of this manuscript in whole or in part may be granted by the Competent Authority of HBNI when in his or her judgment the proposed use of the material is in the interests of scholarship. In all other instances, however, permission must be obtained from the author.

Ekata Nandy

Ekata Nandy

DECLARATION

I, hereby declare that the investigation presented in the thesis has been carried out by me. The work is original and has not been submitted earlier as a whole or in part for a degree / diploma at this or any other Institution / University.

Ekata Nandy

Ekata Nandy

List of Publications arising from the thesis

Journal

1. **“Impact of Baryon anti-Baryon annihilation on hyperon ($\Lambda, \bar{\Lambda}$) production and apparent strangeness enhancement in $\bar{\Lambda}/\bar{p}$ in heavy ion collisions at SPS energy”**,
Ekata Nandy and Subhasis Chattopadhyay,
[European Physical Journal A, 58 \(2022\) 10, 199.](#)
2. **”Searching for Initial state fluctuations in heavy ion collisions at FAIR energy using Principal Component Analysis”**,
Ekata Nandy and Subhasis Chattopadhyay, [Submitted to Nuclear Physics A \(2022\).](#)
3. **“Commissioning and testing of pre-series triple GEM prototypes for CBM-MuCh in the mCBM experiment at SIS18 facility of GSI”**,
A. Kumar, A. Agarwal, S. Chatterjee, S. Chattopadhyay, A. K. Dubey, C. Ghosh, E. Nandy, et.al,
[Journal of Instrumentation 16, P09002 \(2021\) .](#)
4. **“Challenges in QCD matter physics –The scientific programme of the Compressed Baryonic Matter experiment at FAIR”**,
T. Ablyazimov, et.al,
[European Physical Journal A 53, 60 \(2017\).](#)

Proceedings of conferences

1. **”Baryon anti-baryon annihilation effect on strange baryons production & apparent strangeness enhancement at SPS energy”**, Ekata Nandy, Subhasis Chattopadhyay,
[66th DAE Symposium on Nuclear Physics, 978-979 \(2023\).](#)
2. **”Design, development and tests of real size PCBs for 3rd station readout at CBM-MuCH”**, Shuaib Ahmad Khan, Jogender Saini, Ekata Nandy, et.al.,
[66th DAE Symposium on Nuclear Physics, 1140-1141 \(2023\).](#)

3. **”Initial state fluctuations study in heavy ion collisions at FAIR energy using Principal Component Analysis”**, Ekata Nandy and Subhasis Chattopadhyay,
66th DAE Symposium on Nuclear Physics, 1008-1009 (2023).
4. **”Impact of Baryon anti-Baryon annihilation on apparent strangeness enhancement in anti-lambda to anti-proton ratio at SPS energy”**, Ekata Nandy and Subhasis Chattopadhyay,
Presented (talk) in ICPAQGP conference 2023, Puri, Odissa.
<https://events.vecc.gov.in/event/19/timetable/> .
5. **”Performance study of CBM Muon Chamber detectors at the mCBM setup of SIS18 with Pb+Au collisions at 1.06 AGeV”**,
Ekata Nandy on behalf of CBM collaboration,
<https://indico.cern.ch/event/895086/contributions/4721208>, 29th International Conference on Ultra Relativistic Nucleus Nucleus Collisions, ”Quark Matter 2022” (poster presentation).
6. **”Response study of triple GEM chambers to varying intensity in mCBM”**, Apar Agarwal, Ajit Kumar, Ekata Nandy et.al,
65th DAE BRNS Symposium on nuclear physics, 804-805 (2021).
7. **”Effects of Baryon-Anti-baryon Annihilation on the Anti-hyperon to Anti-proton Ratio in Relativistic Nucleus-Nucleus Collisions”**,
Ekata Nandy and S. Chattopadhyay, [Springer Proc.Phys. 261, 611-615 \(2021\).](#)
8. **”Testing Real-Size Triple GEM Chambers with Pb+Pb Collision at CERN SPS”**, A. Kumar, A. K. Dubey, J. Saini, V. Singhal, V. Negi, E. Nandy et. al, [Springer Proc.Phys. 261, 711-718 \(2021\).](#)
9. **”Thermal dimuon signal extraction with the Muon Detector setup of CBM experiment at FAIR at 8 AGeV ”**, Ekata Nandy, Partha Pratim Bhaduri, Subhasis Chattopadhyay,
64th DAE BRNS Symposium on nuclear physics, 828-829 (2019).
10. **”Performance Study of Muon Detector with CBM Experiment at FAIR”**,
Ekata Nandy and Subhasis Chattopadhyay,
[Springer Proc. Phys. 201, 157-165 \(2018\).](#)

11. "Detection of Low Mass Vector Mesons in the Muon Detector of CBM Experiment", Ekata Nandy and Subhasis Chattopadhyay, Springer Proc. Phys. 203, 393-396 (2018).
12. "A systematic investigation of di-muon combinatorial background for ω in the CBM experiment at FAIR ", Ekata Nandy, Partha Pratim Bhaduri, Subhasis Chattopadhyay, 63rd DAE-BRNS Symposium on Nuclear Physics, 1016-1017 (2018).
13. "Strangeness Enhancement at FAIR ", Ekata Nandy & Subhasis Chattopadhyay, 63rd DAE-BRNS Symposium on Nuclear Physics, 1018-1020 (2018).
14. "Hadronic Cocktail Simulation with new CBM Muon Chamber at FAIR ", Ekata Nandy, Partha Pratim Bhaduri, Subhasis Chattopadhyay, 62nd DAE Symposium on Nuclear Physics , 890-891 (2017).
15. "Feasibility study of using RPC in the muon detection system of the CBM experiment at FAIR ", Ekata Nandy, Subhasis Chattopadhyay, Partha Pratim Bhaduri, 62nd DAE Symposium on Nuclear Physics, 880-881 (2017).

Highlight talk : Presented highlight talk in 38th CBM collaboration meeting on " mMUCH@mCBM : Learnings from MCBM campaign " 38th CBM collaboration meeting (2021) .

Awards : Achieved "GROUP ACHIEVEMENT AWARD for the year 2020 under DAE" on " Installation, commissioning and data taking with GEM chambers at the mini CBM experiment at FAIR, Germany".

Ekata Nandy

Ekata Nandy

Dedicated to my family and friends,

ACKNOWLEDGEMENTS

I would like to express my sincerest and deepest gratitude to my Ph.D. supervisor, Prof. Subhasis Chattopadhyay, whose wisdom, knowledge in physics together with his unremitting enthusiasm for research has inspired me immensely to complete this thesis. His constant guidance and support throughout these years in every aspect of my Ph.D. career was extremely helpful and without his guidance it would not be possible to complete the Ph.D. thesis work. I would like to express my profound and heartfelt thanks to Dr. Partha Pratim Bhaduri, my senior colleague, who has helped me substantially to learn the fundamentals of high energy physics and details of computational framework. Without his generous help and guidance completing this thesis would have been much more difficult. I also sincerely acknowledge Dr. Anand Kumar Dubey, who supported me a lot in every aspect. Without his help, it wouldn't be possible for me to learn so many things related to detectors and electronics instruments. I sincerely thank Dr. Zubayer Ahammed for his guidance regarding RPCs, his help, support, and encouragement in every aspect. I am thankful to Dr. Vikas Singhal for his help in computing related issues which allowed me to solve the problems easily, effectively and seamlessly. I would like to thank Dr. Jogender Saini for making me understand technical details of detector-electronics and DAQ systems. I would also thank Dr. Sanjib Muhuri for his guidance in general. I would also like to thank all of my collaborators Mr. Omveer Singh, Mr. Sayak Chatterjee, Mr. Vinod Singh Negi, Mr. Apar Agarwal, Mr. Chandrasekhar Ghosh, Ms. Mitali Mondal, Dr. Sidharth Kumar Prasad, Dr. Shuaib Ahmmed. I am also thankful to Dr. Norbert Hermann and Dr. Christian Strum from GSI, for their valuable suggestions and encouragement when I was doing mini CBM data analysis. I would also like thank VECC grid colleagues, mainly Prasun da and Abhishek for their help during computer and software-related issues. I would like to extend my warm affection and gratitude to my friend Sinjini Chandra, who is also my room mate in office, for her help whenever I needed it. Thanks to my juniors and friends Shreyasi, Mitali, Sanchari, Sumit, Abhishek, Om, Tanay, Gitesh who have provided me a friendly environment and supported me all these years. A special thank goes to Dr. Tilak Ghosh for his guidance and student-friendly behavior. A special note of thanks for Prof. Saikat Biswas of Bose Institute whose valuable suggestions have enriched my understanding on detectors. Besides academia, Saikat da has remained my well-wisher. I also thank the members of my thesis committee, Dr. Chandana Bhattacharya, Dr. Sourav Sarkar, Dr.

Supriyo Das for their constructive suggestions. I would like to thank Dr. Parnika Das and Dr. Jane Alam, for helping me in academic related things in Ph.D.

Finally I want to thank my family members; my parents, my parents-in-law, my husband, my sister and my cute niece and nephew, without them I couldn't have achieved this position in my life. I am specially thankful to my beloved husband Dr. Subikash Choudhury, for his all-round support in my ups and down and for being with me in all situations. I especially would like to thank my sister, Mili Nandy, for being a best friend of mine from my childhood and motivating me to deal with all difficult situations in my life. I thank my brother-in-law, Subrata Ghosh for his kind support and his brotherly behavior and my cute niece and nephew Ms. Sumana Ghosh and Mr. Kaushik Ghosh, they are being my lifeline, talking to them makes me feel happy all the time with their innocence. Lastly, I am grateful to my parents, my mother Shyamaly Nandy and my father Mr. Sunith Kumar Nandy, for loving me unconditionally and supporting me in every steps of my life. I express my gratitude again to all of you, to whom I owe so much.

Ekata Nandy

Ekata Nandy

SUMMARY

The goal of the study of relativistic heavy ion collisions is to investigate the properties of normal nuclear matter when subjected to extreme conditions, like very high temperature or high pressure. Quantum Chromodynamics (QCD), the theory of strong interactions, suggests a possible phase transformation from the normal nuclear matter to a deconfined state of quarks and gluons at an energy density $> 5-6$ times the normal nuclear density ($0.14 \text{ GeV}/\text{fm}^3$) $\sim 1 \text{ GeV}/\text{fm}^3$. The collisions of heavy nuclei at relativistic energies at the LHC at CERN and RHIC at BNL provide experimental access to such a novel form of deconfined matter, particularly in the region of high to intermediate temperature in the QCD phase diagram. By far, the region of low temperature with very high net-baryon density has not been explored in detail. At the Facility for Anti-proton and Ion Research (FAIR) at Darmstadt, Germany, an experiment, Compressed Baryonic Matter (CBM) is getting ready to collide heavy nuclei at relativistic energies in a fixed target mode to determine the fate of the nuclear matter at very high net-baryon density. The main goal of the CBM is to study the properties of nuclear matter at high net-baryon densities using rare and diagnostic probes. To meet such a requirement CBM has to be operated at a large interaction rate reaching up to 10 MHz. Thus the detectors at CBM have to be fast and radiation hard.

Dimuon measurement is a central part of the CBM physics program as muons are considered as a diagnostic probes because they carry the information from their point of origin almost unperturbed. To facilitate muon identification, CBM is equipped with a dedicated muon detection system called the Muon Chamber (MuCh). The MuCh will be a major in-kind contribution from India, being designed and to be fabricated for the CBM experiment. Before actual detector fabrication, design parameters which are crucial for efficient detection of dimuons have been optimized through detail simulation study. This thesis discusses the details of the simulation at each step and presents results of efficiency and signal-over-background ratios of detection of low mass vector mesons (LMVMs) like ρ, ω, ϕ, η through dimuon channels. Low mass vector mesons are very important probes for the CBM physics program, particularly for addressing the issue of chiral symmetry restoration. Besides analyzing the performance through simulation, detectors also needed to be tested in realistic experimental environments. This has been done by an experimental setup at SIS18 facility in GSI, called the mini-

CBM (mCBM) experiment, which is a miniaturized version of the CBM, where all the sub-detectors in CBM with a few modules for each type including their electronics are tested with heavy ion collisions. A uniqueness of CBM is the trigger-less free streaming data acquisition (DAQ) system and the time based event reconstruction, which has been tested as well in high particle density environments. In addition, the integrated response of all the CBM sub-detectors and their time synchronous behavior have been characterized by studying the time and spatial correlations between two sub-detectors with different detector technologies, as well as electronics. For, mini-MuCh (mMuCh) system, two real size GEM prototype detectors for the first station of CBM-MuCh were installed. A clear spatial correlation and time correlation have been observed between the response of GEMs with respect to other sub-detectors. For the first time GEM efficiency has been estimated in a heavy ion collision experimental scenario with high particle density environment and the systematics of GEM efficiency with time, particle velocity (β) and GEM high voltage have been studied.

This thesis also investigates the physics of strong interactions at high net-baryon density region with the help of strangeness production and initial state fluctuations using the Principal Component Analysis technique. As partonic deconfinement is an expected outcome when a normal nuclear matter is subjected to high compression/pressure, a possible signature of deconfinement is the strangeness enhancement. This thesis however, shows how hadronic interactions alone might account for an apparent signature of strangeness enhancement, manifested through a non-monotonic increase in the ratios of $\bar{\Lambda}/\bar{p}$ as a function of collision energy, particularly in the region of high net-baryon density based on UrQMD model calculations.

Further, a new analysis technique called, the Principal Component Analysis (PCA) was applied to heavy ion collision at FAIR energies to test its sensitivity towards the initial conditions by introducing hot spots (large localized fluctuation in energy density) in the initial state. The technique was found to be suitable for deciphering such structures in the initial state from the variable constructed from final states particles thereby demonstrating its effectiveness in capturing the true picture of initial condition in relativistic nuclear collisions.

Contents

Synopsis	xv
1 Introduction to the high energy heavy-ion collisions	1
1.1 Introduction	1
1.2 The Standard Model of Particle Physics	2
1.3 Quantum Chromodynamics (QCD)	3
1.4 Phase Diagram of Nuclear Matter	5
1.5 Relativistic heavy ion collisions experiments	7
1.6 Evolution of a heavy ion collisions at relativistic energies	9
1.6.1 Strangeness Enhancement	12
1.6.2 Quarkonia Suppression	13
1.6.3 Jet Quenching	16
1.6.4 Anisotropic Flow	17
1.6.5 Event by event fluctuations of conserved quantities	19
1.6.6 Dilepton Production	20
1.7 Motivation and organization of this thesis	23
2 The Compressed Baryonic Matter (CBM) Experiment at FAIR	25
2.1 Introduction	25
2.2 The Facility for Antiproton and Ion Research (FAIR)	27
2.3 Diagnostics probes of high density medium at CBM	28
2.4 CBM Physics Motivation	30
2.5 CBM experimental setup	32
2.5.1 Dipole Magnet	33
2.5.2 Micro Vertex Detector (MVD)	34
2.5.3 Silicon Tracking station (STS)	34
2.5.4 Ring Imaging Cherenkov Detector (RICH)	36
2.5.5 Muon Chamber (MUCH)	37
2.5.6 Transition Radiation Detector (TRD)	38

2.5.7	Time of Flight (TOF)	39
2.5.8	Electromagnetic CALorimeter (ECAL)	40
2.5.9	Projectile Spectator Detector (PSD)	40
2.5.10	Data Acquisition (DAQ) and online event selection	41
2.6	Dimuon measurement at FAIR	41
3	Development and performance of Muon Chamber (MuCh) at CBM	45
3.1	Different configurations of the Muon Chamber geometry	46
3.2	Simulation steps in MuCh	49
3.3	Development and modifications of the MuCh geometry	53
3.3.1	Optimization of absorbers and detectors in MuCh	53
3.3.2	Implementation of RPC geometry & digitization in MuCh	67
3.4	Performance of MuCh in detection of LMVM through dimuon channel	81
3.4.1	Input event generators for signal generation	84
3.4.2	Muon identification selection cuts	86
3.4.3	Reconstruction of LMVM cocktails	87
3.4.4	Phase space acceptance of dimuons	89
3.5	Summary	92
4	Performance study of mini muon chamber modules at the mini CBM experiment at FAIR	95
4.1	Objective of mCBM	95
4.2	mCBM setup	96
4.3	mMuCh setup	99
4.4	Results from mCBM data 2020	102
4.4.1	Noisy channels removal	103
4.4.2	Spill structure	106
4.4.3	Digi correlation	107
4.4.4	Time correlation	109
4.4.5	Event building and track reconstruction	111
4.4.6	Spatial correlations	115
4.4.7	GEM efficiency determination	117
4.5	Summary	123
5	Baryon anti-baryon annihilation and it's impact in apparent strangeness enhancement in high density nuclear matter	125
5.1	Introduction	125
5.2	UrQMD Model	129

5.2.1	Baryon-anti-baryon annihilation	129
5.3	Results	130
5.3.1	Particle yields	130
5.3.2	Averaged transverse mass	133
5.3.3	Baryon-anti-baryon annihilation with p_T and rapidity	136
5.3.4	Estimation of annihilation fraction	139
5.3.5	Effect of $B\bar{B}$ annihilation on $\bar{\Lambda}/\bar{p}$ ratios	140
5.4	Summary	142
6	Searching for initial state fluctuations in heavy ion collisions using Principal Component Analysis at FAIR energy	145
6.1	Initial conditions in heavy ion collisions	145
6.2	Principal Component Analysis (PCA)	147
6.3	Implementation of hot spot at the nucleon level in UrQMD	148
6.4	Results	150
6.5	Summary	157
7	Summary & Conclusions	161
	Bibliography	178
	List of Figures	190
	List of Tables	191



Homi Bhabha National Institute

Synopsis of PhD Thesis

- 1. Name of the Student:** Ekata Nandy
- 2. Name of the Constituent Institution:** Variable Energy Cyclotron Centre, Kolkata
- 3. Enrolment No. :** PHYS04201704002
- 4. Title of the Thesis:** Exploring high density nuclear matter with dimuons & hadrons at FAIR energies
- 5. Board of Studies:** Physical Sciences

SYNOPSIS

(Limited to 10 pages in double spacing)

Nuclear matter are believed to be described by different forms under different conditions of temperature and pressure. Under extreme conditions of temperature and pressure, normal nuclear matter is likely to undergo a phase transition from the hadronic phase to a deconfined state of quarks and gluons (partons) known as quark gluon plasma (QGP) [1]. This form of matter is believed to have existed at a few microseconds after the Big Bang and still existing at the core of neutron stars [2]. In terrestrial laboratories, QGP is predicted to be produced in a wide range of temperatures and densities by colliding heavy nuclei at relativistic energies [3]. As predicted by the fundamental theory of strong interactions, Quantum ChromoDynamics (QCD) [4], the transition between the hadronic matter to QGP is supposed to be a smooth crossover at energies available at CERNs' Large Hadron Collider (LHC) and top energy at Relativistic Heavy Ion Collider (RHIC) in BNL. There are also predictions of crossover transition for a critical end point in the phase diagram which is yet

to be discovered. The Beam Energy Scan program at RHIC is particularly aimed at the search for such a critical end point in the QCD phase diagram [5, 6]. There also exists another extreme in the QCD phase diagram where, the transition to the deconfined phase is believed to be possible at very high net baryon densities that can be achieved by colliding heavy nuclei in few tens of AGeV in lab frame [7].

The Compressed Baryonic Matter (CBM) experiment is an upcoming fixed target experiment at the Facility for Antiproton and Ion Research (FAIR) in Darmstadt, Germany which will provide us the unique opportunity to investigate the nuclear matter at very high net baryon densities and moderate temperatures through collisions of heavy nuclei in the beam energy range of 4 - 45 A GeV [7, 8, 9]. The model calculations estimate that the nuclear matter density $\sim 5-10\rho_0$ (where $\rho_0 = 0.17 / \text{fm}^3$ is the normal nuclear matter density) can be achieved in the center of the reaction zone at these energies. The CBM experiment will thus offer an unique opportunity to search for some of the fundamental issues of QCD like hadronic properties in dense nuclear matter that might be connected to the chiral and/or the de-confinement phase transition from hadronic to partonic matter and critical end point along with the nuclear equation of state (EOS) at high net baryon densities [10].

The CBM experiment is particularly focussed on studying this high baryon rich nuclear matter with rare and penetrating probes like low mass vector mesons (LMVMs) [ρ , ω , ϕ], charmonium (J/ψ) through dilepton channels and multi-strange hadrons. Information on the in-medium modifications of these short lived LMVMs can shed light on chiral symmetry restoration and the origin of hadron masses. Whereas, charmonium suppression and strangeness enhancement are sensitive to the onset of partonic deconfinement [11]. However, as the production cross sections of these particles are extremely small at the FAIR energy range, the main challenge is to identify them at good efficiency and with high precision. To facilitate precision measurements of these rare probes, the CBM experiment has been designed to operate at an unprecedented interaction rate of ~ 10 MHz in heavy ion collisions, enabling us to measure these rare observables with high precision. At such high interaction rates, rate of the particles to be detected will be very high, requires fast and high granularity detectors to handle such a high-rate environment and also the detectors should be radiation hard. To cope with this high interaction rate fast and free streaming data acquisition using self triggered readout electronics is a primary prerequisite for the CBM experiment. In this high particle density environment identification of leptons and hadrons is itself a challenging task. A muon chamber (MuCh) detector system for the CBM experiment is being developed in India and is designed to identify muon pairs or dimuons originating from LMVMs, charmonium and thermal decay among others. The novel fea-

ture of the muon detection system in CBM experiment, is that the total absorber is sliced into thinner segments and detector triplet layers called stations are placed in between the absorbers to facilitate momentum dependent track identification. This is done to improve the capturing of low as well as high momentum muons. The Muon Chamber (MuCh) system in SIS100 consists of 4 absorbers and 4 stations for the LMVM setup to be followed by one thick absorber and TRD is used as the 5th station. In the first two stations as the particle density is very high Gas Electron Multiplier (GEM) detectors will be used [11, 12, 13] whereas in the next two stations Resistive Plate Chamber (RPC) detectors have been chosen as a suitable candidate to handle relatively lower particle density.

The work done in this thesis has three parts:

1. Development and optimization of MuCh geometry & performance study of MuCh . It has two parts (a) optimization and design simulation of the muon detector system for identification of low mass vector mesons in the di-muon decay channels. (b) Testing and data analysis of real size MuCh detectors with Pb+Au collisions at the mini CBM experiment at GSI, Germany.

2. Understanding the production mechanism of the strange particles at FAIR/SPS energy and study the effect of hadronic interactions specifically baryon-anti baryon annihilation on strangeness enhancement.

3. Study the initial state fluctuations in heavy ion collisions at FAIR energy using the technique of Principal Component Analysis (PCA).

Development and optimization of Muon Chamber (MuCh) geometry & performance study of MuCh

In this section, a brief description has been given about the design and optimization of muon detection system by simulation for the CBM experiment. The muon system is aimed to be used for identification of LMVMs (ω , ρ , ϕ) and J/ψ mesons from their dimuon decay channels. Thus, the main objective of such a simulation is to find out an optimized version of the muon detection system which would make the above measurements feasible. The novel feature of the muon system for CBM compared to other High Energy Physics (HEP) experiments is that the total absorber is segmented and detector triplet layers (called stations) are placed in between the absorbers to enable momentum dependent track identification. The particle rate in the detectors is highest in the first station and it decreases as we go downstream from the target. Because of very high particle rate in the first two stations, GEM detectors have been used. For the third and fourth station as the particle rate is relatively lower, Resistive Plate Chamber (RPC) detectors have been proposed. This part of the thesis gives a detail account on the optimization of the muon system in terms of absorbers material, their

thickness, absorbers size & shape, stations size, beam pipe and shielding design inside the MuCh portion etc. The details of RPC geometry and detector response implementation for third and fourth stations, together with the study of its performance to test its feasibility of usage are presented as well.

The optimized muon system is used to study the feasibility of LMVMs measurement in central Au+Au collisions at beam energy of 8 A GeV. The feasibility studies are performed within a CBM-compatible simulation framework, called CBMROOT, that allows for full event simulation and reconstruction. For signal, i.e, LMVMs (ω , ρ , ϕ , etc) decaying to dimuons and background particles are generated by event generators PLUTO [14] and UrQMD [15, 16], respectively. The generated particles are then transported through the CBM detector set-up developed using GEANT3 transport package. The produced tracks are then reconstructed using the hits in the chambers with a reconstruction package based on Kalman Filter technique. The reconstructed muon tracks are selected for analysis applying different track quality cuts which include length of the track and track χ^2 w.r.to the primary vertex also χ^2 of global tracks . The reconstructed dimuon invariant mass spectra are studied to estimate the peak over the continuum which comprises the combinatorial background coming from the weak decay of pions and kaons and the single muon detection efficiency due to acceptance loss. This CBM setup can produce the reconstructed cocktails of LMVM invariant mass with good signal to background ratio and significance as shown in Fig. 1.

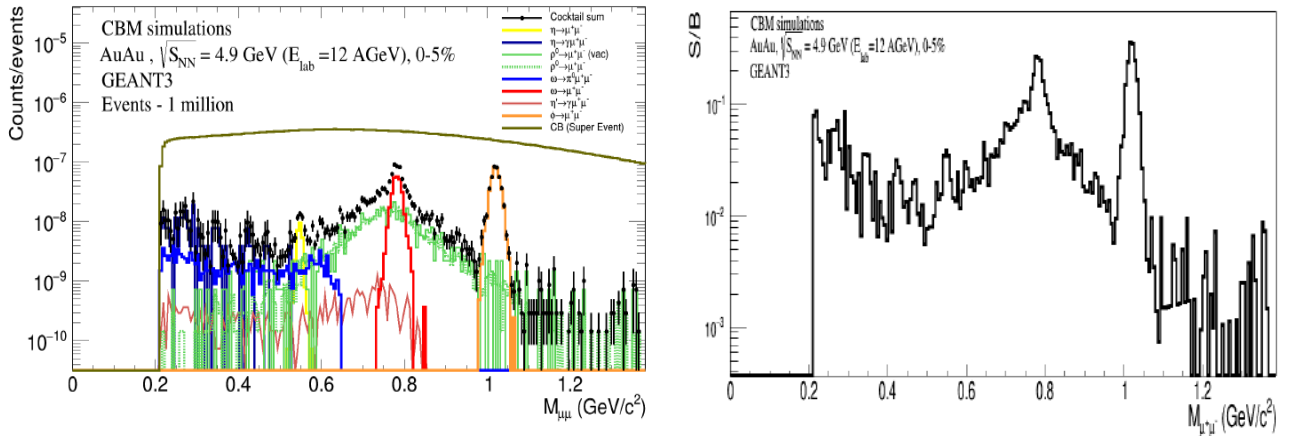


Figure 1: Invariant mass distributions of reconstructed LMVM cocktails (left) and signal to background ratio (right) through CBM-MuCh setup at $E_{lab} = 12$ A GeV , central AuAu collisions.

MuCh prototype test in the mCBM (mini CBM) campaign at GSI, SIS18

In this part of the work, we will focus on the performance of real size MuCh-GEM detector modules in high particle density environment in heavy ion collisions in the mini CBM (mCBM) experiment at Darmstadt, Germany at FAIR. This mCBM campaign at SIS18 facility is a part of the FAIR

phase-0 program where a pre-series production of full CBM set-up is tested with a fewer number of detector modules prior to the final production of main CBM. The primary aim of the mCBM campaign is to install, commission and test the complex integration process of the different detector systems using the real CBM environment. Thereby testing with the triggerless-streaming data acquisition and the fast online event reconstruction and selection. In particular, it allows testing of detectors and electronics components developed for the CBM experiment as well as, the corresponding online/offline software packages under realistic experimental conditions up to top CBM interaction rates of 10 MHz.

To this end, two real-size GEM modules (GEM.1 and GEM.2), corresponding to the module sizes of the first station in CBM-MuCh, were installed and commissioned in the mCBM experiment at GSI. Detectors were tested by varying the beam intensity and the target thickness. Linearity of detector response with the beam intensity has been studied and a linear response of GEM interms of the rate of detector pads with beam intensity has been observed. Detector response in terms of spill structure, time correlation, and time resolution have been studied. The events were reconstructed offline using time-stamps of the detector digis after correcting for time offsets in different front end electronics boards (FEBs). Clustering and local hit reconstruction are also done for the MuCh modules from the free streaming data set of mCBM. For further analysis in this work, hits from the GEM and TOF modules have been used. Uniformity of the detector response has been studied in terms of the time resolutions measured across different pads spread throughout the detector active area. A good time and spatial correlation between the GEM.1 & GEM.2 and, between GEM & TOF modules have been observed as shown Fig. 2 representing a successful event reconstruction and a coherent time-synchronous behavior of two different detectors as well as, even between two different sub-systems that employ different detector technologies and readout electronics .

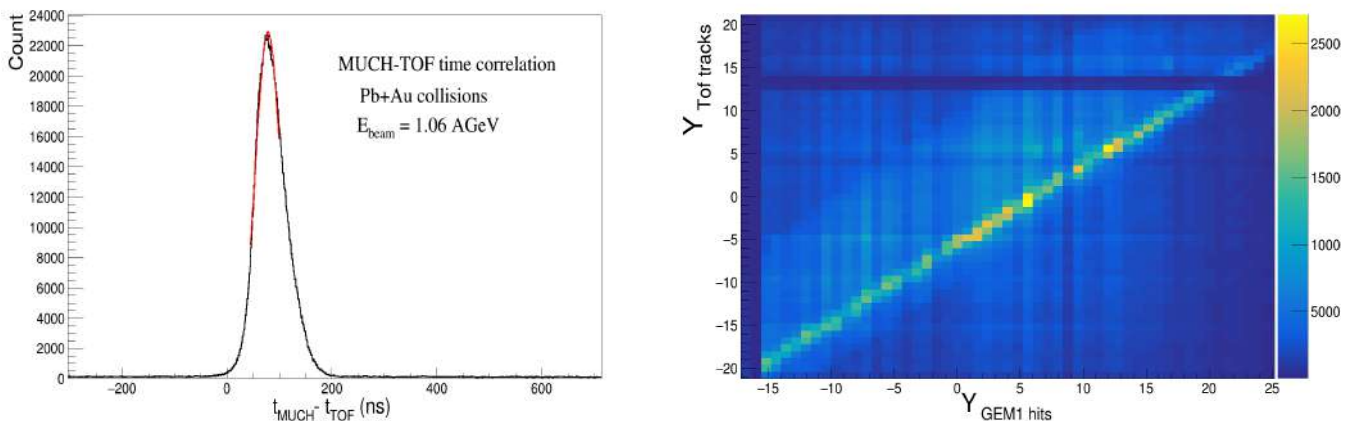


Figure 2: Time (left) and spatial (right) correlation between GEM.1 and TOF from mini CBM data.

A straight line track reconstruction has been performed using the hits in TOF and T0 (diamond detector) detectors. Spatial correlation strengths have been studied for different track multiplicities. Track residuals have been measured for different pad sizes within the GEM detectors. Using this residuals between the projected TOF tracks on the GEM plane and GEM hits, GEM efficiency has been estimated for the first time from mCBM data. Systematics of GEM efficiency has been studied with time, particle velocity β and with GEM high voltage. Encouraging results have been obtained which are close to the expectation from the standalone measurements of detector performance in laboratory with radiation sources. Detailed procedure and results will be presented in the thesis.

Strangeness production study at FAIR/SPS

Strangeness enhancement is one of the proposed signatures of the partonic deconfinement [17]. Results from the heavy-ion collisions of RHIC AGS and CERN SPS appear to be in agreement with such proposition. However, at such low collision energies, where hadronic interactions are dominant, contributions from the hadronic interactions can not be completely ruled out. In this section we have studied how the observations associated with the strangeness enhancement at FAIR/SPS energies can be affected by hadronic interactions. In particular, we have studied the impact of the baryon anti-baryon annihilation on hyperon (Λ , $\bar{\Lambda}$) production and the enhancement in $\bar{\Lambda}/\bar{p}$ ratios that has been interpreted as a signature for strangeness enhancement due to QGP formation in heavy ion collisions at FAIR/SPS energy.

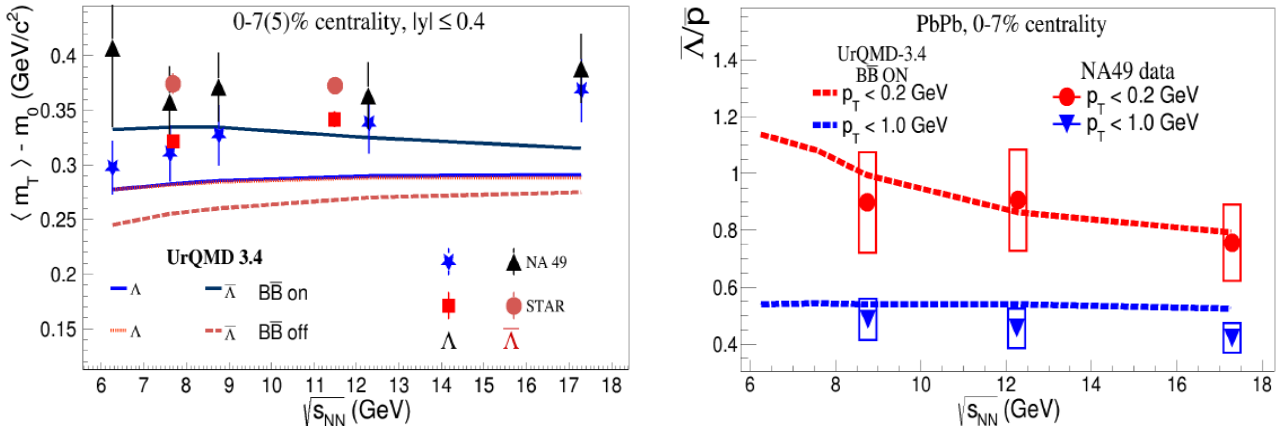


Figure 3: Effect of baryon -anti baryon annihilation on Λ and $\bar{\Lambda}$ mean m_T with $\sqrt{s_{NN}}$ (left) and $\bar{\Lambda}/\bar{p}$ ratio with $\sqrt{s_{NN}}$ (right)

In this work, we use a hadronic transport model UrQMD, to investigate the role of baryon-anti-baryon ($B\bar{B}$) annihilation on Λ , $\bar{\Lambda}$ hyperon production and its effect on $\bar{\Lambda}/\bar{p}$ ratios. The UrQMD calculations that include $B\bar{B}$ annihilation can produce the trend of average transverse mass spectra for Λ and $\bar{\Lambda}$, as well as, the characteristic enhancement in $\bar{\Lambda}/\bar{p}$ ratios in data as a function of central-

ity and collision energy as shown in Fig. 3. Furthermore, $\bar{\Lambda}/\bar{p}$ ratios extracted from the feed-down corrected SPS data are seen to be in good agreement with the UrQMD model calculations with $B\bar{B}$ annihilation. This suggests that $\bar{\Lambda}/\bar{p}$ enhancement is not necessarily because of strangeness enhancement and hadronic interactions, in particular, $B\bar{B}$ annihilation in this case has a significant role to play [18].

Study of initial state fluctuations in heavy ion collisions at FAIR energy using the technique Principal Component Analysis (PCA)

In high energy heavy ion collisions, the knowledge of the initial condition of the colliding nuclei are crucial for the meaningful interpretation and extraction of final state medium properties. By now it is well understood that the initial condition in heavy ion collisions fluctuates from event to event as well as in a single event energy density is not uniform within the overlap region of the colliding nuclei. There could be some localized regions where energy density is larger than the average which are known as hot spots. Such hot spots can induce large fluctuations in the final state but the conventional event averaged measurements mostly remain insensitive to such localized fluctuations. In this work we propose to use the Principal Component Analysis [19] technique to resolve such localized fluctuation using final state observables. We introduce such localized fluctuations or hot spot like initial configuration by implementing a spatial rearrangements of nucleon position in the colliding nuclei in the central Pb+Pb collisions at $\sqrt{s} = 6.27$ GeV using the UrQMD event generator. The final state distributions of one or two dimensional variables e.g., (η, ϕ, p_T) and $(\eta - p_T, \phi - p_T, \eta - \phi)$ of the produced pions have been analysed using the principal component analysis (PCA) technique. The eigenvalues of the principal components have been studied for various initial configurations, event fractions containing hot spots in the initial condition and for event centralities with an aim to find the sensitivity to the initial hot spot configurations [20].

References

- [1] E. V. Shuryak, Phys. Rept. 115, 151 (1984).
- [2] Eemeli Annala, et.al. <https://arxiv.org/abs/1903.09121>.
- [3] J. Cleymans, R. Gavai, and E. Suhonen, Phys. Rept. 130, 217 (1986).
- [4] B. Friman, F. Karsch, K. Redlich, V. Skokov, <https://arxiv.org/abs/1103.3511>

- [5] B. V. Jacak and B. Muller, *Science* 337, 310 (2012).
- [6] P. Braun-Munzinger, V. Koch, T. Schäfer, and J. Stachel, *Phys. Rept.* 621, 76 (2016).
- [7] T. Ablyazimov et al., *Eur. Phys. J. A* 53, 60 (2017).
- [8] The Cbm Experiment, <https://www.cbm.gsi.de/>.
- [9] The Fair Experiment, <https://fair-center.eu/>.
- [10] S. Chattopadhyay, *Eur. Phys. J. ST* 230, 689 (2021).
- [11] S. Chattopadhyay et al., editors. Technical Design Report for the CBM : Muon chambers (MuCh). GSI (2015).
- [12] A.K. Dubey et al., *Nucl. Instrum. Meth. A* 718, 418 (2013).
- [13] R. P. Adak et al., *Nucl. Instrum. Meth. A* 846, 29 (2017).
- [14] I. Froehlichet, et al., *Journal of Physics:Conference Series* 219 032039 (2010).
- [15] S.A. Bass, et al., *Progress in Particle and Nuclear Physics* 41 (1998) 225.
- [16] M. Bleicher et al., *J. Phys. G: Nucl. Part. Phys.* 25 1859 (1999)
- [17] J. Rafelski, B. Muller, *Phys.Rev.Lett.* 48, 1066 (1982), *Phys.Rev.Lett.* 56, 2334 (1986) (erratum).
- [18] E. Nandy, S. Chattopadhyay, *Eur. Phys. J. A* 58, 199 (2022).
- [19] I. Jolliffe, Principal component analysis, in *Encyclopedia of Statistics in Behavioral Science* (Wiley Online Library, 2005).
- [20] E. Nandy, S. Chattopadhyay, submitted to *Nucl. Phys. A* (2022).

List of Publications

a. Publications in Referred Journals:

1. **“Impact of Baryon anti-Baryon annihilation on hyperon (Λ , $\bar{\Lambda}$) production and apparent strangeness enhancement in $\bar{\Lambda}/\bar{p}$ in heavy ion collisions at SPS energy”,**
Ekata Nandy and Subhasis Chattopadhyay, [European Physical Journal A, 58 \(2022\) 10, 199.](#)
2. **“Searching for Initial state fluctuations in heavy ion collisions at FAIR energy using Principal Component Analysis”,**
Ekata Nandy and Subhasis Chattopadhyay, [Submitted to Nuclear Physics A \(2022\).](#)
3. **“Commissioning and testing of pre-series triple GEM prototypes for CBM-MuCh in the mCBM experiment at SIS18 facility of GSI”,**
A. Kumar, A. Agarwal, S. Chatterjee, S. Chattopadhyay, A. K. Dubey, C. Ghosh, E. Nandy, et.al, [Journal of Instrumentation 16, P09002 \(2021\).](#)
4. **“Challenges in QCD matter physics –The scientific programme of the Compressed Baryonic Matter experiment at FAIR”,**
T. Ablyazimov, et.al, [European Physical Journal A 53, 60 \(2017\).](#)

b. Conference Proceedings

1. **“Performance study of CBM Muon Chamber detectors at the mCBM setup of SIS18 with Pb+Au collisions at 1.06 AGeV”,**
Ekata Nandy on behalf of CBM collaboration,
<https://indico.cern.ch/event/895086/contributions/4721208>, 29th International Conference on Ultra Relativistic Nucleus Nucleus Collisions, “Quark Matter 2022” (poster presentation).
2. **“Response study of triple GEM chambers to varying intensity in mCBM”,**
Apar Agarwal, Ajit Kumar, Ekata Nandy et.al,
[65th DAE BRNS Symposium on nuclear physics, 804-805 \(2021\).](#)
3. **“Effects of Baryon-Anti-baryon Annihilation on the Anti-hyperon to Anti-proton Ratio in Relativistic Nucleus-Nucleus Collisions”,**
Ekata Nandy and S. Chattopadhyay, [Springer Proc.Phys. 261, 611-615 \(2021\).](#)

4. "Testing Real-Size Triple GEM Chambers with Pb+Pb Collision at CERN SPS", A. Kumar, A. K. Dubey, J. Saini, V. Singhal, V. Negi, E. Nandy et. al, Springer Proc.Phys. 261, 711-718 (2021).
5. "Thermal dimuon signal extraction with the Muon Detector setup of CBM experiment at FAIR at 8 AGeV ", Ekata Nandy, Partha Pratim Bhaduri, Subhasis Chattopadhyay, 64th DAE BRNS Symposium on nuclear physics, 828-829 (2019).
6. "Performance Study of Muon Detector with CBM Experiment at FAIR", Ekata Nandy and Subhasis Chattopadhyay, Springer Proc. Phys. 201, 157-165 (2018).
7. "Detection of Low Mass Vector Mesons in the Muon Detector of CBM Experiment", Ekata Nandy and Subhasis Chattopadhyay, Springer Proc. Phys. 203, 393-396 (2018).
8. "A systematic investigation of di-muon combinatorial background for ω in the CBM experiment at FAIR ", Ekata Nandy, Partha Pratim Bhaduri, Subhasis Chattopadhyay, 63rd DAE-BRNS Symposium on Nuclear Physics, 1016-1017 (2018).
9. "Strangeness Enhancement at FAIR ", Ekata Nandy & Subhasis Chattopadhyay, 63rd DAE-BRNS Symposium on Nuclear Physics, 1018-1020 (2018).
10. "Hadronic Cocktail Simulation with new CBM Muon Chamber at FAIR ", Ekata Nandy, Partha Pratim Bhaduri, Subhasis Chattopadhyay, 62th DAE Symposium on Nuclear Physics , 890-891 (2017).
11. "Feasibility study of using RPC in the muon detection system of the CBM experiment at FAIR ", Ekata Nandy, Subhasis Chattopadhyay, Partha Pratim Bhaduri, 62th DAE Symposium on Nuclear Physics, 880-881 (2017).

Awards : Achieved "GROUP ACHIEVEMENT AWARD for the year 2020 under DAE" on "Installation, commissioning and data taking with GEM chambers at the mini CBM experiment at FAIR, Germany".

Signature of Student: Ekata Nandy

Date: 25/11/2022

The Doctoral Committee recommends submission of Ph. D. thesis by Ekata Nandy.

Doctoral Committee:

S. No.	Name	Designation	Signature	Date
1.	Dr. Chandana Bhattacharya	Chairman	C. Bhattacharya	25.11.22
2.	Dr. Subhasis Chattopadhyay	Guide/Convener	Subhasis	25/11/22
3.	Dr. Sourav Sarkar	Member 1	Sourav Sarkar	25/11/22
4.	Dr. Zubayer Ahammed	Member 2	Zubayer	25/11/22
3.	Dr. Supriya Das	Member 3	Supriya Das	25/11/2022

Panwih
14/12/2022

Chapter 1

Introduction to the high energy heavy-ion collisions

1.1 Introduction

The ultimate goal of science is to understand nature at the fundamental level. In 1909, Rutherford's gold foil experiment revealed a new concept of the atomic structure that showed - a large part of an atom is empty and most of the atomic mass resides in a tiny positively charged region called nucleus, surrounded by negatively charged electrons. Another important piece of information obtained from the Rutherford's experiment was about the energy or momentum ranges of the probes which are required to perform study of smaller dimensions like that of a size of an atomic nucleus. It was therefore concluded that more energetic probes will be needed to study dimensions which are smaller than the size of an atomic nucleus - typically of the order of 1 fm (10^{-15} m).

Need for high energy particles or probes led to the invention of particle accelerators, that eventually led to the discovery of several sub-atomic and sub-nucleonic particles. Parallely, a lot of theoretical work was done to provide a framework that can consistently describe the creation of these particles and their interactions, which finally evolved into the Standard Model (SM) of particle physics [1-4].

1.2 The Standard Model of Particle Physics

The Standard Model (SM) of particle physics is built on quantum theory of fields [5] which, at present, provides the best possible description of physics at the sub-atomic scale. Main constituents of SM are three generations of quarks & leptons and four force carriers. The quarks and leptons are spin half fermions and force carriers are integer spin gauge bosons. Quarks carry fractional electric charge as well as color charges whereas, leptons, except neutrinos, have integer electric charge. The first generation of quarks, i.e up (u) and down (d), are lightest and stable ones which makes up most of the matter. Higher generation of quarks i.e, strange (s), charm (c), beauty (b) and top (t) are massive and unstable. Basic structure of SM is pictorially depicted in Fig. 1.1.

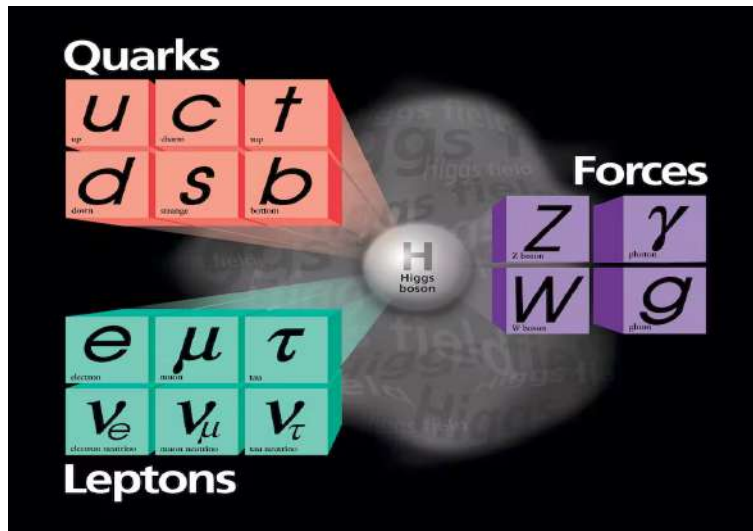


Figure 1.1: Depiction of the elementary particles and forces in the Standard model.

The quarks and leptons in the SM interact via exchange of the four force carriers. There are mainly three fundamental interactions that are well described by SM namely, electromagnetic, weak and strong. Each of these interactions have a specific range beyond which they either vanish or reduce drastically. Also a particular gauge boson (force carrier) is responsible for mediating each of these interactions. For example, electromagnetic interaction is mediated through the exchange of photons that are massless spin 0 particles and has almost infinite range because its potential has $1/r$ type of dependence which asymptotically vanishes when $r \rightarrow \infty$. All particles that carry an electric charge interact via electromagnetic interactions.

On the other hand, weak interactions are limited to a length scale smaller than the size of a nucleus and it is mediated by massive W^\pm and Z_0 bosons. The weak interaction is responsible for radioactivity. Similarly, strong interaction is also a short range interaction, confined to a typical length scale of atomic nuclei and its mediator is gluon. Strong interaction is responsible for binding quarks within the hadrons. At the length scale which is about the size of a hadron (1 fm), strong interaction potential becomes attractive and its strength becomes exceedingly large. As a result, it becomes impossible to separate an individual quark from its bounded counter part. This is the main reason that free quark does not exist in nature under normal condition. Finally, Higgs boson is at the core of SM which is responsible for generating mass [3, 6, 7].

As the main objective of this thesis is to understand the nature of the strong interaction between quarks and gluons when they are nearly free and subsequently how they get confined within hadrons, so, in the next section we will briefly discuss about some basic aspects of the quantum theory of strong interaction, i.e, quantum chromodynamics (QCD) [5, 8–10].

1.3 Quantum Chromodynamics (QCD)

It is now established that quarks and gluons are the fundamental building blocks of matter. In addition to electric charge, quarks also carry color charges or color quantum numbers. The concept of color quantum number was introduced to describe coexistence of quarks in some hadronic resonance states which would be otherwise forbidden. For example, $\Delta^{++}(uuu)$, which has an electric charge of 2 units and total spin, $S=3/2$. This means all the constituent u quark has spin $+1/2$, which violates Pauli's exclusion principle, i.e, no two fermions can have same set of quantum numbers. Thus, there must be an additional quantum number which is different from these existing ones. Greenberg first proposed the idea of color quantum number and associated each quark with three colors (red, blue and green) which eventually validated coexistence of quarks without violating Pauli's exclusion principle. As quarks interact via exchange of gluons so, gluons also have color charges but they are mixture of two colors (color-anticolor: blue-antigreen), such that when quarks interact via exchange of gluons total color of the system remains conserved. Thus the key to the strong interaction in quarks and gluons are these color charges and color force field which is described within the theoretical framework of

quantum chromodynamics (QCD).

QCD exhibits two important features, 'Confinement' and 'Asymptotic Freedom' [11]. The confinement property of the QCD says that, the color force between a quark pair increases depending on their relative distance of separation and the energy required to separate them is almost infinite. As a result, quarks are always bounded within hadrons like baryons and mesons. On the other hand, when two quarks are very close their interaction weakens and they behave like quasi-free particles. This is called 'Asymptotic Freedom' in QCD, discovered by Politzer, Wilzek and Gross for which they were conferred Nobel prize.

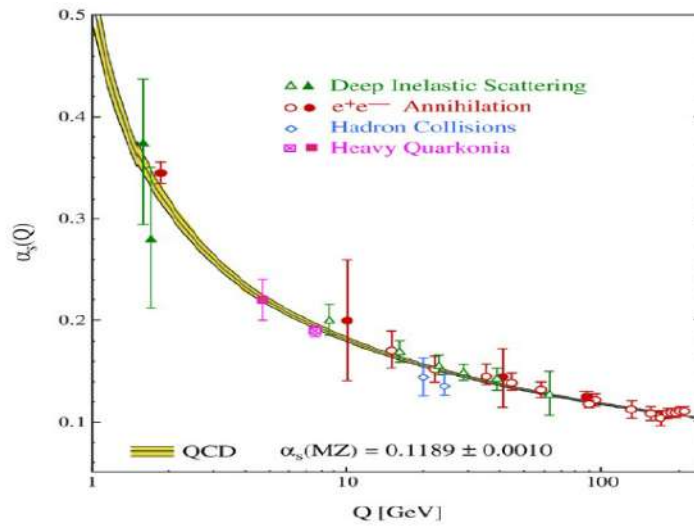


Figure 1.2: QCD running coupling constant α_s as a function of momentum transfer (Q). Solid and open symbols are experimental values overlaid on QCD prediction shown is yellow band. In the limit of large momentum transfer, strong coupling tends to vanish asymptotically.

These two properties of QCD are also manifested in strong coupling constant α_s which can be written as :

$$\alpha_s = \frac{12\pi}{(33 - 2n_f)\ln(Q^2/\Lambda^2)}. \quad (1.1)$$

Here n_f is the number of quark flavors which is determined by the available energy of the probe, quantified by Q^2 (where Q is the momentum transfer) and Λ is a scale parameter in QCD which has a typical value of about 200 MeV that corresponds to 1 fm in length scale. For values of $Q^2 < \Lambda_{QCD}^2$, interaction between quarks becomes strong hence they remain strongly coupled to each other. Whereas, when $Q^2 \gg \Lambda_{QCD}^2$ which is equivalent to small length scale, the coupling becomes weak and α_s vanishes asymptotically. This behaviour of α_s is demonstrated

in Fig. 1.2

A natural consequence of "deconfinement" in QCD is that at very large temperature and/or pressure (compression), strong interaction responsible for confining quarks and gluons inside hadrons become weak enough to liberate them; thereby producing a medium of deconfined quarks and gluons, referred to as the quark gluon plasma (QGP). It is believed that, this novel form of deconfined matter or QGP was present in the early universe few micro-seconds after the Big Bang. Also it is speculated that such a deconfined medium may exist even today in the core of neutron stars. Thus, it is of great interest to study the phases of nuclear matter when subjected to such extreme conditions.

1.4 Phase Diagram of Nuclear Matter

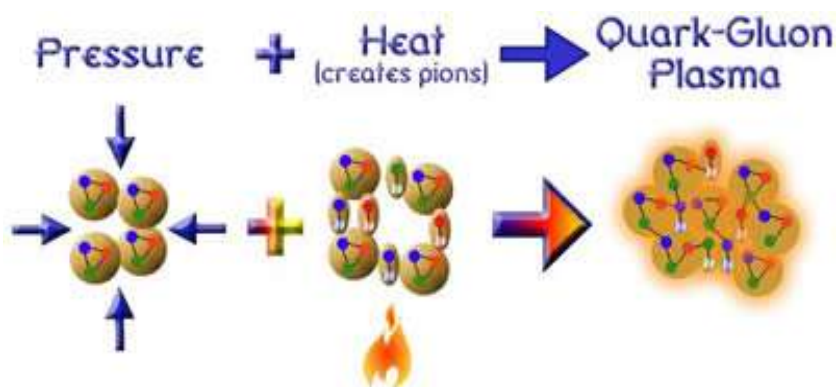


Figure 1.3: A schematic representation of how QGP can be produced in laboratories by subjecting ordinary nuclear matter to high temperature and/or high compression (pressure).

As discussed earlier, normal nuclear matter changes its state from the confined hadronic phase to a deconfined quark-gluon plasma phase at very high temperature or under very high compression. This transition is schematically shown in Fig 1.3 and can be understood in the following way: under normal conditions, the relevant degrees of freedom of nuclear matter are nucleons which are bounded by strong force. If such a nuclear matter is heated up to an extreme temperature so that sufficient thermal energy is available to create new particles then hadrons, mostly pions, are produced. The produced pions would then fill the available empty space between the nucleons. Beyond a certain critical temperature T_c , the number of produced particles would be so high such that the existing nucleons and produced particles

start to overlap. This would cause the confining boundaries between the particles to dissolve - leaving behind a deconfined medium where quarks and gluons are relevant degrees of freedom. Lattice QCD calculations have in fact shown that on increasing temperature or energy density of a medium beyond a critical or threshold value there is a sharp change in the underlying degrees of freedom of the system. Figure 1.4 shows the lattice calculations for effective degrees of freedom, $g = \epsilon/T^4$ where, ϵ and T is the transverse energy density and temperature of a system of ideal, relativistic hadron gas, respectively. It can be seen that the quantity g rises steeply as the temperature T approaches a T_c which is around 150 MeV [12, 13]. This large increase in ϵ/T^4 around $T = T_c$ is an indication for liberation of new degrees of freedom in the system and hence to a phase transition. Here the phase transition is characterised as a smooth cross over because thermodynamic variables does not exhibit any discontinuity.

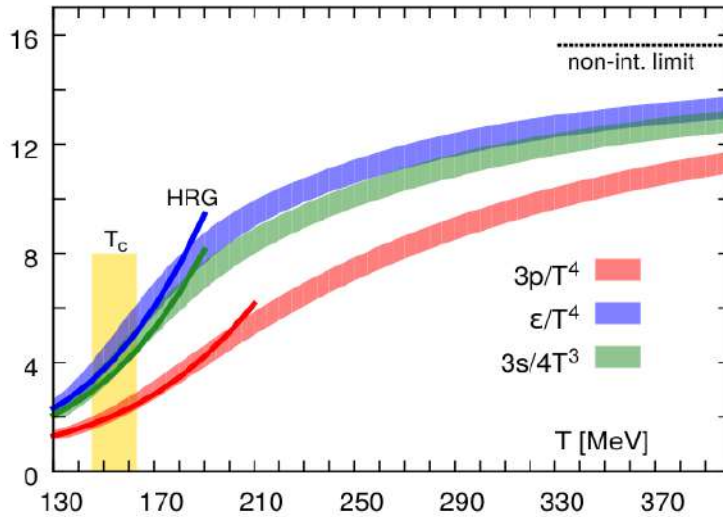


Figure 1.4: Lattice QCD calculations for pressure, energy density, entropy density normalised to 4^{th} or 3^{rd} power of temperature, showing a rapid change with temperature- an indication for phase transition. Vertical yellow band corresponds to cross-over transition region. Solid lines represent predictions from Hadron Resonance Gas (HRG) model and horizontal black dashed line is for energy density in weakly interacting ideal gas limit. The y-axis in the plot corresponds to number of degrees of freedom in the system, which is a dimensionless quantity.

A similar deconfinement transition can also occur when nuclear matter is put under large compression. Density of normal nuclear matter, ρ_0 is nearly $0.14/\text{fm}^3$. Because of compression, a typical nuclear volume gets over-populated by nucleons and at a critical number density, $\rho_c \gg \rho_0$, nucleons overlap and quarks within the nucleon percolate over the entire volume.

Thus, it creates a QGP medium but mostly dominated by quarks at a lower temperature [14]. Here the phase transition is believed to be of first order. There are also predictions for a QCD critical end point (CEP) that separates the region of first-order phase transition from the cross over region.

Thus, there exist two extreme conditions by which QGP can be produced in laboratories, one at high temperature and low baryon density and other at high baryon density (i.e large compression) and low temperature. A scan through these two extreme conditions is being explored by colliding heavy nuclei over a wide range of collision energy, from few GeVs to TeV scale. The fate of the nuclear matter when subjected to such extreme conditions is represented via a phase diagram of nuclear matter or the QCD phase diagram as a function of temperature T which is a measure for energy density and baryon chemical potential μ_B a measure for net-baryon density, as shown in Fig. 1.5

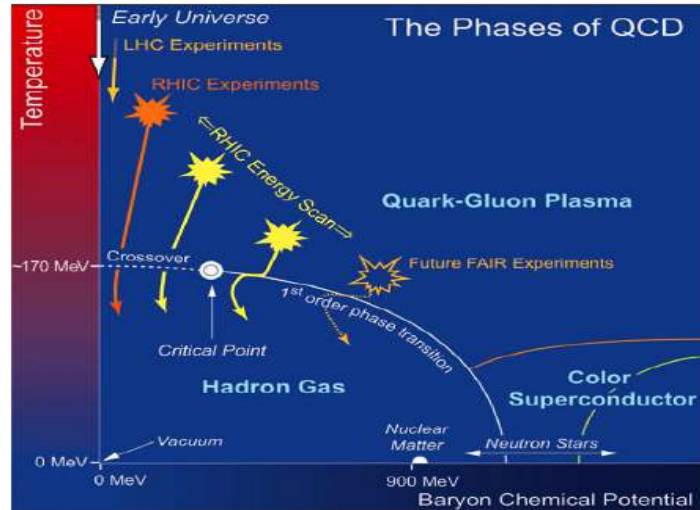


Figure 1.5: Phases of QCD matter under different conditions of temperature and baryon chemical potential. Also shown the experimental facilities that probe different regions of the phase diagram.

1.5 Relativistic heavy ion collisions experiments

Collisions of heavy nuclei at relativistic energies provide opportunities to study strongly interacting nuclear matter at energy densities much higher than that of the normal nuclear matter. It was in fact T. D. Lee and G. C. Wick who were the first to propose the possibility of producing

new states of dense nuclear matter in high energy heavy ion collisions back in 1974 [15,16]. The first search for this novel nuclear matter began at Bevalac in Berkeley National Lab (LBL), USA with 1 GeV/nucleon Au-ion beam. Later, dedicated research program to search for a new state of strongly interacting matter was initiated, almost simultaneously, at the Alternate Gradient Synchrotron (AGS) in Brookhaven National Laboratory (BNL), USA and the Super Proton Synchrotron at CERN Geneva. At both the facilities several experiments were carried out over a period of 15 years which include E802, E810, E814, E864 among others at AGS and WA97, WA98, NA35, NA38, NA44, NA52, NA57, etc at SPS. Results from these experiments, particularly those from the CERN SPS, finally allowed to make a claim of a "New State of Matter" being formed in the collisions of heavy nuclei at relativistic energies.

Thereafter in 2000, Relativistic Heavy Ion Collider or RHIC was commissioned at BNL. RHIC being a collider facility, it allowed a large boost in the collision energy compared to the previous facilities at AGS or SPS, which operated in fixed-target mode thus limiting the available energy to only a few GeVs. Instead, RHIC operated at a top energy of 200 GeV in center-of-mass frame ($\sqrt{s_{NN}} = 200$ GeV). To exploit this high gain in energy, four major experiments were designed namely, BRAHMS, PHENIX, PHOBOS and STAR. Data collected by these experiments not only provided compelling evidence on the formation of a new state of matter but also characterised it as a strongly interacting medium with very high gluon density. Thus, the medium produced at the top RHIC energy was called strongly interacting quark gluon plasma or s-QGP. RHIC also successfully delivered Au-ion beam over a broad energy range from 7.7 to 200 GeV and also accelerated variety of ion species like, Deuteron, Helium, Copper (Cu), Uranium and most recently Ruthenium and Zirconium.

Meanwhile at CERN, the Large Hadron Collider (LHC) was getting prepared to ramp up collision energy further by 10 times by colliding fully stripped Pb-ions at $\sqrt{s_{NN}} = 2.76$ TeV. A Large Ion Collider Experiment (ALICE) was designed specifically to explore quark gluon plasma at the highest ever energy density or temperature achieved at that time. The CMS and the ATLAS which are general purpose detectors designed mainly for Higgs research have also contributed significantly towards understanding the properties of QGP at highest energy density.

It is to be mentioned that both the RHIC and the LHC probed QGP formation in the

limit of large temperature and small net-baryon density. There is however, a growing interest to explore formation of deconfined medium in the region of high net-baryon density and low temperature. Facility for Antiproton and Ion Research (FAIR) at Darmstadt, Germany is an upcoming facility which will allow the study of high density nuclear matter in the limits of very high net baryon density. Thus, together with RHIC and LHC, FAIR will allow to cover most of the QCD phase diagram ranging from high temperature baryon free region resembling the situation at the early universe to low temperature baryon dominated region mimicking scenario at the core of neutron stars in the present day universe.

Having introduced the existing and upcoming facilities of heavy ion collisions, we will now discuss about our general understanding of different stages through which a heavy collision evolves.

1.6 Evolution of a heavy ion collisions at relativistic energies

Heavy ion collisions at relativistic energies is used as a tool to produce QGP in the laboratory. There are however, a series of stages through which a heavy ion collision evolve. First there is an initial state, where two Lorentz contracted nuclei overlap with an impact parameter b . This is followed by a period dominated by high momentum transfer (large Q^2) processes between quarks and gluons (partons) from the projectile nucleons. Subsequently, the energy deposited in the collision zone excites the vacuum to produce a large number of low momentum partons and a pre-equilibrium parton gas phase is formed from a relatively smaller Q^2 interactions. Eventually, an equilibrium state of deconfined quarks and gluon or QGP is produced that undergoes further expansion. As the temperature drops below a critical temperature (or phase transition temperature) hadronization takes place. Hadrons continue to evolve through inelastic collisions until chemical freezeout. Finally all interactions, including elastic scatterings, stop at kinetic freezeout and particles stream freely to detectors. All these stages of evolution is illustrated schematically in Fig. 1.6.

Initial condition in heavy ion collisions is generally described using a Glauber model [17,18]

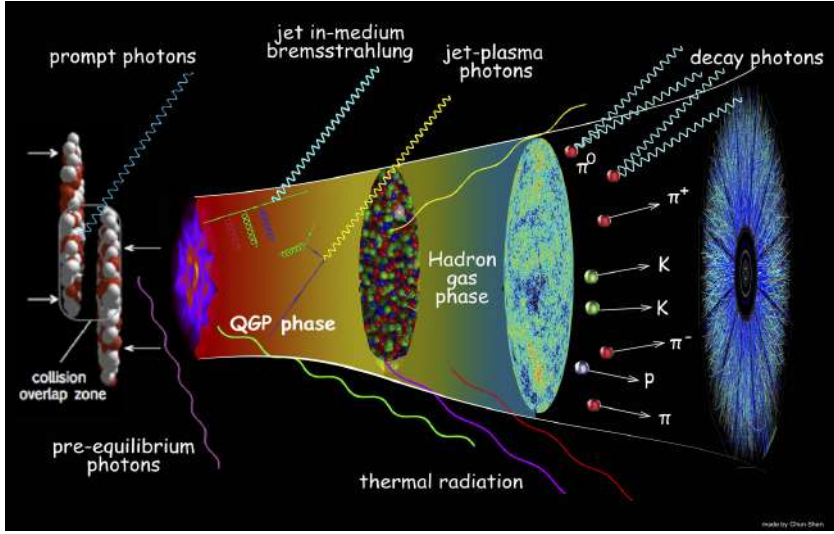


Figure 1.6: Stages in the evolution of heavy ion collision.

where, nucleons are distributed within a nucleus following Woods-Saxon distribution:

$$\rho(r) = \frac{\rho_0}{1 + \exp\left(\frac{r-r_0}{a}\right)}, \quad (1.2)$$

where ρ_0 is the normal nuclear density, r_0 is the mean radius of the nucleus, a is the skin depth and r is the distance from the center of the nucleus. In the Glauber approach, the total number of nucleons that participate in at least one in-elastic scattering is called participant or N_{part} and total number of all inelastic nucleon-nucleon scatterings are called number of binary collisions or N_{coll} . The maximum value of N_{part} that can be reached in a heavy ion collision is 2 times the mass number of a nucleus (A) and N_{coll} scales as $A^{4/3}$. When a collision is not head-on, some of the nucleons remain outside the overlap zone and do not participate in the collision, these are called spectators which continue to travel along the beam direction.

An inelastic nucleon-nucleon scattering include several QCD processes that involve parton-parton interactions over a wide range of momentum transfer. Hard processes or interactions with large momentum transfer are generally responsible for producing high momentum partons or jets and massive quarks like charm and bottom. The rate of hard processes in a nucleus-nucleus collision is driven by total number of binary collision or N_{coll} . On the other hand, low Q^2 processes that determine overall global properties of a medium produced in a collision like initial entropy, energy density, among others, scales with N_{part} .

Whether the produced medium has quarks and gluons as underlying degrees of freedom depends on the magnitude of energy deposited in the initial state. Lattice-QCD calculations predict the threshold energy density required to produce a deconfined medium is $1 \text{ GeV}/\text{fm}^3$. However, there is no direct way to measure initial energy density, nevertheless, an estimate of initial energy density can be obtained by applying Bjorken formalism that relates the initial energy density (ϵ_{Bj}) to charge particle multiplicity in final state, as shown in Eq. 1.3

$$\epsilon_{Bj}(\tau_0) = \frac{1}{A_{trans}} \frac{dE_T}{\tau_0 dy} \approx \frac{3}{2} \frac{\langle m_T \rangle}{A_{trans}} \frac{dN_{ch}}{\tau_0 d\eta} \quad (1.3)$$

Where A_{trans} is the transverse area of the collision. Taking QGP formation time, $\tau_0 = 1 \text{ fm}/c$, the initial transverse energy density was estimated to be $3.0 \pm 1.0 \text{ GeV}/\text{fm}^3$ at top-SPS energy, $6.0 \pm 1.0 \text{ GeV}/\text{fm}^3$ at top RHIC energy and $14.0 \pm 1.0 \text{ GeV}/\text{fm}^3$ at $\sqrt{s_{NN}} = 2.76 \text{ TeV}$ at LHC. These estimates clearly indicate that the initial energy density is well above the lQCD threshold of QGP formation and it can be safely assumed that a deconfined partonic medium is produced in these collisions.

Quark gluon plasma thus produced in these collisions expands and cools down. The QGP expansion dynamics is strongly influenced by the energy deposition profile in the initial state, which has a global asymmetric shape for non-central collisions, as well as, local inhomogeneities or lumpiness in the energy deposition. This non-uniformity in the initial energy deposition creates an asymmetric pressure gradient which reflects itself in the final state as momentum space azimuthal anisotropy. Measurement of this azimuthal anisotropy has actually revealed that the QGP medium behaves like a nearly ideal fluid. As the expansion continues, temperature of the medium continues to drop and when it drops below the transition temperature for deconfinement phase transition, hadronization takes place.

The medium which has now hadrons as relevant degrees of freedom, continues to evolve through hadronic interactions and a state of hadro-chemical equilibration is achieved at a temperature called chemical freezeout temperature (T_{ch}). At T_{ch} all inelastic interactions cease and relative abundances of hadrons are fixed. Thermal model calculations have extracted T_{ch} based on data-thermal-model comparison and found it to be close to the phase transition temperature, i.e. between 150-160 MeV. Although, no new particle can be produced after

chemical freezeout but hadrons in the medium can still interact elastically until temperature of the medium drops below the kinetic freezeout temperature, T_{kin} . A simultaneous blast-wave fit to transverse momentum spectra of more than one particle species is used to extract T_{kin} and extracted value of T_{kin} was found to be as low as 80-100 MeV, depending on the collision energy. Subsequent to kinetic freezeout, the mean free path of the medium becomes much larger than the typical strong interaction length scale causing hadrons to decouple from the medium and stream freely to detectors. Finally, these final state particles are used to construct various experimental probes to investigate various stages of heavy ion collision, in particular, the quark gluon plasma phase.

Below we discuss some of the proposed experimental signatures that are presumably sensitive to QGP formation in heavy ion collisions.

1.6.1 Strangeness Enhancement

Enhanced production of strange baryons and/or mesons was proposed as a potential signature for QGP formation in relativistic heavy ion collisions. As, the initial colliding nuclei have no valance strange quarks or strange anti-quarks, so, strangeness must have been produced during collisions either from the QGP or from the hadronic phase.

In heavy ion collisions, abundant production of strange particles relative to that in pp or pA collisions at same energy is believed to be a consequence of QGP formation, because strangeness production has lower threshold in a deconfined medium compared to that in hadronic interactions. This can be understood in a way mentioned below. In an equilibrated QGP medium, energy levels of valance u and d quarks are filled up to Fermi level (ϵ_F). As new quarks are always produced in pairs ($u\bar{u}$ or $d\bar{d}$) to conserve flavour number and in order to Pauli's exclusion principle, new quark-antiquark pairs must occupy the energy levels above the Fermi surface. So, the minimum energy required to produce a pair of $u\bar{u}$ or $d\bar{d}$ is $2\epsilon_F + 2m_{u\bar{u}}$, which is of the order of 800 MeV. Instead, if a strange quark-anti-quark pair ($s\bar{s}$) is produced from the deconfined plasma, the required energy is twice the current mass of strange quark ($m_s \sim 100-150$ MeV), i.e, 200-300 MeV, which is energetically more favourable.

On the other hand, strange hadron production from purely hadronic interactions are highly suppressed because of large energy thresholds needed to produce strange baryons or mesons .

For example, dominant channel for strangeness production in hadronic interactions like, $\pi^+ + \pi^- \rightarrow K + \bar{K}$ or $N + N \rightarrow N + K + \Lambda$ has Q value of 670 and 700 MeV, respectively which is much higher than that for the $s\bar{s}$ production threshold in a deconfined partonic medium. Thus the QGP formation is expected to be naturally associated with abundant production of strange particles which is reflected in Fig. 1.7. Top panel of Fig. 1.7 shows an enhanced and non-monotonic energy dependence of K^+/π^+ ratio in heavy ion collisions compared to pp collisions at the same energy. This enhancement and non-monotonic variation is often interpreted as a consequence of strangeness enhancement due to partonic deconfinement around $\sqrt{s_{NN}} = 7$ to 8 GeV. Also, a hierarchy in ratios of yields of strange hadron normalised by number of wounded nucleons in A+A to pp collision has been observed with respect to strangeness content, as shown in the lower panel of Fig. 1.7 This is considered as an effect of canonical strangeness suppression in pp collisions that restricts strangeness production in pp collisions due to the requirement of local strangeness conservation in small systems. This restriction is believed to be removed in heavy ion collisions with the formation of large and dense medium of partons allowing easier production of strange and multi-strange hadrons [19, 20].

1.6.2 Quarkonia Suppression

Quarkonia are bound states of heavy quark-antiquark pairs which are produced very early in hadronic and heavy ion collisions. Heavy quark here refers to charm (c) or bottom (b) quarks and their corresponding bound states $c\bar{c}$ and $b\bar{b}$ are called charmonia and bottomonia, respectively. A specific property that makes quarkonia special is their small size. Typical radii of quarkonia ranges from 0.1 to 0.5 fm while that of an ordinary light hadron is 1 fm. As a result quarkonia has large binding energy which makes them stable against strong decay. For example, J/ψ ($M = 3.10$ GeV) which is the lightest charmonium state has a binding energy of 0.64 GeV. This naturally comes from the difference between mass of J/ψ and twice the mass of D-meson (1.869 GeV) [$M_{J/\psi} - 2 M_D$], where $D(c\bar{u})$ is an open charm meson.

Hirosi and Matsui in their seminal work in 1986 [23] proposed to use quarkonia as a probe for partonic deconfinement and suppression of quarkonium states in heavy ion collisions relative to that in pp collisions as a signature for QGP formation. As introduced in the earlier sections, when the temperature of a medium produced in heavy ion collisions is greater than a critical

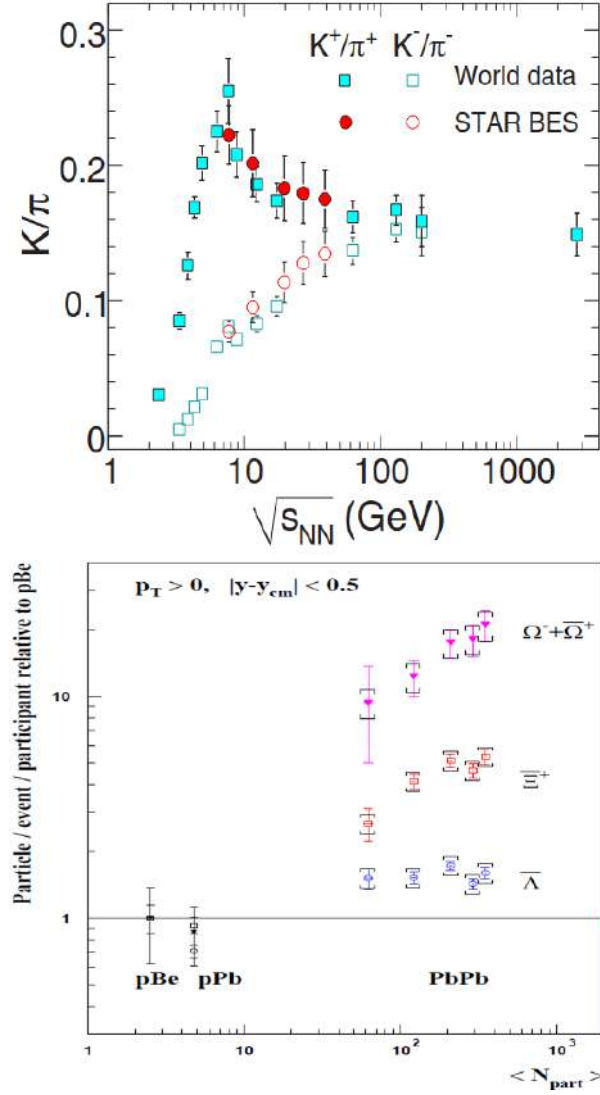


Figure 1.7: Evidence for strangeness enhancement. (Top) K/π ratio at midrapidity as a function of $\sqrt{s_{NN}}$ from RHIC beam energy scan data for most central 0-5% Au-Au collisions. Also shown are the results from the previous experiments at AGS, SPS. (Bottom) Yields of hyperons normalised by number of wounded nucleons in Pb-Pb collision at $\sqrt{s_{NN}} = 17.3$ GeV relative to pBe yields at same energy.

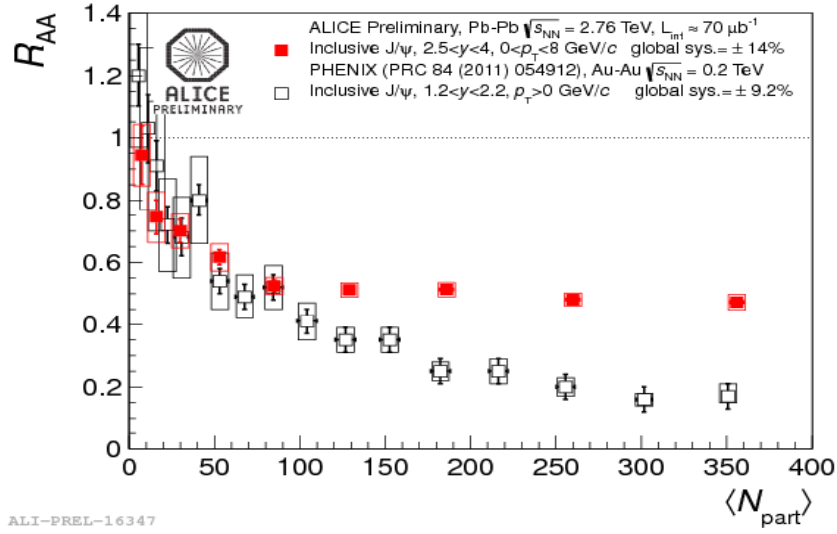


Figure 1.8: J/Ψ suppression in heavy ion collisions quantified by nuclear modification factor as a function of centrality represented by N_{part} . Red solid markers represent J/Ψ R_{AA} measurement in Pb-Pb collisions at $\sqrt{s_{NN}} = 2.76$ TeV [21] at forward rapidity and black open markers are PHENIX measurements for Au-Au collisions at $\sqrt{s_{NN}} = 200$ GeV [22].

temperature T_c , a deconfined medium of quarks and gluons are produced. The produced medium has a characteristic Debye screening radius, r_D , which depends on the temperature of the medium. For, $T > T_c$, the screening radius is of the order of 1 fm, which is typically size of a hadron. As a result, the confining color force between quarks get screened or weakened leading to their dissociation. Quarkonia are also subjected to similar color screening phenomenon when the number density of light quarks in a medium is so high that r_D is of the same order as the typical radii of quarkonia states. This results in the dissociation of quarkonium yields in heavy ion collisions which is reflected as suppression or depletion of quarkonium yields in heavy ion collisions against a properly normalised pp collisions at same collisions energy. Figure 1.8 shows the modification of the J/ψ yields in heavy ion collision with respect to pp collisions at the top RHIC and LHC energies. A clear suppression is observed at both energies. However, at LHC, magnitude of suppression is relatively small than that at RHIC which is because of the regeneration of secondary J/ψ s from $c\bar{c}$ pairs in the medium that compensates the suppression to certain extent.

1.6.3 Jet Quenching

Just like heavy quarks or quarkonia, jets are also produced from large momentum transfer process (hard scatterings) between partons from incoming nuclei which occur very early in a collision. These hard scattered partons then develop a shower of secondary partons that finally fragment into collimated bunches of hadronic final states known as jets.

In pp collisions, the secondary shower is formed in vacuum but, in heavy ion collisions, shower develops in presence of QGP. Thus, in heavy ion collisions, constituent of shower partons scatter against the partons in the medium, which results in energy loss of high- p_T partons or jets. This energy loss of high- p_T partons manifest itself in the final state as large modification or suppression of high- p_T hadron yields in heavy ion collision relative to number of nucleon-nucleon binary collision (N_{coll}) scaled pp reference. The nuclear modification factor or R_{AA} defined in equation 1.4

$$R_{AA} = \frac{d^2 N_{AA}/dydp_T}{N_{coll} \times d^2 N_{pp}/dydp_T} \quad (1.4)$$

is a standard way to quantify such a modification.

R_{AA} is actually a measure of deviation of hadron yields in heavy ion collisions relative to that in pp collisions under the assumption that a heavy ion collision is an incoherent superposition of N_{coll} number of pp collisions. $R_{AA} = 1$, if there is no modification from the said assumption. Any deviation from unity is however, an indication of modifications of hadron yields because of medium effects. By construction, $R_{AA} > 1$ implies enhancement and < 1 stands for suppression of yield in heavy ion collision with respect to N_{coll} scaled pp reference.

Figure 1.9, shows a collection of R_{AA} results for light flavour hadrons from SPS to LHC energy. From SPS to LHC, magnitude of suppression has increased significantly for example, between 2 to 3 GeV/c in p_T there is almost 50% more suppression at LHC than that at SPS. This large suppression of hadron yields at RHIC and LHC energies is consistent with energy loss models that consider very high mid-rapidity gluon density ($dN_g/d\eta$) which is about 1500 at RHIC and 2000-4000 at LHC. Thus the produced medium at RHIC and LHC is highly opaque to initial high Q^2 processes like jet production. As a result, the suppression of yields of high- p_T particles in heavy ion collision also known as jet quenching is a clear indication towards the formation of a gluon rich deconfined medium at top-RHIC and LHC energies.

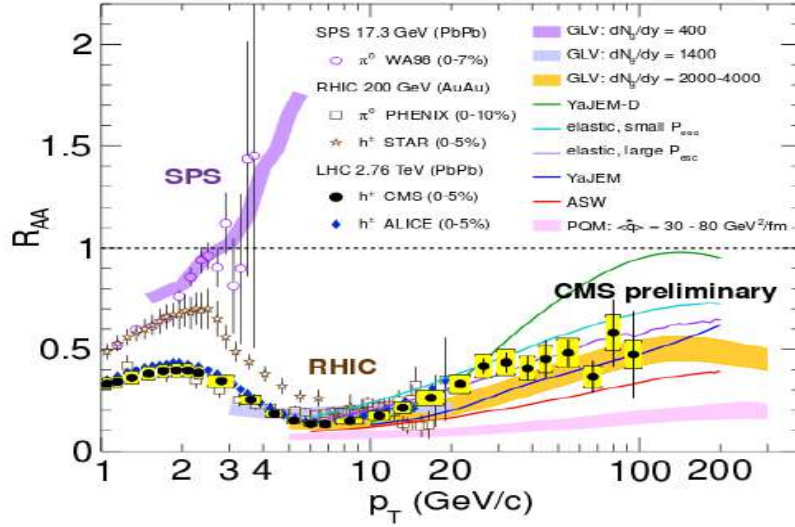


Figure 1.9: A compilation of R_{AA} measurements in central heavy ion collisions at SPS ($\sqrt{s_{NN}} = 17.3$ GeV), RHIC ($\sqrt{s_{NN}} = 200$ GeV) and LHC ($\sqrt{s_{NN}} = 2.76$ TeV) energies. Also shown are the predictions from different model calculation. Figure adapted from [24].

1.6.4 Anisotropic Flow

In non-central heavy ion collisions, the overlap region has a spatial asymmetry that creates an anisotropic pressure gradient. The medium produced in these collisions expands under the influence of this anisotropic pressure gradient thus translating initial spatial asymmetry to final state momentum space anisotropy as illustrated schematically in Fig. 1.10. As a result, particles produced from the collision zone exhibit an azimuthal anisotropy. This azimuthal anisotropy is generally quantified by Fourier decomposition of azimuthal distribution of final state particles in a plane transverse to the beam axis as shown in Eq. 1.5 [25].

$$\frac{dN}{d\phi} = \frac{1}{2\pi} \left(1 + 2 \sum v_n(p_T) \cos[n(\phi - \Psi_n)] \right) \quad (1.5)$$

In the above equation, n is the order of Fourier harmonic, ϕ is the azimuthal angle of the final state particles, Ψ_n is n^{th} -order harmonic plane and v_n s are the n^{th} -order Fourier coefficients also known as flow coefficients.

The second-order flow coefficient, v_2 or elliptic flow is most dominant flow coefficient among others and has been studied extensively both theoretically and experimentally. It is found that the magnitude of v_2 is highly sensitive to the initial spatial anisotropy and the equation of

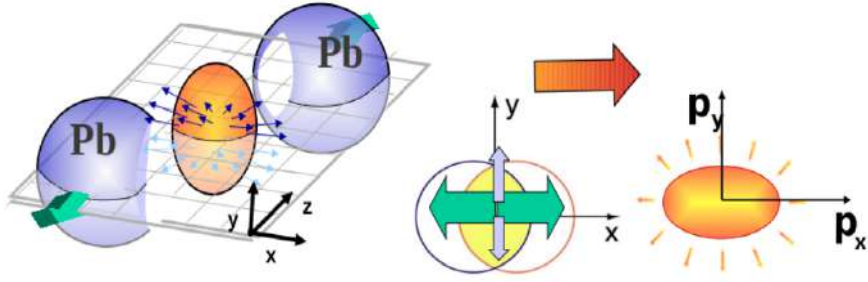


Figure 1.10: A schematic representation of how initial anisotropy is converted into momentum space azimuthal anisotropy.

state (EOS) of the produced medium. The magnitude of v_2 increases almost monotonically as a function of $\sqrt{s_{NN}}$ and reaches a hydrodynamic limit of a "perfect fluid" at top-RHIC energy, as shown in Fig. 1.11. This large elliptic flow observed at RHIC was found to be consistent with hydrodynamic calculations that include an early thermalization of partonic phase as well as, an EOS where QGP to hadronic phase transition is invoked. Thus, it suggests that produced medium has partons as relevant degrees of freedom at some stage that subsequently undergoes a phase transition to a hadronic medium.

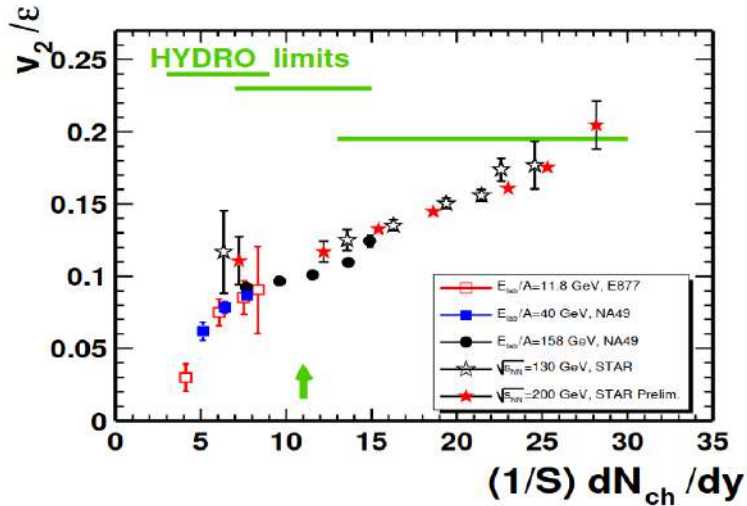


Figure 1.11: Elliptic flow (v_2) normalised by initial eccentricity ϵ_2 as a function of particle density.

The differential measure of v_2 as a function of p_T revealed more information about the nature of interaction and particle production mechanism. Figure 1.12, shows p_T -differential v_2

of different particles that exhibit two important features: first there is mass ordering in the low p_T region and then at the intermediate p_T , there is an ordering depending on whether the particle is a baryon or meson. This difference in v_2 for baryons and mesons has been explained as a consequence of particle production via quark coalescence or quark recombination which is dominant at intermediate p_T . Thus, it gives an indirect evidence for the onset of partonic deconfinement and presence of quark degrees of freedom at the time of hadronization. Recent studies have also shown that NCQ scaling vanishes at lower energy where the medium is expected to be baryon rich thus confirming that such a scaling behaviour is a result of partonic deconfinement or QGP formation [26].

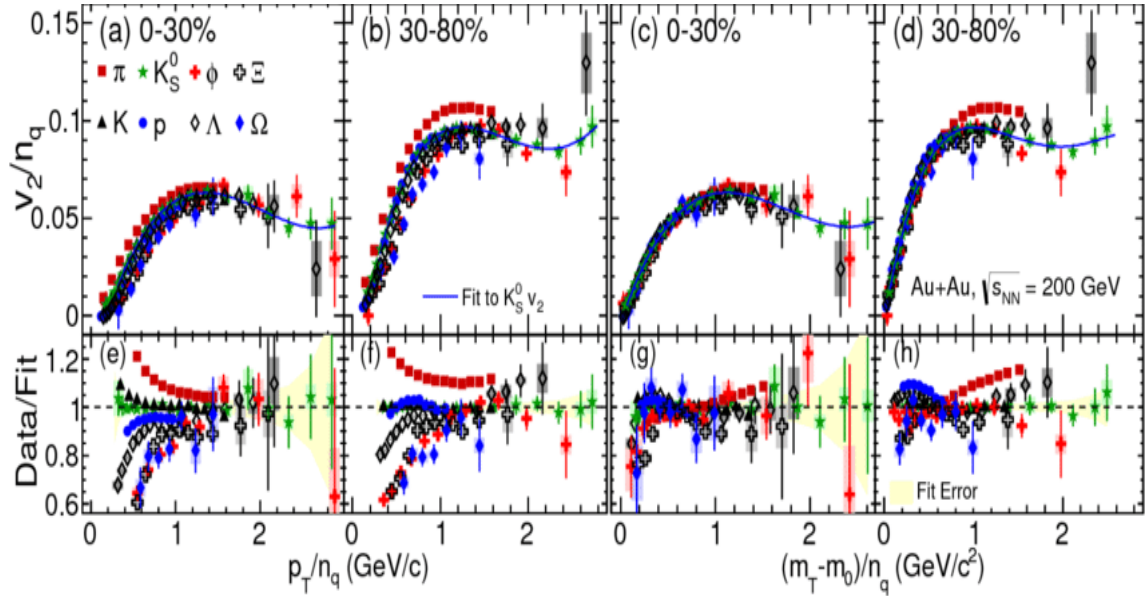


Figure 1.12: Constituent quark number scaling of v_2 as a function of (top) p_T and (bottom) $m_T - m_0$.

1.6.5 Event by event fluctuations of conserved quantities

As introduced previously, there are two distinct phases in the QCD phase diagram: a quark gluon plasma phase which is a medium of deconfined quarks and gluons and a hadronic phase, where quarks and gluons are confined. It is known that the phase transitions are generally associated with divergence of susceptibilities of thermodynamic quantities which are in turn related to correlation length. Event by event fluctuations of conserved quantities, like net-baryon, net-charge and net-strangeness are sensitive to correlation length of the produced

medium. Higher order fluctuations of these conserved quantities like sigma, skewness and kurtosis have higher sensitivity to correlation length and therefore serve as tool search for QCD phase transition and most importantly predicted critical end point (CEP) in QCD phase diagram.

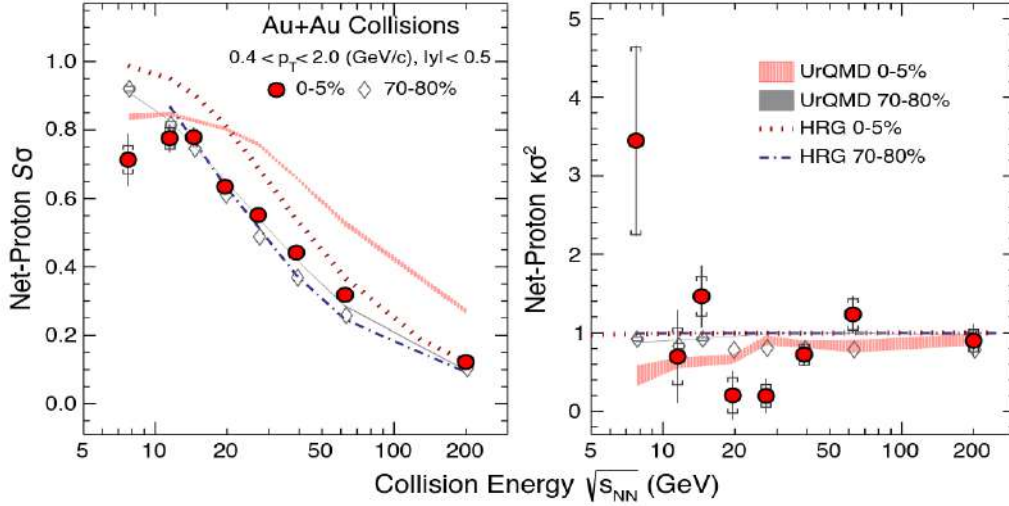


Figure 1.13: Higher moments of net-proton distributions as function of collision energy measured in Au-Au collisions; (left) $S\sigma$ and (right) $\kappa\sigma^2$. A non-monotonic energy dependence observed for $\kappa\sigma^2$ as a function of $\sqrt{s_{NN}}$.

The beam energy scan program at RHIC was designed to search for such signatures of phase transition and CEP. Figure 1.13 shows a measure of higher order fluctuations of net-proton (proxy for net-baryon) as function of $\sqrt{s_{NN}}$. The measured quantities $S\sigma$ and $\kappa\sigma^2$ are related to baryon-number susceptibilities. A non-monotonic behaviour is observed for net-proton $\kappa\sigma^2$ in central collisions, which is absent in peripheral collisions as well as in models where critical point is not included. This non-monotonic variation of $\kappa\sigma^2$ for net-proton may be an indication for a critical point in QCD phase diagram [27].

1.6.6 Dilepton Production

Dileptons are oppositely charged lepton pairs, i.e., e^+e^- or $\mu^+\mu^-$ which are produced in all stages of a heavy ion collision. As dileptons dominantly interact via electromagnetic interactions, they remain mostly transparent to the surrounding QCD medium and thus carry the information from their point of origin completely unperturbed. Thus, dileptons are regarded

as penetrating probe of the medium produced in a collision [28].

Dileptons produced in a collision can be broadly classified in the following categories:

- Primordial dileptons from Drell-Yan processes like $N+N \rightarrow \gamma^* \rightarrow l^+ + l^- + X$
- Thermal dileptons from the annihilation of quark-antiquark pairs in QGP phase, $q^+ + \bar{q}^- \rightarrow l^+ + l^-$ and $\pi^+ + \pi^- \rightarrow l^+ + l^-$ in hadronic phase. Also decay of short-lived resonances like ρ, ω, Δ , etc
- Decay from long-lived hadrons (π^0, η, ϕ) and quarkonia (J/Ψ and Ψ'), etc

Dilepton invariant-mass spectra is rich in information and gives access to medium properties at different stages of the collision. For example, in low mass region (LMR), $M_{l+l^-} < M_\phi$, dilepton invariant mass distribution is dominated by decay of vector mesons, thus sensitive to in-medium modifications of spectral functions of vector mesons, like shift in the pole mass or broadening of width. These changes in spectral shape of vector mesons is closely related to chiral symmetry restoration. It has been predicted that at high temperature or at large baryon chemical potential, deconfinement phase transition is also accompanied by chiral symmetry restoration which results in the mass modification of chiral partners like ρ and a_1 at the phase boundary [29]. This may cause either reduction in ρ mass (melting) or broadening of its width. Either situation would lead to an excess dilepton production in low mass region. Recent theoretical calculations which include ρ -melting scenario in addition to dilepton emission rate from partonic medium can achieve very good agreement with experimental results, as shown in Fig 1.14 [30, 31].

The intermediate region (IMR) of dilepton mass spectra ($M_\phi < M_{l+l^-} < 2.5$) is mostly populated by lepton pairs from partonic sources and therefore sensitive to the temperature of QGP phase. A parameterization of dilepton invariant mass spectra in IMR region with $M^{3/2}\exp(-M/T)$ has allowed to extract the temperature of the medium, as shown in Fig. 1.15 for collision energy between 6 to 200 GeV. The inverse slope parameter, T which is equivalent to the temperature of the medium, ranges from 160 to 200 MeV [30, 31]. This extracted temperature range is well above the QCD phase transition temperature and thus indicate formation of a QGP medium.

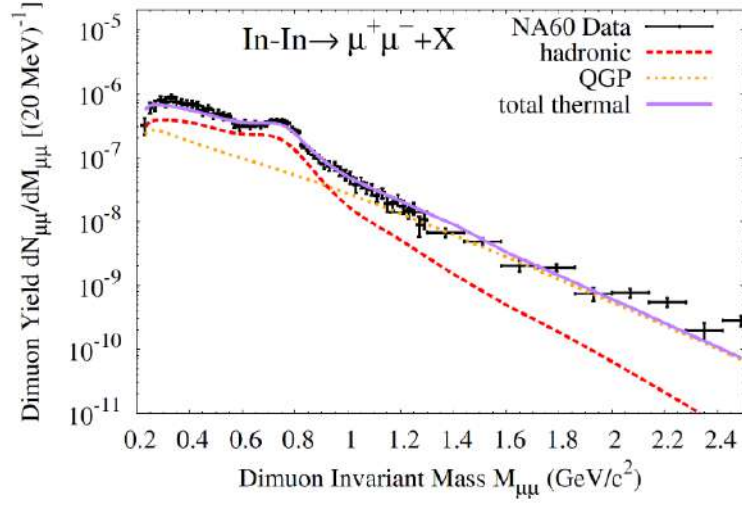


Figure 1.14: Dimuon invariant mass spectra from In-In collisions in SPS at $\sqrt{s_{NN}} = 17.3$ GeV compared with theoretical model calculation that include; in-medium modification of spectral functions of ρ and ω along with chiral mixing and dimuons from QGP.

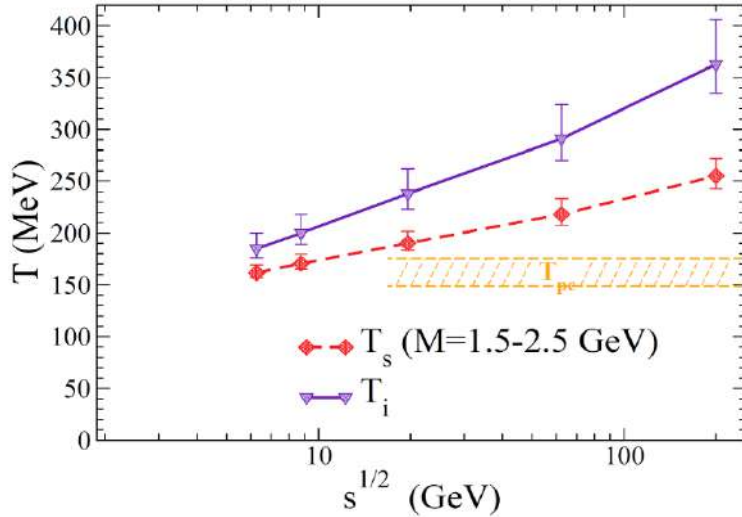


Figure 1.15: $\sqrt{s_{NN}}$ dependence extracted temperature, T , from dilepton mass spectra in the intermediate mass region. Yellow hatched region indicates phase transition temperature at zero baryon chemical potential.

Having discussed the signatures of QGP formation, we now proceed to give a brief motivation for carrying out this thesis work in the next section.

1.7 Motivation and organization of this thesis

High density nuclear matter produced in relativistic heavy ion collision can undergo a deconfinement phase transition under two conditions viz: high temperature and large compression (or large baryon chemical potential). The high temperature limits in the QCD phase diagram are currently being explored at top RHIC and LHC energy. The other extreme in QCD phase diagram, i.e, the region of large compression or high net-baryon density is partly covered by the BES program at RHIC. The FAIR is an upcoming facility at Darmstadt, whose main objective is to explore the region of QCD phase diagram in the limit of very large baryon density and low temperature. The Compressed Baryonic Matter (CBM) is one of the major experiments at FAIR, dedicatedly designed to pursue experimental investigations of the properties of nuclear matter at very high baryon chemical potential, particularly, using rare and diagnostic probes. A muon chamber (MuCh) detector system for the CBM experiment is being developed in India which is designed dedicatedly to identify muon pairs or dimuons originating from the decay of LMVMs, charmonium, thermal decay among others. One of the main motivation or purpose of this thesis work is to determine an optimised version of muon detection system that would allow the measurements feasible, in terms of reasonable detection efficiency and signal-over-background ratios. This optimization has been done based on several parameters that include, material type and material budget of absorbers, their size & shape, size of detectors, beam pipe material, shielding design among others. As Resistive Plate Chambers or RPCs are foreseen to be used as active detector component in MuCh, a study was also needed to test its feasibility of usage which has been addressed in this thesis as well. Secondly, a mini-CBM (mCBM) campaign was driven at SIS18 in GSI to test the performance of real size detectors in high particle density environment in heavy ion collisions. Data collected from this campaign has been analysed to test detector performance, electronics, event reconstruction schemes and most importantly time synchronous behaviour of two sub-systems employing different detector technologies and readout electronics.

One of the main physics goals at CBM is to study the deconfinement with rare and diagnostic probes. In this regards, strangeness production is a long known potential signature of deconfinement. Previous measurements that include non-monotonic energy dependence of K/π and $\bar{\Lambda}/\bar{p}$ ratios in AGS and SPS appeared to be consistent with a deconfinement scenario. However, in the region of high net-baryon density, which will be the main focus of the CBM experiment, hadronic interactions can contribute significantly. In this thesis we have thus investigated whether such non-monotonic energy dependence could arise from hadronic interactions alone, in particular, we have studied the role of baryon-antibaryon annihilation in Λ , $\bar{\Lambda}$ production and enhancement in $\bar{\Lambda}/\bar{p}$ ratios observed in data. In addition we have also studied, whether Principal Component Analysis technique (PCA) can be applied on final state particles to achieve more insights on the initial conditions in heavy ion collisions.

This thesis has been organized in the following way: in Chapter 2, a brief introduction to FAIR facility at Darmstadt, Germany and detailed description of the CBM experiment that include, different sub-detectors, readout electronics, data collection schemes, etc have been given. Then followed by the feasibility studies of CBM-MuCh in Chapter 3 and analysis of mCBM data in Chapter 4. Phenomenological studies of strangeness production and search for initial state fluctuations using PCA at FAIR energy range is presented in Chapter 5 and Chapter 6, respectively. Finally, we summarise in Chapter 7.

Chapter 2

The Compressed Baryonic Matter (CBM) Experiment at FAIR

2.1 Introduction

In relativistic heavy ion collisions, when ordinary nuclear matter is subjected to extreme conditions of temperature or pressure/density, then normal nuclear matter transforms from the hadronic phase to the quark gluon plasma phase (QGP). The Quantum Chromodynamics (QCD), the theory of strong interactions, suggest a possible phase transformation from the normal nuclear matter to a de-confined state of quarks and gluons at an energy density $> 5-6$ times the normal nuclear density ($0.14 \text{ GeV}/\text{fm}^3$) $\sim 1 \text{ GeV}/\text{fm}^3$. The Compressed Baryonic Matter experiment at the Facility for Antiproton and Ion Research (FAIR) [32] situated at Darmstadt, Germany, provides an opportunity to study the nuclear matter at very high pressure, where the net-baryon density will be very high and temperature will be moderate. At FAIR, heavy ions will collide in the energy range (E_{lab}) of 2 - 40 AGeV. In this energy range, probability of baryon stopping is high, particularly at mid-rapidity, resulting in high net baryon density at mid-rapidity. This high net-baryon density will cause the nucleons to overlap with each other within a small nucleonic volume resulting in a likely formation of a soup of deconfined quarks and gluons, where a parton loses its identity of its parent nucleon in the medium. The medium will be dominated by parton degrees of freedom and this type of matter is believed to be present at the core of neutron star [33]. Model calculations have

been performed to study the net-baryon density of the matter formed in heavy ion collisions at this energy. These calculations predict that the net-baryon density may reach 7 to 10 times the normal nuclear density ($\sim 0.14 \text{ /fm}^3$) depending on the beam energy [34–37], as shown in Fig. 2.1.

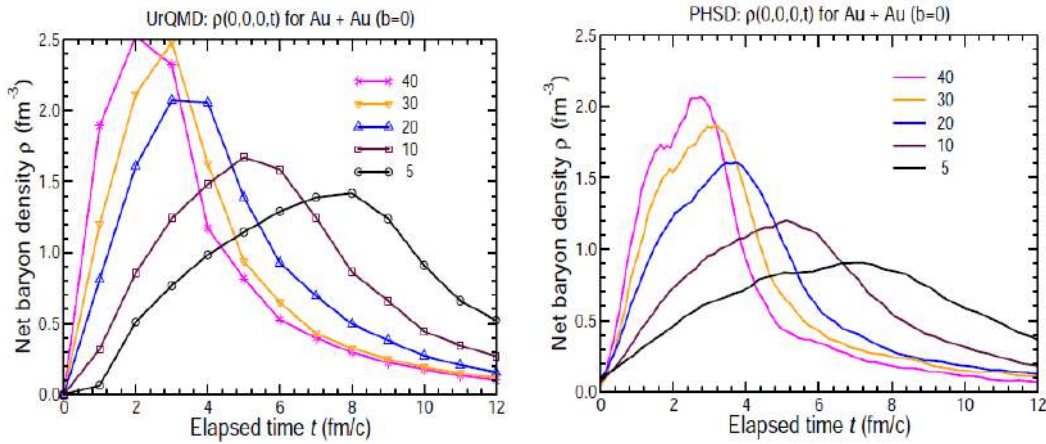


Figure 2.1: Evolution of net baryon density with time at different collision energies, calculated from UrQMD and PHSD [35, 38].

The CBM experiment at FAIR is designed to study the medium produced in these collisions with rare and diagnostic probes like multi-strange hadrons, charmonia, low mass vector mesons, that will probe the core & the initial state of the fireball. But the abundance or the production cross-section of these particles at FAIR energy is very less. For detection of these rare particles CBM will be operated at very high interaction rate $\sim 10 \text{ MHz}$. In Fig. 2.2 we show the interaction rate with collision energy for different experiments under construction or in operation. It shows the interaction rate in CBM is much higher compared to that being handled by any other experiment and that makes CBM unique as well as, challenging to operate. To cope with this high interaction rate, the CBM detectors will be dedicatedly designed with the quality of high rate capability and radiation hardness. In this chapter we will discuss the FAIR facility, the main CBM physics goals and the detailed description of the experiment with its detector components.

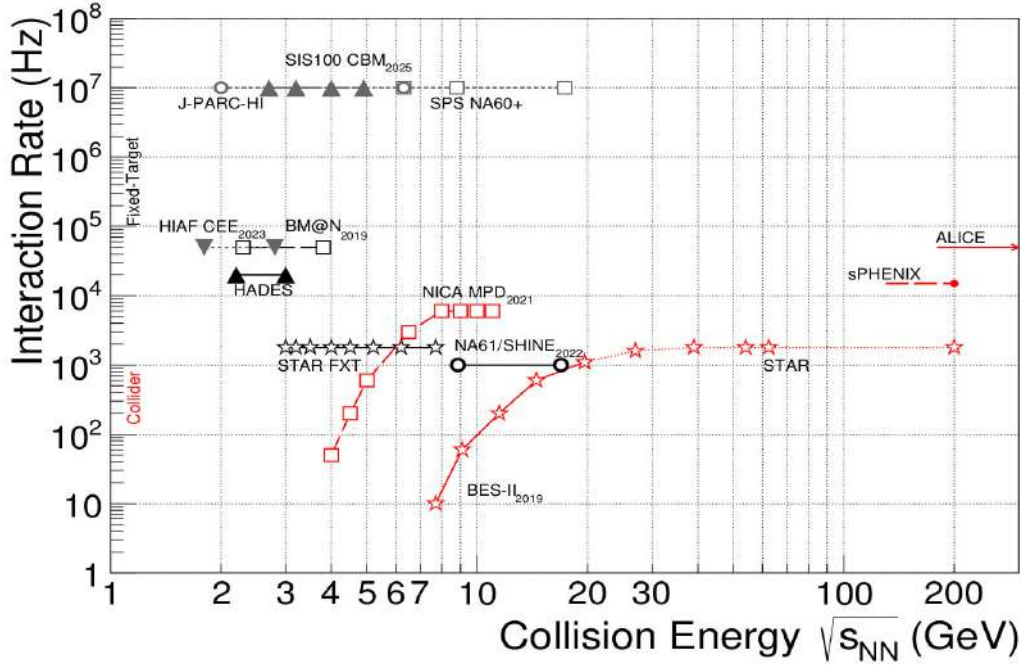


Figure 2.2: Interaction rate with collision energy has been shown for different experiments.

2.2 The Facility for Antiproton and Ion Research (FAIR)

FAIR is the Facility for Antiproton and Ion Research, an upcoming International large scale accelerator facility at Darmstadt, Germany. The layout of the complete FAIR and the existing GSI facilities at Darmstadt are shown in Fig 2.3 [39].

FAIR comprises of four scientific experimental pillars : APPA (Atomic, Plasma Physics and Applications), PANDA (anti-Proton ANnihilation at DArmstadt), NuSTAR (NU-clear SStructure, Astro-physics and Reactions) and CBM (Compressed Baryonic Matter experiment). It will provide an unique opportunity to study a wide range of topics in nuclear and hadron physics, atomic and plasma physics and applications in condensed matter physics and biology. The heart at the initial phase of the FAIR facility is the double ring synchrotron SIS100 accelerator. This ring is of 1.1 km in circumference and 17 m underground. The beam rigidity for SIS100 is 100 Tm [41]. Heavy ion (HI) beams will be injected from the existing GSI UNILAC (Universal Linear Accelerator) and SIS18 accelerators. SIS18 will be used as booster for the SIS100 synchrotron. Apart from SIS100, FAIR has multiple cooler and storage rings, like the storage ring for antiprotons (High-energy Storage Ring HESR), the Collector Ring (CR),

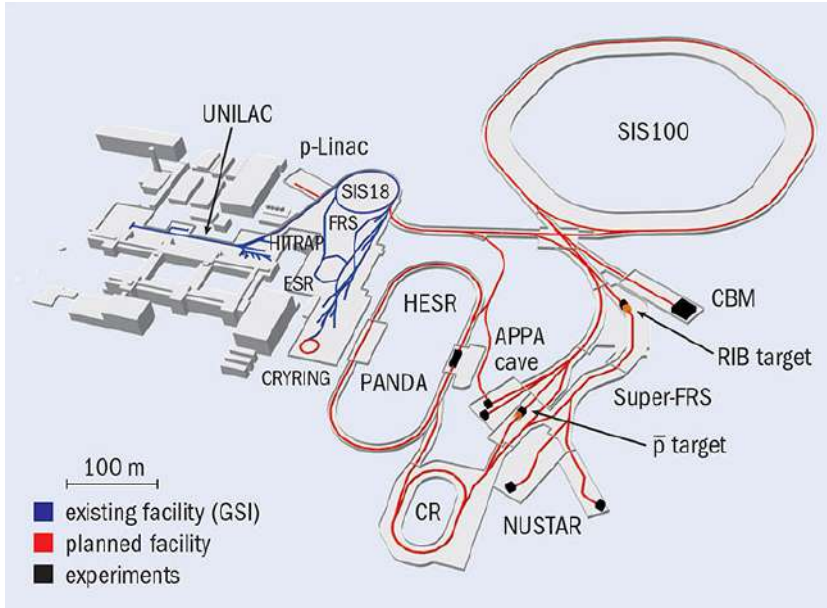


Figure 2.3: The existing GSI facilities are shown in blue which includes UNILAC , ESR and SIS18 accelerator. Planned FAIR facilities are shown in red. FAIR has four major experiments APPA, PANDA, NUSTAR and CBM [39]. Experiments are shown in black [40].

and the New Experimental Storage Ring (NESR) and Superconducting Fragment Separator (Super-FRS) [42]. SIS100 accelerator will provide wide range of beams from proton, antiproton to the heavy ions up to Uranium-238 with promising very high intensity and excellent beam characteristics [43]. The beam energy available from this facility depends on the magnetic rigidity $B.r$ of the magnet. Depending on the Z (atomic number) and A (mass number) of the atoms, the accessible beam kinetic energies for SIS100 are listed for different ion species in the table 2.1 and it follows from the formula shown below [44] -

$$E/A = \sqrt{(0.3.B.r.Z/A)^2 + m^2} - m \quad (2.1)$$

where m is the mass of the nucleon.

2.3 Diagnostics probes of high density medium at CBM

Here we discuss the diagnostics probes to study the high density nuclear matter formed at FAIR energies [44, 45]. The Fig. 2.4 shows formation of various particles at different stages of the heavy ion collisions based on UrQMD [38] model calculation. The heavier particles

Table 2.1: Accessible beam kinetic energy are listed for SIS100 for different Z/A of ion species.

Beam	Z	A	E/A GeV
p	1	1	29
d	1	2	14
Ca	20	40	14
Ni	28	58	13.6
In	49	115	11.9
Au	79	197	11
U	92	238	10.7

like charm quarks are produced at the early stages of the collision. Thus, J/ψ and D mesons are treated as a probe for the onset of partonic medium. On the other hand, low mass vector mesons (LMVMs) like, ρ , ω , ϕ are treated as diagnostics probes for chiral symmetry restoration in the medium. They are produced via pion-pion annihilation in the medium and decay into hadrons or dileptons. These dileptons offer unique opportunity to look deep into the fireball, as dileptons are not affected by the final state strong interactions, so, they carry the initial information of the medium undisturbed. Also, the multi-strange hadrons and ϕ mesons also provide direct information of the fireball via measurements of the collective flow due to their very low hadronic interaction cross-sections.

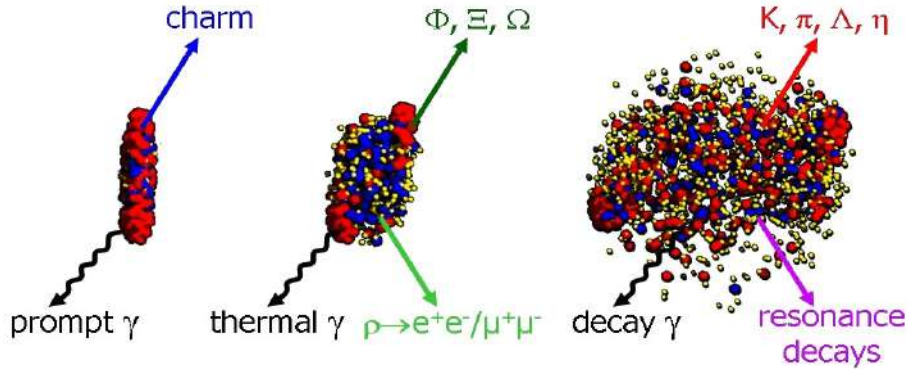


Figure 2.4: different stages of heavy ion collisions from UrQMD has been shown for U+U at 23 AGeV. At different stages different particles are emitted at different time.

Up-to date no dilepton or multi-strange hadrons measurements have been performed in heavy ion collisions at this FAIR energy range i.e 2-40 AGeV. So, at CBM, these diagnostics probes will be the first measurement in this energy range. However, the production cross-section of these multi-strange hadrons, charmonium or the vector mesons is very low at the

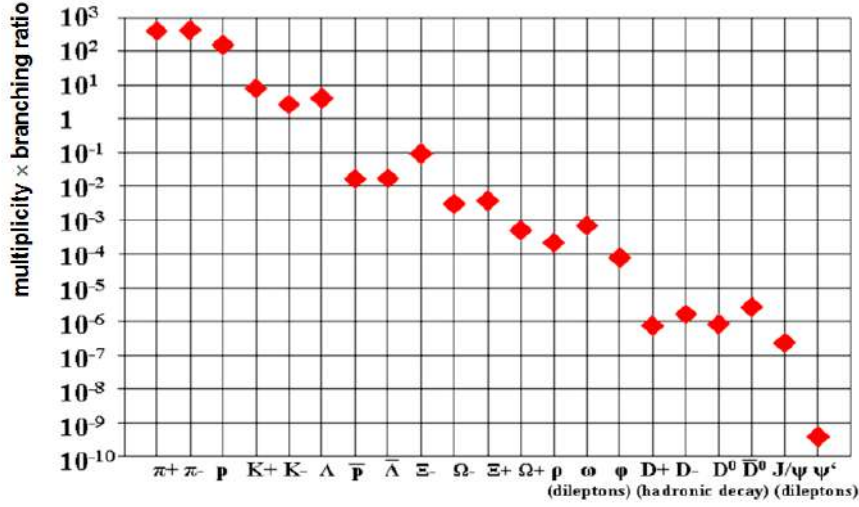


Figure 2.5: Multiplicity times branching ratio for various particles at 25 AGeV Au+Au collisions as calculated from HSD [46]. For vector mesons (ρ , ω , ϕ , J/ψ) their decay through dilepton channels have been considered. For D meson their decay to hadronic channels in pions and kaons have been assumed.

FAIR energy range, as shown in the Fig. 2.5 for 25 AGeV. This figure shows the multiplicity times branching ratio of various particles at 25 AGeV AuAu collisions calculated from HSD transport model [46]. Yields of vector mesons via dilepton channels are 6 orders of magnitude less compared to that of pions because dileptonic decay of vector mesons are suppressed by square of electromagnetic coupling constant $(1/137)^2$. Mesons comprising of charm quarks are suppressed by order of 9 compared to pions. Besides that, multi-strange hadrons production are also rare at the FAIR energy. For precise measurement of these rare particles, CBM will be operated at very high collision rate ~ 10 MHz. This will meet the requirement of large statistics for accurate measurement of these rare particles.

2.4 CBM Physics Motivation

CBM is dedicated to search for the high net-baryon density region of the QCD phase diagram under utmost condition of compression or pressure. According to the model calculations, density may reach 5 - 10 times the normal nuclear density at the centre of the fireball. This condition is believed to exist at the core of neutron stars or at the neutron star merger [33]. The main motivation of CBM experiment is to search for the fundamental properties of high

density nuclear matter that are listed below [44, 45].

- **Equation of state of high net-baryon density matter**

The EOS of nuclear matter at high density is a matter of intense investigations and, CBM gives an opportunity to perform such studies with high accuracy and good precision. The relevant observables will be the excitation functions of collective flow and yields of multi-strange hyperons in heavy-ion collisions, which are sensitive to the compressibility of baryon-rich matter at this extreme conditions [45].

- **Search for the Critical End Point (CEP) in the phase diagram and onset of partonic deconfinement**

The beam energy scan program at RHIC was initiated to scan the QCD phase diagram from low to high baryon chemical potential and to investigate how the nature of phase transition changes, as there are QCD predictions that at high baryon chemical potential phase transition is of first-order and at lower baryon chemical potential it is a smooth cross over. Therefore, one important objective was to search for the critical end point (CEP), the point behind the two orders of transitions. However, it is still not clear whether the CEP exists and if it exists, what is its location in the QCD phase diagram. The promising observables will be the event-by-event fluctuations of the conserved quantities like net charge, net baryons and net strangeness measured through their higher order moments. As well as, the excitation function of spectra, yields and collective flow of strangeness, charm or lepton pairs can provide the information of phase transition from hadronic to partonic medium. Large data volume foreseen to be collected at CBM will certainly facilitate these measurements to achieve good statistical significance [44, 45].

- **Search for chiral symmetry restoration and in-medium modifications of hadrons**

The properties of hadrons specifically the mass and width of the vector mesons are expected to be modified due to the chiral symmetry restoration inside the dense baryonic medium. The yield and spectra of vector mesons (ρ , ω , ϕ) decaying to lepton pairs are useful probes to extract these information. As the leptons are not influenced by the

final state strong interactions they can be treated as a penetrating probe to study such medium effects leading to mass or width modifications of LMVMs. Particularly, ρ meson that has a very short life time, it decays to lepton pairs inside the medium and thus carry undistorted information of medium [44, 45].

- **Production mechanism of multi-strange hadrons at dense medium**

Production mechanism of strangeness is a broad area of research in the high net baryon density region particularly at this CBM energy range. Theoretical models predict the enhanced production of strange dibaryons, single and double hypernuclei and heavy multi-strange short-lived objects at this FAIR energy mostly by means of coalescence. Measurement of the decay products of these particles gives some insight of their production mechanism at this energy [44, 45].

- **Study charm production mechanism & in-medium modification at high net baryon density**

Heavy quarks like charm quarks are produced in the early stage of the collision. A bound state of $c\bar{c}$ pair i.e charmonium production can be considered as thermometer or chronometer of the medium. Yields and momentum spectra of D-mesons or open charm hadrons and charmonia in proton-nucleus or nucleus-nucleus collisions provide information of the in-medium modification and production mechanism of the charm quarks in the medium. In particular, the sub-threshold production and the suppression of charmonia give us the properties and transition of the nature of nuclear matter at high net baryon density [44, 45].

2.5 CBM experimental setup

CBM is a fixed target experimental high energy heavy ion collision setup that is designed to detect all the forward focused particles with the aim of integral and differential measurements of particle species in proton-nucleus and nucleus nucleus collisions [44]. The uniqueness of CBM comes from accelerating the high beam intensity at SIS100 accelerator with $\sim 1\%$ interaction length of the target that makes ~ 10 MHz interaction rate. This high interaction

rate enables precision measurement of rare particles with enormous statistics. The detectors are required to be fast with high rate capability and radiation hard [47]. There is no hierarchical triggering for event selection in CBM and the data taking will be conducted using self triggered read-out electronics. Apart from the measurement of the hadronic observables, the dilepton measurement is a central part of CBM physics plan. Dedicated measurements of dimuons and dielectrons will be performed by a Muon Chamber (MuCh) detectors and Ring Imaging Cherenkov (RICH) detectors respectively. A schematic view of the CBM experimental setup with all its sub-detectors are shown in Fig. 2.6. Here we discuss briefly the components of CBM setup [44] -

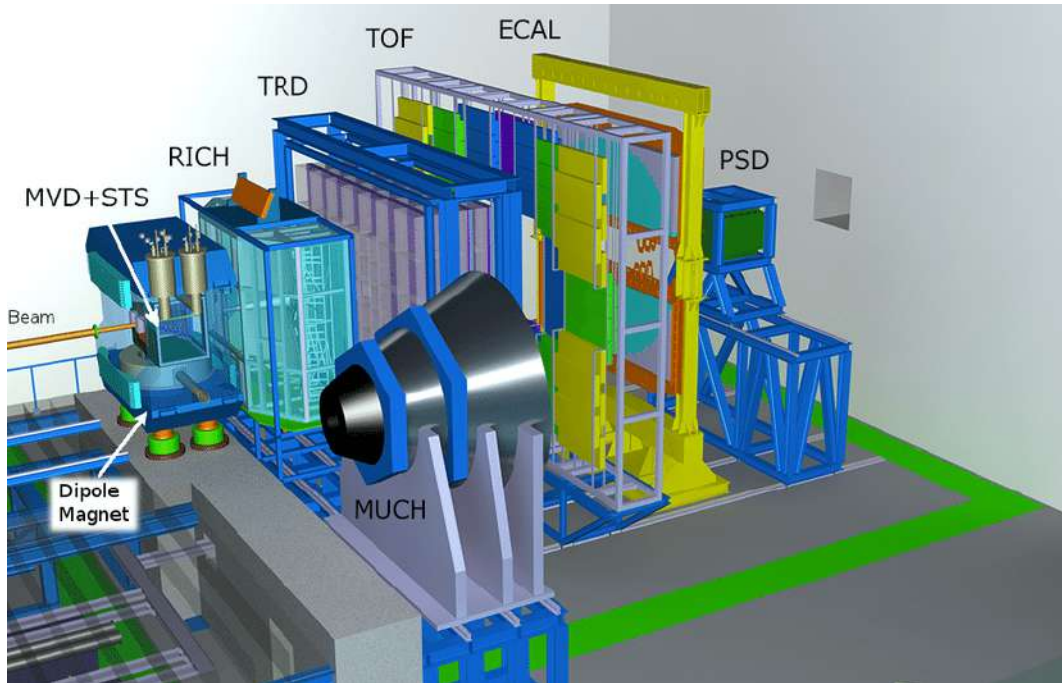


Figure 2.6: CBM experimental setup with all its sub detectors.

2.5.1 Dipole Magnet

In CBM, magnet is made of superconducting dipole magnet of H type. The magnet yoke/pole made of iron and coils are cylindrical superconducting coils of Nb-Ti superconductor and it is directly cooled by liquid helium. The total length of the magnet is ~ 1.5 m. The target and the silicon tracking station (STS) detector are housed inside the magnet. It has total integral magnetic field of 1 Tm which is required to get momentum resolution $\sim 1\%$ in STS.

The magnet gap has 1.4 m height and 2.5 m width with polar angular acceptance of $\pm 25^\circ$ and horizontal angular acceptance $\pm 30^\circ$.

2.5.2 Micro Vertex Detector (MVD)

MVD is stationed just after the target and at a distance of ~ 5 -20 cm downstream the target and before the STS [48]. It is positioned just after the collision point to enable tracking with high precision in the very high particle density environment at CBM. The main aim of MVD is to locate the secondary decay vertex of open charm meson or D meson into their weak decay to pion and kaon. The decay lengths of D^0 and D^\pm are $c\tau \sim 123 \mu\text{m}$ and $314 \mu\text{m}$ respectively. This demands the excellent position resolution and very low material budget of MVD detector ($\sim 0.5\%$ X_0 , X_0 being the radiation length) to suppress the multiple scattering. The detector coverage of MVD is 2.5° to 25° . Monolithic Active Pixel Sensors (MAPS) are the main active components of MVD detector with pixel sizes from $25 \times 25 \mu\text{m}^2$ to $40 \times 40 \mu\text{m}^2$ [48]. A spatial resolution of $\sim 5 \mu\text{m}$ can be achieved using the MVD pixels. MVD focuses the track reconstruction of low momentum charged particles which do not reach or partially reach STS due to their low momenta. It allows the momentum determination down to 300 MeV/c, thus significantly reduces background contribution. MVD has 4 stations located at 5 cm, 10 cm, 15 cm and 20 cm respectively from the target with total material thickness is about 200 μm silicon equivalent for sensors and support structure [48]. It is demonstrated that reconstruction efficiency of hyperons improve with the use of MVD detector together with STS.

2.5.3 Silicon Tracking station (STS)

A Silicon Tracking Station is placed just after the MVD and is housed inside the CBM magnet as shown in Fig. 2.7. STS is at the heart of the CBM experiment as it is responsible for particle tracking and momentum identification of the charged particles in a high interaction rate (~ 10 MHz) environment [50]. Multiplicity of the generated charged particles are around 700 in central Au+Au collisions at 12 AGeV which is passing through STS as shown in Fig 2.8. This requires very high spatial and momentum resolution with good rate handling capability of STS. The momentum resolution $\Delta p/p \sim 1\%$ can be achieved with STS detectors placed inside the magnet with single track reconstruction efficiency of $\sim 95\%$ at momentum of 1 GeV/c [50].

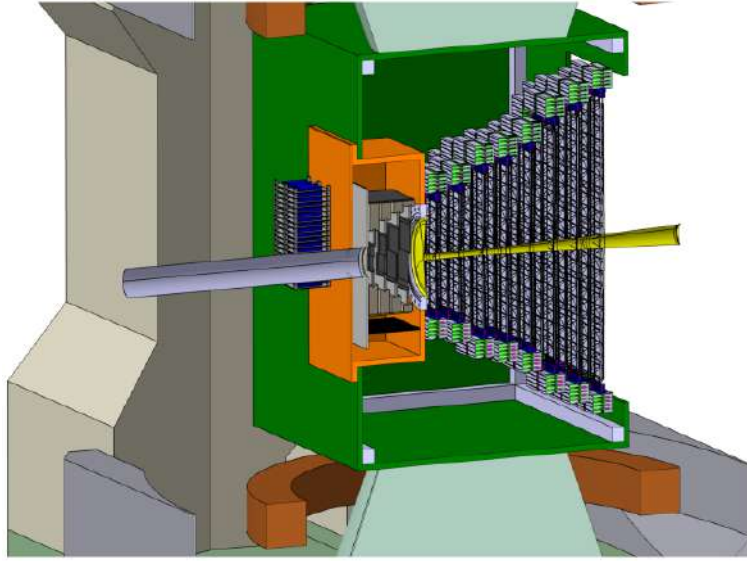


Figure 2.7: A view of STS with MVD housed inside magnet is shown [49].

The detector angular acceptance is 2.5° to 25° with 8 layers of detectors stationed between 30 cm to 100 cm downstream the target. The design spatial resolution $\sim 25 \mu\text{m}$ requires the strip size in STS of $58 \mu\text{m}$. The sensors are mounted on a light weight support structure with micro strips arranged in a double sided stereo angle of 7.5° of n-strip with p-strip [51]. The detector consists of strips of pitch $58 \mu\text{m}$ and length between 20 to 60 mm with thickness $300 \mu\text{m}$ [52].

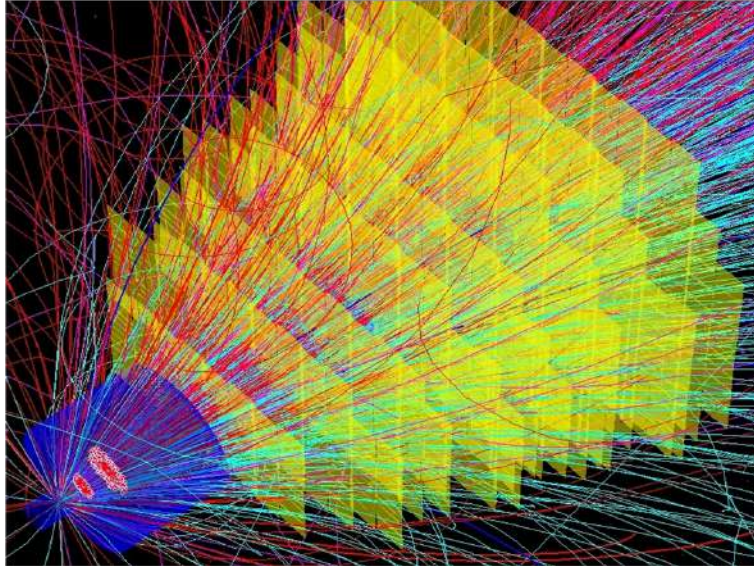


Figure 2.8: Tracks passing through STS detectors of 8 layers from central Au+Au collisions at 12 AGeV using GEANT simulation.

Readout of sensors will be performed by multi-line micro cables with fast electronics. STS

is operated in temperature zone of -5° to keep the leakage current under control for limiting radiation damage. The material budget of STS is kept as small as possible $< 1\%$ X_0 [52]. The track reconstruction in STS under magnetic field is governed by the Cellular Automaton technique [47] followed by track extrapolation and fitting through Kalman Filter technique [53, 54]. Charged particles will be reconstructed at STS and particle identification will be done by time of flight technique using the TOF detector located around 10 m downstream the target.

2.5.4 Ring Imaging Cherenkov Detector (RICH)

A Ring Imaging Cherenkov Detector (RICH) will be dedicatedly used for dielectron measurement. It is positioned after the dipole magnet and STS at a distance of 1.6 m downstream the target. Here the electron identification from low momentum up to 8-10 GeV/c can be attained by suppressing the pion background at least in order of 100 [55]. It will measure the dielectrons in a broad mass range starting from the mass of low mass vector mesons up to that of charmonia. It will also focus on the measurement of excess dilepton yield down to LMVM region with much improved precision which was first observed at the NA49 dimuon measurement. This goal can be achieved with RICH detector which is a gaseous detector using CO_2 as the radiator gas with 1.7 m long gas radiator. It uses the principle of cherenkov radiation for particle identification.

RICH uses a projective geometry for focusing the mirror elements and photo detectors are used for photon identification. The mirror plane is split horizontally into two arrays of spherical glass mirrors, (4×1.5) m^2 each. The 72 mirror tiles have a curvature of 3 m radius and thickness of 6 mm. The mirrors are coated with reflective Al and protective MgF_2 . In photon detectors multi-anode photo multiplier tubes are used. The radiator gas CO_2 has γ_{th} of 33.3 and refractive index $n = 1.00045$ ($T = 0^{\circ}$ and $p = 1$ atm). Saturated cherenkov opening angle is 1.72° with cherenkov threshold momentum for pion is 4.65 GeV/c. Here pions and electrons can be separated upto 10 GeV/c momentum assuming that pions can be separated from electrons up to 90% of the maximum cherenkov opening angle θ_c ($\cos\theta_c = 1/n$). Electron identification momentum range depends upon the factor γ_{th} . Fig. 2.9 shows that pions can be detected at high momentum ($p > 5\text{GeV}/c$) also. Threshold of cherenkov light for kaon is ~ 16 GeV/c. Detectors are of high granularity and fast detectors to cope the high interaction rates in

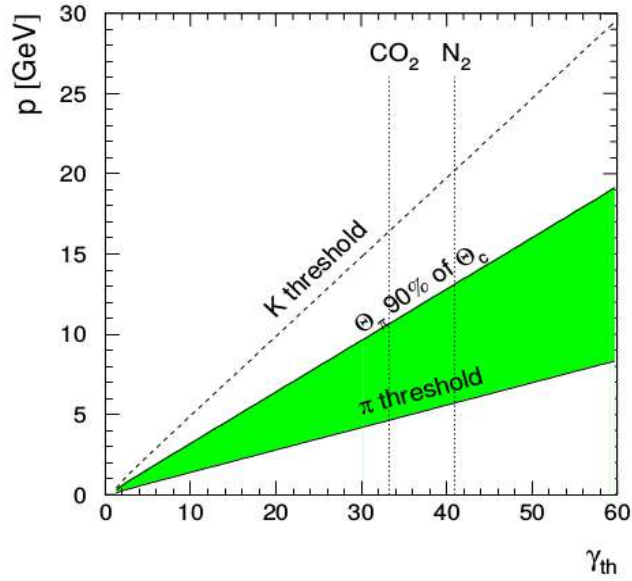


Figure 2.9: Momentum threshold for pion and kaon production for cherenkov light in RICH detector [55].

CBM. After RICH there will be Transition Radiation detector which contributes to additional electron identification at high momentum and tracking. This RICH detector system is built in such a way that it can be moved out from the CBM setup easily when dimuon measurement is required. During dimuon measurement, RICH will be replaced by Muon Chamber at the same location.

2.5.5 Muon Chamber (MUCH)

The experimental challenge for muon detection at CBM is to identify low momentum muons in a very high particle density environment. The concept for Muon Chamber is the use of segmented absorbers and detector triplet layers called stations installed in between the absorbers. This is done to identify low momentum as well as high momentum muons [56]. Hadron absorbers are used to absorb the hadrons and allow to pass the weakly interacting muons through it. MuCh position starts at the distance of 125 cm from the target. Depending on the beam energy there are modularized versions of MuCh for detection of dimuons. For 12 AGeV beam energy it requires 4 stations and 4 absorbers for low mass vector meson detection. MuCh will use gaseous based detectors. In the first two stations Gas Electron Multiplier (GEM) detectors are used whereas for the third and fourth stations Resistive Plate Chambers (RPC) are considered

as suitable candidate. MuCh covers a total active area of about 70 m^2 . A projective pad geometry has been chosen for MuCh modules to accommodate with the high particle rate. The details of the design of MuCh has been discussed in the next chapter with the performance of MuCh for dimuon detection.

2.5.6 Transition Radiation Detector (TRD)

TRD is positioned in between MUCH and Time Of Flight detector with its detector stations located at the position of approximately 5 m, 7.2 m and 9.5 m downstream the target. The main aim of TRD is to identify electrons and positrons with momentum above $1.5 \text{ GeV}/c$ and also it is required for particle tracking purpose. It basically extends the electron identification capability of RICH detector above $5 \text{ GeV}/c$ by means of extra pion suppression. Here pion suppression factor is 10-20 and makes the precision measurement of dielectrons from LMVMs up to charmonium mass range with good signal to background ratio. It has the capability to identify charged particles through their specific energy loss. So TRD is also advantageous for nuclear fragment measurement.

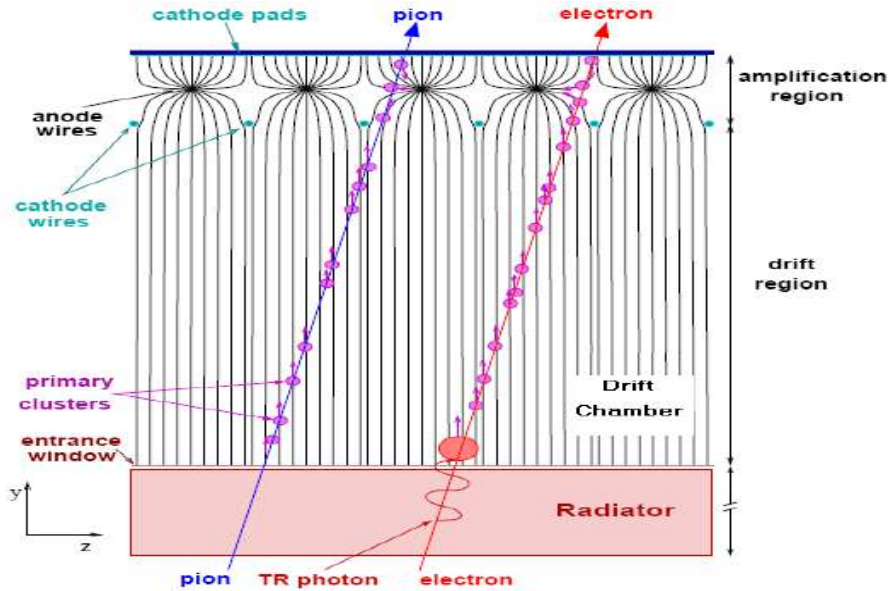


Figure 2.10: TRD consisting of drift chamber and radiator is used for pion and electron identification by the principle of transition radiation is shown by the schematic diagram [57].

The particle detection principle in TRD is based on the emitting electromagnetic radiation known as transition radiation when a relativistic charged particle passes through two medium

with different dielectric constant. The intensity of radiation is different for different particles and depends on the Lorentz factor $\gamma = E/mc^2$ [58]. Due to this principle electrons and pions can be distinguished by their Lorentz factor which is high for electrons and low for pions. The detection principle is shown in Fig. 2.10. This TRD is made of 3 layers of detectors in a station with total 3 stations. It is made of gaseous detector where Xe/CO₂ based Multi-Wire Proportional Chambers (MWPC) are used in addition the adequate radiator [59]. The second TRD layer is rotated by 90°. The total active area of TRD is around 600 m². TRD detector readout pads are rectangular pads and to keep occupancy below 5 % the minimum size of a cell is around 1 cm² [57]. The TRD will be used as fifth tracking station for MUCH [57]. For SIS100 setup only one station of TRD detector will be installed in between MUCH and TOF detector.

2.5.7 Time of Flight (TOF)

Time of Flight detector in CBM will identify the charged hadrons i.e pions, kaons, protons etc that are emitted in the beam target interaction and fall into the detector acceptance covered by STS and TOF with an angular acceptance 2.5° to 25°. It uses the principle of time of flight for particle identification that depends on simultaneous measurement of momentum and velocity of the particles. With the particle velocity β and momentum p of the particle from the tracks reconstructed at STS the mass of the particle can be computed as

$$m^2 = p^2(1/\beta^2 - 1) \quad (2.2)$$

The m^2 versus momentum distribution of the charged hadrons from TOF is shown in Fig.2.11 from simulation.

The TOF is a gaseous detector with array of Multi-Gap Resistive Plate Chambers (MRPC) with total active area about 120 m² [61]. It will be positioned at 6 m or 10 m downstream from the target depending on the SIS100 or SIS300 setup. With 10 MHz interaction rate at CBM, TOF can handle rate up to 25 kHz/cm² [62]. The required time resolution for TOF is 80 ps. MRPC uses low resistive glass electrodes with an occupancy below 5 % for 5 cm² pad sizes at 25 AGeV Au+Au interactions.

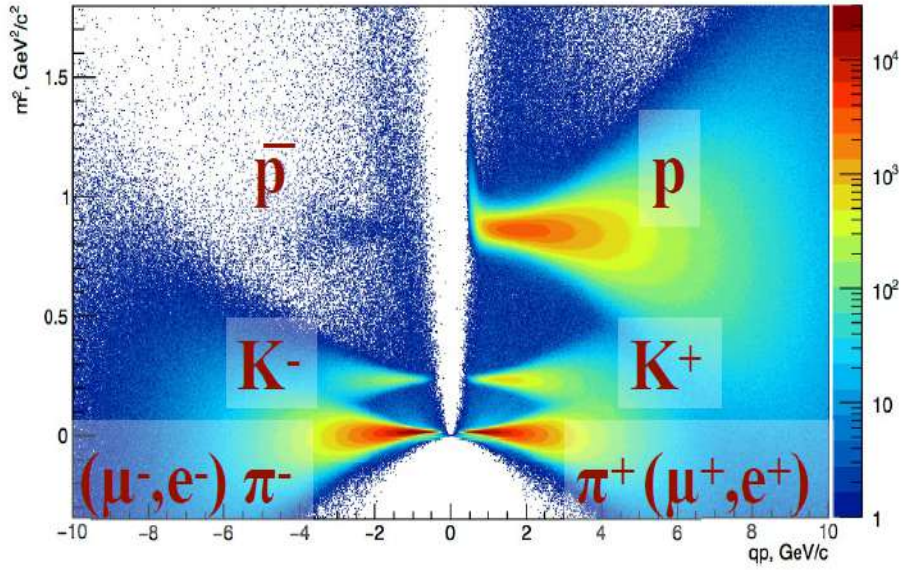


Figure 2.11: The reconstructed TOF m^2 versus momentum for the charged hadrons at 10 AGeV Au+Au interaction by simulation [60].

2.5.8 Electromagnetic CALorimeter (ECAL)

The Electromagnetic CALorimeter will be used for photon detection that includes the direct photons and decay photons from the neutral mesons (π^0 , η). It will be installed in between TOF detector and Projectile Spectator Detector (PSD). Here a "shashlik" type calorimeter will be installed like in HERA-B, LHCb and PHENIX experiment. These shashlik modules will be installed as tower or as a wall with different distances from the target. This ECAL will be made of modules of 140 layers with 1 mm thin lead and 1 mm thin scintillators with cell sizes of $3 \times 3 \text{ cm}^2$, $6 \times 6 \text{ cm}^2$ and $12 \times 12 \text{ cm}^2$.

2.5.9 Projectile Spectator Detector (PSD)

The Projectile Spectator Detector will be used for event centrality and reaction plane determination. This event centrality and reaction plane determination is of crucial importance for many physics studies like collective flow, particle multiplicities and fluctuations which strongly depend on event centrality [63]. The detector has forward rapidity coverage and aims to measure the energy distribution of nuclear fragments or spectators and the particles which are produced close to the beam rapidity. It has excellent energy resolution and granularity for precise collision centrality determination. It comprises of lead-scintillator calorimeter. The scintillator

light is readout by micro pixel avalanche photodiodes via wavelength shifting (WLS) fibres. It has active area of $3 \times 3 \text{ mm}^2$ and pixel density of $10^4 / \text{mm}^2$. The calorimeter has 44 modules. Each module consists of 60 lead or scintillator layers with surface area of $20 \times 20 \text{ cm}^2$ [63].

2.5.10 Data Acquisition (DAQ) and online event selection

The CBM aims to measure the rare particles like charmonium, low mass vector mesons or multi-strange hyperons with unprecedented interaction rate $\sim 10 \text{ MHz}$. For this high collisions rate the detectors will face huge particle density. Assuming an archiving rate of 1 GByte/sec and an event volume of about 10 kByte for minimum bias Au + Au collisions, an event rate of 100 kHz can be accepted by the data acquisition DAQ. For this reason online event selection is very crucial for rejection of unnecessary events which contains no signal events that unnecessarily loads the DAQ. So for 10 MHz interaction rate we need online event selection algorithm which suppresses background by a factor of 100 or more. Event selection will be based on online with very fast high performance computer supplied with many core CPUs and graphics cards. GreenIT Cube [64] is dedicatedly designed for this purpose at GSI. CBM will be operated in self triggering mode unlike any hierarchical triggering that is used in other experiments like ALICE or STAR. Track reconstruction will be the most time consuming step in online event reconstruction based on Cellular automaton [47] or Kalman Filter technique [53,54]. For open charm event selection triggering will be based on the secondary decay vertex finding. Highest background event suppression can be achieved in J/ψ event selection.

2.6 Dimuon measurement at FAIR

Dimuons are pairs of oppositely charged muons i.e, $\mu^+ \mu^-$, which are produced throughout the stages of a heavy ion collision. Since dimuons have very small strong interaction cross section so, they mostly remain unaffected by the surrounding QCD medium. Thus, dileptons are capable of carrying information from their point of origin completely undisturbed. Hence, dileptons are considered as penetrating probe of the medium produced in a collision. Measurements of dilepton invariant mass up to a few GeVs provide essential information on different aspects of the medium produced in heavy ion collisions, that include, in-medium modification

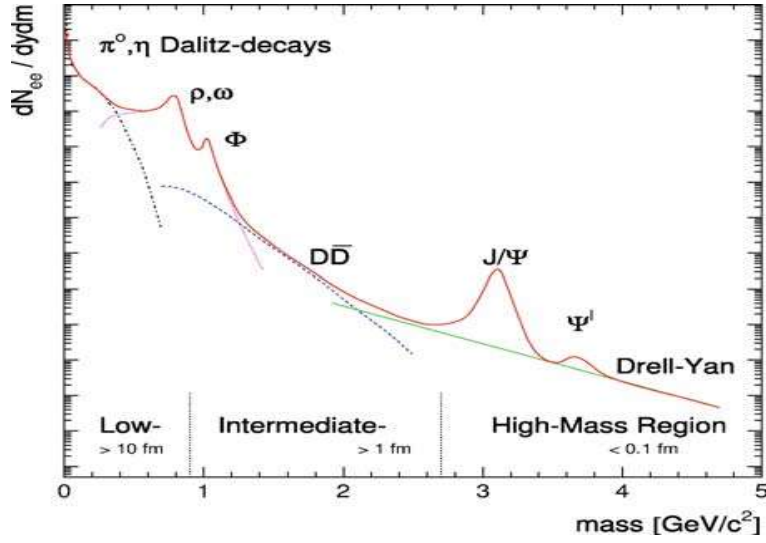


Figure 2.12: Schematic diagram of dilepton/dimuon sources from different invariant mass regions.

of the spectral functions of vector mesons, temperature of the medium and the charmonium production. Based on the production mechanism, origin of dimuons are broadly classified into three categories, which populate different regions in the invariant mass spectra, demonstrated graphically in Fig. 2.12 and also enlisted below [44] :

(a) Low mass vector mesons : dimuons originating from the decay of low mass vector mesons (ρ , ω , ϕ , η) conventionally below mass of ϕ meson is considered as low mass range. The dimuon invariant mass spectra in the low mass region is believed to be sensitive to the modifications in spectral functions of vector mesons that include broadening of width or the shift in the pole masses of vector mesons, which are said to be an indication for the chiral symmetry restorations. A possible consequence of the chiral symmetry restoration is the mass modification of chiral partners like ρ and a_1 [29], which leads to an excess dimuon yields in the low mass region. Recent theoretical calculations with a ρ -melting scenario on top of the dimuon emission rate from partonic medium lead to a very good agreement with the experimental results. In Fig.2.13 dimuon measurement from NA60 data has been shown in In+In collisions at 158 AGeV compared it with the theoretical calculations. According to the theoretical estimates, in the low mass range, below $0.8 \text{ GeV}/c^2$ is dominated by broadening of ρ meson, QGP radiation and the freezeout ρ meson [30, 31, 44].

(b) Intermediate mass / thermal radiation : Thermal muon pairs originating from the quark

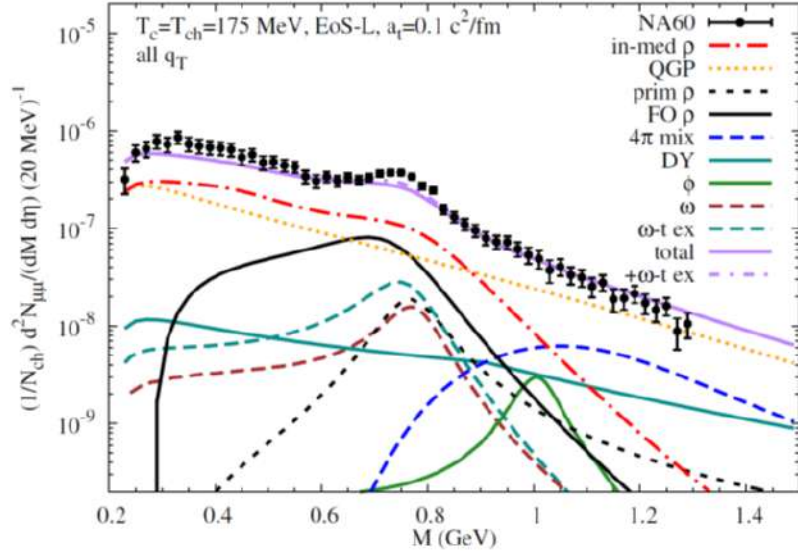


Figure 2.13: Invariant mass distribution of dimuon spectra from NA60 data in In+In collisions at 158 AGeV and compared with theoretical calculations including in medium vector spectral functions.

- anti quark annihilation contribute to the region with $M_\phi < M_{inv} < M_{J/\psi}$. There is also contribution from Drell-Yan from quark - anti quark annihilation in this region. A parameterization of dilepton invariant mass spectra in IMR region with $M^{3/2}\exp(-M/T)$ provides the temperature of the medium [44].

(c) High mass/Charmonium : Muon pairs originating from the decay of charmonium ($M_{inv} > M_{J/\psi}$) belongs to this region. Drell-Yan has also a significant contribution [44, 45].

So, it is important to note that dileptons provide valuable information of the hot dense medium formed in heavy ion collisions. However, there is lack of dilepton data at low energy where net baryon density is very high. At low energy dilepton measurement has been performed only at CERN-SPS mainly at $E_{lab} = 158$ AGeV. There is no dilepton data in the FAIR energy range i.e 2 to 40 AGeV where medium is expected to be very high baryon rich. So CBM will measure very precisely these dimuons along with dielectrons in p+p, p+A and A+A collisions as a function of beam energy and system size. These dimuon and dielectron measurements will complement each other and will give the complete picture of the dilepton production and associated physics mechanism at this FAIR energy. In the next chapter we will discuss the development and technical layout of Muon Chamber for CBM and the performance study of

this Muon Chamber for dimuon measurement at FAIR energy.

Chapter 3

Development and performance of Muon Chamber (MuCh) at CBM

In this chapter, we will discuss the development and optimization of the Muon Chamber (MuCh) geometry in accordance with the physics criteria and realistic requirements. The muon system is aimed to be used for the identification of Low Mass Vector Mesons (LMVMs) (ρ , ω , ϕ) and J/ψ mesons from their dimuon decay channels. In this high particle density environment, of heavy ion collision, identification of leptons and hadrons simultaneously is itself a challenging task. Thus, the main objective is to find out an optimized version of the muon detection system by simulation, which would make the above measurements suitable for physics observables.

The Muon chamber (MuCh) detector [56] system for the CBM experiment is one of the major in-kind contributions from India. The CBM experiment's muon detection method is unique as it divides the whole absorber into thinner segments and inserts detector triplet layers, called stations in between the absorber pairs. It is intended to make momentum-dependent track identification easier. This is done to enhance the capability of detection of muons of both low and high momenta. The rate of the incident particles on the detectors is highest for the first station which is closest to the target and it decreases as we go downstream from the target. The first two stations used GEM detectors due to their ability to handle extremely high particle rates. The use of Resistive Plate Chamber (RPC) detectors is the baseline option for

the third and fourth stations since the particle rate is relatively lower at these locations. This part of the thesis gives a detailed account of the optimization of the muon system in terms of absorbers material, their thickness, absorbers size & shape, size of the detectors in the stations, beam pipe and shielding design inside the MuCh section, among others. The details of RPC geometry and detector response implementation for the third and fourth stations, together with the study of its performance to test its feasibility of usage are parts of the study. Lastly, the performance of the optimized muon system for LMVM detection in central Au+Au collisions for the beam energy range of 8 - 12 AGeV has been discussed.

3.1 Different configurations of the Muon Chamber geometry

Depending on the physics requirements at various energies, the CBM experiment will be run at different phases. Collisions will be studied using beams from the SIS100 accelerators at various energy levels. In SIS100, the accelerator will produce beam energy up to 12 AGeV starting at 2 AGeV [39]. SIS100 will be the starting phase of CBM physics programme to be followed by beams for SIS300 [32]. To examine the conditions inside the fireball produced in the collisions, dimuons are used as diagnostic probes. The CBM's muon detector is specifically designed to detect muon pairs decaying from LMVMs and J/ψ at various stages of the collision. MuCh detector will have several configurations depending on the number of detector layers and absorber segments in order to detect muon pairs with high efficiency over a wide range of energies. In order to satisfy this purpose, a modular approach will be taken for configuring the MuCh system starting at $E_{lab} = 2$ AGeV energies and going up to $E_{lab} = 12$ AGeV energies for SIS100, with a provision of upgradation in accordance with the physics requirement. The different geometry configuration of MuCh [56] have been shown in Fig. 3.1. Based on the following factors, the modular design criteria will be implemented :

(A) The absorber segments will only be created once, and they will be placed appropriately based on the required total absorber thickness for a certain physics interest. Additionally, the first absorber will be composed of low Z graphite of density 2.67 g/cm^3 , with a 60 cm thickness in order to reduce the combinatorial background. However, later the 60 cm graphite of density 2.67 g/cm^3 has been replaced with 28 cm thickness graphite of density 1.3 g/cm^3 [65], plus

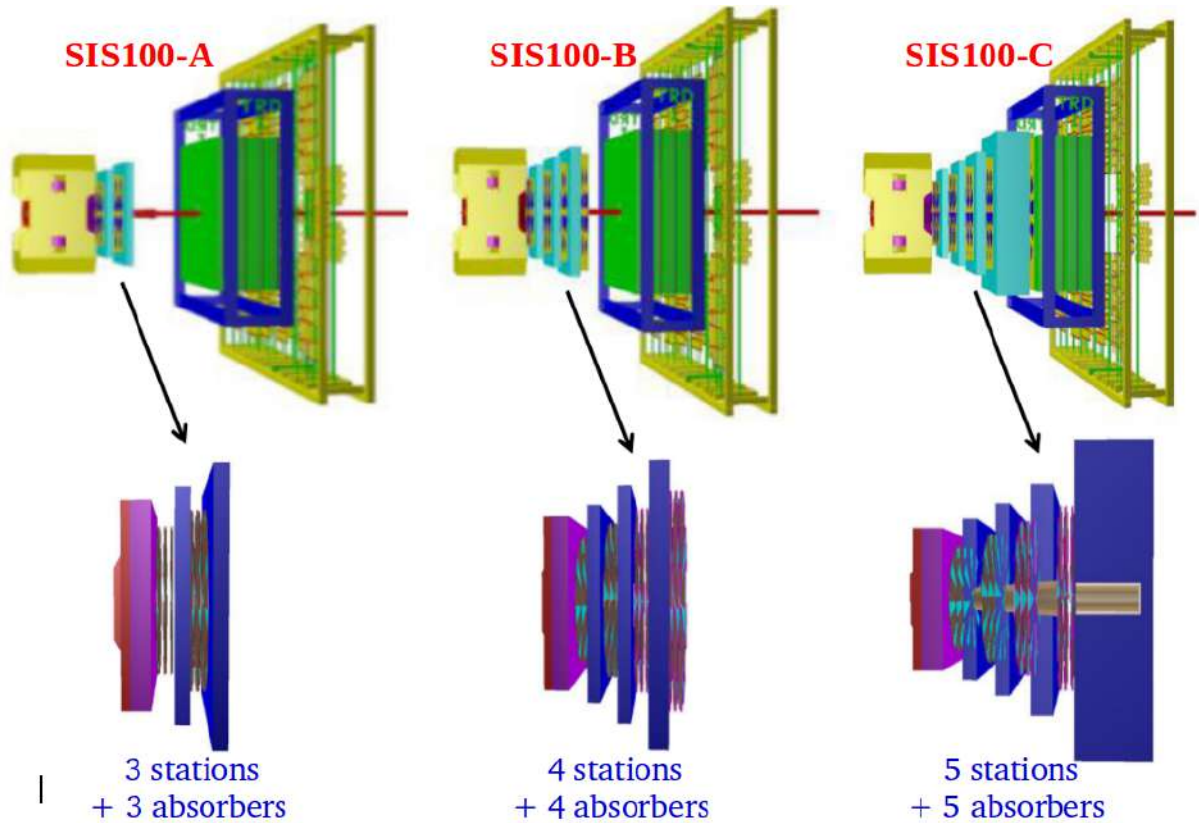


Figure 3.1: Different modular versions of MuCh geometry depending on beam energy and physics criteria. SIS100-A (left), which consists of 3 stations and 3 absorbers, SIS100-B (middle) with 4 stations and 4 absorbers and SIS100-C (right) with 5 stations and 5 absorbers along with Magnet, Silicon Tracking Stations (STS), Transition Radiation Detector (TRD) and Time of Flight (TOF) detectors.

concrete of thickness 30 cm, so total thickness is now 58 cm, which is discussed in detail in last part of the section 3.3.2. (B) Based on physics requirements, the number of detector layers, or tracking layers, for dimuon detection will be decided. For low energy and LMVM detection, number of tracking layers will be less compared to the case in high energy which is focused on detection of J/ψ . (C) The detector technology to be optimized for the tracking stations. The optimization depends on the detectors' capacity to handle particle rates, how well they operate in large area detector operation, and the cost of the detectors. The table 3.1 shows different configurations of MuCh system at different energies.

Table 3.1: Different configurations of MuCh geometry for SIS100

MuCh Confi gurations	First absorber thickness (Graphite + Concrete)	No. of iron absorber blocks	Total Thickness of iron	Total station numbers	Detector technology	physics case
SIS100-A	58 cm	2	40 cm	3	2 GEM, 1 RPC	LMVM A +A 4- 6 AGeV
SIS100-B	58 cm	3	70 cm	4	2 GEM, 2 RPC	LMVM A +A 8- 12 AGeV
SIS100-C	58 cm	4	170 cm	5	2 GEM, 2 RPC, 1 TRD	J/ψ p +A 29 AGeV

The table shows that the SIS100-A version has three tracking stations and three absorbers. Here, goal is to detect LMVM in heavy ion collisions with beam energies between 4 and 6 AGeV. In this scenario, the iron absorber will be 40 cm thick overall. In the next version the SIS100-A will be extended to SIS100-B with increased beam energy range 8-12 AGeV. Here 4 stations and 4 absorbers will be used with total iron thickness of 70 cm. It is also dedicated to measure LMVM in heavy ion collisions at this energy range. There is also an aim to study J/ψ sub-threshold production at this energy. SIS100-C consists of an extra 1 m thick iron absorber in addition to SIS100-B with TRD as the 5th tracking stations and the primary aim is to measure J/ψ in p+A collisions [56].

3.2 Simulation steps in MuCh

The CBM detectors' geometry is being developed to meet the requirements of a realistic scenario and hence optimization via simulation is a part of development of a suitable MuCh geometry. Here we discuss the simulation steps for optimization and performance study of MuCh geometry. To create a realistic heavy ion collision like scenario, UrQMD [38] event generator is used as input particle generator and PLUTO [66] is used as a dimuon signal generator from LMVMs and J/ψ . A detailed discussion on PLUTO and UrQMD event generators have been done in section 3.4.1. GEANT3/GEANT4 is used as the transport engine for particles transport and interactions with detector materials. The simulation has the following steps for final particle reconstruction through the SIS100 MuCh detector. (a) Implementation of geometry in CBMROOT framework. (b) generate input particles using UrQMD event generator and transport the generated particles using GEANT3/GEANT4 [67] through the detector setup. (c) detector segmentation or digitization (d) hit reconstruction (e) track reconstruction and propagation (f) final dimuon analysis with reconstructed global tracks.

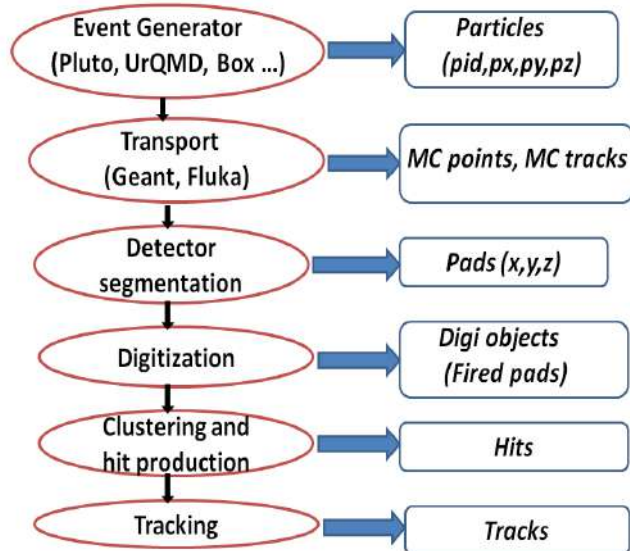


Figure 3.2: Simulation steps for track reconstruction in MuCh.

(a) Geometry implementation in CBMROOT framework

The novel feature of MuCh detector in CBM is that the total absorber is segmented and we study the propagation of the reconstructed tracks through the segmented absorbers. The

triplet detector layers are placed in between the absorber pairs to collect the space points for track reconstruction. The overall detector setup is conical shaped to accept the forward focused particles after the collisions. In the first and second stations GEM detectors will be used whereas in the third and fourth stations RPCs are considered as suitable detector technology. Each detector layer is of circular profile consisting of trapezoidal shaped detector modules of suitable number which makes the layer profile circular. The detector modules are arranged in a staggered manner are placed on both sides of a support structure to avoid the dead zone in between the consecutive modules. Optimizations have been performed on absorbers size, shape and absorber materials. Optimization is also performed for detector technology, size, segmentation or granularity of the detectors. The MuCh geometry includes the beampipe with the shielding inside the MuCh section and optimization has also been performed in this section. Optimization is still ongoing to meet the realistic scenario and physics interest. The muon pair reconstruction efficiency and the signal to background ratios are the parameters studied to optimize the detector layout.

(b) Event generation and transport through detectors

For particle generation UrQMD is used as the event generator in the input. It is suitable to study at the FAIR energy because it describes the phenomenology of particle production at low energy mainly SPS or FAIR reasonably well. At this low energy particle production is dominated by hadronic interactions which are well described by the UrQMD event generator. Now for dimuon signal generation from decay of LMVMs or J/ψ , PLUTO phase space generator with decay is used, as the default UrQMD does not contain the dimuon decay channels from these mesons. These generated particles are transported through the CBM dimuon detector setup that includes Magnet, STS, MuCh, TRD and TOF detectors. The transportation is performed by GEANT3/GEANT4 transport engine. FLUKA [68] can also be used as transport for study of rate calculation or radiation damage study.

(c) Detector segmentation and digitization

In the next step, detector segmentation is done to create detector readout pads. In MuCh detectors projective pads with varying pad dimensions have been implemented. This is done in accordance with nature of the particle density profile with respect to detector radius. Particle density decreases with radius r following the nature $\sim 1/r$, so density is highest at inner radii

and lower at higher radii. Accordingly pad granularity is highest at the inner radii and decreases with radius r . Here azimuthal segmentation of pads is done with dimension of $\delta r = r\Delta\phi$, where δr corresponds to the radial separation [56]. After creating the pads, digitization is performed. GEANT provides the point of energy deposition by charged particles inside the detector active volume. This energy deposition points are called Monte Carlo points or MC points. The method of distributing the MC points in the pads is known as digitization. It contains the detailed procedure of implementing of detector response inside the detector volume. A digi is created by adding together points that lie inside a specific pad area in the basic digitization scheme. In the advanced digitization scheme, however, a large number of points are exposed to primary ionisation, multiplication, and signal production inside the gas volume.

(d) Hit reconstruction

After digitization, hit reconstruction is performed. In hit reconstruction, the digis are grouped into clusters according to suitable clustering algorithm. The clusters are then divided into small sub groups or say hits. The centroid of the sub clusters is considered as the location of the hit or cluster point. These hits are then considered as tracking candidate in the next step.

(e) Track reconstruction and propagation

Track recognition and propagation through the CBM setup in a very high particle density environment in CBM is itself a challenging task. Around 1000 charged particles will be produced in central Au+Au collisions at the top CBM energy. This leads to very high particles hit density or track density in the detectors. Here tracking will be performed using a Cellular Automaton [47] and the Kalman Filter technique [53, 54]. The tracks will be reconstructed at STS detector which is inside the CBM magnet using Cellular Automaton technique. Track propagation and estimation of track parameters through iteration will be carried by Kalman Filter technique. Tracking involves the steps of track propagation, track finding, track fitting and selection of good tracks.

The track propagation predicts the trajectory of tracks and estimates the error in covariance matrix in track propagation [69]. Track propagation considers the following parameters for its trajectory extrapolation like energy loss, multiple scattering in the material and the effect of magnetic field. The effect of ionization according to Bethe- Bloch and Bremsstrahlung of the

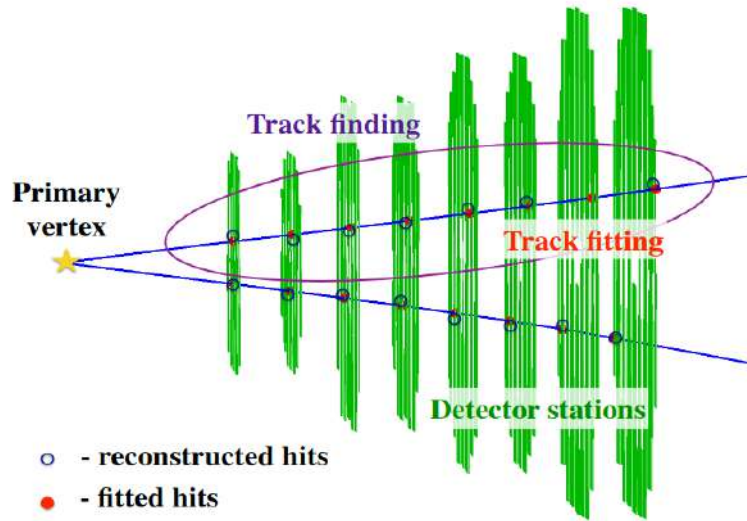


Figure 3.3: Schematic representation of track propagation and track finding process in detector stations [69]

charged particles interaction with the medium are taken care during tracking. Here a Gaussian approximation is considered with Highland formula [70] for calculating the average scattering angles. The track propagation is estimated using equation of motion of the charged particles in the magnetic field. It considers the 4th order Runge-Kutta method [71] for solving the equation for track propagation. When there is no magnetic field it considers the straight line propagation of tracks and transport matrix calculation. For track finding and fitting, it takes the nearest neighbour hits as its track candidates. This attachment of hits is done step by step in each detector stations and after attaching hits with the tracks the track parameters are updated accordingly by Kalman Filter. After reconstructing the tracks good quality tracks are selected according to the track length and good χ^2 of the tracks. The ghost tracks and clone tracks are rejected to find the correct tracks with high efficiency. The criteria for correctly found track in simulation is that it should have atleast 70 % of its hits from one MC track, otherwise the track will be defined as ghost track.

(f) Dimuon candidate selection and analysis

After getting global reconstructed tracks, we apply some selection cuts for muon candidate selection. The selection cuts are based on the track length and χ^2 of the tracks. For this we apply some threshold cuts on STS hits and MuCh hits associated with the tracks. For

selection of good quality tracks χ^2 cut is applied on the MuCh segment tracks, STS segment tracks and also on the primary vertex χ^2 . This is basically done to reduce the background due to non-muonic tracks and mostly weak decay of pions and kaons into muons. Selection cuts depends on the type of particles and the input beam energy. For detection of dimuons from LMVM at 8 to 12 AGeV, the number of MuCh layers can be upto 12 whereas for charmonium detection it should be atleast 15 MuCh layers because for charmonium detection an extra 1 m thick iron absorbers and an additional detector station is used.

3.3 Development and modifications of the MuCh geometry

In this section, the general concept, evolution, and optimization of the muon detection mechanism in the CBM will be discussed [72–77]. The basic idea behind a muon detector system is that it will include absorbers and detectors to find muons. The particles produced by collisions will be absorbed by the absorber, especially the hadrons since they interact strongly with the hadron absorbers while muons, which have weaker interactions, can pass through the absorbers and reach the downstream detectors. In CBM, the detectors are inserted inside segmented absorbers. This is done to identify both high and low momentum muons. If a single thick absorber is utilised in the low energy collisions, as has been used in many other experiments like NA60, ALICE, STAR, etc., the majority of the muons will otherwise cease. The major goal of the CBM muon chamber is to increase the detection efficiency of individual low momentum muons, which is a necessary condition for increasing the detection efficiency of LMVMs. For muon detection, the total thickness of the absorber as well as the thickness and material of the segmented absorbers have all been optimised in this case. Optimizations have also been performed for selecting suitable detector technology at different distances from the target, its shape, size, number of layers and granularity of the detectors.

3.3.1 Optimization of absorbers and detectors in MuCh

First we discuss the optimization of hadronic absorbers for muon detection in MuCh followed by optimization of detector technology and other aspects. Detection of low momentum muons is an essential need for reconstruction of LMVMs. This necessitates the use of a hadron absorbers

made of appropriate material with segmentation of right thicknesses. For determining the hadron absorber material in CBM, one important quantity is the hadronic interaction length (λ_I). This hadronic interaction length is basically the average length traversed by a hadron inside a medium before it undergoes nuclear interactions. This λ_I is related to the material property as,

$$\lambda_I = \frac{A}{N_A \sigma \rho} \quad (3.1)$$

Where A is atomic mass number, N_A is Avogadro's number, σ is the total inelastic cross section for hadron nucleus interactions and ρ is the density of the material. This σ , the total inelastic cross section for hadron-nucleus collisions can be calculated as

$$\sigma = \sigma_0 (A_{target}^{1/3} + A_{projectile}^{1/3} - \delta) \quad (3.2)$$

Where σ_0 is 68.8 mb and δ is 1.32 [78]. By this λ_I becomes $\sim 35 A^{1/3}$ gm/cm².

For designing the hadron absorbers for muon detection following points to be kept in mind :

- The total muon detector system should be as compact as possible. This is required to suppress the combinatorial background mainly due to weak decays of pions and kaons. This requires absorber material with high atomic mass A with low λ_I to manage the design as compact as possible.
- LMVM and J/ψ decay to dimuon channel and after muon pair reconstruction the invariant mass distribution provide the identification of mother particles. So mass resolution of the reconstructed particles should be as good as possible.

Taking these into considerations, iron has been chosen as the main component for hadron absorber because its hadronic interaction length is small so improves the hadron absorption quality. The major background originates from the weak decay of pions and kaons decaying into muons. And these decay muons contribute to the background and it should be suppressed as much as possible. However there is an alternating effect of multiple scattering in the material which describes the several scattering suffered by the particles or muons inside the absorbers.

The absorber material should be appropriate for low multiple scattering in order to reduce the fake background tracks. This multiple scattering increases the chance of mismatched tracks during track reconstruction and thus results fake tracks that yields more combinatorial background. It is to be noted that if the momentum determination of the particles is done after passing the absorber material then there will a large degradation of the momentum resolution due to the multiple scattering of the particles suffered inside the material and it will lead to poor mass resolution of the reconstructed LMVMs. However in case of CBM this is not the case because the momentum determination is done in the STS detector which is placed before muon chamber. However multiple scattering degrades the pointing resolution and hit findings of the tracks. So a compromise has to be done in between the hadronic interaction length λ_I and the multiple scattering which is related with radiation length X_0 of the material. This λ_I is proportional to $A^{1/3}$ and the radiation length varies as A/Z^2 . This X_0 should be as large as possible in order to reduced multiple scattering. This multiple scattering angle θ_{mult} is anti correlated with radiation length X_0 as-

$$\theta_{mult} = 13.6z/\beta p\sqrt{z/X_0}[1 + 0.038\ln(x/X_0)]$$

Where p , β and z are the particle's momentum, velocity and charge. x/X_0 is the thickness of the material in terms of radiation length X_0 .

Table 3.2: Characteristics of different absorber materials for hadron absorption.

Material	λ_I (cm)	X_0 (cm)	ρ (gm/cc)
C	44.72	22.1	1.93
Fe	18.32	1.92	7.2
W	10.4	0.38	17.8
Pb	3.98	0.55	11.35

In the table 3.2, the characteristics of some well-known absorber materials have been shown in terms of radiation length and hadronic interaction length and the density of the material. So λ_I should be small enough for absorption of hadrons within the absorber material with proper absorber length. At the same time, radiation length X_0 should be as large as possible in order to reduce multiple scattering.

The required thickness of the iron absorber can be estimated from the Fig. 3.4 [72], where

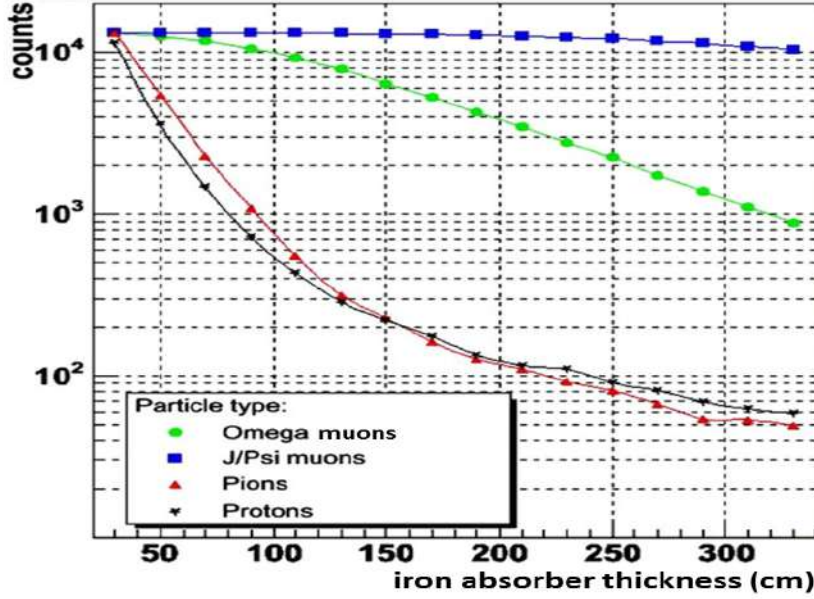


Figure 3.4: Particle count as a function of distance travelled in iron absorber for muons from omega, J/ψ and other hadrons like pions and protons. The muons that result from the decay of J/ψ and omega mesons are produced by the PLUTO event generator, while the remaining particles are produced by the UrQMD event generator.

the absorption of muons decaying from ω and J/ψ along with that of the other hadrons like pions and protons has been shown with the thickness of the iron absorber. These optimizations from the simulations have been performed for 25 AGeV central Au+Au collisions using GEANT3 as a transport engine and UrQMD as an event generator. This 25 AGeV energy corresponds to SIS300 at FAIR, which is expected in the next phase. We can see from the figure that inside the iron absorber, muons from J/ψ may travel a distance of around 250 cm without experiencing much suppression. Contrarily, with such a thick iron absorber, muons from omega mesons are 10 times more suppressed. Furthermore, it can be seen from the figure that after an iron thickness of 150 cm, the absorption of muons from omega and that of pions and protons are nearly similar. As can be seen that their slopes of absorption are similar after 150 cm of the iron block, which means there is no chance of improvement of signal to background ratio of omega mesons beyond this thickness of 150 cm. It concludes that for efficient LMVMs detection, the iron absorber length should not exceed 150 cm, whereas, for J/ψ detection, it requires an additional 1 m thick iron absorber for efficient detection of muons from J/ψ . For LMVMs detection, the total iron absorber thickness is typically set at 125 cm, which is equivalent to

7.5 λ_I whereas for J/ψ it is 225 cm that, corresponds to 13.5 λ_I .

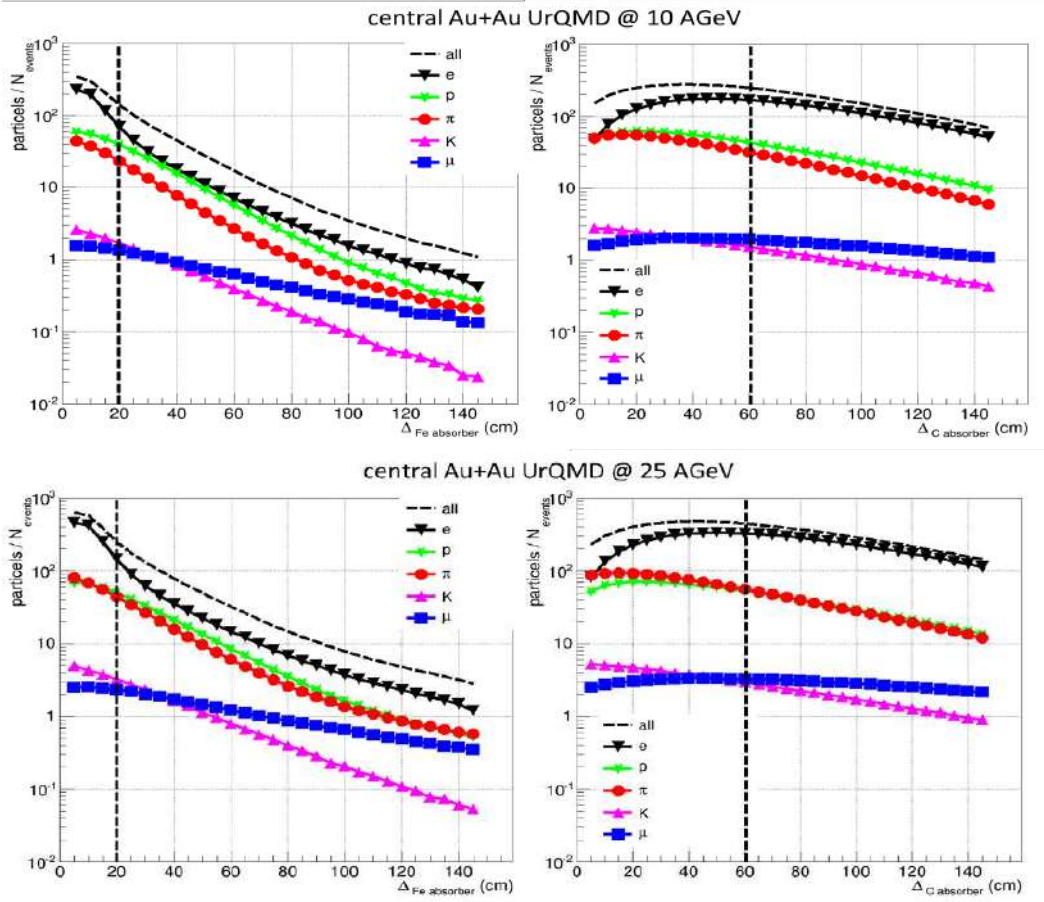


Figure 3.5: The variation in particle multiplicity with C and Fe absorber thickness at 10 AGeV (top) and 25 AGeV (bottom) central Au+Au collisions [72].

In the MUCH system, one must also tune the thickness of each individual absorber layer in addition to the overall absorber thickness. The thickness and composition of the first absorber slice, where a compromise between hadron absorption and multiple scattering must be made, are particularly crucial. The absorber needs to be thick enough to lower the hadron multiplicity and hit density, which determine the rate that needs to be handled by the tracking chambers that are put just after the absorber. Contrarily, a thick absorber increases multiple scattering and for a given thickness scattering increases with Z of the material. Thus, the quantity of mismatched tracks (false tracks) increases, which ultimately leads to an increase in the combinatorial background and a subpar S/B ratio. In Fig. 3.5 the comparison between carbon and Fe as a first absorber material has been shown. This simulation was done at 10

AGeV and 25 AGeV central Au+Au collisions using GEANT3 as transport engine [72]. The simulations show that for both absorber materials, the yield of secondary electrons dominates the particle multiplicity. It can be seen that the yield of the secondary electron first increases and subsequently decreases with the increasing material thickness. It can be seen from the figure that the number of particles that remain after 60 cm of carbon or 20 cm of iron could be found to be somewhat similar. But in the MUCH configuration, carbon has been selected as the primary absorber material mostly because of some practical issues of ease of use. Here we are discussing the the baseline version of the geometry which is based on the carbon absorber for the first one. However due to some practical limitations, the configuration of first absorber has been changed later, which has been discussed in section 3.3.2.

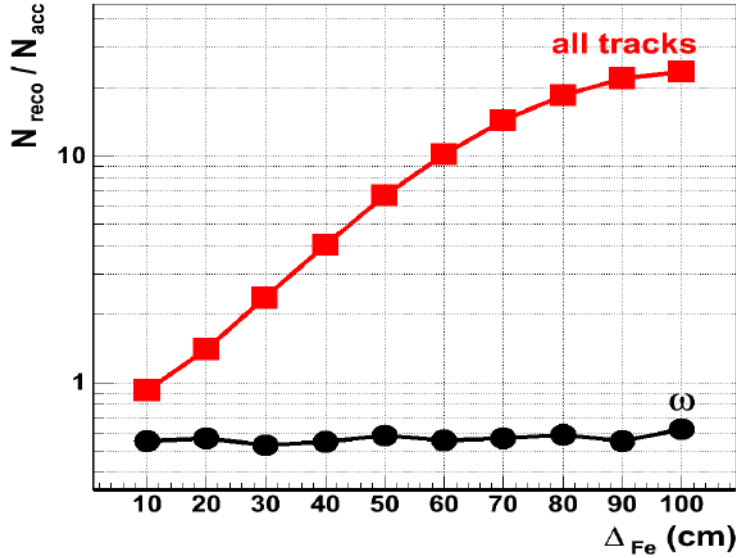


Figure 3.6: The ratio of reconstructed tracks to the accepted tracks has been shown with the iron absorber thickness.

As already discussed, the small-angle multiple scattering, which rises with absorber thickness, is a crucial factor for controlling mismatched background tracks. This impact is evident in Fig. 3.6 which illustrates how the ratio of the reconstructed tracks to the accepted tracks varies with thickness of first absorber, when iron was selected. From this plot it can be seen that the number of reconstructed background tracks increases significantly as the amount of iron absorber material increases. The resultant invariant mass distribution reveals that the reconstructed background strongly increases from 10 cm to 40 cm of iron absorber thickness,

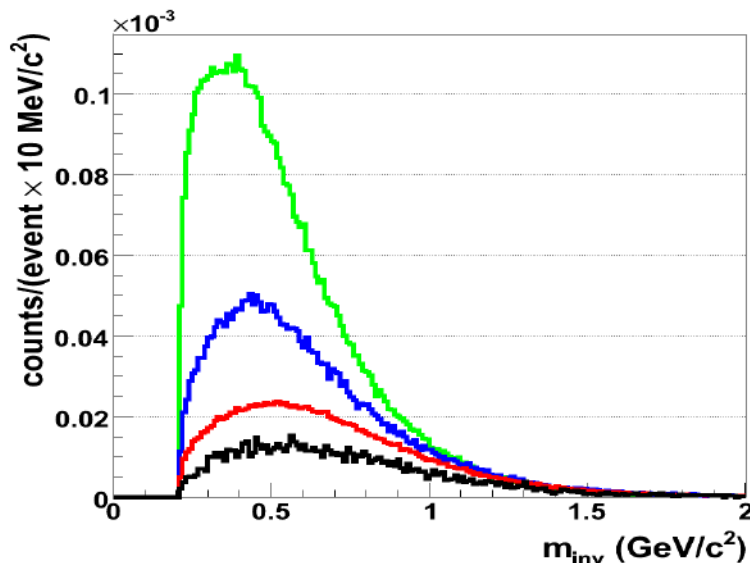


Figure 3.7: The reconstructed background tracks invariant mass distribution for different iron absorber thickness of 40 cm (green), 30 cm (blue), 20 cm (red) and 10 cm (black line) for the first absorber.

almost by a factor of 10 as shown in Fig. 3.7. Accordingly, a first iron absorber of 20 to 30 cm in thickness, or 60 cm in carbon absorber, appears to be the best option depending on hit density and background recordings.

From Fig. 3.8 it can be seen that the ratio of the number of reconstructed tracks to the input accepted Monte Carlo tracks increases largely for iron when compared to that for the carbon material [72]. This is because the multiple scattering in carbon is less compared to iron. Initially iron was assumed to be the only material for absorbers in simulation studies. However carbon absorbers with a 60 cm thickness are preferred when also taking into account the mechanical integration of the first absorber inside the strong magnetic field of the CBM magnet. Iron is chosen in all other absorbers except the first absorber. This is to maintain the compactness of the size of the muon chamber. The first absorber is divided into two parts for practical purposes; one part of around 20 cm is housed inside the CBM magnet and the other part of about 40 cm is outside the magnet. It should be noted that all the other absorbers, with the exception of the first one, are made of iron, but they are all made of stainless steel to prevent any effects from a residual magnetic field.

The sketch diagram of SIS100-B muon setup is shown in Fig. 3.9 which consists of four

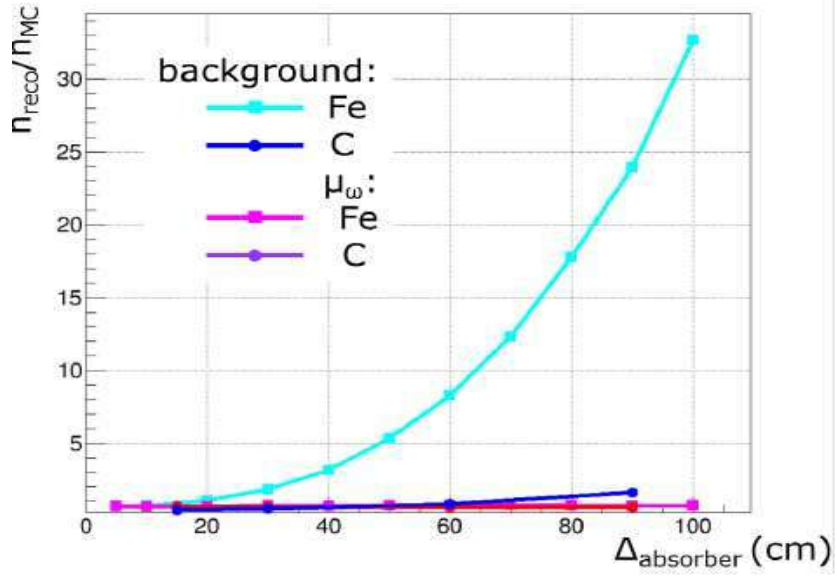


Figure 3.8: Ratio of reconstructed to acceptable input MC tracks for absorber material thickness of C and Fe.

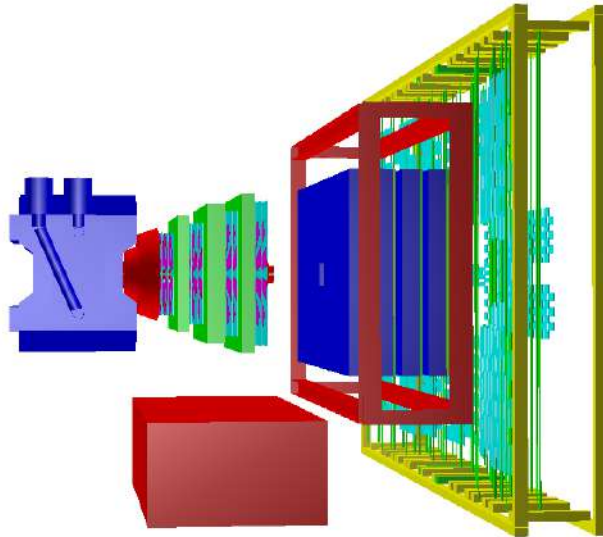


Figure 3.9: The sketch diagram of SIS100-B muon setup which consists of four stations and four absorbers along with TRD and TOF detectors.

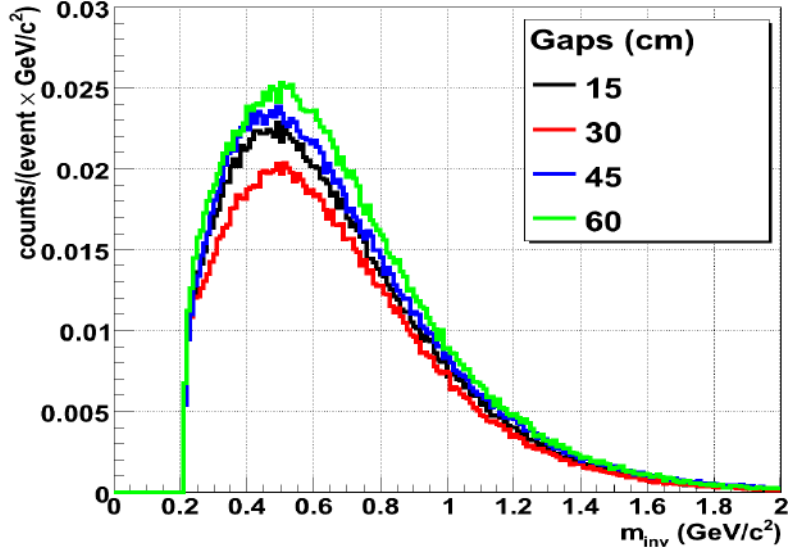


Figure 3.10: Invariant mass distribution of reconstructed background tracks for different gaps of 15 cm, 30 cm, 45 cm and 60 cm in between absorbers.

stations and four absorbers in MuCh along with TRD and TOF detectors. First absorber is of 60 cm Carbon and rest absorbers are made of iron with 20 cm, 20 cm and 30 cm in thickness. The detector stations are placed in between the absorber segments and each tracking station has three layers of tracking chambers to allow for effective tracking. The stations are located within a gap of 30 cm in between the absorber segments. To reduce the contribution of combinatorial background from weak decays, the muon setup should be as compact as possible. Also the increased gaps in between absorbers will increase the total size of MuCh. So optimization has been performed from simulation as shown in Fig. 3.10. This plot shows the invariant mass distribution of the combinatorial background for different gaps 15 cm, 30 cm, 45 cm and 60 cm in between the absorbers. It shows that background is maximum for 60 cm and minimum for 30 cm. The background increases with increasing gaps in between absorbers because the combinatorial background increases due to increased fraction of meson decays. On the other hand for very small gaps the background increases due to secondary electrons that originate from absorbers and reach the detectors due to short distance. In this comparison 30 cm has been selected as an optimized gap. Also a minimum gap of 30 cm is required to accommodate the cooling arrangements, mechanical structure and service works. Also gap of 10 cm is ensured in between the center of each detector layers for the electronics and cooling arrangements etc.

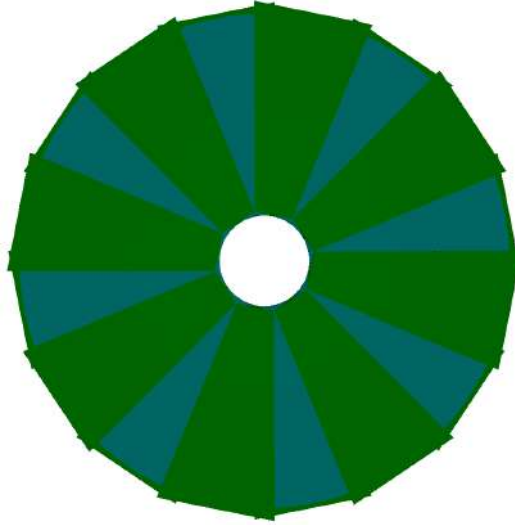


Figure 3.11: The detector layers are of circular profile. The total active area in a layer is divided in trapezoidal sector shape modules with overlapping with each other to avoid dead region.

The MuCh stations' angular coverage is from 5.7° to 25° . In the first and second station Gas Electron Multiplier (GEM) detectors will be used, whereas Resistive Plate Chamber (RPC) detectors are proposed for usage at the third and fourth stations. The detector layers are of circular profile. The total active area in a layer is divided in trapezoidal sector shape modules as shown in Fig. 3.11. The modules are arranged on a support structure with half modules in front and half in the rear side of the support structure. The modules are arranged in a staggered manner with a radial overlap in between the modules to avoid the dead region in the detectors. The number of sectors in a detector layer depends on the outer radius of the layer. Due to the lack of big size GEM modules, the trapezoidal sector shape design which is also utilised in other experiments like CMS, has been chosen.

The optimization has also been performed in selecting suitable pad size or granularity in the MuCh detectors. Projective pad segmentation has been taken into consideration for MuCh in order to account for the variation in MC point density profile with the radius from the beam pipe. The MC point density is the Monte Carlo point density which is basically the point of energy deposition by the charged particles inside the detector active volume. In Fig. 3.12 the density profile of Monte Carlo points has been shown for different stations in MuCh detector [79] for 4 stations and 4 absorber configurations. It can be noted that MC point density

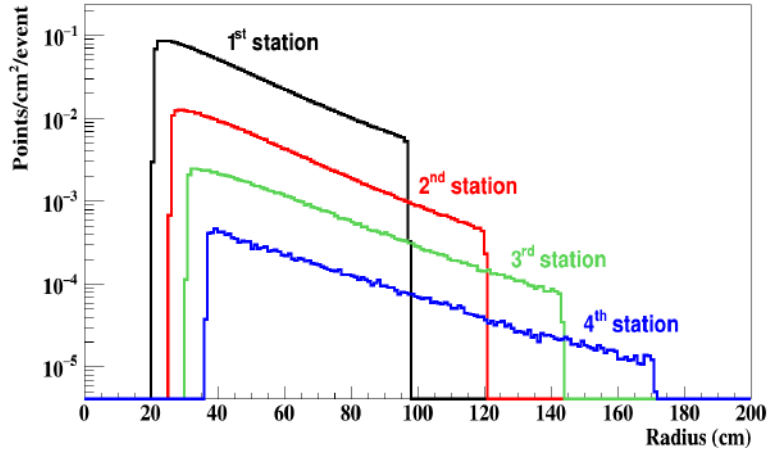


Figure 3.12: The MC point density (points/cm²/event) distribution of different stations in MuCh with radius from the beam pipe at 8 AGeV central Au+Au collisions [79].

is maximum at the inner radius zone and falls gradually with radial distance. Accordingly, in order to achieve segmentation, projective pads with radially increasing sizes are used as shown in Fig. 3.13.

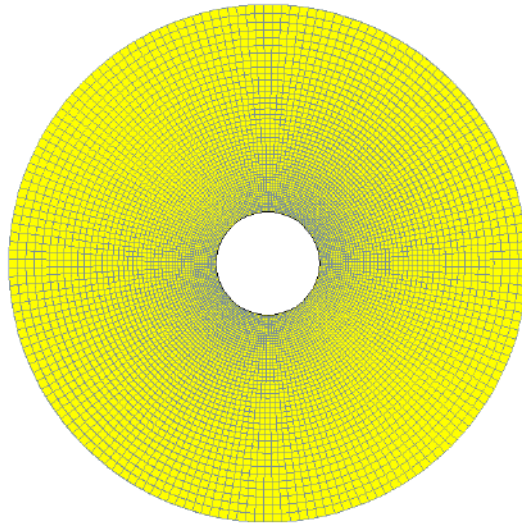


Figure 3.13: Schematic view of projective pad segmentation in MuCh detector layers.

Appropriate shapes and sizes of pads are required to obtain the desired pad occupancy within the acceptable limit ($< 5\%$). The angle of separation in the transverse plane governs the size of the pads. In the present segmentation scheme, the radial dimension of each pad is almost equal to the azimuthal dimension ($\Delta r = r\Delta\phi$) at a given radius,

Next comes the selection of suitable detector technology in MuCh detector stations. From Fig. 3.12 it can be seen that MC point density is maximum for first stations and it gradually decreases with increasing z distance from the target. GEM detectors have been chosen to operate due to the higher particle rate at the first and second stations. Whereas RPCs are proposed as a good detector choice for the third and fourth stations because of the decreased particle rate. All of the stations will contain detectors that use gaseous medium. This enables us to employ gas throughout as a sensitive medium. The detailed description for CBM-GEM chambers can be found in technical design report of MuCh [56].

So far, we have discussed the baseline geometry configuration of MuCh. In addition, the shape of the muon chamber absorbers, the MuCh beam pipe and shielding, the size of the second station, and the selection of the appropriate detector technology for the third and fourth station have all undergone some modifications and optimizations.

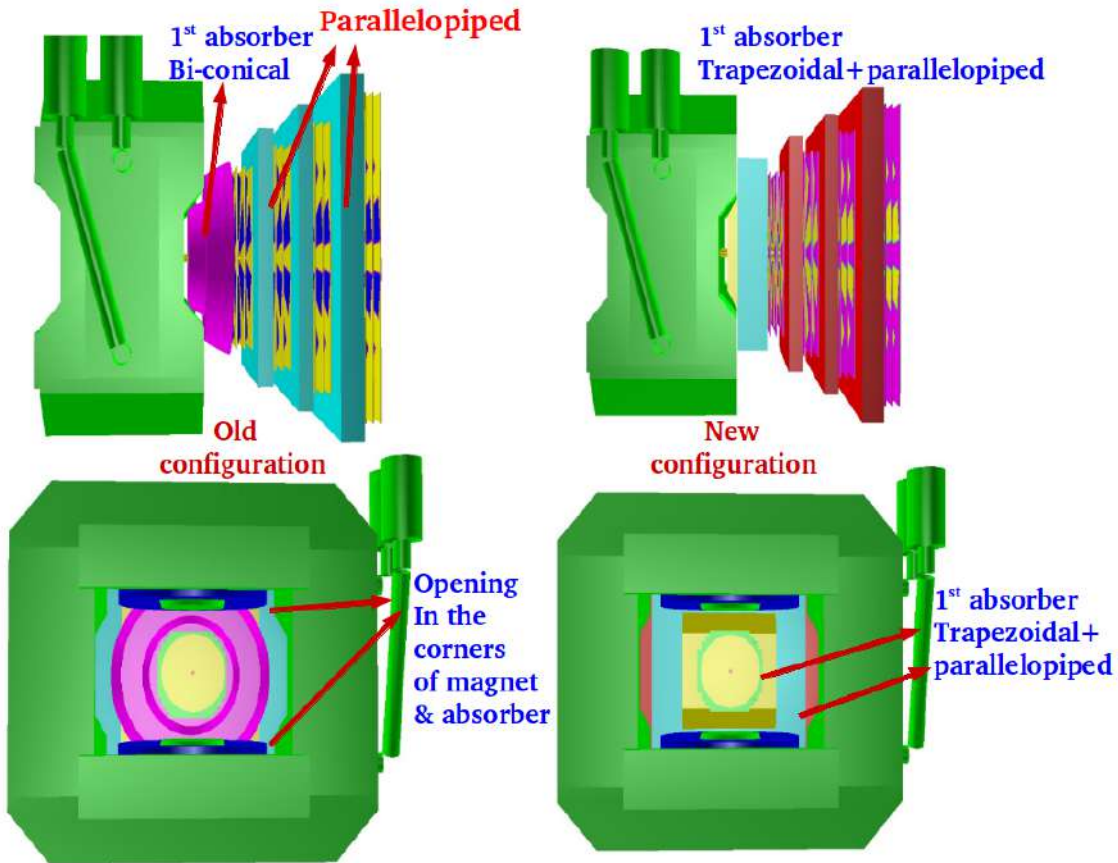


Figure 3.14: Modification of first absorber shape from biconical (left) to trapezoidal + parallelepiped (right). Rest all absorbers are made of parallelepiped shape.

To accept the forward focused particles from the collision in this fixed target experiment, MuCh absorbers were first configured in conical shapes. However, it was later realized that parallelepiped-shaped absorbers are simpler to manufacture than conical ones due to their simplicity of machining and construction [80]. First absorber design is special because it has a section inside the magnet and the other section outside magnet. In the initial configuration it was biconical but then it was transformed to trapezoidal inside the magnet portion and parallelepiped outside the magnet as shown in Fig. 3.14. This special design of first absorber was done because it was observed that due to its biconical shape there was some gap in between magnet opening (which was square) and the conical absorber and that was creating large neutron dose in the first station. With these absorbers shape modification we can see that there is a reduction in MC point density in the outer radius of first station as shown in Fig. 3.15 which was as expected.

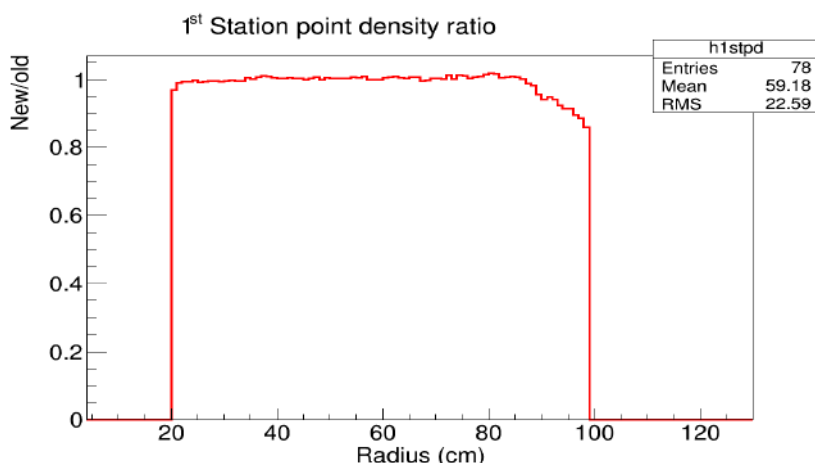


Figure 3.15: Ratio of the point density in first station of modified trapezoidal + parallelepiped shape of the first absorber to that of the biconical absorber.

For detector stations, design of the GEM modules for first station has already been finalized and it is ready for large scale production. But for the second station GEM detector size optimization has been performed because there was a limitation of the local industry in the production of readout PCB for the second station larger than 90 cm. So an investigation has been done to study the performance of the reduced size of the second station [81]. The original length of second station is ~ 97 cm, so performance checks were done with the 90 cm and with 80 cm because this is the length of the first station which has already been finalized. With

these investigations it is found from the Fig. 3.16 that in the point density distribution, it is losing a large number of particles. As a result, the detector is becoming less effective in reconstructing muon pairs from LMVMs. Therefore, the 97 cm length of the second station was found to be the final option [81]. The final readout PCB design is completed by joining two readout PCBs for the second station due to a restriction on readout PCB sizes bigger than 90 cm in the local industry.

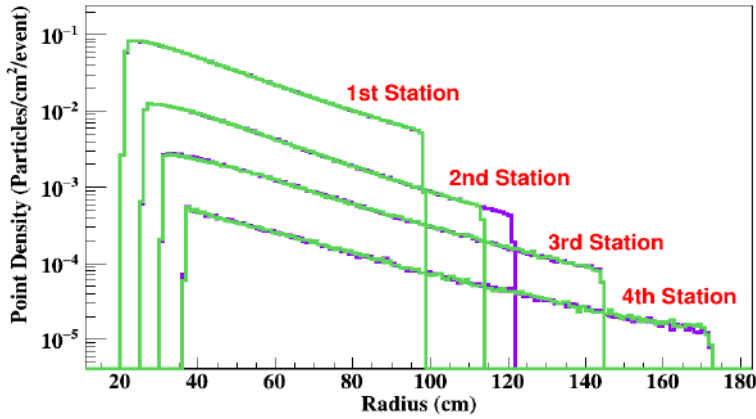


Figure 3.16: MC point density distribution of the detector stations with the reduced size of second station (green colour) compared with default size of second station (purple colour).

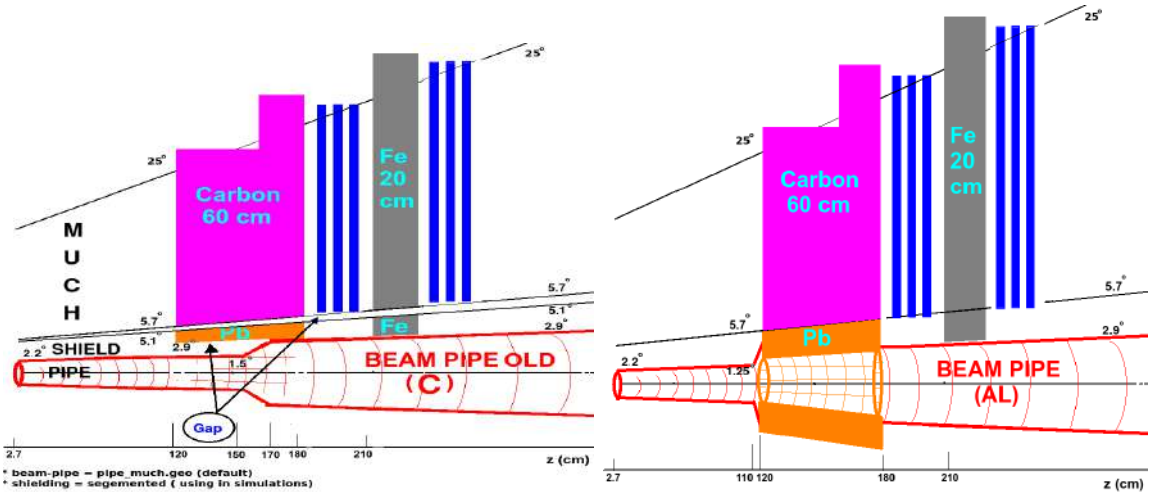


Figure 3.17: Initial configuration of beampipe and shielding where gaps were present (left) and modified shielding and beampipe with the gaps filled with shielding material (right) [82, 83].

Another change was made to the beam pipe and shielding in the CBM setup's MuCh section [82, 83]. To capture the secondaries coming from the beam particles, shielding is placed

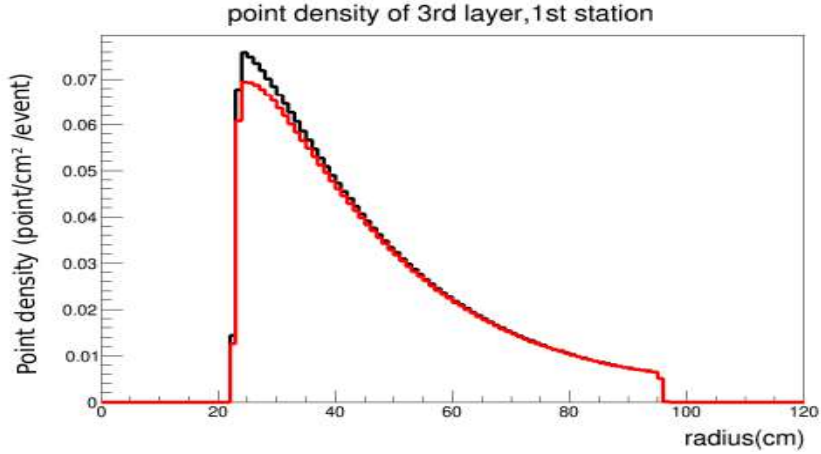


Figure 3.18: Reduction of point density in first station by $\sim 10\%$ with the filled up shielding materials as shown in the red color, whereas black color is the point density for the default initial configuration of beampipe and shielding [82].

between the beampipe and the MuCh-absorber. In the initial configuration of the shielding, there was a gap in between the shielding and the absorber material as shown in Fig. 3.17. As a result, the inner zone of detector region is facing a high particle rate specially in the first station. Due to this, shielding materials were used to cover these gaps. For the first absorber, Pb material is used as shielding component to absorb more secondaries, whereas for rest of the absorbers Fe is used as shielding material. As a result, the inner zone of the first station is now experiencing a lower particle rate due to these modifications, as illustrated in Fig. 3.18. Next we move to the topic of implementation of RPC geometry and digitization in the third and fourth MuCh stations.

3.3.2 Implementation of RPC geometry & digitization in MuCh

In this section, a detailed description of the implementation of Resistive Plate Chamber (RPC) geometry, its readout pad segmentation and digitization process as implemented in software for 3rd and 4th CBM-MUCH station have been discussed [79].

As MUCH will be constructed in phases in accordance with the energy range of the beam. In the first phase, SIS100B MUCH setup will be operated with 4 stations and 4 absorbers configuration. This SIS100B setup will be used up to beam energy 12 AGeV. In the first two stations GEM will be used as active detector technology. However, because the particle rate is low at the third and fourth stations, an inexpensive option could be chosen. There has been

a search for less expensive solutions, such as RPC detectors, and these appear to be capable of handling the expected rates of a few tens of KHz/cm². RPCs could be an optimal choice because at 3rd and 4th station particle rate is lower, RPCs are cost effective, they are simple to construct in large sizes and their capability of handling moderate rates made them an optimal choice in many previous heavy-ion collision experiments (RHIC/LHC experiments). However, investigation into the practicality of their application is currently ongoing. Hardware activities and R&D is on-going to characterize the performance of RPCs and establish it's feasibility of usage in CBM. In the software part, we have also implemented RPCs in the 3rd and 4th station and studied its performance. In this section we discuss our software implementation of RPC geometry, readout pad segmentation and digitization process in the CBMROOT software which is specifically created for CBM, in FAIRsoft and FAIRROOT environment. The simulation was performed with GEANT3 transport engine with UrQMD as the particle event generator and for signal muon generation decaying from omega low mass vector meson we have used PLUTO event generator.

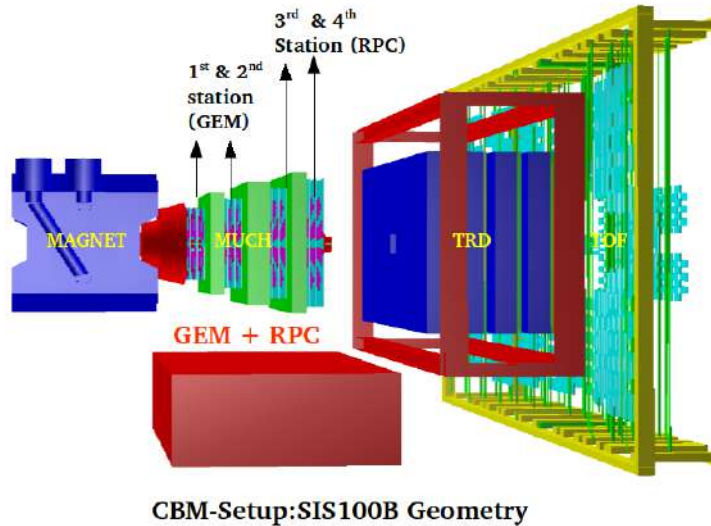


Figure 3.19: Schematic layout of the MuCh geometry with two GEM detectors in first and second station and two RPC detectors in third and fourth station in SIS100B geometry along with TRD and TOF detectors.

Implementation of the RPC Geometry

Sector-shaped GEM detector modules with 3 mm Argon gas as the active medium for the primary ionisation are employed in simulation in the first and second MUCH-stations. Similarly for 3rd & 4th station, we have taken into consideration sector-shaped modules for RPC that may be employed in a modularized framework and are likewise simple to construct. The modules are arranged in a staggered manner on both sides of the support structure. Here, a cooling plate is employed as a support structure. Each RPC module consists of 2 mm RPC gas (TetraFluorethan (C₂H₂F₄) 85%, Sulfurhexafluoride (gas composition: SF₆) 10% & 5% Isobutane (C₄H₁₀) sandwiched between 2 mm RPC glass as shown in Fig. 3.20. 3rd & 4th station each has three detector layers and the detector layers are of circular profile. They have circular profiles because of the staggered placement of the trapezoidal modules. There are 18 modules in the 3rd station each of length 116 cm & 20 modules in the 4th station each length 138 cm.

RPC readout pad segmentation

MUCH detectors cover an angular acceptance region from 5.7° to 25°. Projective pad geometry with angular segmentation in transverse plane has been implemented for both GEM and RPC modules. The size of the pads is determined by the angle of separation in the transverse plane. The radial dimension of each pad in the current segmentation approach is almost equivalent to the azimuthal dimension ($\Delta r = r\Delta\phi$) at a given radius. For the GEM modules the azimuthal segmentation angle is set to 1° due to the high particle density at the first and second stations, that requires high granularity in GEM detectors. For the 3rd & 4th stations, as the track-density is rather low, we implement azimuthal pad segmentation of 5° & 6° respectively, as shown in Fig. 3.21.

Pads have projectively increasing dimensions, the smallest one being close to the beam pipe and the biggest one towards the outer edges of the module. The smallest pad dimension for the 3rd station is 2.58 cm & for the 4th station is 3.728 cm and largest pad dimension 11.63 cm and 16.61 cm taking this 5° and 6° segmentation. One module width covers an angle of 20° for the third station and 18° for the fourth station. However the segmentation angle optimization

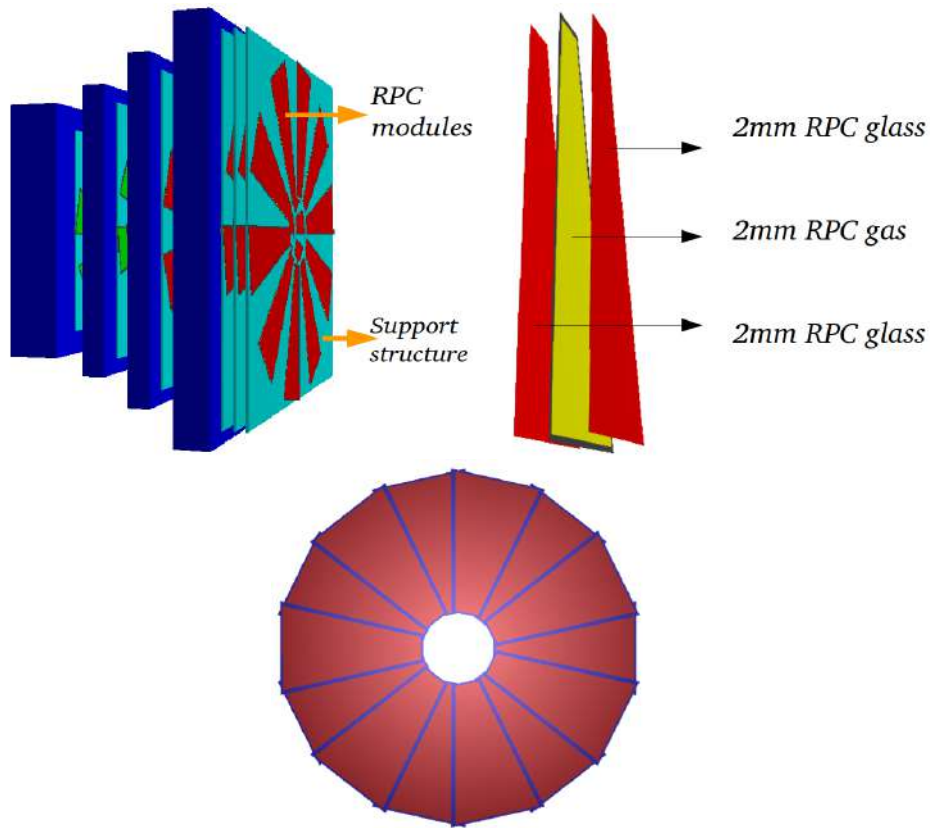


Figure 3.20: Arrangement of modules in staggered manner on both sides of a support structure (top left). Single RPC module structure (top right) and total modules making circular detector profile (bottom).

for RPC is still ongoing and some study on different segmentation angles have been discussed later.

RPC detector digitization

In digitization we implement the detailed response of the detectors inside the active medium. Here the gaseous detector response have been implemented for RPC. The readout planes of the RPC modules are segmented in pads which represents the units for collection of signals. Digitization is a process of allocating the MuCh Monte Carlo (MC) points to the pads. The locations of energy deposition along with the magnitudes of the deposited energy inside the active volume of the detector are known as MC points. This energy deposition is provided by GEANT3 which takes into account the interaction of the charged particles with the active material of the detectors.

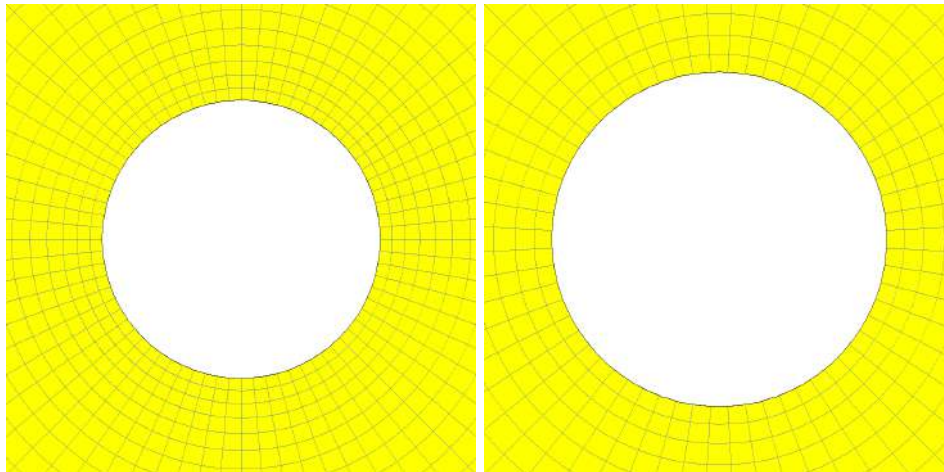


Figure 3.21: 5° (left fig) & 6° (right fig) azimuthal segmentation in station 3 & station 4 respectively.

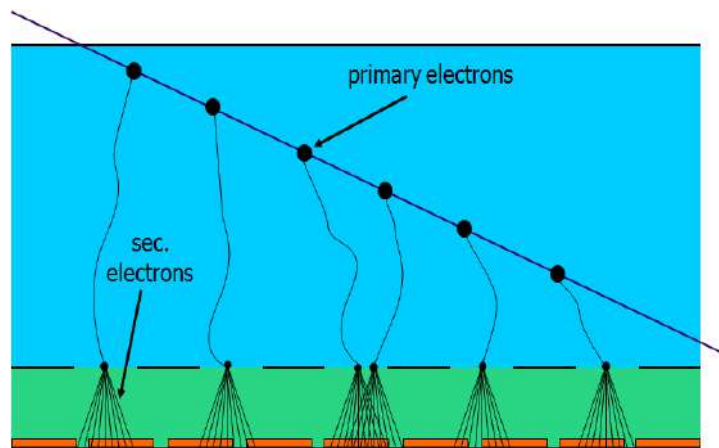


Figure 3.22: Schematic representation of generation of the primary electrons inside RPC gas volume along the track.

The generation of primary electrons inside the active gas medium in the RPC module is schematically shown in the Fig. 3.22. Based on the Landau distribution, the number of primary electrons released inside the drift volume for each Monte-Carlo point is calculated for the RPC gas and its track length inside the drift volume. Along the track, primary electrons are created randomly. Parameters for Landau distribution are chosen based on the experimental measurements as shown in Fig. 3.23.

Secondary electrons are generated from the primary electrons depending on the gas gain in the detector. An exponential gas gain distribution with a mean gain of 3×10^4 is used for RPC to determine the number of secondary electrons released in the avalanche region per primary

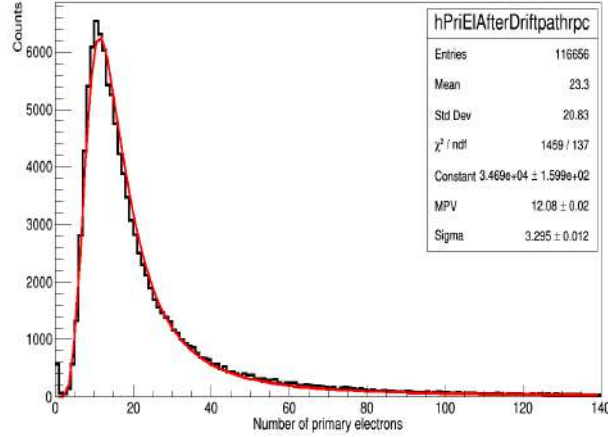


Figure 3.23: Number of primary electrons distribution within RPC drift volume.

electron. The spot size or spot radius is defined as the transverse diffusion of the avalanche size. The spot radius is chosen to closely match to the experimental data. Spot radius for RPC is taken 2 mm. The charge collected by each pad is converted into ADC channels. The amount of charge collected in a pad is limited by a maximum and a minimum value of ADC with the following relation :

$$ADC = \frac{(Q_{charge} - Q_{th})}{(Q_{max} - Q_{th})} \cdot nADC \quad (3.3)$$

where Q_{charge} stands for signal charge, Q_{max} is the maximum charge that a pad may build up, Q_{th} stands for charge threshold, and $nADC$ represents the number of ADC channels for each pad. The difference in maximum and minimum values of charge collected in a pad defines the dynamic range for the readout ASIC (Application Specific Integrated Circuit). If for a particular pad the accumulated charge goes beyond the maximum limit then that ADC gets saturated, and if the charge deposited does not cross the minimum charge threshold limit then that charge deposition will not be considered as a digi and thus gets rejected. The minimum charge threshold is set in such a way that it is above the expected noise level. According to the hardware input, the charge threshold for RPC is set at 30 fC. However the detector parameters are tunable and could take values depending on the exact detector technology. ADC used is a 5 bit ADC with 32 channels for both GEM and RPC. Here in table 3.3 different digitization parameters for RPC and GEM are listed.

Table 3.3: Digitization parameters for GEM and RPC.

	GEM	RPC
ADC	5 bit	5 bit
Gain	5000	3×10^4
Spot Radius	$500 \mu\text{m}$	2 mm
Charge threshold	2 fC	30 fC
Maximum Charge	80 fC	130 fC
MPV for Landau dist. for primary electrons	from HEED	12

RPC Hit reconstruction

Hit reconstruction is done after digitization. The digis are clustered during hit reconstruction using the appropriate clustering method. According to the particle multiplicity, the clusters are then separated into tiny subgroups, or let's call hits. The position of the hit or cluster point is thought to be the centroid of the sub-clusters. The following steps of reconstruction then treat these hits for tracking.

Performance of MuCh with 2-RPC stations in 3rd and 4th stations & comparison with a configuration of GEM in all stations

With the RPC geometry and the digitization parameters described above, we have simulated the performance of MUCH. This simulation is done with SIS100B (4 stations + 4 absorbers) geometry at 8 AGeV central Au+Au collisions using UrQMD and PLUTO embedded events. The primary electron distribution from each MC point, within RPC detector drift volume has been shown in Fig. 3.23 which shows MPV ~ 12 (number of electrons) and sigma ~ 3.2 (number of electrons). The event averaged charge distributions in station 3 and station 4 is shown in Fig. 3.24 which shows the MPV values of the Landau distribution ~ 50 fC ($1.6 \text{ fC} \equiv 10000$ no. of electrons), which is within the dynamic range of the RPC electronics.

Next we have studied the performance of MuCh for implementation of RPC geometry and digitization and compared it with that of GEM, i.e if GEM would have been used at the third and the fourth stations as well. The MC point density for the third and fourth stations have been studied for performance of RPC and compared it with GEM as shown in Fig. 3.25 and Fig. 3.26 respectively. The figures show that the that point density for both the primary and secondary particles for RPCs decreases compared to that at the GEM chambers and a ratio of

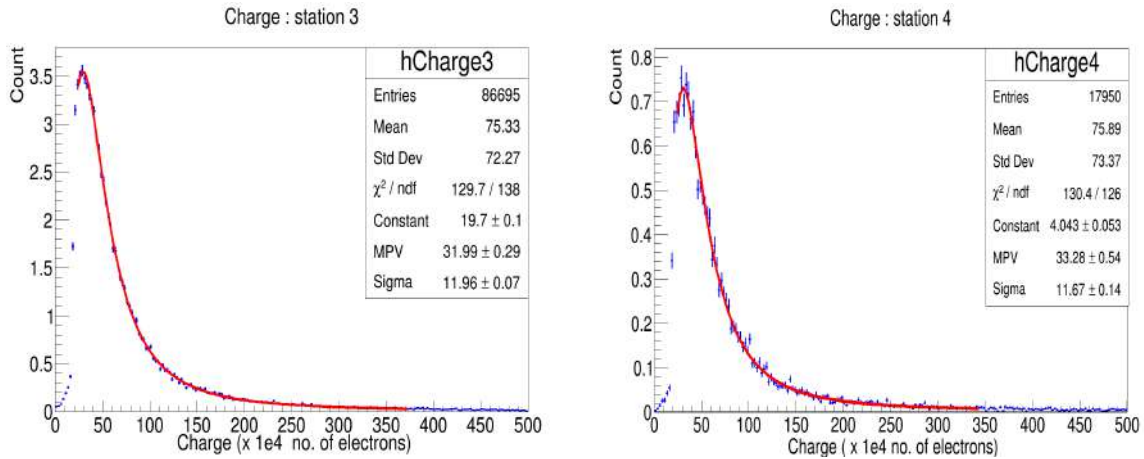


Figure 3.24: The event averaged charge distribution in station 3 (left) and station 4 (right) at 8 AGeV central Au+Au collisions.

MC point density for RPC to that for the GEM have been plotted. The ratio is less than 1, as the gas compositions are different in RPC and GEM. In RPC we have implemented 2 mm RPC gas with TetraFluorethan ($\text{C}_2\text{H}_2\text{F}_4$) 85%, Sulfurhexafluoride (gas composition: SF_6) 10% & 5% Isobutane (C_4H_{10} , whereas GEM has Argon with 3 mm gas gap.

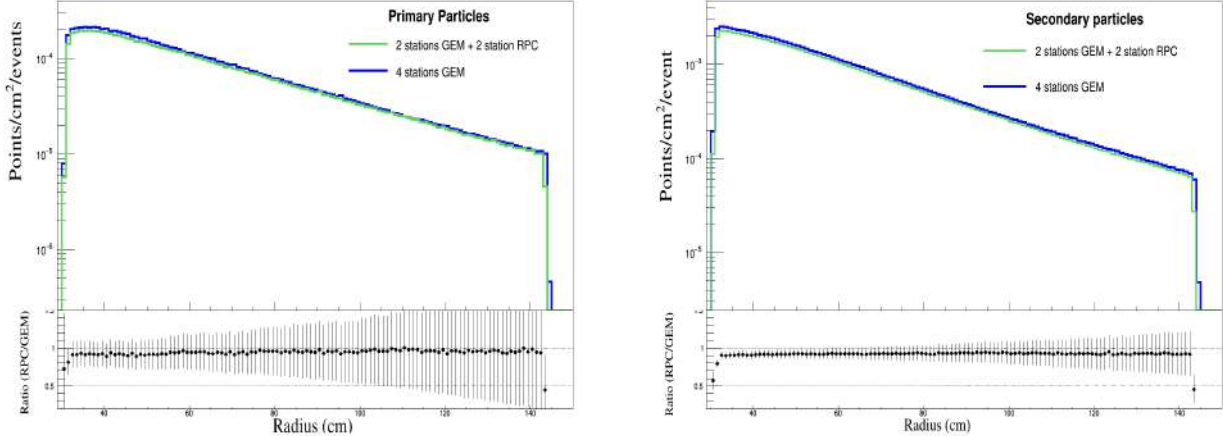


Figure 3.25: The point density distributions for primary (left) and secondary particles (right) has been shown for 2 GEM + 2 RPC configuration and all 4 GEM configurations in the third station.

For the third and fourth stations as shown in Fig. 3.27 there is a significant reduction in hit density compared to earlier GEM case. This is due to the new RPC digitization parameters. The charge threshold for RPC is set 30 fC which is much higher and is playing a dominant role in cutting the signals. There are other effects also due to other digitization parameters

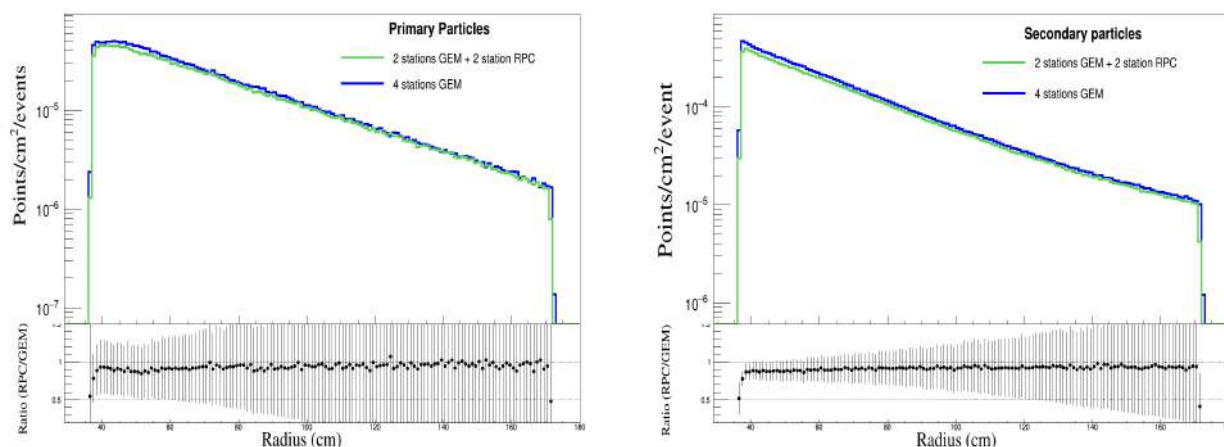


Figure 3.26: The point density distribution for primary (left) and secondary particles (right) has been shown for 2GEM + 2 RPC configuration and all 4 GEM configurations in the fourth station.

like spot radius, detector gain, gas volume etc. MC points per cluster, digis per cluster and hits per cluster information for RPC are shown in Fig. 3.28.

With these digitization parameters of RPC, we have studied the final dimuon ω pair reconstruction efficiency and S/B at 8 AGeV central Au+Au collisions. The invariant mass distribution of signal ω embedded with background is shown in Fig. 3.29 for two different geometries. We can see that the invariant mass yield in case of RPC is lower compared to that for GEM detectors. This is due to the effect of digitization parameters for RPC, with the dominant role of charge threshold parameter for RPC which is set 30 fC. This higher charge threshold is responsible for rejecting more signals which in turn causes the lowering of the efficiency of the signal dimuons. Also the readout pad segmentation angle for RPC is taken 5° and 6° in third and fourth stations, whereas in case of GEM the segmentation angle is 1° , which is also a reason for low efficiency in RPC because the smaller segmentation angle in readout electronics increases the granularity of detectors, which in turn increases the efficiency with the power of separating nearby tracks. This is why we get less efficiency in case of 2 GEM and 2 RPC geometry compared to the 4 GEM geometry. The S/B is nearly same for 2 cases. The comparison in efficiency and S/B is shown in Table 3.4.

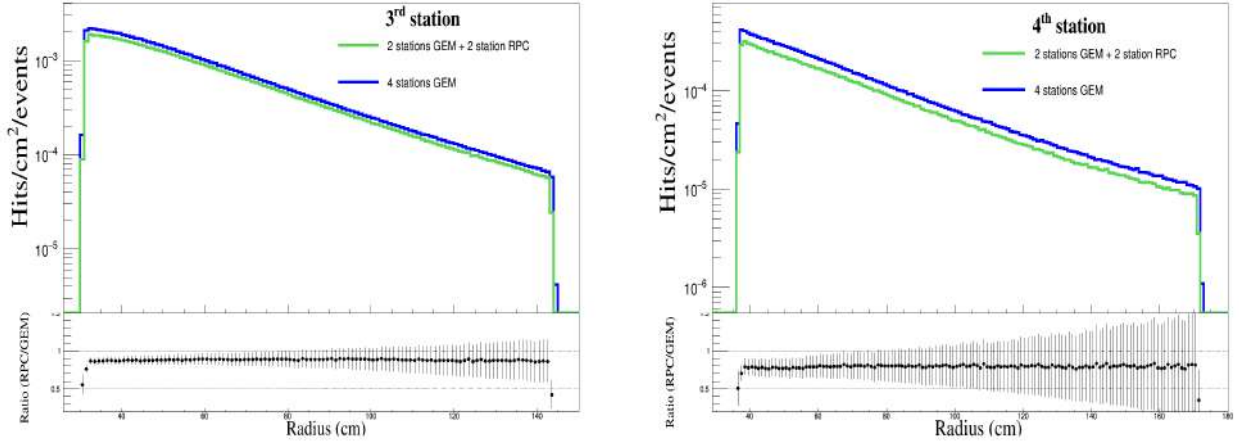


Figure 3.27: The hit density distribution for 2GEM + 2 RPC configuration and all 4 GEM configurations in third (left) and fourth station (right).

Table 3.4: Comparison of efficiency and S/B of signal ω for 2GEM and 2RPC and 4 GEM case geometry.

	4 stations GEM	2 GEM + 2RPC
Efficiency(%)	1.08	0.73
S/B	0.23	0.22

Study on different segmentation angles & charge threshold

We explored the possibilities of using finer detector segmentation angle also in RPC with 1° and 2° , because due to the fact that the largest pads size for 5° and 6° , are significantly larger, so the detectors may experience a problem with noise pickup due to higher capacitance in bigger pads. Additionally, we investigated how the charge-threshold parameter in RPC digitization affected overall MuCh performance [84].

Figure 3.30 shows the granularity of detector pads for different segmentation angles. With smaller azimuthal angle granularity increases. The details of segmentation has been mentioned in table-3.5.

Figure 3.31 shows the occupancy distribution in the 3^{rd} & 4^{th} station with different segmentation angles. Occupancy is the fraction of fired pads with respect to the total number of pads. This occupancy plot shows that with higher segmentation angle where pad size is bigger, occupancy is higher. Figure 3.32 shows the invariant mass distribution of dimuons for signal ω embedded in background for different segmentation angles of 1° , 2° and 5° (third station), 6°

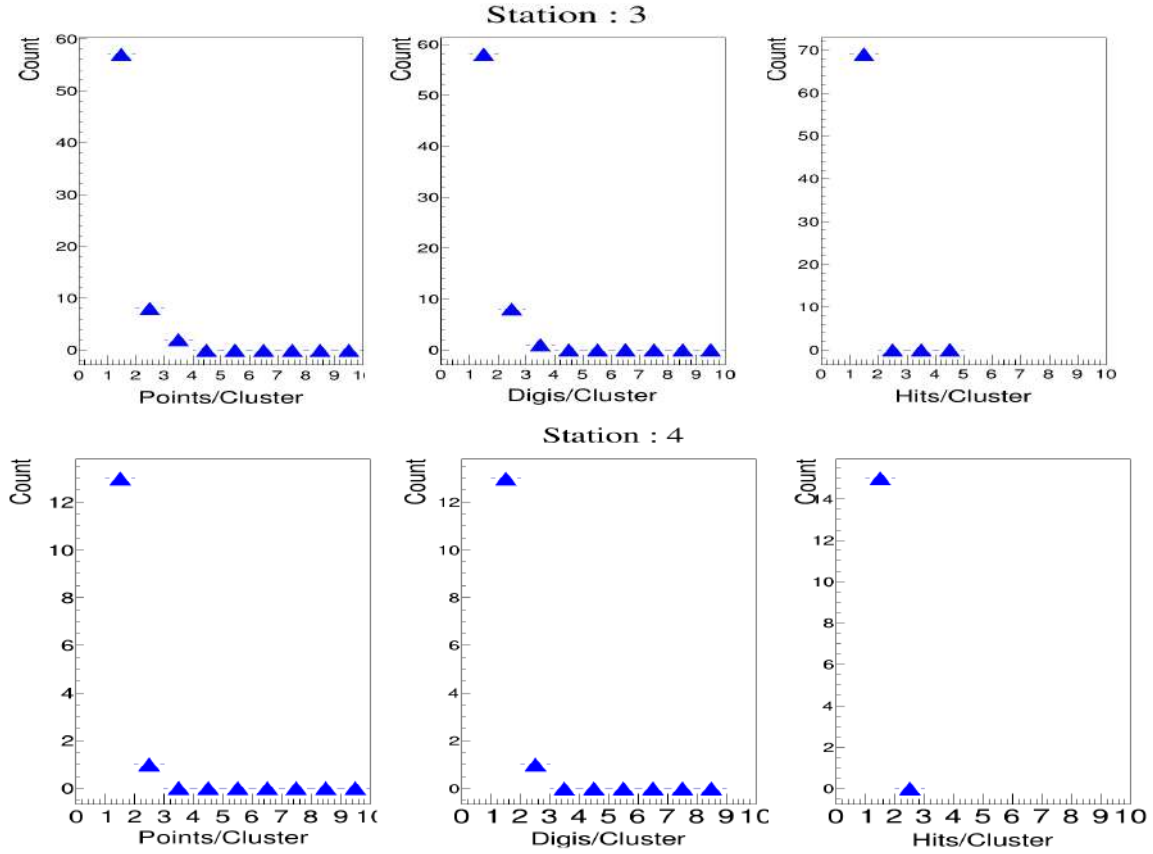


Figure 3.28: Points per cluster, digis per cluster and hits per cluster info for station 3 and 4.

(fourth station). We see for 1° segmentation invariant mass yield is maximum. This is because of the higher granularity of the detector pads, the probability of separation of nearby tracks increases. Table 3.6, shows the comparison of final efficiency and S/B of ω at 8 AGeV central Au+Au collision. We observed efficiency and S/B are slightly better for 2° segmentation and improves further for 1° . However 1° segmentation for readout pads increases production cost significantly. So possibility is to go with 2° segmentation.

Next we have studied the performance of MuCh for different charge threshold in digitization. In this digitization scheme we have studied how does the charge threshold parameter gets reflected in the formation of digis. At present 30 fC charge threshold has been used in simulation with the dynamic range 100 fC, i.e, maximum charge limit is 130 fC [56]. However, RPCs can be operated at 20 fC as well. So we have simulated the final performance of detector at 20 fC and also at 10 fC charge threshold for both 1° and 5° (third station), 6° (fourth station) segmentation. Figure 3.33 shows the dimuon invariant mass distributions of signal

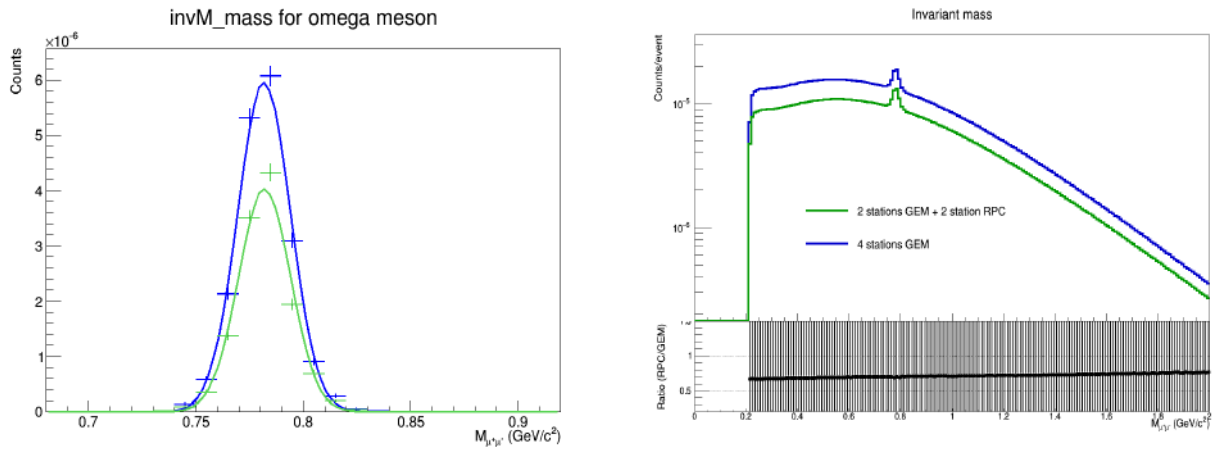


Figure 3.29: The invariant mass distribution of signal ω and background. Signal omega is embedded into the background events.

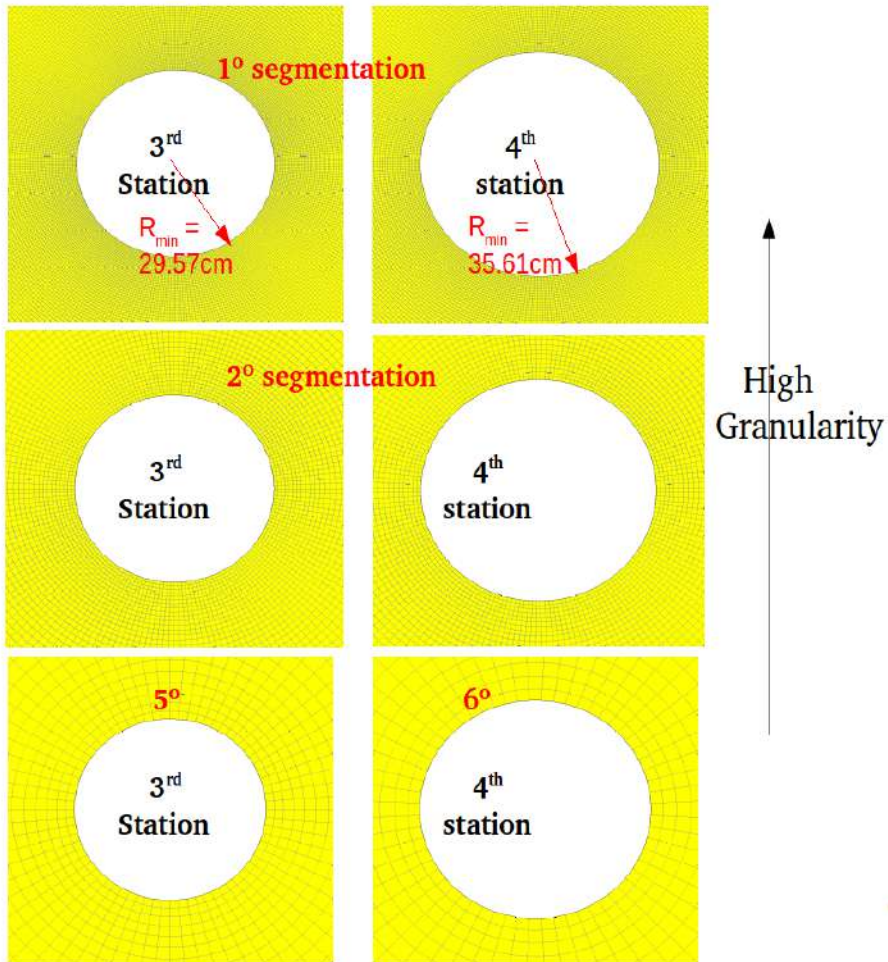
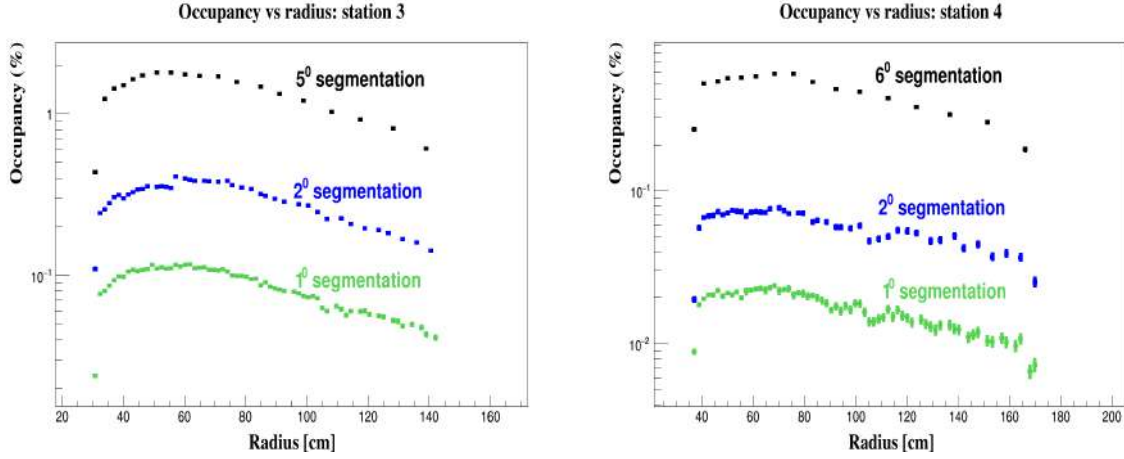


Figure 3.30: RPC detector segmentation with different azimuthal angle 1° , 2° in 3^{rd} and 4^{th} station and 5° in 3^{rd} and 6° in 4^{th} station.

Table 3.5: Details of different segmentation angles.

1° segmentation		
Station	3 rd station	4 th station
Sectors/layer	92	91
Smallest pad size (cm)	0.5161	0.6216
Largest Pad size (cm)	2.492	2.950
Modules/layer	18	20
Module angle	20°	18°
2° segmentation		
Station	3 rd station	4 th station
Sectors/layer	47	46
Smallest pad size (cm)	1.032	1.243
Largest Pad size (cm)	5.003	5.822
Modules/layer	18	20
Module angle	20°	18°
5° and 6° segmentation		
Station	3 rd station	4 th station
Sectors/layer	19	16
Smallest pad size (cm)	2.58	3.729
Largest Pad size (cm)	11.63	16.61
Modules/layer	18	20
Module angle	20°	18°


 Figure 3.31: Occupancy distribution for the 3rd & 4th station with different segmentation angles.

(ω) + background at different charge threshold values for 1° and 5° (third station), 6° (fourth station) segmentation. Table 3.7, shows the efficiency and S/B of ω for different cases and we observe efficiency is highest for 10 fC threshold conditions.

In the next section we will discuss performance of MuCh in detection of LMVM through

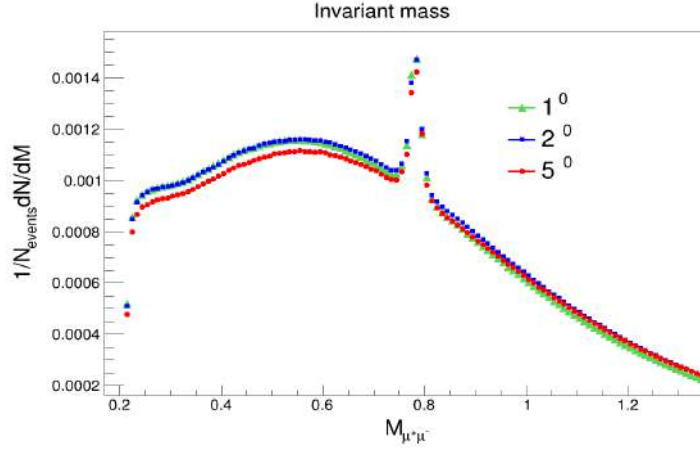


Figure 3.32: Invariant mass distribution of ω embedded in background at different segmentation angles for third and fourth stations.

Table 3.6: comparison of final efficiency and S/B of ω at 8 AGeV central Au+Au collision for different segmentation angles.

segmentation	ω pair reconstruction efficiency (%)	S/B
5° and 6°	0.83	0.24
2°	0.85	0.24
1°	0.90	0.26

Table 3.7: Efficiency and S/B of ω for different segmentation angles and different charge threshold values.

5° & 6° segmentation (3 rd & 4 th station)	ω pair reconstruction efficiency (%)	S/B
30 fC	0.83	0.243
20 fC	1.00	0.236
10 fC	1.05	0.233
1° segmentation (3 rd & 4 th station)	ω pair reconstruction efficiency (%)	S/B
30 fC	0.90	0.261
20 fC	1.10	0.261
10 fC	1.13	0.254

dimuon channel. Before proceeding to that it is to be noted that in latest updates there are some modification in MuCh geometry. In recent modifications the MuCh first absorber, which was formerly comprised entirely of graphite material, is now built of graphite (C) and concrete [65]. The portion which is inside the magnet is of carbon material of thickness 28 cm and the other portion is of concrete, which is outside the magnet of thickness 30 cm. In previous version with the MuCh detector setup, the first absorber was composed of high density ($\rho=2.26$ g/cc) pure carbon having a thickness of 60 cm. Subsequent studies for the mechanical design

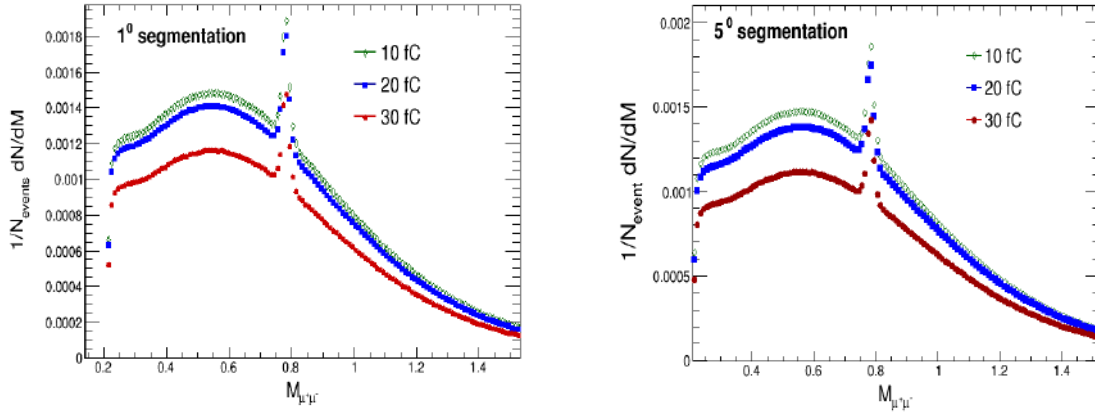


Figure 3.33: Invariant mass distribution of ω embedded in background at 1° and 5° segmentation for different charge threshold.

of the absorber blocks and a detailed market survey reports the unavailability of high-density pure carbon in bulk. Rather low density carbon of 1.7 g/cm^3 is available. On the other hand, concrete is chosen compared to other materials because of the mechanical and activation point of view [65]. So now as per the modified setup, the thickness of the first absorber is 58 cm with 28 cm of low density graphite and 30 cm of concrete. This would allow an extra 2 cm gap between the absorber and detector stations, which could be helpful for MuCh service works for the detector chambers. Additionally, in the most recent simulations, we utilised RPC geometry with 2° as the detector azimuthal segmentation angle in the third and fourth stations, together with 18 detector modules in each layer of the stations. With these modifications in MuCh geometry, we now proceed to the next simulations which describe the performance of MuCh detector for dimuon detection in CBM.

3.4 Performance of MuCh in detection of LMVM through dimuon channel

Here we will discuss the muon chamber performance for the SIS100B geometry (4 stations + 4 absorbers) in the energy range of 8 to 12 AGeV for the detection of dimuons resulting from the decay of low mass vector mesons. MuCh's segmented absorbers make it possible to detect both high and low momentum muons. After reconstruction of global tracks as discussed in the section

of simulation steps in MuCh (section 3.2), muon candidate tracks are selected. The selection method of muon candidate tracks will be discussed in the following section 3.4.2. Muons being weakly interacting pass the absorbers with least interactions. After collecting opposite sign muon candidates, its invariant mass distribution is obtained to get the information of mother particles.

Each muon track has its associated four-momentum vector as follows [78]:

$$P_\mu = (E_\mu, \vec{p}_\mu) \quad (3.4)$$

where $E_\mu = \sqrt{m_\mu^2 + \vec{p}_\mu^2}$.

The four momentum vector of muon pair or dimuon can be represented as the combination of four momentum of each muons and can be written as :

$$P_{\mu_1\mu_2} = P_{\mu_1} + P_{\mu_2} = (E_{\mu_1} + E_{\mu_2}, \vec{p}_{\mu_1} + \vec{p}_{\mu_2}) \quad (3.5)$$

From this we can calculate invariant mass formula as

$$m_{inv}^2 = P_{\mu_1\mu_2}^2 = 2m_\mu^2 + 2(E_{\mu_1}E_{\mu_2} - \vec{p}_{\mu_1} \cdot \vec{p}_{\mu_1}) \quad (3.6)$$

Here $m_\mu = 105$ MeV, which is the rest mass of muon. This invariant mass is invariant under Lorentz transformation. Some other fundamental variables are muon pair p_T or rapidity (Y) and opening angle between the muon pair. This opening angle is the angle between p_{μ_1} and p_{μ_2} . Neglecting the muon mass in Eq. 3.6 we get,

$$m_{invm} \simeq \sqrt{2p_1p_2[1 - \cos\theta_1\cos\theta_2 - \sin\theta_1\sin\theta_2\cos(\phi_1 - \phi_2)]} \quad (3.7)$$

Where p_i , θ_i and ϕ_i are the magnitude of 3-momentum, polar and azimuthal angle of the single muon tracks. From four momentum conservation, pair p_T can be written as

$$p_{T,\mu_1\mu_2} = \sqrt{p_{x,\mu_1,\mu_2}^2 + p_{y,\mu_1,\mu_2}^2} \quad (3.8)$$

where,

$$p_{i,\mu_1\mu_2} = p_{i,\mu_1} + p_{i,\mu_2}; (i = x, y, z) \quad (3.9)$$

The pair rapidity in the laboratory frame is

$$Y_L = \frac{1}{2} \log\left(\frac{E + p_z}{E - p_z}\right) \quad (3.10)$$

Where E and p_z are the pair energy and longitudinal momentum in the laboratory frame. The pair rapidity in the centre of mass frame of the collision (Y^*) is obtained using the following relation

$$Y_L = Y^* + Y_{CM} \quad (3.11)$$

This Y_{CM} is the rapidity of the centre of mass system in the laboratory.

$$Y_{CM} = \frac{1}{2} \log\left(\frac{1 + \beta_c}{1 - \beta_c}\right) \quad (3.12)$$

where β_c is the velocity of the center of mass of the collision system in the laboratory and can be calculated as -

$$\beta_c = \frac{|\vec{P}_{lab}|}{E_{lab}} = \frac{P_{beam}^{\vec{}}}{E_{beam} + m_{target}} \quad (3.13)$$

Where P_{beam} and E_{beam} are projectile momentum and energy and m_{target} is the mass of the target.

Kinematics resolution

Three parameters, in general, control the kinematic resolutions of dimuon experiments.

- Multiple scattering of the tracks with the interaction target and the hadron absorbers
- The energy loss of the muons in the hadron absorber
- Proper error estimation and propagation in the measurement in the tracking chambers

An important feature in the CBM experiment is that the momentum measurement is carried out in the STS detector, which sits before the MuCh detector. Consequently, the multiple scattering in the hadron absorbers won't have an impact on the momentum measurement or say in momentum resolution of the particle. In addition, the target interaction length in CBM is very small $\sim 1\% \lambda_I$, which is significantly smaller than the interaction length in other experiments like the NA50 experiment, which ranges from 7 to 30 $\% \lambda_I$. Thus it helps to improve the momentum resolution. Here the momentum resolution will be considerably affected by the magnetic field from the dipole magnet. The momentum resolution depends on -

$$\frac{\Delta p}{p} \propto \frac{p}{BL^2} \quad (3.14)$$

where p is the momentum of the track and B and L is the magnetic field strength and length of the magnet. In CBM the momentum resolution $\frac{\Delta p}{p}$ of muon tracks are $\sim 1\%$. For dimuon resolution, from Eq. 3.6 neglecting the muon mass, we get

$$m_{inv}^2 = 2p_{\mu 1} p_{\mu 2} (1 - \cos(\theta_{\mu 1 \mu 2})) \quad (3.15)$$

Multiple scattering, which contributes to angular resolution ($\Delta\theta_{\mu 1 \mu 2}$), is more significant at low masses and has very less effect on high masses since the average momentum of the single muons increases with mass. If we neglect the angular resolution then one can estimate mass resolution from this,

$$\frac{\Delta m_{inv}}{m_{inv}} = \frac{\Delta p_{\mu}}{\sqrt{2} p_{\mu}} \quad (3.16)$$

which results 0.7 %.

3.4.1 Input event generators for signal generation

Using the CBMROOT software framework, the simulation for dimuon measurement is carried out. It simulates and reconstructs the whole event. In addition, we require event generators for the production of signal dimuons and background particles generator. PLUTO event generator is used for dimuon signal generation whereas UrQMD has been used to simulate the background

events which is discussed here briefly.

PLUTO

PLUTO uses thermal fireball model to generate dimuon spectra from low mass vector mesons. It generates the vector meson with thermal p_T and gaussian rapidity distributions in the centre of mass frame of the collisions and decays them isotropically in dimuons. The detailed description of PLUTO can be found in ref. [66]. It generates the p_T spectra of the signals according to the form :

$$\frac{dN}{m_T dm_T} = \frac{dN}{p_T dp_T} = m_T K_1\left(\frac{m_T}{T}\right) \quad (3.17)$$

where $m_T = \sqrt{m^2 + p_T^2}$, m_T is the transverse mass and m is the rest mass of the particles. K_1 is the Bessel function of second kind and first order in $\frac{m_T}{T}$

$$K_1 \frac{m_T}{T} = \frac{e^{-(m_T/T)}}{\sqrt{m_T/T}} P_6(T/m_T) \quad (3.18)$$

Where P_6 is the Polynomial of order 6 and the inverse slope parameter can be identified with freezeout temperature T_f . The rapidity distribution is generated using a Gaussian function of mean $\mu_y = 0$ and sigma σ_y at the centre of mass frame.

$$\frac{dN}{dy} = \exp\left(\frac{-y^2}{2\sigma_y^2}\right) \quad (3.19)$$

Where y is the rapidity of the vector meson in centre of mass. To generate the vector mesons it requires two inputs which are beam energy and temperature of the system. The input parameters for different beam energies are listed below-

Table 3.8: Input parameters for different beam energies and temperature in PLUTO.

System	$\sqrt{s_{NN}}$ (GeV)	Lab energy E_{lab} (AGeV)	Temperature (GeV)
Au+Au	2.9	3.42	0.09
Au+Au	4.1	8.0	0.12
Au+Au	4.9	12	0.13

UrQMD

UrQMD (Ultra-relativistic Quantum Molecular Dynamics) is a microscopic transport model that provides a unified framework to describe the phenomenology of particle production in pp, p+A and A+A collisions over a broad energy range. The underlying degrees of freedom in UrQMD are hadrons and strings. Here an individual particle propagates on a straight line until the relative distance between two particles is smaller than a critical distance given by the total interaction cross-section between two particles. These cross-sections in UrQMD are either calculated by the principle of detailed balance or additive quark model (AQM) [38] or parameterized from the available experimental data. For resonance excitations or decays the Breit-Wigner formalism is implemented. In UrQMD, the particle production dynamics is either governed by the decays of baryon or meson resonances or via a string excitation and fragmentation. Until now, UrQMD has 55 Baryons and 32 Mesons that also include ground state particles and all resonances with mass upto 2.25 GeV.

3.4.2 Muon identification selection cuts

Here we will discuss the reconstruction of ω meson decaying to dimuons at 12 AGeV central Au+Au collisions. These ω mesons are generated and decayed into dimuons by the PLUTO event generator and embedded into UrQMD events. Then these embedded events are transported through CBM setup using GEANT3. After reconstruction of tracks, we get reconstructed global tracks that includes the track segments from all the detectors. From these reconstructed global tracks, muon candidates are selected based on some criteria. The criteria are based on the length of the tracks that passes through the detector layers and the χ^2 of the fitted tracks at different detector segments like in STS or in MuCh. The selection criteria used for selecting muons from low mass vector mesons at 12 AGeV are :

- The track should have at least 7 hits of STS detectors.
- At least 11 hits from MuCh detector layers should be associated with the global track.
- The track should have $\chi_{STS}^2 < 2.0$
- The track should have $\chi_{MUCH}^2 < 2.5$

- χ_{Vertex}^2 of the track < 2.0 .
- Additionally, TOF mass cut is applied.

These χ^2 are normalized with number of degrees of freedom (NDF). The TOF mass cut helps to improve in rejection of background tracks in significant amount. Figure 3.34, shows the TOF mass m^2 vs momentum plot for signal muon candidate tracks from the ω and from background plus signal tracks. It can be seen that apart from the signal muons (left panel) there is a large amount of background contribution (right panel). So we need to reduce this background by fitting the TOF mass distribution with a parabola cut, which is shown below-

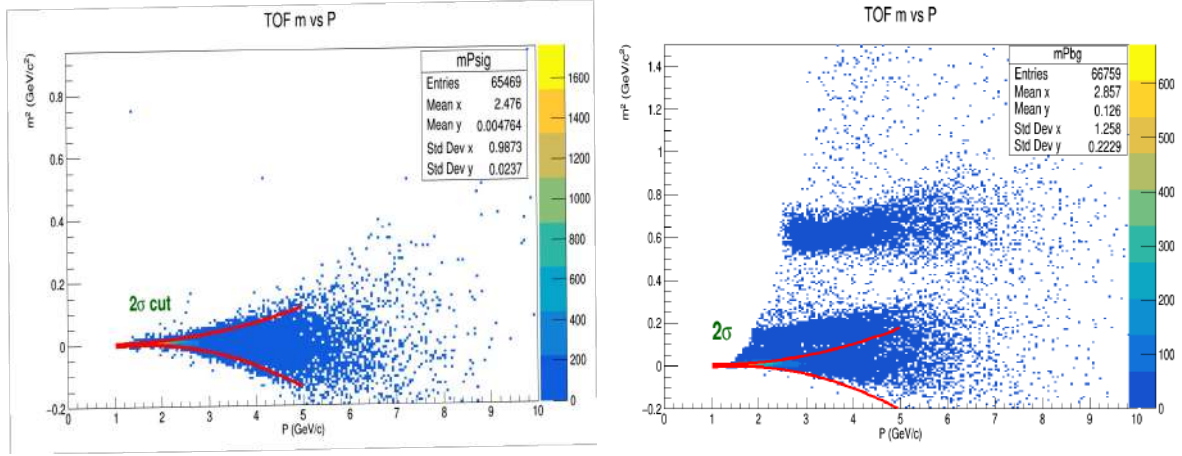


Figure 3.34: TOF m^2 vs momentum distribution of the reconstructed global tracks for signal muon candidates (left) from ω and right plot is background + signal tracks (right).

parabola fitting function

$$p0 + p1 * P + p2 * P^2 \quad (3.20)$$

Where P is the momentum and $p0$, $p1$, $p2$ are the parameters for fitting. A 2σ cut on the parabola fit is applied. So these are the major selection cuts for the muon candidate selection. After passing these selection cuts the tracks are accepted for dimuon invariant mass distribution.

3.4.3 Reconstruction of LMVM cocktails

After selection of muon candidate tracks, positive and negative charges are stored separately. The simulation is performed using the conventional event by event basis. For invariant mass

reconstruction of signal ω , opposite sign muon candidates four momentum are paired event by event from embedded PLUTO+UrQMD events. For background invariant mass reconstruction, opposite sign muon candidates four momentum are paired by Super Event technique taking tracks from different UrQMD events only. In the super event technique, a muon candidate track's four momentum is combined with all other oppositely charged muon candidate from all the events to construct an uncorrelated distribution of invariant mass for combinatorial background. For super event technique, only central events are selected where track multiplicity is nearly same for all the events. The advantage of super event technique is that it increases the statistics quadratically for reconstructed background pairs.

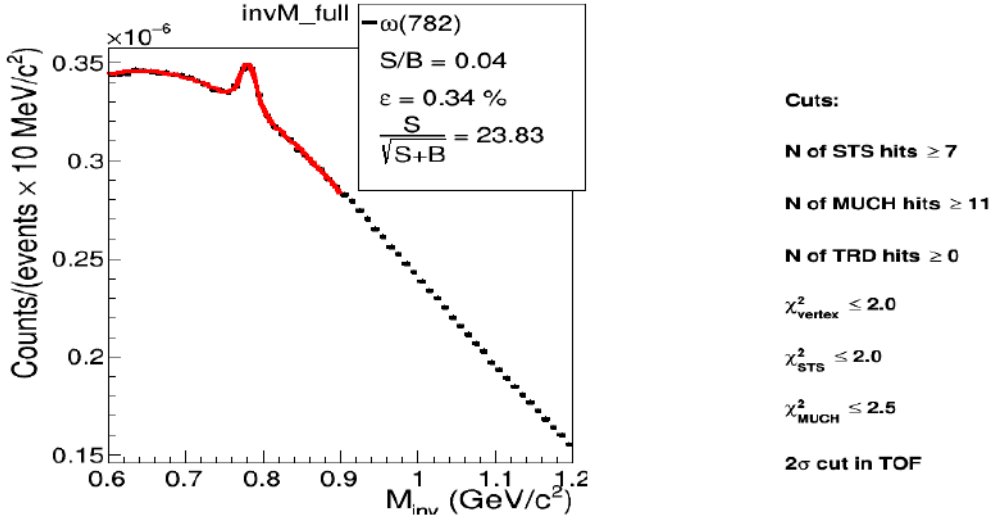


Figure 3.35: The invariant mass distribution of ω at 12 AGeV central Au+Au collisions. The total signal+background fitted with Gaussian (signal) + pol-2 (background).

To obtain the whole invariant mass distribution, the total signal and background are then combined. Then total signal + background are fitted with Gaussian (signal) + pol2 (background) as shown in Fig. 3.35. From the total fitting signal is extracted after subtracting the background in the $\pm 2\sigma$ region around the mean of the Gaussian distribution. The signal efficiency is determined by reconstructing the signal through embedded events. And the efficiency is defined as the ratio of number of reconstructed to the input ω . For signal to background ratio calculation, proper normalization of signal multiplicity and branching ratio for dimuon decay channels are taken into account along with the proper normalization of the background.

The dimuon reconstruction efficiency is directly related to the single muon detection effi-

ciency. Single muons are selected by satisfying all the criteria mentioned in section 3.4.2. If ϵ_μ is the efficiency for single muon tracks originated from ω , then efficiency for ω is the product of single muons efficiencies as written below-

$$\epsilon_\omega = \epsilon_{\mu^+} \times \epsilon_{\mu^-} \quad (3.21)$$

Use of a strict selection cuts like χ^2 or number of hits associated with the tracks for muon candidate selection decreases the muon pair reconstruction efficiency, whereas increases the signal to background ratio as the background is reduced. To ensure higher efficiency, a large data sample is collected, whereas S/B indicates the actual figure-of-merit of any measurement.

Next we have simulated the invariant mass distribution of the low mass vector meson cocktails which includes $\eta \rightarrow \mu^+ \mu^-$, $\eta \rightarrow \gamma \mu^+ \mu^-$, $\rho^0 \rightarrow \mu^+ \mu^-$ (vacuum), $\rho^0 \rightarrow \mu^+ \mu^-$, $\omega_D \rightarrow \pi^0 \mu^+ \mu^-$, $\omega \rightarrow \mu^+ \mu^-$, $\phi \rightarrow \mu^+ \mu^-$.

Their respective multiplicities are obtained from the recent calculations of Thermal-FIST (Thermal- Fast and Interactive Statistical Toolkit) model [85] and branching ratios from PDG log book [86].

The invariant mass distribution of the reconstructed cocktails along with the signal to background ratio has been shown in Fig. 3.36. Here, the S/B is derived by summing all the cocktails, which is referred to as the cocktail sum in the Fig. 3.36, and dividing it by the combinatorial background as determined by the superevent technique, which was discussed earlier. The multiplicity and branching ratios for the LMVM cocktails at 12 AGeV Au+Au collisions have been mentioned in the table 3.9.

Table 3.9: The multiplicity and branching ratios for the LMVM cocktails at 12 AGeV Au+Au collisions.

Particles	η	η'	ρ^0	ω	ω_D	ϕ
Multiplicity	14.87	0.80	19.03	5.82	5.82	1.018
Branching ratio	5.8e-6	1.09e-4	4.55e-5	7.4e-5	1.34e-4	2.86e-4

3.4.4 Phase space acceptance of dimuons

We have plotted the p_T and rapidity distribution of reconstructed ω meson at 12 AGeV central Au+Au collisions as shown in the Fig. 3.37. We can see that the rapidity is shifted in the

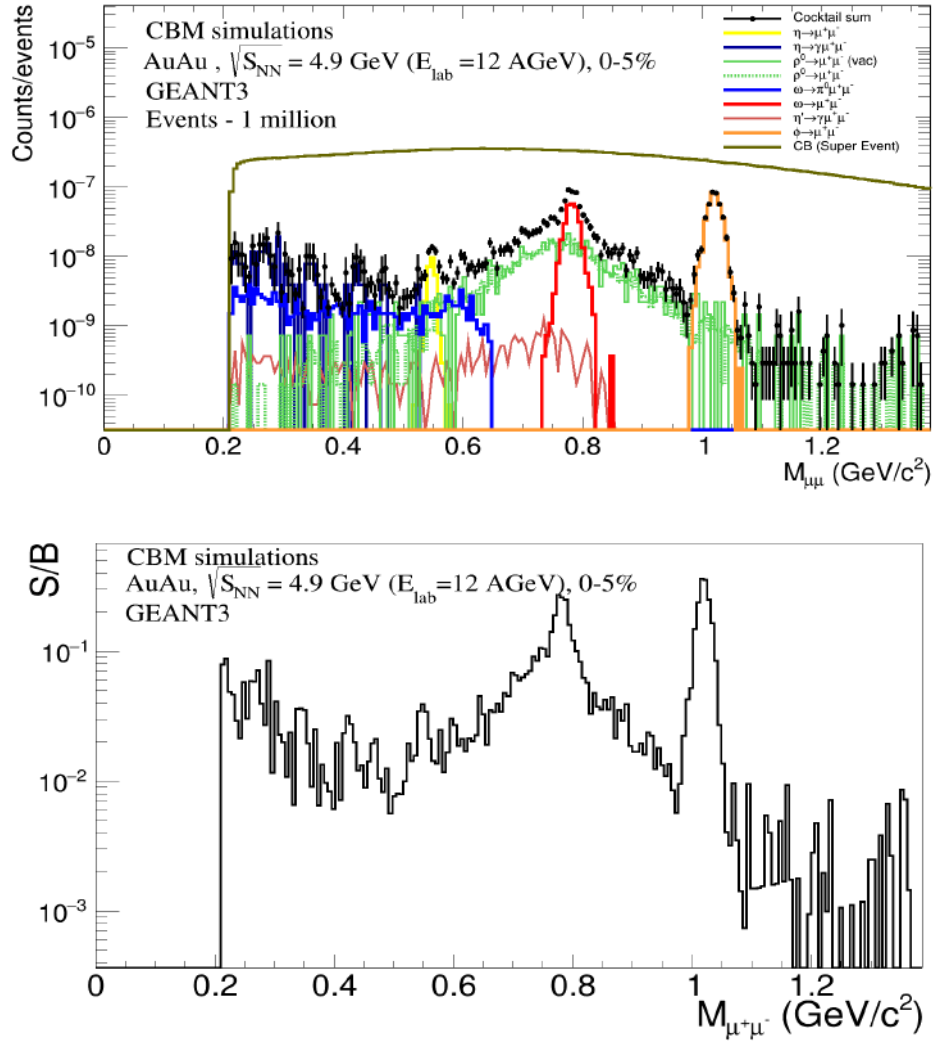


Figure 3.36: The invariant mass distribution of reconstructed cocktails along with the signal to background ratio at 12 AGeV central Au+Au collisions.

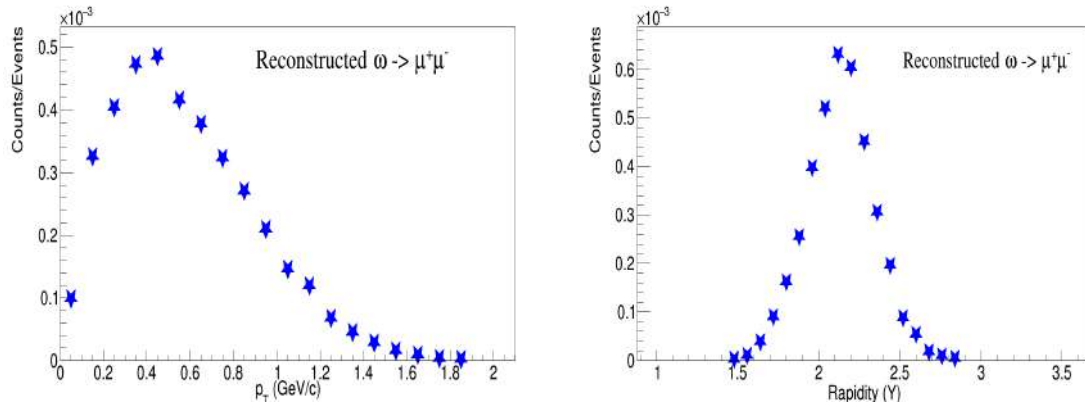


Figure 3.37: p_T and rapidity of reconstructed ω at 12 AGeV central Au+Au collisions.

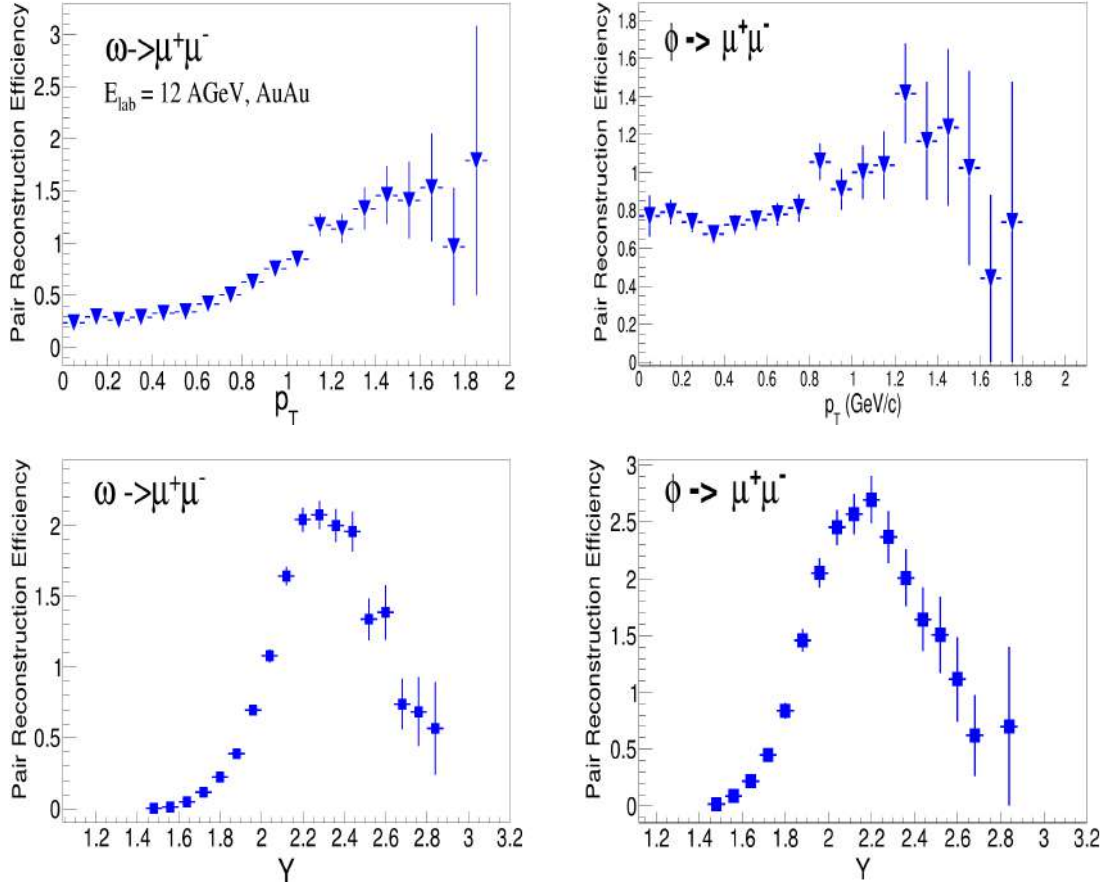


Figure 3.38: Pair reconstruction efficiency of ω and ϕ meson with respect to p_T (top) and rapidity (bottom) at 12 AGeV central Au+Au collisions.

forward region as the simulation performed for energy of collision at the laboratory frame and also there is an effect of detector acceptance. The Fig. 3.38 shows the pair reconstruction efficiency of ω and ϕ mesons with p_T and rapidity Y for 12 AGeV central Au+Au collisions. From the plot we can see that efficiency rises with p_T for both ω and ϕ . This is due to higher acceptance of muon pairs at high p_T . The opening angle between the muon pairs decreases at high p_T due to the conservation of energy and momentum. We also see that efficiency with respect to the rapidity Y is highest at around rapidity of 2.2. This is because at this rapidity the detector acceptance is maximum for muon pairs. The acceptance Y - p_T of ω and ϕ has been shown from input PLUTO and from the reconstructed dimuon spectra at 12 AGeV central Au+Au collisions as shown in Fig.3.39. The PLUTO shows a 4π distribution of ω and ϕ , whereas the reconstructed Y - p_T of ω and ϕ shows a region covered in the forward rapidity

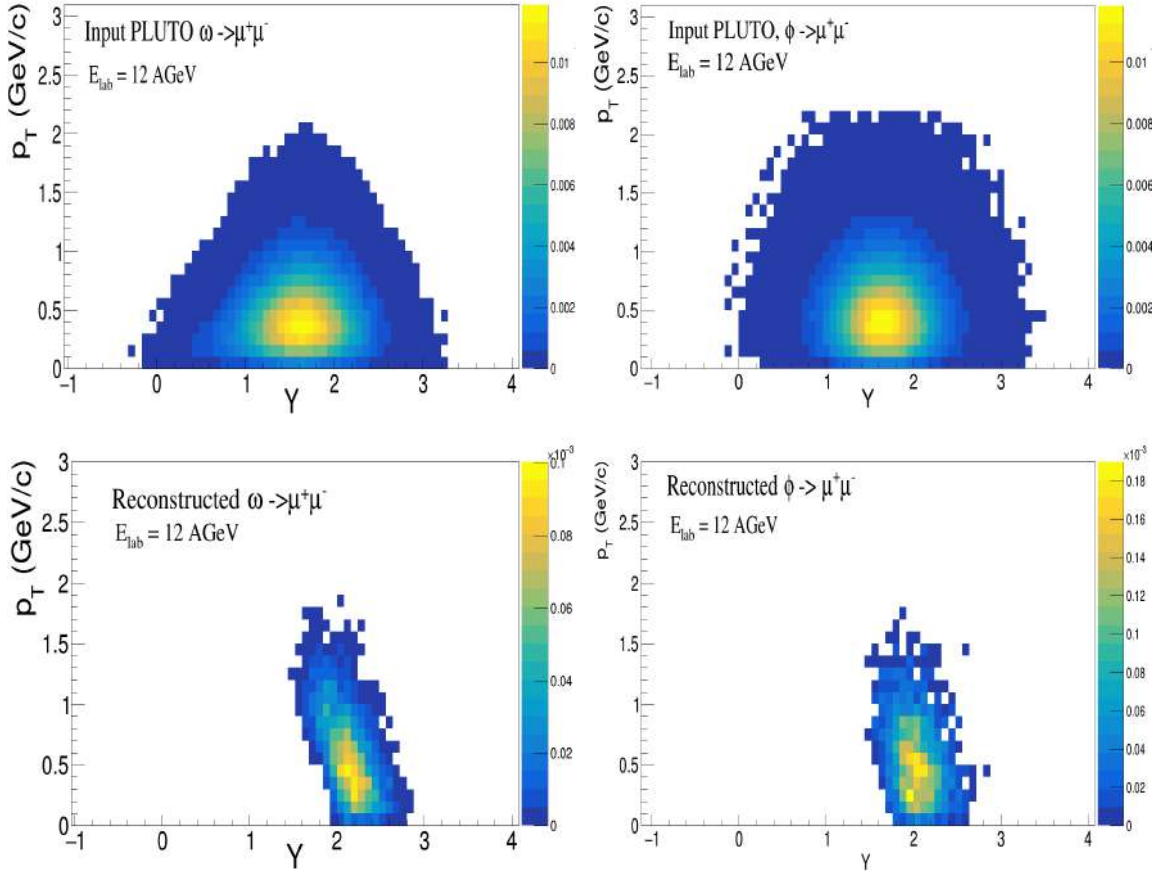


Figure 3.39: Phase space acceptance y - p_T of ω and ϕ from input PLUTO (top) and after reconstruction (bottom) at 12 AGeV central Au+Au collisions.

only. This is due to the effect of detector acceptance and muon pair reconstruction efficiency of the vector mesons.

3.5 Summary

In this Chapter, development and optimizations of the design of muon detector system in CBM have been described. The novel feature of muon chamber geometry is that the total absorber is segmented and triplet detector layers are stationed in between the absorber pairs. Optimizations have been performed in the selection of total absorber thickness as well as the individual absorber segments. Optimizations have been performed in the selection of suitable hadron absorber materials in the first absorber along with other absorbers. First absorber is of special design with one section inside CBM dipole magnet and other part outside the magnet, so

accordingly suitable material selection optimizations have been performed. Different detector technologies have been selected based on the particle rates at different z distances from the target. The first two stations face the maximum particle rates so accordingly high rate capable detectors with very high granularity, the Gas Electron Multiplier (GEM) based detectors have been selected. For third and fourth stations, as the particle rates are relatively lower, the Resistive Plate Chamber (RPCs) detectors have been proposed to use at these locations. The RPCs are cost effective as well as they can be built in large areas, so performance check have been done in CBMROOT simulations by implementing RPC geometry and its detector response. Next the dimuon detection performance have been checked with the optimized and most realistic muon detector system with four stations and 4 absorbers at 8 - 12 AGeV beam energy which corresponds to SIS100B geometry. Optimized selection cuts have been used for selection of muon candidates. Extraction of signals have been performed from signal embedded into background (PLUTO [66] + UrQMD [38]) events. The reconstruction of low mass vector mesons have been performed and cocktail invariant mass distributions have been extracted. Efficiency and S/B of LMVMs have also been calculated from the invariant mass distribution.

Chapter 4

Performance study of mini muon chamber modules at the mini CBM experiment at FAIR

4.1 Objective of mCBM

The Compressed Baryonic Matter (CBM) experiment at GSI, Darmstadt, aims to explore the QCD phase diagram in the region of very high net baryon density at moderate temperatures by colliding heavy nuclei in the fixed target mode. The main objective of CBM is to study the deconfined medium of quarks and gluons using clean and diagnostic probes, e.g., dileptons, multi-strange hadrons, charmonia, hyper-nucleons, among others produced inside the medium at different stages of evolution. However, these probes are very rare as well, i.e, their production cross section are very low. Thus, in order to make studies with such rare probes feasible, CBM is designed to operate at an unprecedented interaction rate, up to 10 MHz, to facilitate collection of large data sample which will benefit high precision measurements with rare probes [56].

In order to meet such a requirement, CBM has to be equipped with fast and radiation hard detectors, which are to be operated in triggerless free-streaming mode with an expected rate of data transport of about 1 TB/s. So far, high energy physics experiments at RHIC and/or LHC have mostly employed event-by-event data processing, where an event is identified online

based on some predefined trigger logic. However, at such a high data rate which is expected at CBM, conventional trigger based data acquisition system becomes inefficient. Instead, CBM has implemented timestamped data collection system, where a continuous stream of data in the form of signals (called digi) from various detectors are registered within a time-slice of certain length. Later in the post-processing stage, digis from various detectors are grouped together if they are within a certain time window, which might be related to an event. Thus a 4D event reconstruction technique has been adopted in CBM that requires both space and time information of detector responses (digis).

As CBM is foreseen to be operated at a very high collision rate with complex detectors, triggerless DAQ and new time based event reconstruction technique, it is essential to test the readiness of CBM detectors, readout electronics, data transport and data-processing softwares for 4D event reconstruction under realistic experimental conditions. Therefore, a miniaturized version of the full CBM test setup, called mCBM in short, was constructed at SIS18 facility at GSI/FAIR as a part of FAIR Phase-0 program and use the setup to optimize pre-series productions of the CBM detector systems along with their readout electronics [87]. Main aim of the mCBM experiment was to scrutinize the preparedness and performance of the CBM detectors, free-streaming DAQ systems, data transport to high performance computing systems (HPCS), online event and track reconstruction algorithms, offline data analysis software packages and overall integrated response of all CBM detectors. Additionally, mCBM also targets to explore Λ reconstruction using the straight line tracks from mCBM data. In this chapter we will provide a detailed description of mCBM test setup and present results characterising, the performance of mini-MuCh (mMuCh) modules particularly from the data collected during March to May 2020.

4.2 mCBM setup

A conceptual layout of mini CBM setup is shown in Fig. 4.1. As of May 2020, mCBM test setup included detector stations of all the CBM sub-detectors which are placed downstream of a solid target and are aligned at an angle of 25° with respect to the beam-axis, also shown, the geometry as obtained by using ROOT-software based simulation package as shown in Fig.

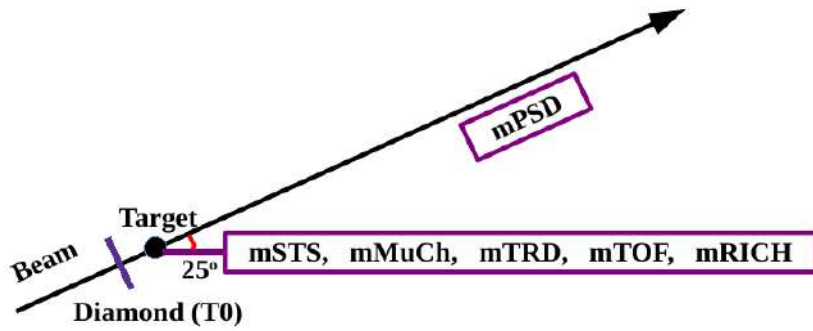


Figure 4.1: A conceptual layout of mCBM setup.

4.2. In mCBM, no magnet is used. Below we discuss some details of the sub-detectors used in the mCBM campaign in 2020 [88] :

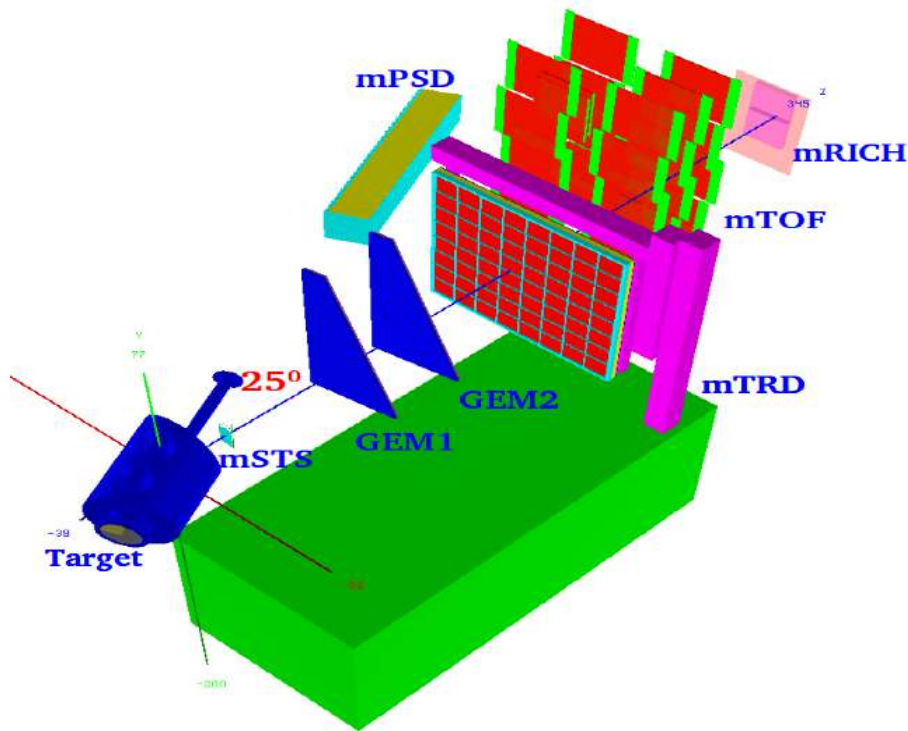


Figure 4.2: CBMROOT Simulation generated setup for mCBM 2020.

- mT0 : mT0 (not shown in the Fig 4.2) is a time-zero (T0) diamond counter detector comprising of 8 vertical strips each of width 2 mm. It is a fast and radiation hard detector which is mounted 20 cm upstream of the target inside the target chamber. Main goals of mT0 are beam monitoring, providing reference start time to mTOF detectors

and event building.

- mSTS : mSTS consists of two $6 \times 6 \text{ cm}^2$ modules of Silicon Tracking Stations (STS) placed around 28 cm downstream of the target. Each module has 1024 channels per-side which are readout through 8 STS-XYTER v2.1 ASIC [89, 90].
- mMuCh : mMuCh consists of two sector-shaped GEM prototype modules with the same dimension as that of the first MuCh station. The first and second GEM modules are placed at $\sim 84 \text{ cm}$ and $\sim 106 \text{ cm}$ from the target, respectively. Each module has 2304 pads which are readout via STS-XYTER v2.1. Further details of mMuCh modules and results from mCBM test will be discussed later.
- mTRD : mTRD has one TRD prototype module of dimensions $95 \times 95 \text{ cm}^2$ placed at $\sim 150 \text{ cm}$ downstream of the target. mTRD module is segmented into 768 rectangular pad and it uses SPADIC readout electronics which are arranged on Quad-FEBs.
- mTOF : mTOF setup in mCBM consists of five TOF prototype modules, equipped with 5 MRPC counters of dimensions $32 \times 27 \text{ cm}^2$ each placed between 230 cm and 340 cm downstream of the target. In total, mTOF has 1600 readout channels which are read-out using PADI and GET 4 electronics. Five modules of mTOF were further grouped into a double- and triple-stack in order to enable tracklet reconstruction within the mTOF system and efficiency measurement of MRPC modules. mTOF also allows to measure velocity of a particle that passes through its active volume.
- mRICH : mRICH subsystem in mCBM consists of two aerogel blocks each of volume $20 \times 20 \times 3 \text{ cm}^3$ which are placed directly after mTOF at a distance of 350 cm from the target. mRICH together with mTOF boosts the capability of mCBM for the determination of particle velocity, as well as, particle identification.
- mPSD : The mCBM setup also has a single PSD prototype module (mPSD), placed directly under the primary beam axis and tilted 5° relative to the beam axis pointing to the target. mPSD is used to measure particle energies that fall within its acceptance.

Figure 4.3 shows a photograph of mCBM test setup in March-May, 2020. The setup consists

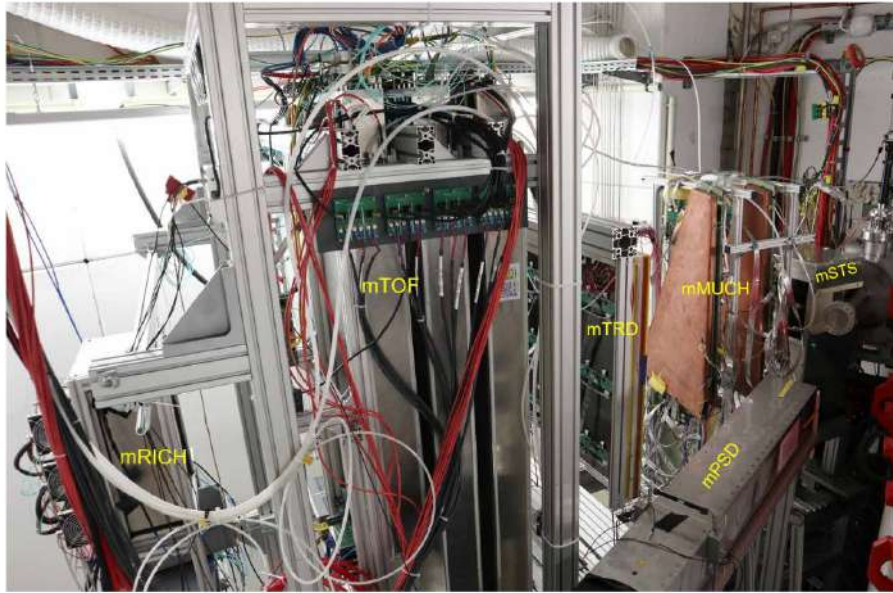


Figure 4.3: Actual photograph of mCBM setup 2020.

of the sub-detectors; mSTS, mMUCh, mTRD, mTOF, mRICH and mPSD. The mCBM was operated in a fixed target mode with Au^{197} solid target of varying thicknesses, which was bombarded with Pb^{206} , Pb^{208} and Bi^{209} beams at 1.075 AGeV beam kinetic energy of varying intensity.

4.3 mMuCh setup

The mMuCh setup at mCBM consisting of two real-size triple GEM modules of dimensions corresponding to the first station of MuCh is installed in the mCBM experiment in 2020. The detectors were operated with Ar-CO₂ gas mixture in 70:30 by volume [91, 92]. The chambers were first installed in December 2018 beamtime but operated with only one FEB (Front End Boards) because of limited electronics and DAQ resources. Later in March 2019, more FEBs were connected that increased the active area considerably. Also, the readout electronic, STS/MuCh-XYTER v2.0 [89, 90], which were used during December 2018 and March 2019 were replaced with v2.1 during December 2019 campaign as v2.0 chips were found faulty. It was identified that because of a logical error in v2.0 chip design, there are duplication of hits or hit losses when certain number of channels are fired in coincidence. This error in v2.0 was subsequently addressed in v2.1 and data were taken with this new chip from December 2019

beamtime onwards [93].

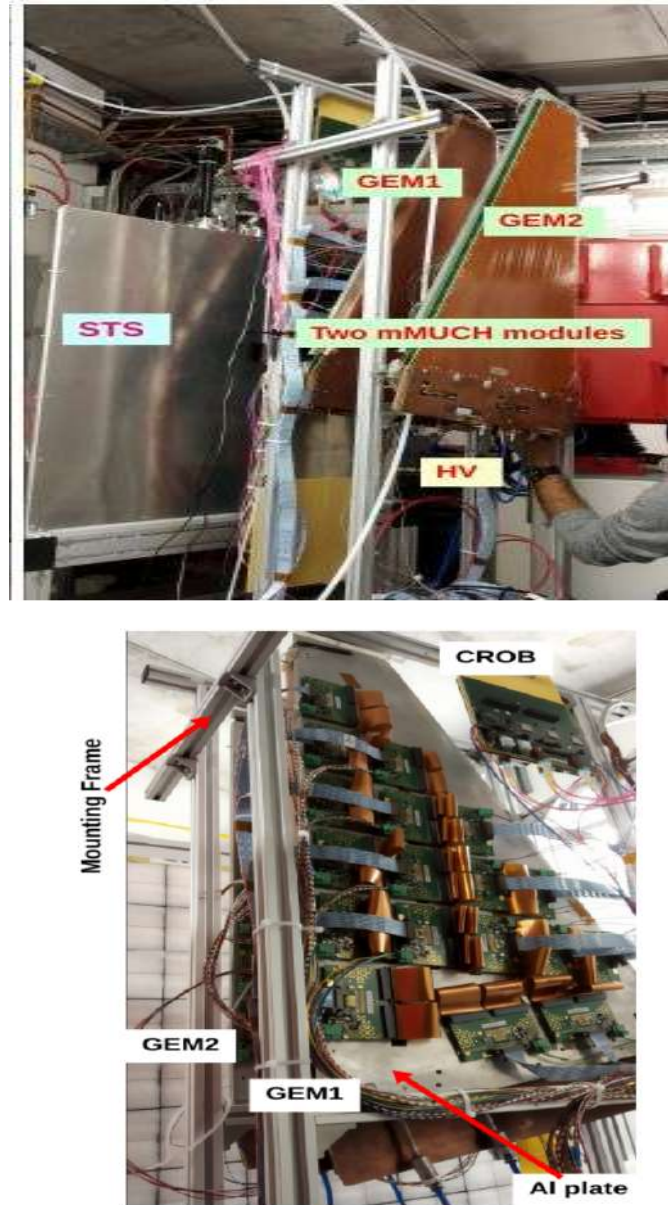


Figure 4.4: Two real size GEM modules for prototype of MuCh-first station have been installed in March-May 2020 beamtime (top). And the Al cooling plate support structure (bottom).

Figure 4.4 shows a photograph of the mMuCh system that includes two GEM modules installed in the mCBM cave at SIS18 facility in GSI as of November 2019. As already mentioned, all sub-detectors including mMuCh modules are aligned along the detector axis which is 25° to the beam axis and the point, where the detector axis intercepts the detector is considered as origin, which is approximately 2 m above the ground. The orientation of mMuCh modules were

such that the longer trapezoidal sides of modules was along the vertical axis and the readout plane faced the target. Each of the GEM modules are mounted on an Aluminium structure where 6 mm thick Cu-tubes are grooved-in for carrying chilled water for cooling the FEBs [94]. At different locations, temperature sensors are fitted to monitor temperature variation across the length and breadth of the modules. Figure 4.4 shows a photo of cooling system used in mMuCh setup.

As of December 2019, the first module of mMuCh (GEM1) had 16 working FEBs and the second module (GEM2) had 9 working FEBs [95]. Each of these FEBs were equipped with STS/MuCh-XYTER v2.1 self triggered readout electronics, capable of measuring time and amplitude of a signal [89, 96, 97]. Some of the main features of this readout chip are listed below [95]:

- 128 channels + 2 test channels
- Can provide both time and amplitude (ADC) information
- handles average hit rate 250 kHz/channel
- 14-bit for time measurement
- dynamic range of 100 fC and it can be changed
- ADC of 5 bit
- timing resolution ~ 4 to 5 ns and time stamp resolution 1 ns

In mCBM, data have been collected in free streaming mode, where signal from all electronic channels are recorded along with their time stamps, provided it is above a preset threshold. Subsequently, signals from each electronic channels (there are 128 channels in total) are digitized using a 5-bit flash ADC and a digitized electronics signal is called a "digi". The signal digis from all sub-detectors are collected by Front End Electronics (FEE). Then data are transferred to Data Processing Boards (DPB) and are grouped in time within an interval of 100 μ s. Each such time-grouped is called micro-slice (μ S). Next the data is forwarded via FLES input board (FLIB) to the First Level Event Selector (FLES) computer farm which is located at the Green IT cube (Computing node of GSI, FAIR) [64]. Here the micro-slices are clubbed together

to form time-slice (TS) and the subsequent online data reconstruction is performed [88]. The data processing system for May 2020 is shown in Figure 4.5 [87].

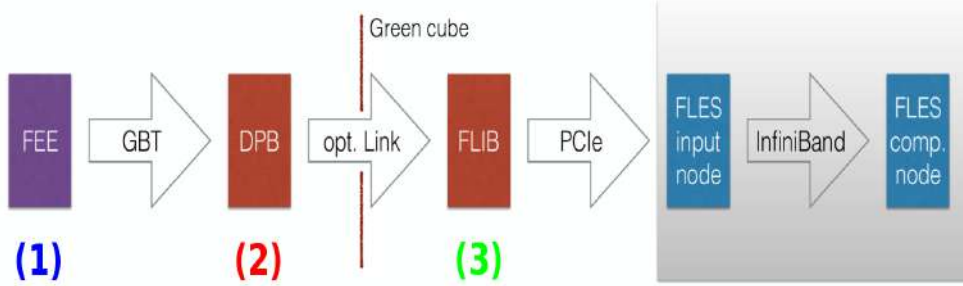


Figure 4.5: The readout chain for mCBM operated in May 2020, based on the DPB and FLIB.

Now, the Raw data are available for further analysis, which are first unpacked or converted to ROOT format with the help of CBMROOT framework [98]. The "rootified" data has a particular hierarchy, where each entry in the ROOT-tree corresponds to 1 TS and each branch of a ROOT-tree is populated with digitised signal from each sub-detector.

In the next section, results obtained from analysing the data collected during mCBM campaign of 2020 will be discussed in details.

4.4 Results from mCBM data 2020

The details of the data collected during March- May 2020 have been summarized below in table 4.1 Data were collected at different intensities of the primary beam and of different target thickness of the Au target. The beam was primarily Pb^{206} , Pb^{208} and Bi^{209} . Beam kinetic energy was 1.075 AGeV. Data were also taken for different HV of GEM detectors at different intensities.

Table 4.1: Run details for mCBM campaign March- May 2020.

Intensity	Target Thickness	Run numbers
2×10^6 per 9s spill	0.25 mm	812 - 828
2×10^6 per 9s spill	2.5 mm	831
2×10^7 per 9s spill	0.25 mm	834 -836
2×10^7 per 9s spill	2.5 mm	846, 849-852
1×10^8 per 9s spill	0.25 mm	854 - 855
1×10^8 per 9s spill	2.5 mm	856, 859
1×10^8 per 3s spill	2.5 mm	861 - 865

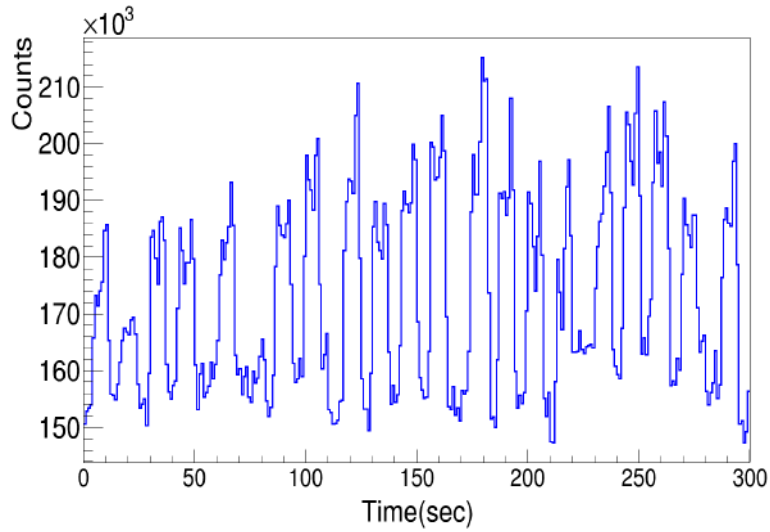


Figure 4.6: Spills in GEM1 including noise.

As already mentioned, mMuCh has two GEM modules installed in the mCBM experiment, called as GEM1 and GEM2, which were placed along the detector axis at 84 cm and 106 cm from the target, respectively. From the data the first plot we look at, is the spill structure of the beam particles detected by the GEM chamber. The Fig. 4.6 shows the spill distribution of the beam by the GEM1 detector. This is basically the time distribution of the digis in GEM. It shows that the spill structure can be clearly seen by the GEM1 detector. However, it can be seen from the plot that the spills sit over a background that extends over the entire time span of the spill distribution. The source of this background is from the noisy channels/pads in the GEM detector and also from the noise in the detector electronics. So before we proceed to analyse the data, the first thing we should do is to remove the noisy channels from the data, which is very important to get any meaningful results. So in the next section 4.4.1 we will discuss the method of noisy channel detection and rejection.

4.4.1 Noisy channels removal

Noisy channels are defined as the channels which gives very high count in digis/hits both in the presence or absence of beam. Due to these noisy channels detectors face very high amount of data rate that may damage the electronics channels also. So it is very necessary to remove the noisy channels which contains mostly the background. Figure 4.7 shows the distribution of channel counts for 128 channels in a FEB of GEM1. The channel distribution including the

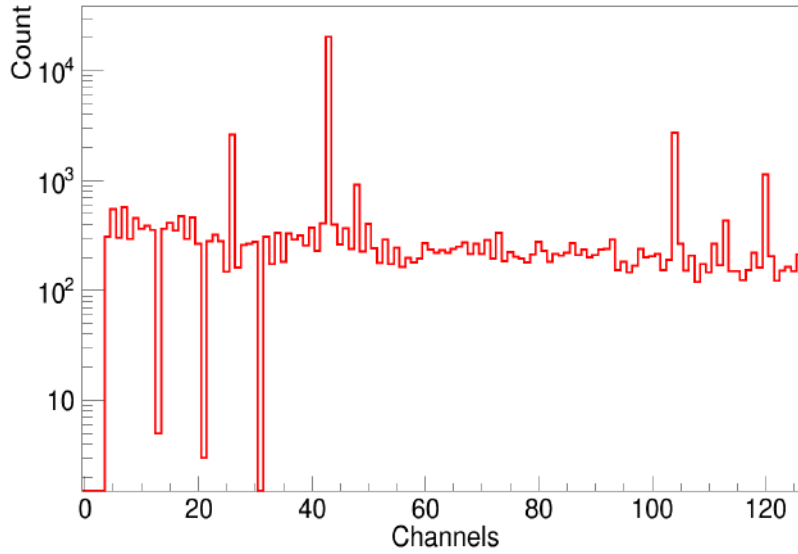


Figure 4.7: The channels counts have been shown for a FEB in GEM1 including the noisy channels.

noisy channels is shown in the figure. It can be seen that for the noisy channels, the channel count is very high compared to the other channels which follows a baseline counts. One way to remove the noisy channels is to put threshold cut manually by looking into the baseline count. It requires precise manual intervention since a wrong threshold might filter out a good channel and cause data loss. The count rate in channels also vary with detector voltages and other electronic parameters and that also vary run by run. Thus to reduce the manual effort, an automated approach will be appropriate for setting the threshold cut. For this we calculate a quantity as shown below,

$$Ratio = \frac{(ON\ spill - OFF\ spill) Count\ Rate}{(ON\ spill + OFF\ spill) Count\ Rate} \quad (4.1)$$

which defines the ratio of difference of channel counts in ON spill and OFF spill to the summation of channel counts in ON spill and OFF spill. The criteria for selecting good channels will be ~ 1 . In absence of beam there should not be any counts in the detector channels but we see some counts in the channels due to noise. For no noise condition the channel counts should be zero in the absence of beam. So from the equation 4.1, for good channels the ratio is 1, if we consider there is no noise in OFF spill. For noisy channels the ratio is nearly zero. Here

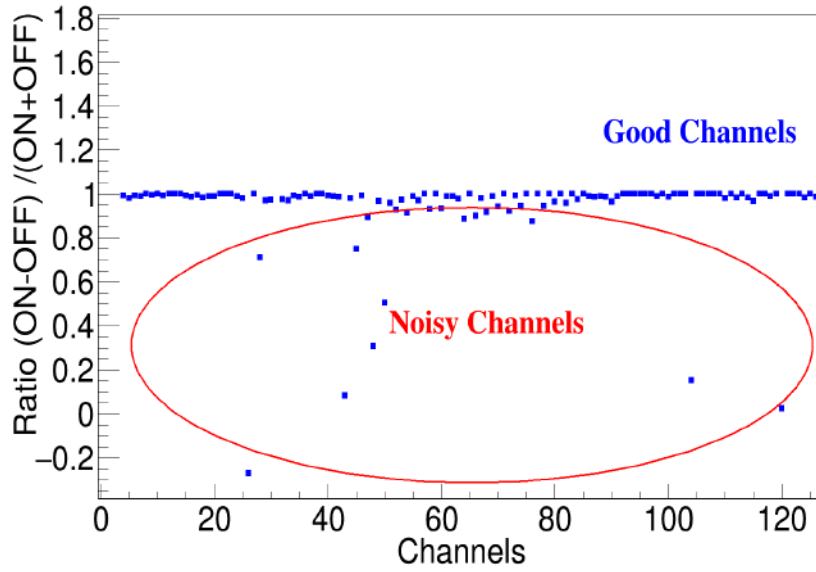


Figure 4.8: Ratio of difference of channel counts in ON spill and OFF spill to the summation of channel counts in ON spill and OFF spill for all the channels have been plotted.

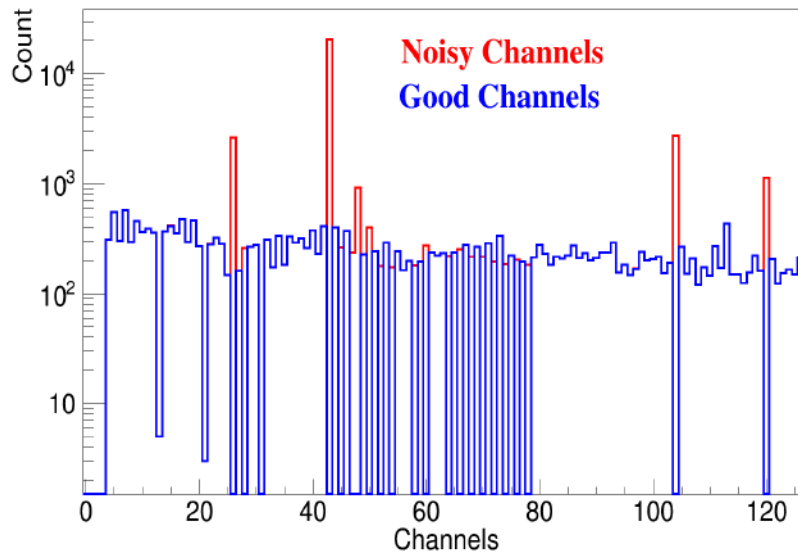


Figure 4.9: After rejecting noisy channels the good channels are shown in blue lines.

the ratios are calculated for all the channels for all the FEBs. Figure 4.8 shows the ratio for a FEB channels in GEM1. It can be seen that for good channels the ratio is 1, whereas for the noisy channels ratio is much less than 1. We can easily separate the noisy channels by putting a threshold cut, which is around 0.95 to 0.97 in this analysis. After rejecting noisy channels the good channels can be seen in blue colour in the Fig.4.9.

4.4.2 Spill structure

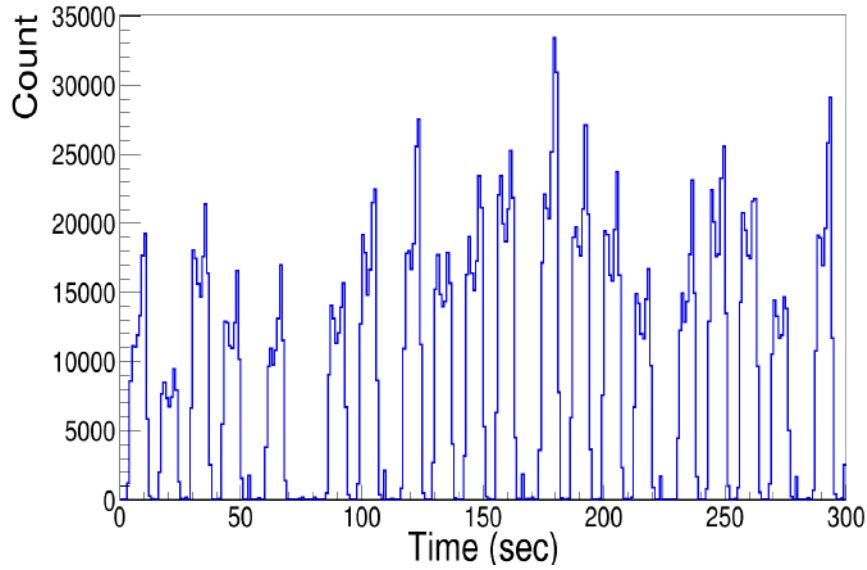
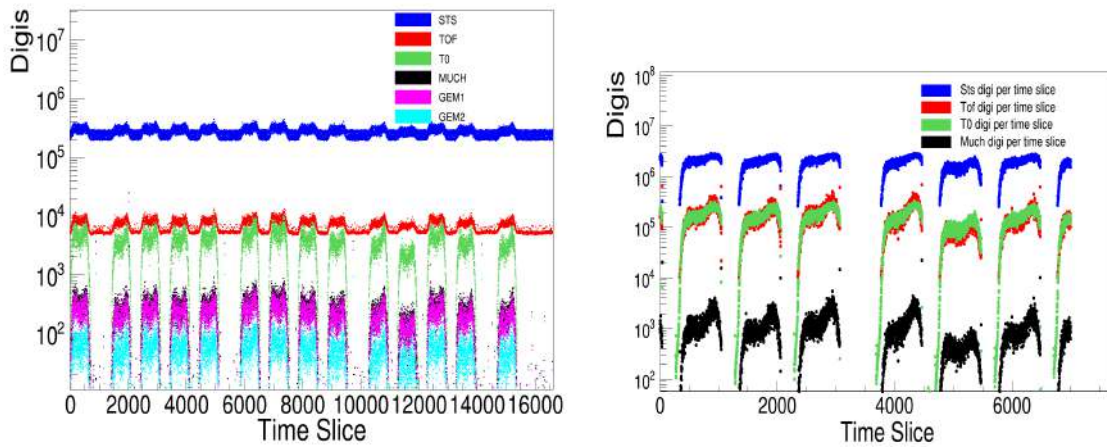


Figure 4.10: After rejecting noisy channels the spill structure in GEM1.

Figure 4.11: The spill distribution for all the sub-detectors in mCBM at low intensity (left) $2 \times 10^6/9s$ spill and high intensity (right) of $1 \times 10^8/9s$ spill for $Pb_{67+}^{208} + Au$ collisions with thin 0.25 mm gold target.

After rejecting the noisy channels, the spills in GEM1 has been plotted in Fig.4.10. It shows that now the background level is almost eliminated after rejecting the noise. A spill is basically the beam delivered by the accelerator followed by a short break which represents the absence of the beam or off spill. The spill length in most of the runs were around 10 sec and the off spill is around 2-3 sec. Figure 4.11 shows the spill distribution for all the sub-detectors in mCBM at

a low intensity of $2 \times 10^6/9\text{s}$ spill and a high intensity of $1 \times 10^8/9\text{s}$ spill for $\text{Pb}_{67+}^{208} + \text{Au}$ collisions with thin 0.25 mm gold target. So, it can be seen that the GEM detectors show very good beam structure at low intensity as well as high intensity of the beam.

4.4.3 Digi correlation

To check the linear performance of the detectors with beam intensity we checked the digi correlations among the detectors. In digi correlation we do a 2D plot for the number of digis per time slice among the detectors. It demonstrates how linearly a detectors perform with respect to the other detectors and also with the beam intensity.

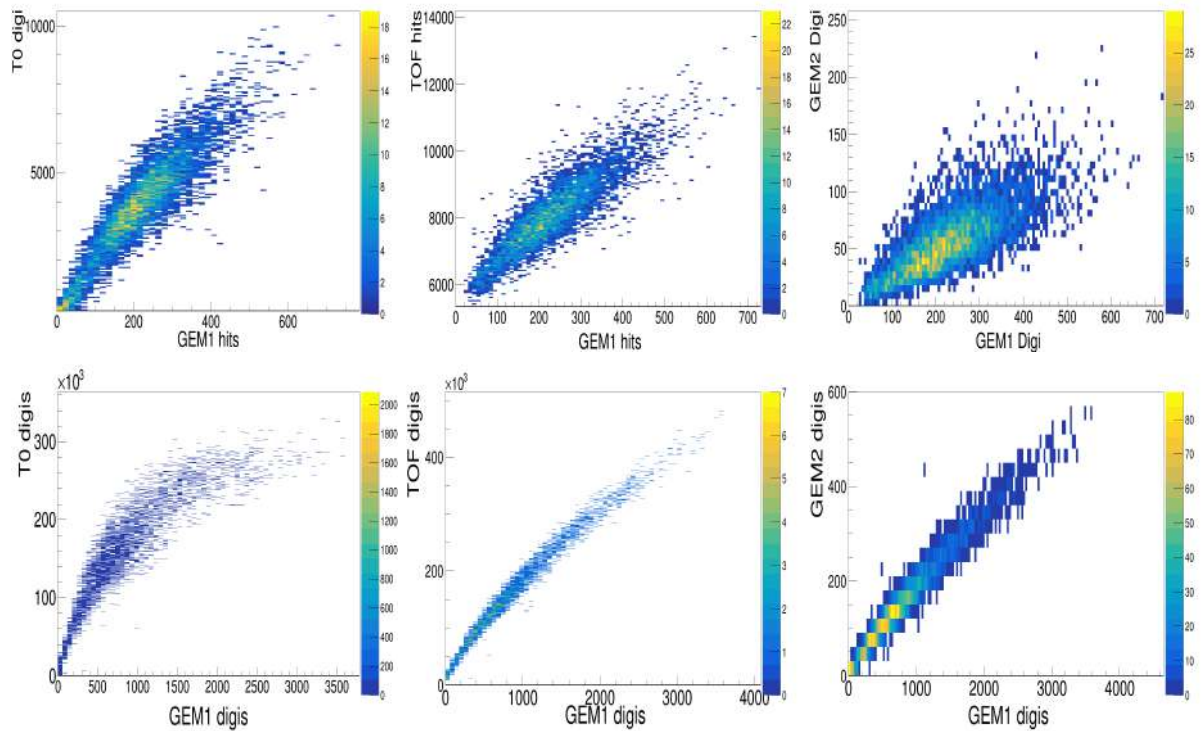


Figure 4.12: The digi correlations between GEM1-T0, GEM1-TOF and GEM1-GEM2 at low intensity $2 \times 10^6/9\text{s}$ spill (upper row) and at high intensity $1 \times 10^8/9\text{s}$ spill (lower row) for $\text{Pb}_{67+}^{208} + \text{Au}$ collisions with thin 0.25 mm gold target.

Figure 4.12 shows the digi correlations between GEM1-T0, GEM1-TOF and GEM1-GEM2 at low intensity $2 \times 10^6/9\text{s}$ spill and at $1 \times 10^8/9\text{s}$ spill for $\text{Pb}_{67+}^{208} + \text{Au}$ collisions with thin 0.25 mm gold target. From the figure we can see that digi correlations are linear for GEM1-T0, GEM1-TOF and GEM1-GEM2 at low intensity, however at high intensity there is a hint of

saturation in T0 and TOF detectors. Although GEM1-GEM2 digi correlation at high intensity is still showing a linear behaviour.

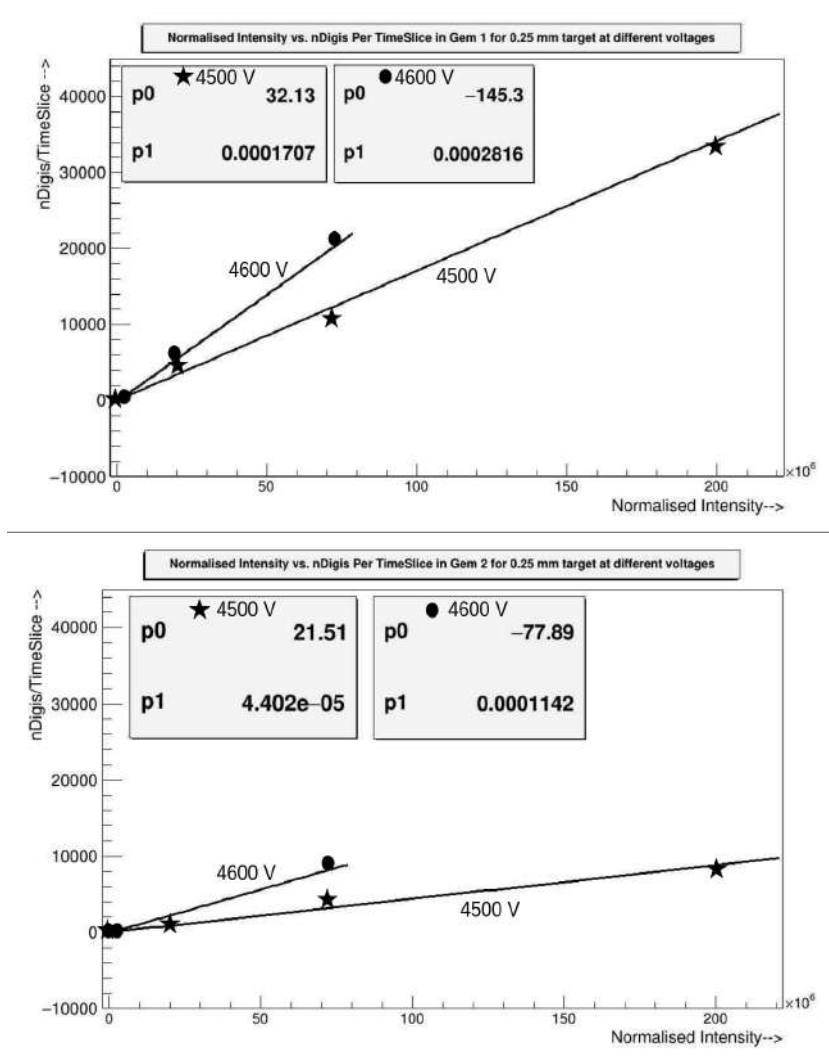


Figure 4.13: The number of digis per time slice with respect to the normalized beam intensity for GEM1 (top) and GEM2 (bottom) for two different GEM's high voltages of 4500 V and 4600 V [99].

The linearity of GEM detectors can further be studied through the number of digis per time slice with respect to the normalized beam intensity as shown in Fig.4.13 [99]. Here the normalized beam intensity means the beams of different intensities at different spill length have been normalized accordingly to make it in the same footing. The study has been done for GEM1 and GEM2 for two different high voltages of 4500 V and 4600 V for two GEMs. We can see that both GEM1 and GEM2 behaves linearly with the beam intensity at both the high

voltages of the GEM detector [99].

4.4.4 Time correlation

We next move on to look at the synchronisation of various detectors with time. For that we plot the time difference of GEM detectors with respect to the other detector. If there is any correlation between the detectors then it will show a single peak in the time correlation plot. In time correlation plot, the time difference is taken of one digi with respect to all the other digis in each time slice window.

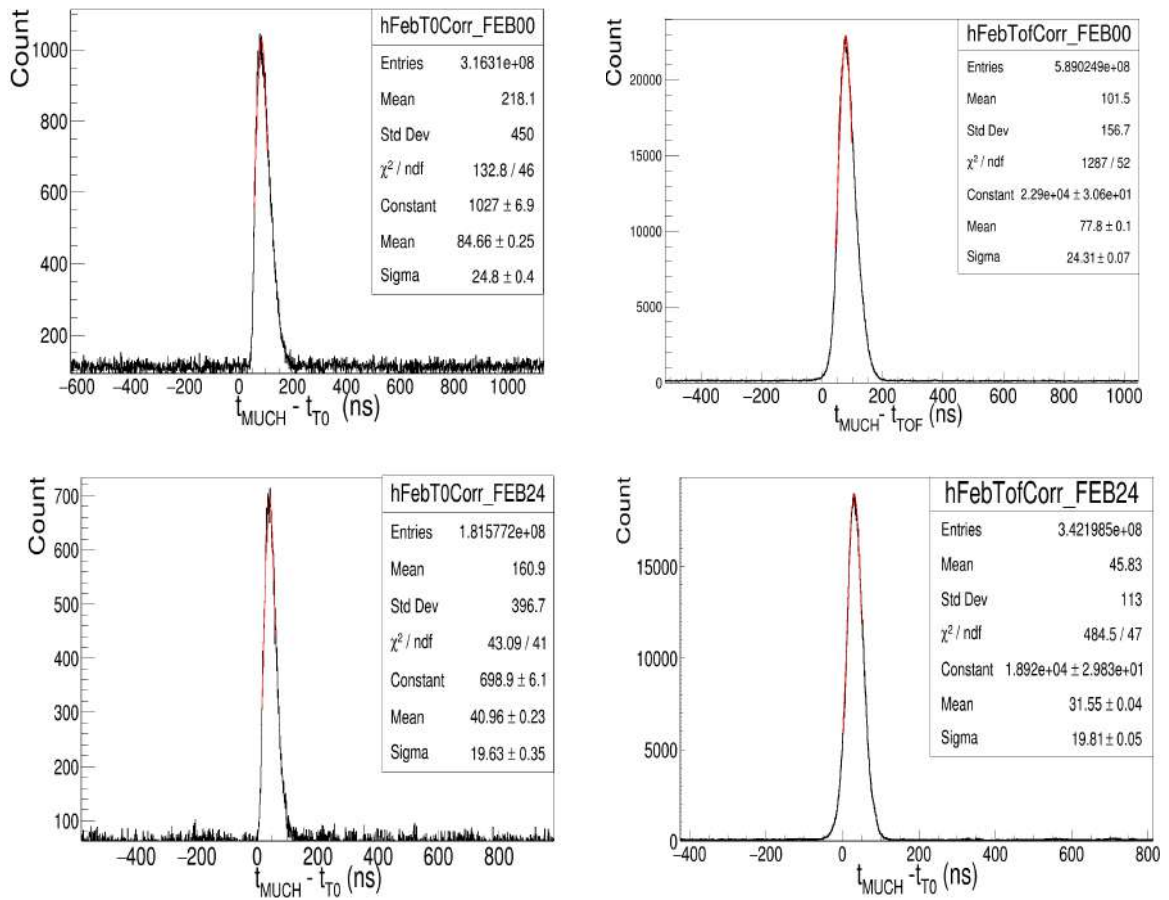


Figure 4.14: Time correlation between GEM1-T0, GEM1-TOF (upper row) and GEM2-T0, GEM2-TOF (lower row) at intensity of $2 \times 10^6 / 9\text{s}$ spill for $\text{Pb}_{67+}^{208} + \text{Au}$ collisions with thin 0.25 mm gold target.

Figure 4.14 shows the Time correlation between one FEB of GEM1-T0, GEM1-TOF and GEM2-T0, GEM2-TOF. We can see a nice peaks in time correlation both for GEM1 and GEM2 with respect to T0 and TOF detectors. That means the detectors are correlated in time

and showing synchronous behaviour and this is the proof of free streaming data acquisition in mCBM. This free streaming of data can further be established from the spatial correlation plots as will be discussed in section 4.4.6. Next each time correlation peak is fitted with a Gaussian distribution and the sigma of the distribution gives an idea about the time resolution of the GEM detectors (time resolution of GEM \sim 15-20 nsec). Here the sigma represents the combined time resolution of GEM along with T0 or TOF detector.

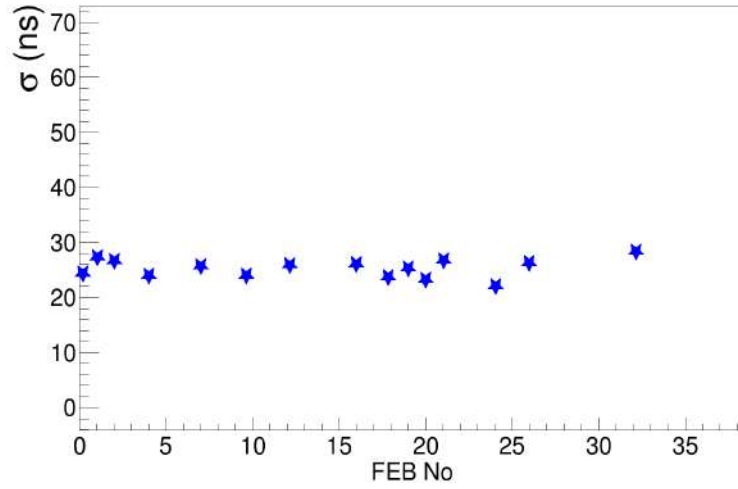


Figure 4.15: This time correlation width σ has been calculated across different FEBs in GEM, to study to spatial uniformity of GEM detectors.

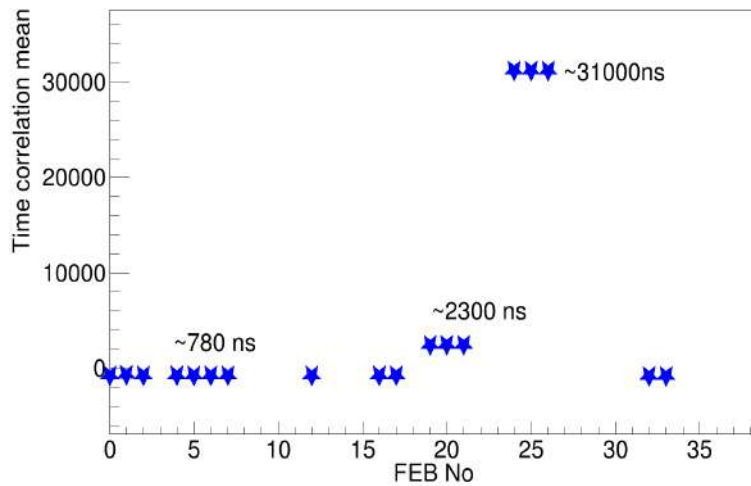


Figure 4.16: The time correlation mean for different FEBs before time offset correction. Different FEB has different offset.

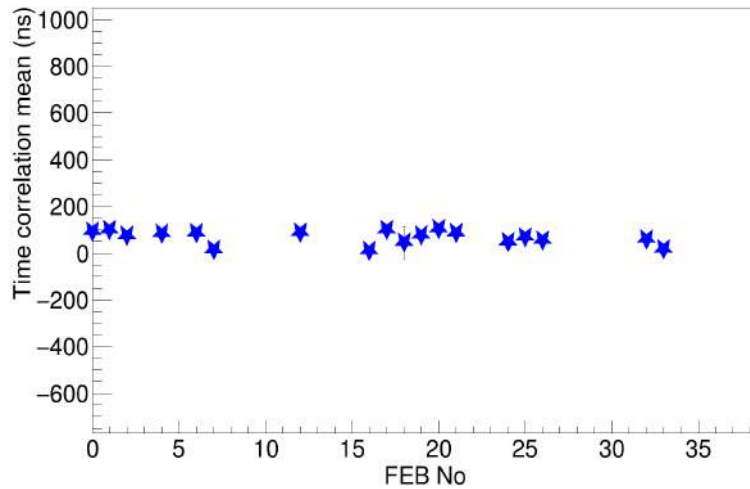


Figure 4.17: The time correlation mean for different FEBs after time offset correction. The mean is around zero for all the FEBs.

This GEM1-T0 time correlation width, σ has been calculated across different FEBs in GEM, which indicates different positions in GEM. The aim is to study the spatial uniformity of GEM detectors as shown in Fig.4.15. Here FEBs of both GEM1 and GEM2 are present. We can see that σ of time correlation width is nearly uniform across different FEBs in GEM and it varies between $\sim 19 - 25$ nsec, showing the spatial uniformity of time resolution. The mean of the GEM1-T0 time correlation is also plotted in Fig.4.16. It can be seen from the Fig.4.16 that different FEBs have different time offsets. This is due to the different time offsets present in the readout electronics for different FEBs, which need to be corrected for further analysis of event building that will be discussed in the next section 4.4.5. We can see the time offsets are very large ~ 31000 nsec for some FEBs. According to the time offsets, this is corrected for all the FEBs while doing time correlation. After offset correction, it can be seen from Fig.4.17 that the time correlation mean is now around zero for all the FEBs.

4.4.5 Event building and track reconstruction

After time offset corrections of different FEBs in GEM and also between other sub-detectors with respect to T0, we proceed for the event reconstruction from the raw mCBM data. We have done the time based event reconstruction for the raw data using a Fixed Time Window algorithm of 200 ns. In this algorithm it makes sorting of the time stamps of all collected raw

data from all the sub-detectors in the mCBM setup. Then starting from the first time stamp it makes a time window of 200 ns and considers all the digis within this window as an event and do it subsequently. Figure 4.18 depicts the concept of the Fixed Time Window algorithm of 200 ns time window in event reconstruction from the raw mCBM data. Some additional constraints are also imposed for the event reconstruction, such as, an event must have at least 1 T0 digi and 10 TOF digis [100].

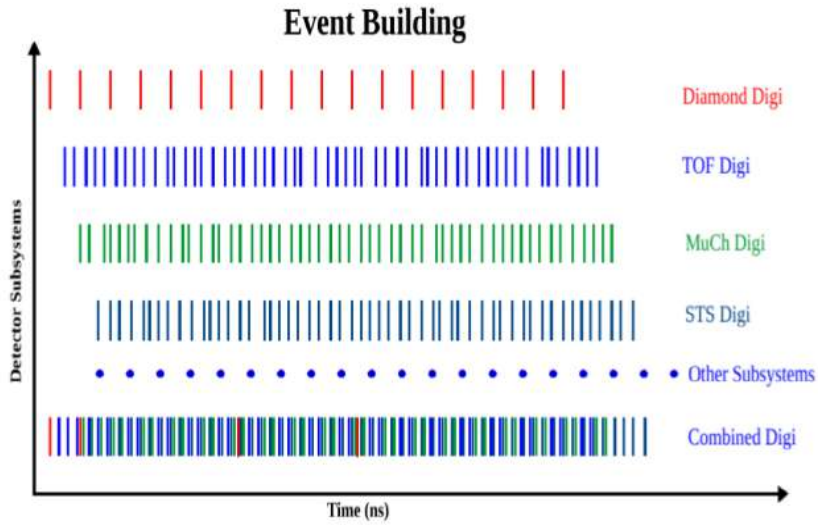


Figure 4.18: The schematic of the Fixed Time Window algorithm of 200 ns time window in event reconstruction from the raw mCBM data.

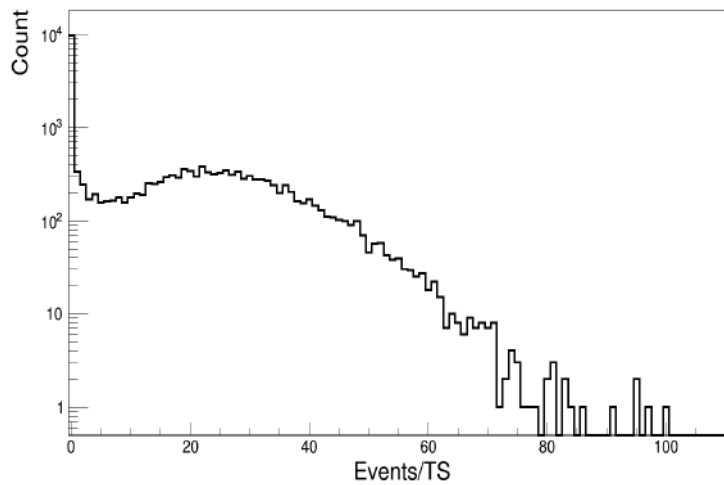


Figure 4.19: The number of reconstructed events per time slice from the raw mCBM data.

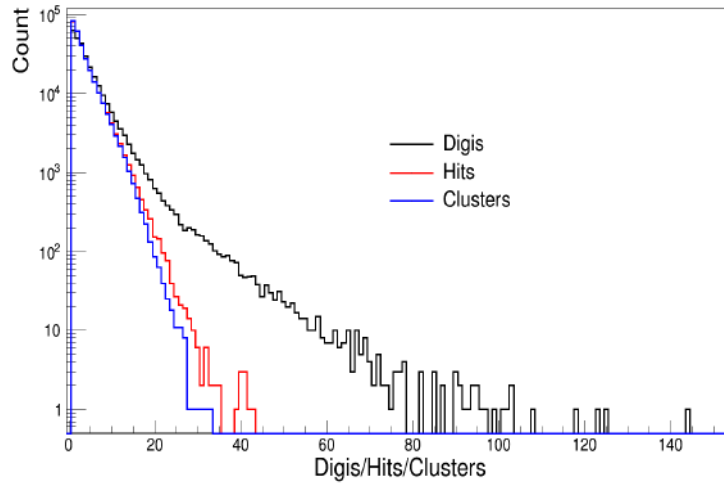


Figure 4.20: The event by event distribution of digis, hits and cluster multiplicity in mMuCh system from the raw mCBM data.

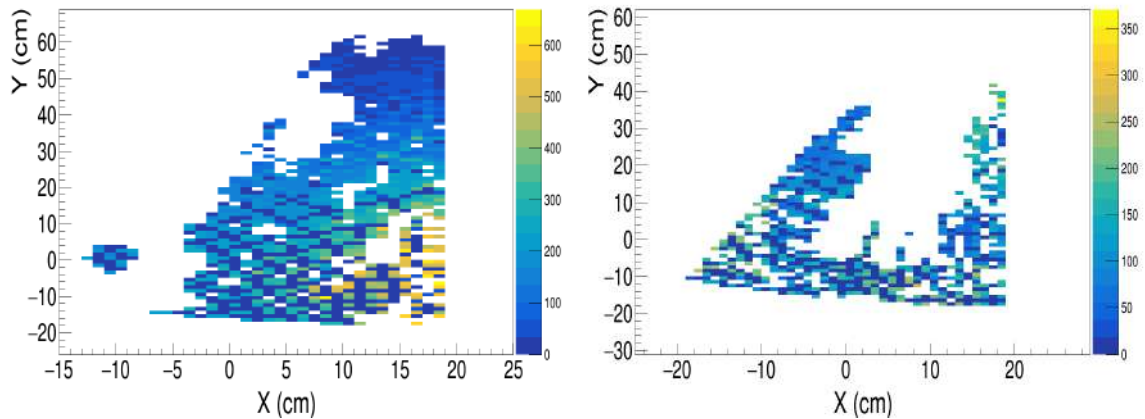


Figure 4.21: The XY coverage of hits in GEM1 and GEM2 from mCBM data.

The number of reconstructed events per time slice is shown in Fig.4.19. After event building, hit reconstruction is performed by the standard procedure of CBM hit and cluster reconstruction as discussed in Chapter 3 (section 3.2). Figure 4.20 shows the event by event distribution of digis, hits and cluster multiplicity in the mMuCh system. The XY coverages of hits in GEM1 and GEM2 are shown in Fig.4.21. The gaps in the XY distribution shows the dead area in GEM1 and GEM2. This dead area is due to unavailability of resources of some GEM-FEBs and also some non-working FEBs in the run. Also there are some contributions of noisy channels in the run, which were removed for the analysis as discussed in the section 4.4.1.

After event reconstruction, we proceed to the track reconstruction step from the mCBM

data. Here track reconstruction is done using mTOF detector and T0 detector. A straight line approach for track reconstruction is performed using the hits from mTOF detectors. 3 layers of mTOF detectors allow to construct the track segments in mTOF. These mTOF tracks then extrapolated to the vertex where the information of T0 detector is used for good selection of tracks.

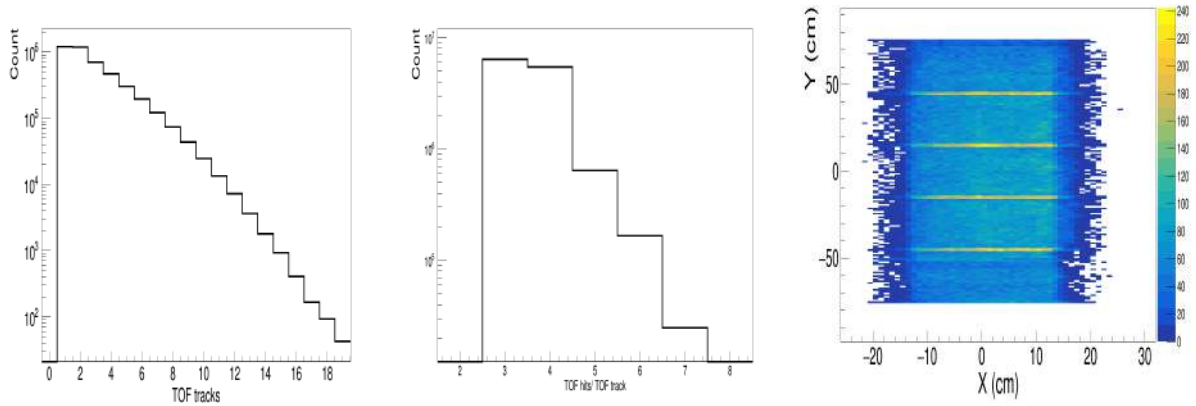


Figure 4.22: Event by event distribution of TOF track multiplicity (left). The number of TOF hits per TOF tracks (middle) and the XY distribution of the reconstructed TOF hits in mTOF detector.

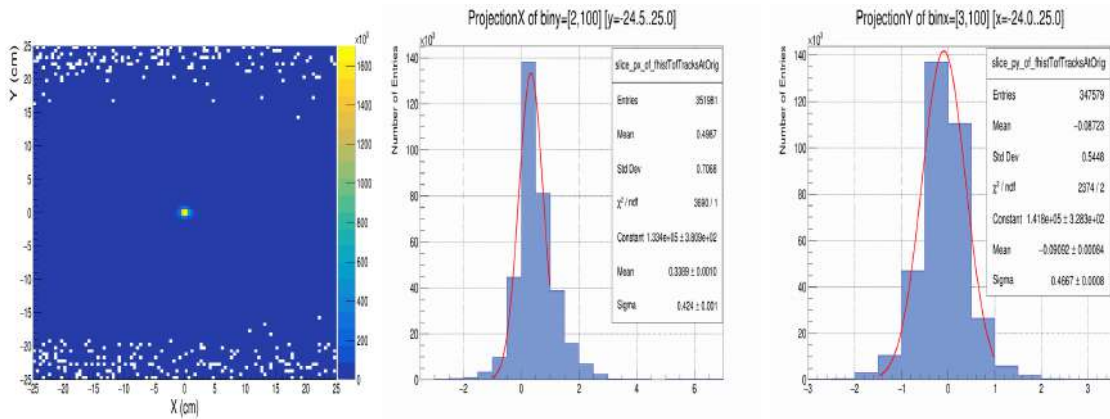


Figure 4.23: The XY projection of mTOF tracks at the origin (0,0,0). The X projection and Y projection are shown separately.

Figure 4.22 shows the TOF tracks multiplicity distribution (left) and the number of TOF hits per TOF tracks (middle). The XY distribution of the reconstructed TOF hits is also shown in Fig.4.22 (right). The horizontal lines in the TOF XY, is due to the overlaps of different TOF modules. Next the projection of mTOF tracks at the origin (0,0,0) has been done. Figure 4.23

shows the XY projection of mTOF tracks at the origin. The X projection and Y projection is done separately, which shows a Gaussian distribution of narrow width, $\sigma \sim 0.4$ cm.

In order to select good quality mTOF tracks and to reduce the number of fake tracks, following selection criteria are applied for selecting mTOF tracks: (a) mTOF tracks should have at least 4 hits (3 hits from mTOF layer and 1 from T0), (b) mTOF tracks should be within 5 cm radial cut around the target origin (0,0,0) and, (c) time correlated mTOF tracks with GEM hits (3σ time window) are selected to reduce background fake tracks [101].

4.4.6 Spatial correlations

As a first conceptual verification of the free-streaming DAQ system of CBM and usefulness of GEM chambers as a tracking detector we have plotted the spatial correlations between mMUCH and mTOF detectors using reconstructed mMUCH hits and mTOF tracks projected at GEM1 plane. Figure 4.24 shows the spatial correlations of mMUCH (GEM1) and mTOF detector in XX and YY. In XX correlation, the difference of all mMuCh hits X to all other X positions of mTOF tracks at GEM1 plane is done, similarly done for YY correlation [100].

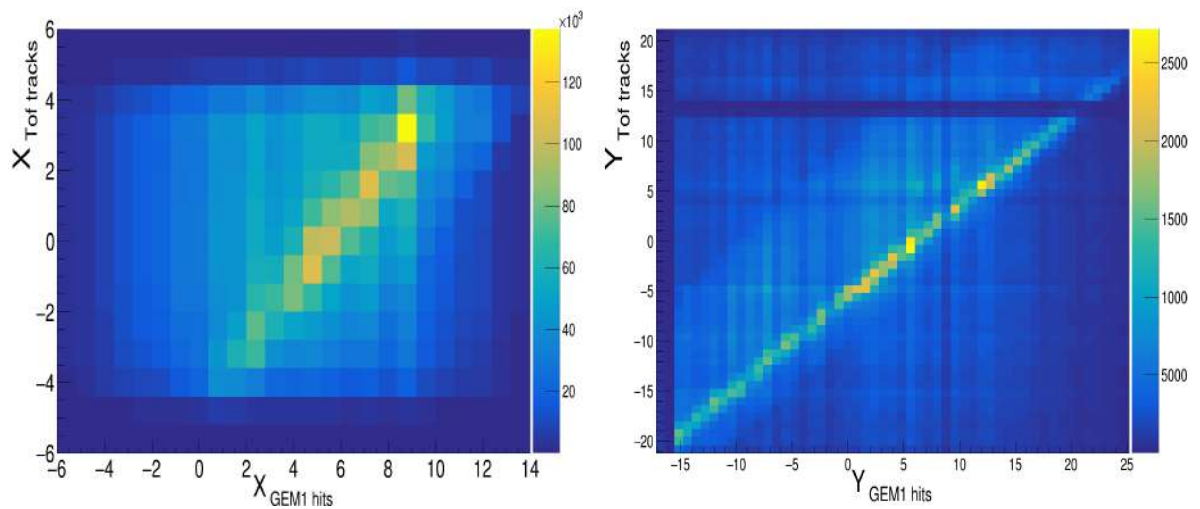


Figure 4.24: Spatial correlations XX and YY between mMUCH and mTOF detectors using reconstructed mMUCH hits and mTOF tracks projected at GEM1 plane [102].

The diagonal bands in the XX and YY correlation show a clear correlations among the detectors in spatial coordinates. The observed time correlations as seen in Fig.4.14 and spatial correlations between detector sub-systems demonstrate a first conceptual verification of the

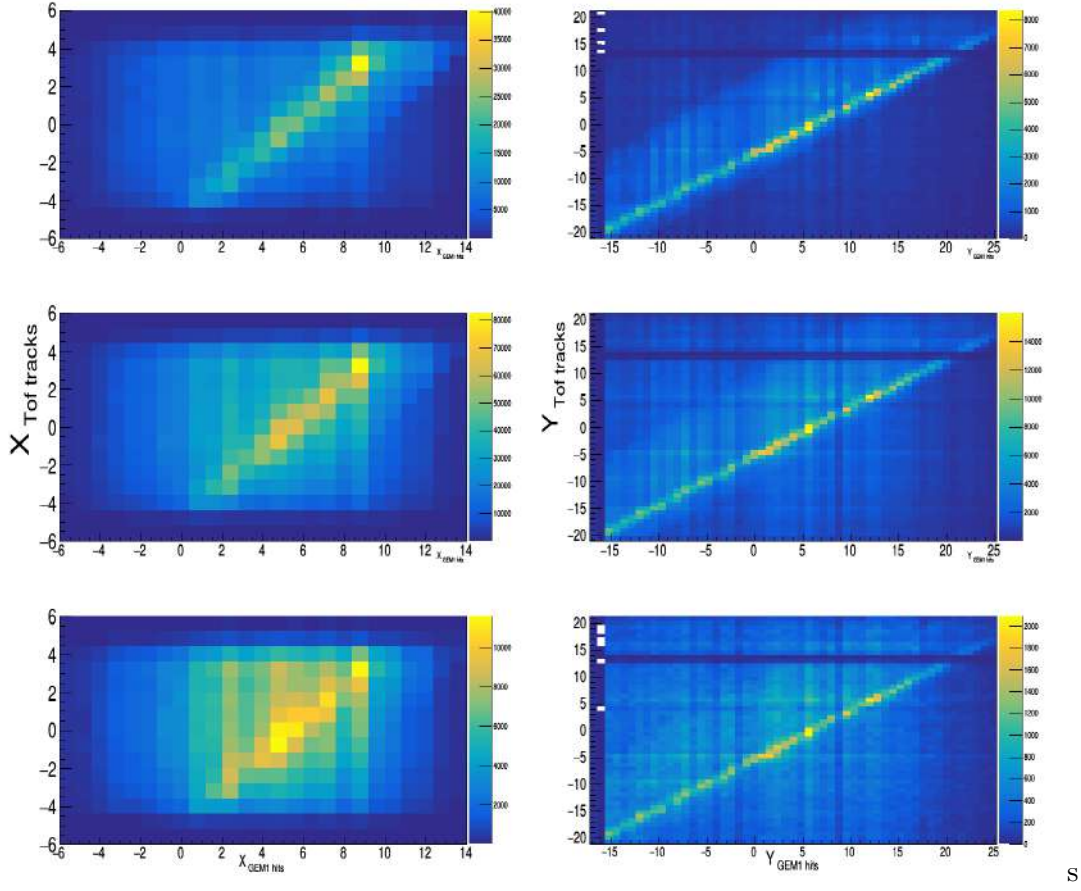


Figure 4.25: The XX and YY spatial correlation coefficient with different mTOF track multiplicity has been studied. XX and YY spatial correlations have been plotted for three regions in mTOF tracks multiplicity (a) $N_{TOFtracks} \leq 4$ (top row) (b) $4 < N_{TOFtracks} < 10$ (middle row) and (c) $N_{TOFtracks} \geq 10$ (bottom row). The correlation coefficient R for XX correlation is 0.3, 0.17, 0.10 and for YY correlation 0.51, 0.29 and 0.18 for the cases of (a), (b) and (c) respectively.

free-streaming and trigger-less DAQ system of CBM [102]. This correlation also signifies that GEM chambers can also be used as an efficient tracking detector.

Further the dependence of spatial correlation coefficient with different mTOF track multiplicity has been studied as shown in Fig.4.25. The spatial correlation coefficient R is defined as

$$R = \frac{n \sum xy - (\sum x)(\sum y)}{\sqrt{n(\sum x^2) - (\sum x)^2} \sqrt{n(\sum y^2) - (\sum y)^2}} \quad (4.2)$$

Where n is the number of data pairs. Here we have taken three regions in mTOF tracks multiplicity (a) $N_{TOFtracks} \leq 4$ (b) $4 < N_{TOFtracks} < 10$ and (c) $N_{TOFtracks} \geq 10$ as can be seen

from the Fig.4.22. For these three regions of mTOF track multiplicity, correlation coefficient R has been calculated. The correlation coefficient R for XX correlation are 0.3, 0.17, 0.10 and for YY correlation are 0.51, 0.29 and 0.18 for the cases of (a), (b) and (c) respectively. This suggests that for low multiplicity case, correlation strength is maximum and as we go to the higher multiplicity the correlation strength decreases.

4.4.7 GEM efficiency determination

After getting good spatial and time correlations between GEM and TOF, we therefore proceeded further to calculate efficiency of a GEM chamber taking mTOF tracks as a reference. In order to have good quality mTOF tracks and reduce the number of fake tracks, mTOF tracks are selected based on the criteria as discussed in the section 4.4.5.

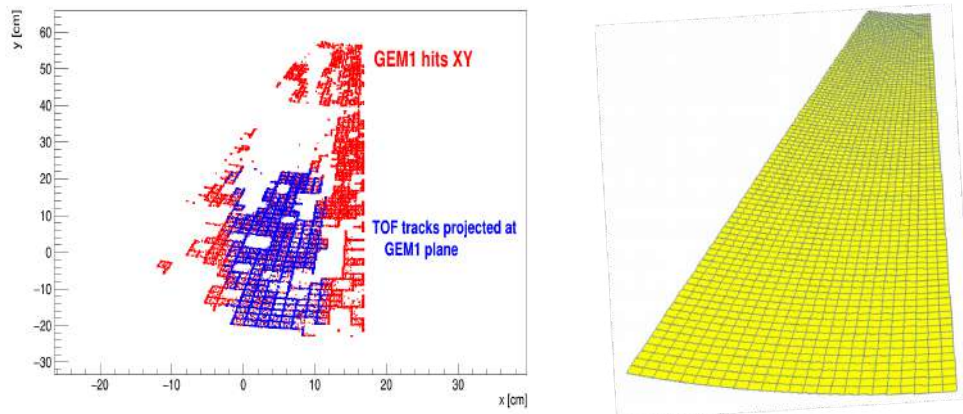


Figure 4.26: The XY distribution of GEM1 hits and the mTOF tracks projected at GEM1 plane. The common acceptance between GEM1 and the projected mTOF tracks is shown in blue colour (left). Simulation plot of the pads in a GEM module (right).

First we focused on XY of GEM1 hits and mTOF tracks at GEM1 plane. We find that there is a misalignment between mTOF and mMUCH planes which we corrected by shifting GEM1 hits (X and Y) in the line of mTOF tracks. After correcting for the mutual misalignment, we have shown the common acceptance between GEM1 and the projected mTOF tracks, which is shown in Fig.4.26. For efficiency calculation we use only those mTOF tracks that fall within this common acceptance of GEM1 and mTOF. Our definition for GEM1 efficiency with respect to mTOF tracks is as follows:

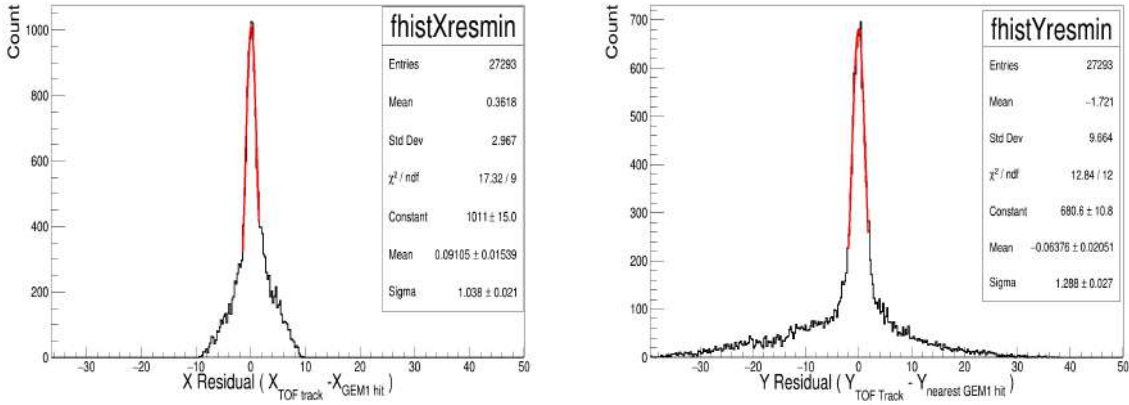


Figure 4.27: The residual X and Y distributions taking the spatially nearest GEM1 hit w.r.to the projected mTOF tracks.

$$Efficiency = \frac{\text{Number of mTOF tracks with associated GEM1 hits}}{\text{Number of projected TOF tracks in common acceptance}} \quad (4.3)$$

For the numerator we have taken only those GEM1 hits which are within 3σ spatial window of residual X and residual Y mean positions as shown in Fig.4.27. Here we have plotted the residual X and Y distributions taking the X and Y difference of spatially nearest GEM1 hit with respect to the projected mTOF tracks. These residuals are fitted with Gaussian, and we have taken GEM1 hits which are within $\pm 3\sigma$ around the Gaussian mean position. For denominator all mTOF tracks within the common acceptance between GEM1 and mTOF tracks are selected.

Within the common acceptance between mTOF tracks and GEM1 hits on the GEM1 plane, we first investigated the variation of x and y residuals of GEM1 hits with respect to the projected mTOF tracks at GEM1 plane for different pad sizes as shown in Fig.4.28. At first, we have divided a GEM chamber according to the pad dimensions. Pads with the smallest dimension are in $5 < y < 20$ cm, middle size pads are in $-5 < y < 5$ cm and large size pads are in $-20 < y < -5$ cm, as shown in Fig. 4.26 in the common acceptance between GEM1 and mTOF. We can see that the residual width in the X, Y residual distribution is lower in small granularity pads and as we go to the large size pads, the residual width also increases [101]. This is because as the pad size increases, the difference of X and Y in residuals also increases as we take hit positions at the center position of pads.

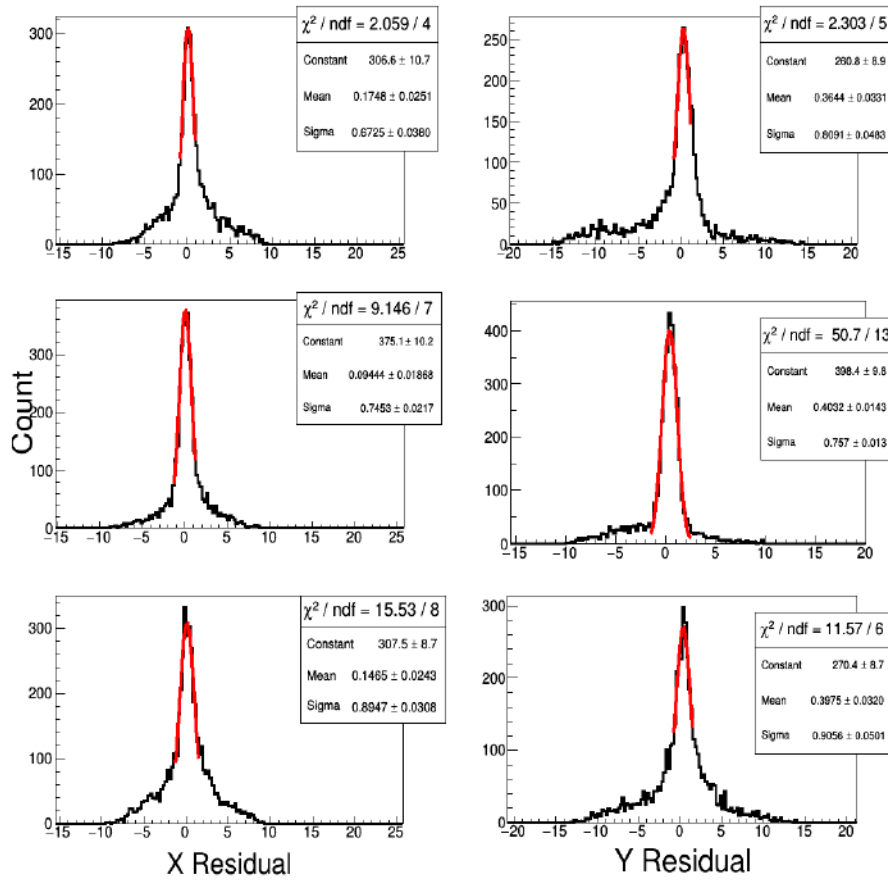


Figure 4.28: The variation of x and y residuals of GEM1 hits w.r.t projected mTOF tracks at GEM1 plane within the common acceptance of GEM1 and mTOF with different pad sizes : small pads $5 < y < 20$ cm (top), middle pad sizes $-5 < y < 5$ cm (middle) and large pads sizes $-20 < y < -5$ cm (bottom) [101].

Dead area calculation

The fired pad positions, which are basically center positions of the pads, is shown in Fig.4.29 within the common acceptance of GEM1 and mTOF. We can see from the Fig.4.29, that there are some dead portions in the common acceptance. These dead regions are due to the non-connecting FEBs in that position of GEM, which is due to the resource limitations of availability of FEBs. Additionally, some noisy pads have also been removed, which were giving very large counts in some pads due to noise. So before proceeding to the GEM efficiency calculation, we have to take care of this dead area. However this dead area calculation is a bit complicated as the pads have different sizes in different positions. So with the help of simulations, we first look into the fired pad positions, from that we extract the digi address and from the digi address

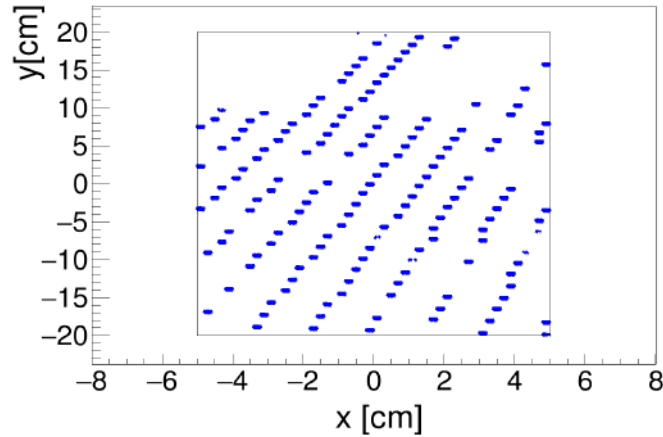


Figure 4.29: Common acceptance of GEM1 hits and mTOF tracks shown in black boundary, blue points are the fired pads centers.

we get the information of the pads, pad sizes etc. As in the dead area we do not have the information of the pads, or say the digi address, so we calculated the total fired pads area from the simulation and subtracted it from the total common area of GEM1 and mTOF. As the GEM detector has 1° azimuthal segmentation of the pads, we calculated pad area by $\pi(r_2^2 - r_1^2)/360^\circ$, where r_2 and r_1 are the outer radius and inner radius of the pads. So, the dead area is -

$$\text{Dead area} = \text{Total common area} - \text{Total fired pads area} \quad (4.4)$$

Corrected efficiency with time

Next we calculated efficiency of GEM1 module within 3σ of the residual mean in x and y according to the definition of efficiency. Next we studied the variation of efficiency with time. This is to check the uniformity of GEM detectors with time. We plotted the efficiency as a function of time which is shown in Fig. 4.30. Here time slice is plotted in X axis, one time slice is ~ 10 ms. It can be seen that efficiency is nearly uniform with time. Here the efficiency is dead area corrected efficiency. In this particular run dead area was 24 %. So after dead area correction, average efficiency is ~ 84 % for GEM HV of 4700 V, at low intensity 2×10^6 /9s spill, thick target.

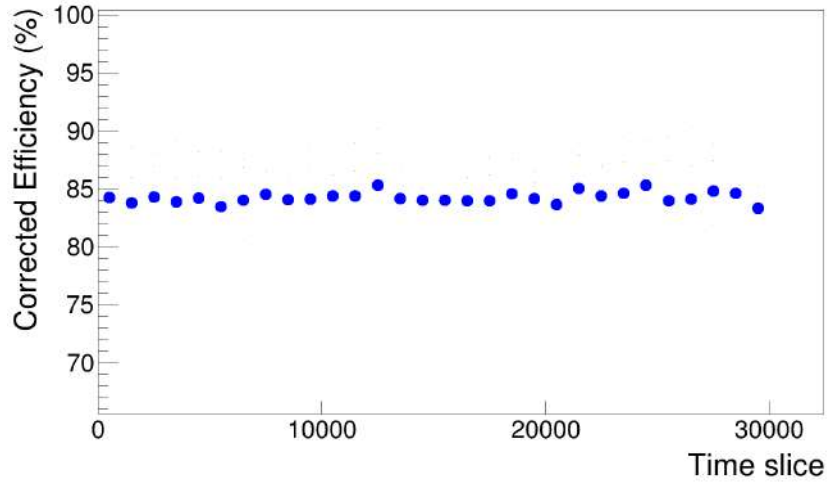


Figure 4.30: Efficiency with time for GEM HV of 4700 V, at low intensity 2×10^6 /9s spill, thick target.

Efficiency with β

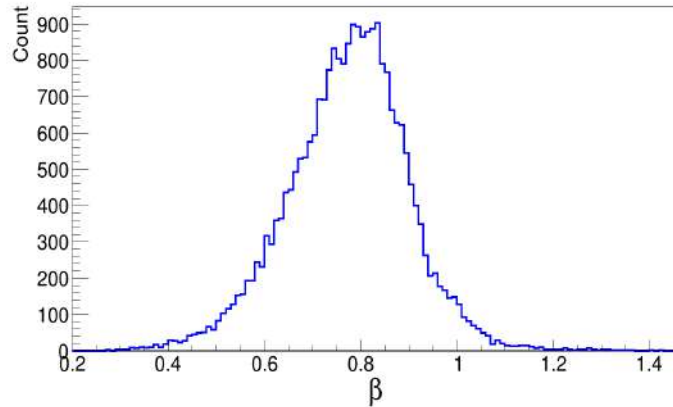


Figure 4.31: GEM HV of 4700 V, at low intensity 2×10^6 /9s spill, thick target.

We further studied the mTOF track β dependence of GEM efficiency [101]. Figure 4.31 shows the β distribution of particle's tracks at mTOF detector. β signifies the velocity of the particle/track. So depending upon velocity of the charged particle, energy deposition in detector active area will be different. Here systematic study on GEM efficiency have been performed for different range of velocity β . We have taken four ranges of β ; $0.2 < \beta < 0.6$, $0.4 < \beta < 0.8$, $0.8 < \beta < 1.2$ and inclusive β . As can be seen from Fig. 4.32, at lower values of β efficiency is higher and at higher values of β efficiency is lower [101]. This is because the energy

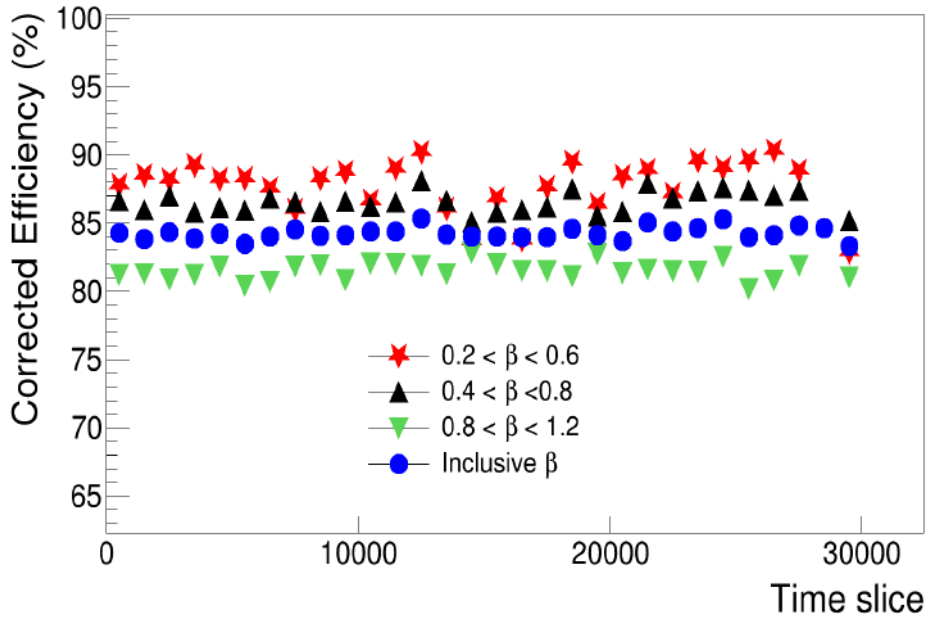


Figure 4.32: GEM efficiency has been calculated for different range of velocity β . We have taken four ranges of β ; $0.2 < \beta < 0.6$, $0.4 < \beta < 0.8$, $0.8 < \beta < 1.2$ and inclusive β for GEM HV of 4700 V, at low intensity 2×10^6 /9s spill, s thick target.

deposition in the detector follows $\sim 1/\beta$ from Bethe-Bloch formula. Higher charge deposition increases higher chance of detecting the signals in detector. Thus the observed variation in the efficiency with β is consistent with expectation.

Efficiency with HV

Next we studied the dependence of GEM1 efficiency with GEM1 high voltage (HV) for two values of GEM1 HV 4700 V and 4800 V at low intensity 2×10^6 /9s spill, thin and thick gold target respectively. Figure 4.33 shows the GEM1 efficiency with different GEM1 HV. We notice that as GEM1 HV increases, GEM1 efficiency also increases. The increase in GEM1 efficiency is about 8% for an increase of 100 Volts in GEM1 HV [101]. For 4700 V the dead area corrected GEM1 efficiency is ~ 84 % and for 4800 V corrected efficiency is ~ 92 %, which is quite consistent with the lab tests for GEM efficiency with cosmic muons. However, due to lack of data under similar conditions at other GEM1 HVs, we did only for two GEM HVs. Further we will do these exercises with more HV settings and different charge thresholds of GEM detector in future mCBM campaigns.

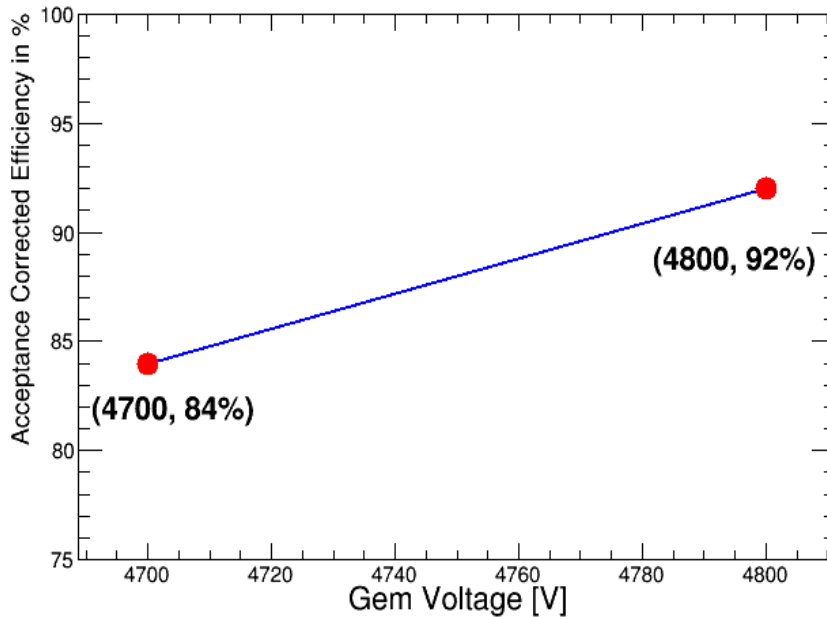


Figure 4.33: Dependence of GEM1 efficiency with GEM1 high voltage (HV) for two values of GEM1 HV 4700 V and 4800 V for inclusive β , at low intensity 2×10^6 /9s spill, thin and thick gold target respectively.

4.5 Summary

The mini CBM (mCBM) experiment at SIS18 facility, situated at Darmstadt, Germany is a part of FAIR phase-0 program. It is a miniaturized version of the CBM full system test setup, which is tested under high particle density environment of heavy ions collisions. In mCBM all the sub detectors are arranged in the same order as of main CBM and in the mCBM campaign 2020, mini muon chambers of two GEM modules have been installed and tested. These are the real size GEM prototype modules same as the first station of CBM-MuCh. In this experiment, data were taken at different intensities and different target thicknesses of the gold target with different GEM high voltage configurations. We have analysed the data collected by the GEM modules in Pb+Au collisions at 1.06 AGeV. Substantial noise have been removed from each FEBs connected in the GEM detector. It can be seen that GEM can produce good spill structure of the beam particles at low as well as at high intensities. Linear response of the detectors with beam intensity have been observed from digi correlations of GEM with respect to other detectors. A good time correlation have been observed with a nice time correlation

peak, which indicates the synchronicity of the detectors in time. A spatial uniformity of time resolution has been studied across different FEBs in GEM. A time based event reconstruction has been performed taking the raw mini-CBM data. Here Fixed Time Window algorithm has been applied to reconstruct events with 200 ns time window. Tracking has also been performed taking hits in 3 layers of mTOF detectors used in mCBM. With the help of mTOF tracking, spatial correlations have been studied between GEM1 hits and mTOF tracks at GEM1 plane and it shows a nice correlation band. These time correlations along with spatial correlations indicate the proof of free streaming data acquisition in mCBM. The correlation strength has been calculated using the correlation coefficient and studied its dependence with the different TOF track multiplicity. Finally GEM efficiency has been estimated from the mCBM data using the mTOF tracks after calculating properly the dead area in GEM. Efficiency has been studied with time, which shows good uniformity of efficiency with time. Systematics of GEM efficiency has been studied with the variation of particle velocity (β) and the GEM high voltages and it is showing consistent result with β and GEM high voltage, that means GEM efficiency increases with lower β and higher GEM high voltage.

Chapter 5

Baryon anti-baryon annihilation and its impact in apparent strangeness enhancement in high density nuclear matter

5.1 Introduction

Quantum Chromodynamics (QCD) based on lattice formalism have predicted that a deconfinement phase transition may occur when heavy-nuclei ($A+A$) are collided at relativistic energies [103]. Such a phase transition is likely to produce a novel form of QCD matter consisting of a deconfined state of quarks and gluons (partons), the Quark Gluon Plasma (QGP). Over the last two decades, data from the Relativistic Heavy Ion Collider (RHIC) in BNL and CERN's Large Hadron Collider (LHC) have presented convincing evidences in favour of this partonic deconfinement [104–108].

For a long, strangeness enhancement has been considered as one of the most important signatures for the QGP formation [109]. Strangeness production was proposed to be enhanced in a partonic environment because of abundant production of strange-antistrange ($s\bar{s}$) quark pairs. A non-monotonic energy excitation of strange hadron production relative to non-strange

hadrons were actually observed at low energy collision at SPS, with a maximum around 7-8 GeV collision energy. In order to understand the higher abundance of strange hadrons in low energy heavy ion collisions, let us consider a baryon rich medium which is generally formed due to baryon stopping in low energy collisions at SPS. At these collision energies, baryon density reaches approximately $10\rho_0$, where ρ_0 is the normal nuclear matter density. In terms of quark number density, ρ_0 can be expressed as follows:

$$\rho_0 = \frac{n_u + n_d}{3} = \frac{2n_u}{3}, \quad (5.1)$$

where n_u and n_d are number densities of up and down quarks, respectively and one can further assume $n_u \approx n_d$. It is known that normal nuclear matter density $\rho_0 = 0.16 \text{ fm}^{-3}$. Substituting the value of ρ_0 in Eq. 5.1, one can estimate the quark number density n_u to be $\frac{3\rho_0}{2} = 0.24 \text{ fm}^{-3}$. For nuclear matter density, $\rho \approx 10 \times \rho_0$, quark number density, n_u is 2.4 fm^{-3} . As quarks are Fermions, it is possible to relate the quark number density n_u to Fermi-momentum for massless particles as

$$p_F^3 = \frac{2\pi^2}{g} 3n_u, \quad (5.2)$$

where g is the degeneracy factor which for two flavoured system is 12. Therefore at low temperature (say at $T = 0\text{K}$), Fermi momentum, p_F amounts to 450 MeV (obtained by substituting degeneracy factor, g and quark number density n_u in Eq. 5.2). As we know that for a Fermionic system, highest filled energy level at 0 Kelvin for massless Fermions is p_F or E_F , so, for producing any new u/d-quark or -antiquark, minimum energy required is $2E_F + m_{u\bar{u}}$ (as quarks are always produced in pairs), which is about 800 MeV. This is because of Pauli blocking- as all the energy levels up to Fermi level are filled with existing u and d quarks from the incoming nuclei, no new u or d quarks can be produced below the highest filled Fermi level. Also quarks must be produced in pairs to obey conservation laws that apply to them. As a result, new u or d quarks and anti-quarks can only occupy the energy levels above the Fermi energy. On the other hand, strange quarks carry a different quantum number (different flavor from u and d) and thus its production is not prohibited by Pauli-blocking below the E_F . Therefore, the production of $s\bar{s}$ quark pairs are energetically favoured which is only twice the mass of strange quarks that is about 200 MeV. This naturally leads to abundant production

of $s\bar{s}$ quark pairs in low to intermediate energy nuclear collisions.

Subsequent to production, these strange quarks/antiquarks may eventually find another non-strange or strange (anti)quarks from the deconfined partonic medium to produce strange hadrons [110–115]. Enhancement in the yields of strange particles and/or of the ratios of yields of strange-to-non-strange particles have been reported in central heavy-ion collisions when compared with elementary pp interactions [116]. Nevertheless, this relative strangeness enhancement from a small to large system can also occur in a pure hadronic environment because of the volume effect. Due to the requirement of local strangeness (quantum number) conservation, strangeness production in small systems is canonically suppressed [117,118]. This constrain is however, relaxed for a large system where strangeness neutrality may be achieved globally [119]. Thus, it reduces the phase space penalty for the production of a strange or multi-strange hadrons in A+A collision as the strangeness conservation can be taken care-of by another anti-(multi-)strange hadron elsewhere in the extended volume. Consequently, even in the absence of partonic medium, ratios of yields of strange particles in A+A over pp collisions can exhibit an enhancement simply because the strangeness production in small systems are canonically suppressed.

Strangeness enhancement has been extensively studied at RHIC-AGS and CERN-SPS. A non-monotonic variation in K^+/π^+ ratios as a function of beam energy, popularly known as the horn structure, was reported [120–122]. This non-trivial energy dependence in the K^+/π^+ ratios was speculated as a signature of strangeness enhancement in high energy heavy-ion collisions however, there also exists some alternative explanations [123]. Similar signatures of enhancement were also observed in the strange baryon sector where prominent increase in the yields of Λ -hyperons and multi-strange hyperons Ξ and Ω have been demonstrated [19,124–127]. In terms of strange-to-non-strange particle ratios, a large enhancement in $\bar{\Lambda}/\bar{p}$ ratio from 0.26 in peripheral collisions to ~ 3.6 in central Au+Au collisions at 11.7 AGeV was reported by the E917 experiment at AGS [128], although with large uncertainty. A large value of $\bar{\Lambda}/\bar{p}$ ratio of $2.9 \pm 0.9(\text{stat}) \pm 0.5(\text{sys})$ in central Si+Au collisions at 14.6 AGeV was also measured by the E859 experiment [129].

Considering inclusive \bar{p} yields from two different experiments- E864 and E878, an indirect estimate of $\bar{\Lambda}/\bar{p} > 2.3$ was obtained in central Au+Pb collisions at 11.5 AGeV at $y \sim 1.6$ and

$p_T \sim 0$ [130]. Also, a significant rise from 0.25 in pp collisions to 1.5 for heavy-ion systems was published by the NA35 experiment at CERN SPS. Subsequent studies in Pb+Pb collisions between 20 to 158 AGeV by NA49 experiment supports earlier findings of large enhancement in $\bar{\Lambda}/\bar{p}$ ratios [131]. In terms of quark composition, $\bar{\Lambda}$ and \bar{p} are unique because they are comprised of anti-quarks alone, which can only be produced during reaction. As in the entrance channel of nuclear collisions there are no antibaryons or strangeness, it might appear that this large enhancement in $\bar{\Lambda}/\bar{p}$ ratios is because of partonic deconfinement [132]. However, it must be remembered, at this concerned energy range, high baryon densities may have a significant impact on the final spectra and yields of strange and ordinary baryons or anti-baryons, of particular interest, for $\bar{\Lambda}$ and \bar{p} is baryon-antibaryon($B\bar{B}$) annihilation. Importantly, the $B\bar{B}$ annihilation effects are shown to be more effective at SPS energies [133, 134].

It is known that $\bar{\Lambda}$ and \bar{p} can have different annihilation cross-sections and it may be possible that because of this difference final yields of $\bar{\Lambda}$ and \bar{p} are modified differently, which may cause an apparent enhancement in $\bar{\Lambda}/\bar{p}$ ratios. Therefore, before attributing $\bar{\Lambda}/\bar{p}$ enhancement to a signature for strangeness enhancement and hence to the formation of QGP, it is crucial that we understand the impact of $B\bar{B}$ -annihilation on $\bar{\Lambda}$ and \bar{p} production in detail.

In this work, our goal is to demonstrate the sensitivity of Λ -hyperon production and $\bar{\Lambda}/\bar{p}$ ratio to $B\bar{B}$ -annihilation by analyzing average transverse mass of Λ & $\bar{\Lambda}$ and ratios of $\bar{\Lambda}$ -to- \bar{p} as a function of centrality and collision energy in central Pb+Pb collisions at $\sqrt{s_{NN}} = 6.27, 7.62, 8.77, 12.3$ and 17.3 GeV (corresponding to the $E_{lab} = 20, 30, 40, 80$ and 158 AGeV, respectively) with and without including the effect of $B\bar{B}$ annihilations in a hadronic transport model, UrQMD (Ultra-Relativistic Quantum Molecular Dynamics) [135, 136]. As the dynamics of particle production at SPS energies are believed to be dominated by hadronic interactions so we choose UrQMD model because it describes the phenomenology of particle production at SPS energy reasonably well.

The organization of this work is as follows. In section 5.2 we briefly describe the UrQMD transport model and implementation of $B\bar{B}$ -annihilation in UrQMD followed by results and discussions in section 5.3. Finally we summarize our findings in section 5.4.

5.2 UrQMD Model

UrQMD (Ultra-relativistic Quantum Molecular Dynamics) is a microscopic transport model that provides a unified framework to describe the phenomenology of particle production in pp, p+A and A+A collisions over a broad energy range [136]. This model is based on an effective solution to relativistic Boltzmann equation on a non-equilibrium approach as shown below,

$$p^\mu \partial_\mu f_i(x^\nu, p^\nu) = C_i. \quad (5.3)$$

The above equation describes the time evolution of the distribution function f_i in coordinate and momentum space for a particle species "i" and includes the full collision term C_i . The underlying degrees of freedom in UrQMD are hadrons and strings. Here an individual particle propagates on a straight line until the relative distance between two particles is smaller than a critical distance given by the total interaction cross-section between two particles. These cross-sections in UrQMD are either calculated by the principle of detailed balance or additive quark model (AQM) or parameterized from the available experimental data. For resonance excitations or decays the Breit-Wigner formalism is implemented. In UrQMD, the particle production dynamics is either governed by the decays of baryon or meson resonances or via a string excitation and fragmentation. Until now, UrQMD has 55 Baryons and 32 Mesons that also include ground state particles and all resonances with mass up to 2.25 GeV.

5.2.1 Baryon-anti-baryon annihilation

In UrQMD, to model $p\bar{p}$ annihilation cross-section, the elementary annihilation cross-sections are obtained by fitting the available data. It is to be noted that UrQMD uses same data driven parameterization for $p\bar{p}$ and $B\bar{B}$ annihilation cross-sections at same $\sqrt{s_{NN}}$. The parameterized annihilation cross-section used in UrQMD is shown below,

$$\sigma_{ann}^{p\bar{p}} = \sigma_0^N \frac{s_0}{s} \left[\frac{A^2 s_0}{(s - s_0)^2 + A^2 s_0} + B \right]. \quad (5.4)$$

Where σ_0^N , s_0 , A and B are arbitrary free parameters used to describe \sqrt{s} dependence of annihilation cross section and their values are 120 mb, $4m_N^2$, 50 MeV and 0.6, respectively [135].

For annihilation channels that involve a strange-baryon/antibaryon, such as $\bar{\Lambda}p$ or $\Lambda\bar{p}$, an additional correction factor is introduced based on AQM, given by

$$\sigma_{ann}^{B\bar{B}} = (1 - 0.4\frac{s_B}{3})(1 - 0.4\frac{s_{\bar{B}}}{3})\sigma_{ann}^{p\bar{p}}, \quad (5.5)$$

where s_B and $s_{\bar{B}}$ is the strangeness number for baryon and antibaryon, respectively. Thus, annihilation cross-section of $\bar{\Lambda} - p$, ($\sigma_{ann}^{\bar{\Lambda}p}$) is less than annihilation cross-section of $p-\bar{p}$ ($\sigma_{ann}^{p\bar{p}}$). From equation 5.5 we see the annihilation cross-section (σ_{ann}) has an approximate $\frac{1}{\sqrt{s_{NN}}}$ dependence with beam energy.

5.3 Results

For this study, we generated about 1 million Pb+Pb UrQMD events with impact parameter, $b < 3.4$ fm at $\sqrt{s_{NN}} = 6.27$ GeV, 7.62 GeV, 8.77 GeV, 12.3 GeV and 17.3 GeV in two configurations i.e, with and without incorporating the $B\bar{B}$ annihilation.

5.3.1 Particle yields

As a first step we study the mid-rapidity yields of Λ , $\bar{\Lambda}$ and \bar{p} in central Au+Au collisions at $\sqrt{s_{NN}} = 4.7$ GeV (11.7 AGeV) and Pb+Pb collisions from $\sqrt{s_{NN}} = 6.27$ to 17.3 GeV (20 AGeV to 158 AGeV in laboratory frame). Solid and dashed lines in Fig. 5.1 shows the collision energy dependence of Λ , $\bar{\Lambda}$ and \bar{p} yields (dN/dy) at mid-rapidity ($|y| < 0.5$) from UrQMD, compared with the corresponding data from E917, NA49 and STAR. The NA49 data are from 0-7% central Pb+Pb collisions for $\sqrt{s_{NN}} = 6.27$ to 12.3 GeV and 0-10% central collision for $\sqrt{s_{NN}} = 17.3$ GeV. STAR data are from $\sqrt{s_{NN}} = 7.7$ and 11.5 GeV Au+Au collisions in 0-5% centrality. Data from the E917 experiment are slightly offset from the mid-rapidity (mid-rapidity is $y \sim 1.6$ at this beam energy). The yields of both $\bar{\Lambda}$ and \bar{p} are measured in the rapidity range $1.0 < y < 1.4$ and centrality class of 0-12%. The \bar{p} yields in E917 data are not feed down corrected. NA49 and STAR Λ and $\bar{\Lambda}$ yields are corrected for feed-down from weak decays of Ξ but include contributions from the electromagnetic decays of Σ^0 . In order to be consistent with the existing data, final yields of $\Lambda(\bar{\Lambda})$ from UrQMD also include the yields of $\Sigma^0(\bar{\Sigma}^0)$ but for the simplicity of the notation hereafter in texts and figures we will only denote $\Lambda(\bar{\Lambda})$.

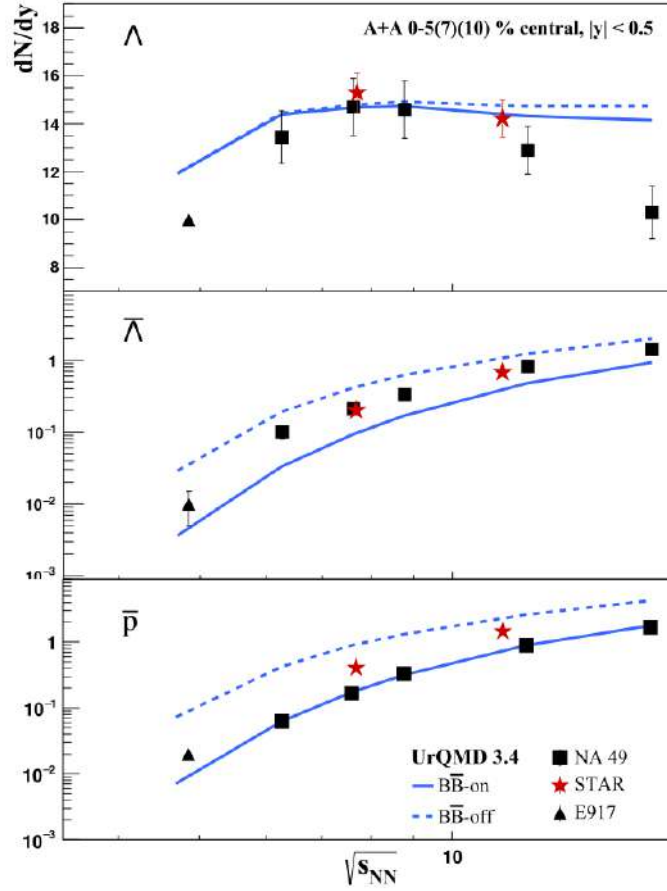


Figure 5.1: [Color online] Collision energy dependence of $\Lambda, \bar{\Lambda}$ and \bar{p} yields (dN/dy) at mid-rapidity ($|y| < 0.5$) in central Au+Au/Pb+Pb collision from UrQMD with $B\bar{B}$ annihilation (solid line) and without $B\bar{B}$ annihilation (dashed line) from $\sqrt{s_{NN}} = 4.7$ to 17.3 GeV. Also shown a comparison with available data from AGS [128], NA49 [127] and STAR BES [20].

As shown in Fig. 5.1, dN/dy of $\bar{\Lambda}$ and \bar{p} , both in data and UrQMD, is a rapidly increasing function of collision energy but Λ dN/dy exhibits a non-monotonic energy dependence in data. The Λ dN/dy first increases from 4.7 to 8 GeV followed by a decrease towards top SPS energies. A peak in Λ dN/dy is observed between 7-8 GeV. This non-trivial energy dependence of Λ dN/dy may be because the Λ production is dominated by the associated production channel at high net-baryon densities or low beam energies and the observed peak around $\sqrt{s_{NN}} = 8$ GeV is perhaps consistent with the speculation of maximum net-baryon density at this collision energy [137]. Data-to-model comparison, also presented in Fig. 5.1, shows a reasonable agreement for Λ and \bar{p} dN/dy , but for $\bar{\Lambda}$, mid-rapidity dN/dy is underestimated.

In addition, we also study the effect of $B\bar{B}$ annihilation on $\Lambda, \bar{\Lambda}$ and \bar{p} dN/dy which is

also shown in Fig. 5.1. The effect is most prominent for $\bar{\Lambda}$ and \bar{p} because, in a baryon-rich environment, as produced in these collisions, it is more likely for $\bar{\Lambda}$ and \bar{p} to get annihilated with protons. The effect is however, not so significant for Λ s except at higher energies where, $\bar{\Lambda}$ and \bar{p} yields have also increased thereby, providing necessary phase space for Λ s to annihilate with $\bar{\Lambda}$ and \bar{p} .

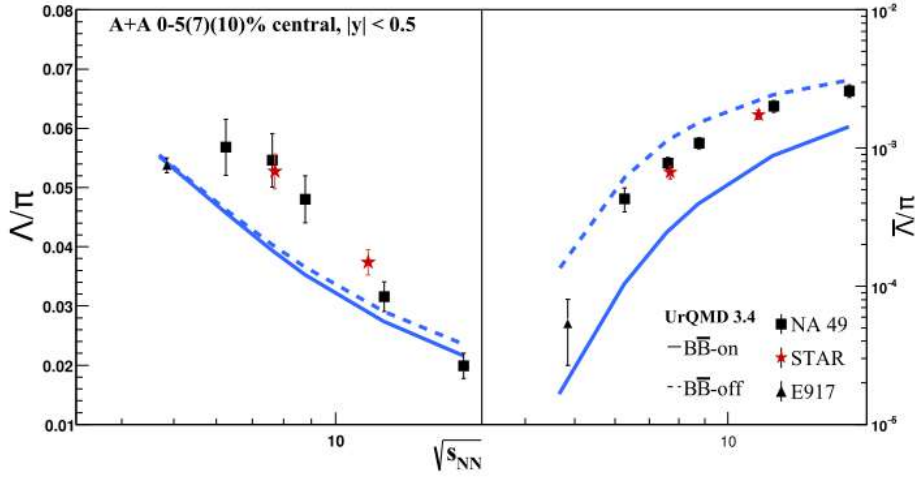


Figure 5.2: [Color online] Beam energy dependence of Λ and $\bar{\Lambda}$ to pions ($1.5(\pi^+ + \pi^-)$) at mid-rapidity ($|y| < 0.5$) in central Au+Au/Pb+Pb collision from UrQMD with $B\bar{B}$ annihilation (solid line) and without $B\bar{B}$ annihilation (dashed line) from $\sqrt{s_{NN}} = 4.7$ to 17.3 GeV. UrQMD results are compared with available data from AGS [128, 138, 139], NA49 [127] and STAR BES [20, 122].

Fig. 5.2 shows results of the ratios of the mid-rapidity yields of Λ and $\bar{\Lambda}$ to that of $1.5(\pi^+ + \pi^-)$ as a function of $\sqrt{s_{NN}}$ from the UrQMD model calculation. Also shown in the same, data from central 0-5% Au+Au and 0-7% Pb+Pb collisions in RHIC and SPS energies, respectively. The general trend in the existing data are in good agreement with the UrQMD model calculations. The Λ/π ratios both in data and UrQMD hadronic transport calculations exhibit a sharp decrease with increasing energy however, quantitatively, UrQMD can not describe the data very well between $\sqrt{s_{NN}} = 6-9$ GeV. This may be because UrQMD overestimates pion yields in this energy range. For $\bar{\Lambda}$, just like the yield, UrQMD (with $B\bar{B}$ on) underestimates the ratios of $\bar{\Lambda}/\pi$ as well. As it is argued that the associated Λ production dominates at lower energies, we plot Λ/K^+ in Fig.5.3 and overlay available data from NA49 and STAR. UrQMD calculations describes the data reasonably well. It is however, interesting

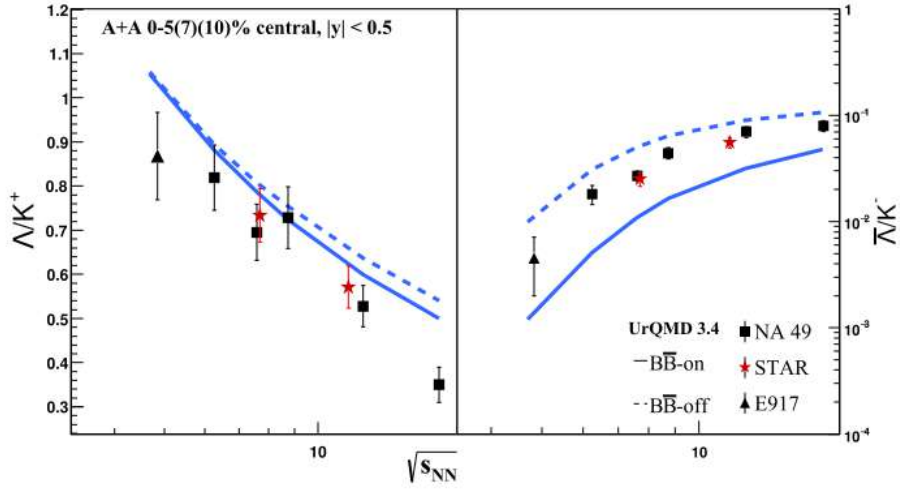


Figure 5.3: [Color online] Beam energy dependence of Λ/K^+ and $\bar{\Lambda}/K^-$ at mid-rapidity ($|y| < 0.5$) in central Au+Au/Pb+Pb collision from UrQMD with $B\bar{B}$ annihilation (solid line) and without $B\bar{B}$ annihilation (dashed line) from $\sqrt{s_{NN}} = 4.7$ to 17.3 GeV. UrQMD results are compared with available data from AGS [128, 138, 139], NA49 [127] and STAR BES [20, 122].

to note that despite the large mass difference between Λ and K^+ , ratios of yields at lower energies approach unity. This indicates Λ s and K^+ s are indeed produced in association but this is not the case for $\bar{\Lambda}$. $\bar{\Lambda}/K^-$ ratios are significantly below unity and exhibit a monotonous energy dependence implying Λ - $\bar{\Lambda}$ pair-production as a dominant source of $\bar{\Lambda}$ production.

5.3.2 Averaged transverse mass

Next, we study the effect of $B\bar{B}$ annihilation on the average transverse mass ($\langle m_T \rangle - m_0$) of Λ and $\bar{\Lambda}$ as a function of $\sqrt{s_{NN}}$. The average transverse mass represents an effective temperature (T_{eff}) of a thermalized medium that include the original thermal energy (T_{th}) of the medium and the particle-specific kinetic energy from the hydrodynamic radial flow (β). The kinetic energy of particles in a thermal medium depend on the mass of the particle alone ($m\beta^2$). Massive particles have higher T_{eff} and vice-versa. Interestingly, although Λ and $\bar{\Lambda}$ have same mass, their $\langle m_T \rangle - m_0$ are however, different in magnitude and the difference is seen to increase with the decrease in beam energy or increase in net baryon-density [20]. In Fig. 5.4, UrQMD calculations for $\langle m_T \rangle - m_0$ for Λ and $\bar{\Lambda}$ as a function of $\sqrt{s_{NN}}$ are shown together with the data points from NA49 and STAR [20, 127]. UrQMD calculations also show a similar trend in

the difference in magnitudes of $\langle m_T \rangle - m_0$ for Λ and $\bar{\Lambda}$ as a function of $\sqrt{s_{NN}}$. This observed split in the magnitude of $\langle m_T \rangle - m_0$ for Λ and $\bar{\Lambda}$ can be understood as a consequence of $B\bar{B}$ annihilation. In a medium with high baryon density, low momenta $\bar{\Lambda}$ s have higher chance to annihilate with p compared to Λ s that annihilate with \bar{p} . This causes lowering of low p_T yields while keeping the high p_T yields unchanged, resulting in a hardening of $\bar{\Lambda}$'s p_T -spectra and leading to systematically higher values of average $\langle m_T \rangle - m_0$ for $\bar{\Lambda}$. This difference in the magnitude of $\langle m_T \rangle - m_0$ between Λ and $\bar{\Lambda}$ diminishes with increasing $\sqrt{s_{NN}}$ as the effect of $B\bar{B}$ annihilation gradually weakens with decreasing baryon density. Although, UrQMD can qualitatively reproduce the trend in the data well but the quantitative mismatch is because UrQMD underestimates the radial flow.

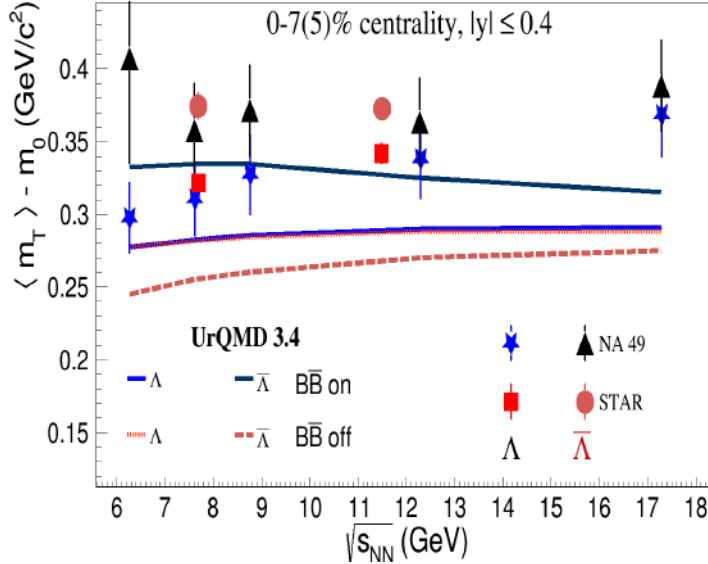


Figure 5.4: Energy dependence of mean transverse mass, $\langle m_T \rangle - m_0$, at mid-rapidity ($|y| < 0.4$) for Λ and $\bar{\Lambda}$ in central Pb+Pb collisions at $\sqrt{s_{NN}} = 6.27$ to 17.3 GeV from UrQMD with $B\bar{B}$ annihilation and without $B\bar{B}$ annihilation. UrQMD calculations are compared with existing results from central Pb+Pb collisions at $\sqrt{s_{NN}} = 6.27$ to 17.3 from NA49 [127] and STAR results from central Au+Au collisions at $\sqrt{s_{NN}} = 7.7$ and 11.5 GeV [20].

It is interesting to note that UrQMD calculations without incorporating $B\bar{B}$ annihilation also show a difference in the magnitudes of $\langle m_T \rangle - m_0$ for Λ and $\bar{\Lambda}$ but with an opposite trend i.e, $\langle m_T \rangle - m_0$ of Λ is systematically higher than $\bar{\Lambda}$. In absence of $B\bar{B}$ annihilation, this split in $\langle m_T \rangle - m_0$ can be explained taking into account different energy thresholds of Λ and $\bar{\Lambda}$ production in hadronic interaction channels. At lower $\sqrt{s_{NN}}$ where baryon density is high, Λ s

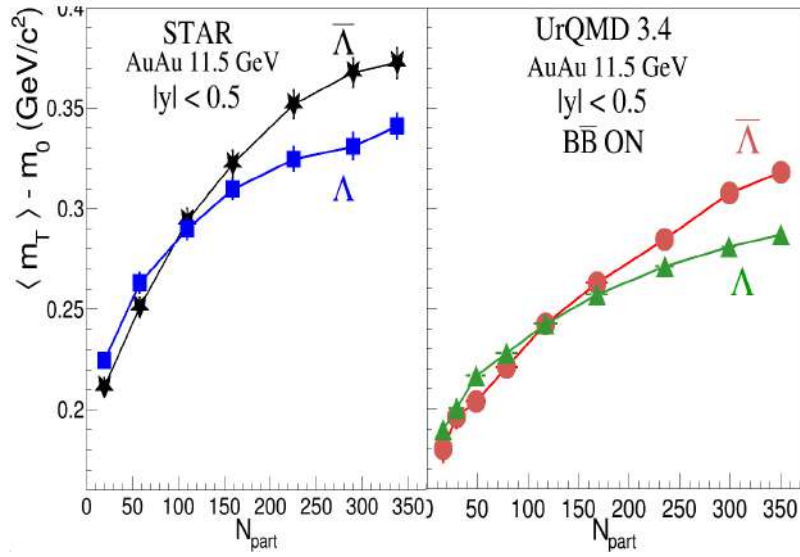


Figure 5.5: The $\langle m_T \rangle - m_0$ spectra for Λ and $\bar{\Lambda}$ as a function of N_{part} as obtained from the STAR data for Au+Au collisions at $\sqrt{s_{NN}} = 11.5$ GeV (left) [20] and compared it with UrQMD calculations including BB annihilation at the same $\sqrt{s_{NN}}$ (right).

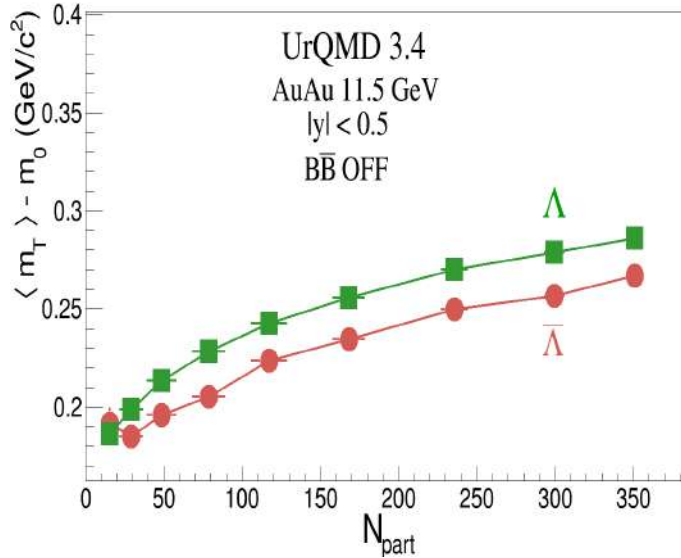


Figure 5.6: $\langle m_T \rangle - m_0$ for Λ and $\bar{\Lambda}$ w.r.to N_{part} at $\sqrt{s_{NN}} = 11.5$ GeV, AuAu collision, mid-rapidity $|y| < 0.5$ in UrQMD without including BB annihilation.

are dominantly produced in associated production channel $N + N \rightarrow \Lambda + K^+ + N$, which has an energy threshold of ~ 700 MeV, whereas, $\bar{\Lambda}$ production is dominated by $\Lambda\text{-}\bar{\Lambda}$ pair production channel in $N + N \rightarrow \Lambda + \bar{\Lambda} + N + N$ that has an energy threshold of ~ 2200 MeV. Therefore, the energy, in excess to threshold energy, available to impart kinetic energy to the produced particles in $\Lambda\text{-}\bar{\Lambda}$ pair-production channel is small. Thus, produced $\bar{\Lambda}$ s mostly have smaller transverse momenta and hence lower values of average transverse mass than Λ s.

We further study the interplay between $B\bar{B}$ annihilation and threshold energy for producing Λ and $\bar{\Lambda}$ by calculating $\langle m_T \rangle - m_0$ for Λ and $\bar{\Lambda}$ as a function of collision centrality represented by the number of participating nucleons (N_{part}). Fig. 5.5 shows the $\langle m_T \rangle - m_0$ for Λ and $\bar{\Lambda}$ as a function of N_{part} as obtained from the STAR data for Au+Au collisions at $\sqrt{s_{NN}} = 11.5$ GeV (left) [20] and compared it with UrQMD calculations including $B\bar{B}$ annihilation at the same $\sqrt{s_{NN}}$ (right). Both data and UrQMD model exhibit similar behaviour in $\langle m_T \rangle - m_0$ for Λ and $\bar{\Lambda}$ as a function of N_{part} . When the system size is small or at low N_{part} ($N_{part} < \sim 100$), the so called ‘‘threshold effect’’ is dominant as the baryon density is low, as discussed earlier. This results in higher values of $\langle m_T \rangle - m_0$ for Λ than $\bar{\Lambda}$ and then followed by a switch-over for $N_{part} > 100$, where the trend gets reversed i.e., $\langle m_T \rangle - m_0$ for $\bar{\Lambda}$ is greater than Λ . This happens because as the system size increases, baryon stopping becomes higher which causes more baryons to accumulate at mid-rapidity. Thus, the effects of $B\bar{B}$ annihilation start to become more significant causing low p_T $\bar{\Lambda}$ s to annihilate more than Λ s resulting in hardening of $\bar{\Lambda}$ s p_T spectra, as discussed earlier. As can be seen from Fig. 5.6, when $B\bar{B}$ annihilation is not included in UrQMD, $\langle m_T \rangle - m_0$ for Λ is higher than $\bar{\Lambda}$ at all N_{part} . This essentially suggests that in central collisions at lower $\sqrt{s_{NN}}$ effects of $B\bar{B}$ annihilation can not be ignored particularly while considering any phenomenon that involves yields or spectra of baryons and anti-baryons in the final state.

5.3.3 Baryon-anti-baryon annihilation with p_T and rapidity

Having seen that $B\bar{B}$ annihilation can significantly impact final spectra of baryons and anti-baryons, we now proceed to study the effect of $B\bar{B}$ annihilation on $\bar{\Lambda}/\bar{p}$ ratios. Before that first we investigate how $B\bar{B}$ annihilation modify yields of $\bar{\Lambda}$ and \bar{p} as a function of p_T and rapidity (y) at different $\sqrt{s_{NN}}$.

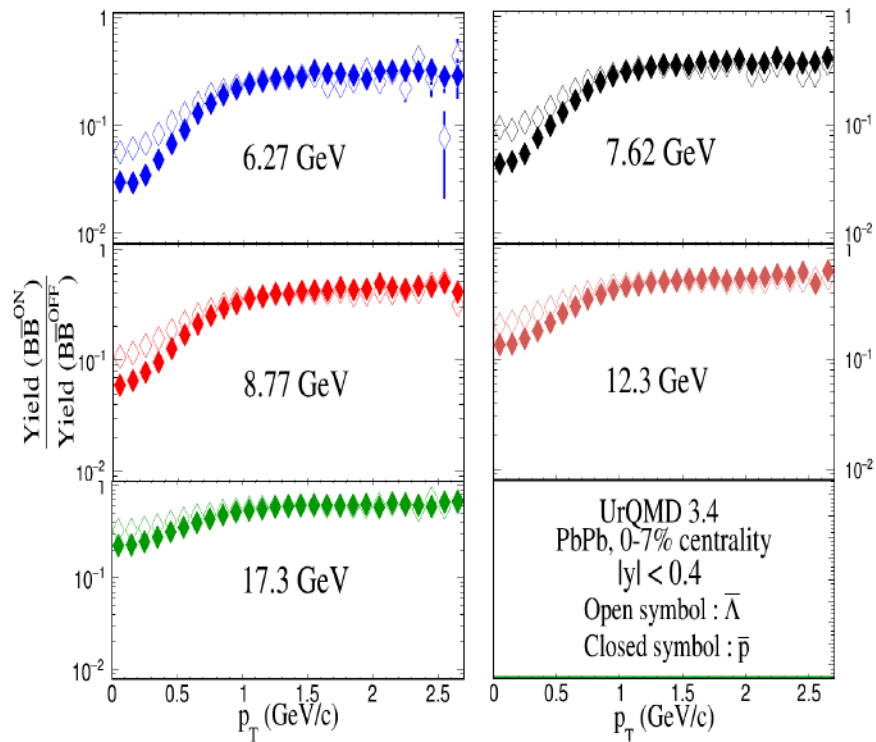


Figure 5.7: The p_T dependence of ratios of yields of $\bar{\Lambda}$'s (open marker) and \bar{p} 's (closed marker), with and without incorporating $\text{B}\bar{\text{B}}$ annihilation calculated from UrQMD in central Pb+Pb collisions at $\sqrt{s_{NN}} = 6.27$ to 17.3 GeV.

In Fig. 5.7, we plot the ratio of yields for $\bar{\Lambda}$ (open symbol) and \bar{p} (closed symbol) as a function of p_T with and without incorporating $B\bar{B}$ annihilation in UrQMD. This plot suggests that the effect of annihilation is maximum at low- p_T and there is a particle species dependence i.e, \bar{p} is annihilated more than $\bar{\Lambda}$ thus, final yields of \bar{p} are more suppressed than $\bar{\Lambda}$. For $p_T > 1$ GeV/c the effect of $B\bar{B}$ annihilation on both $\bar{\Lambda}$ and \bar{p} appear to be same. The overall nature of the p_T dependent modification of $\bar{\Lambda}$ and \bar{p} yields because of $B\bar{B}$ annihilation appears to be similar at all $\sqrt{s_{NN}}$ studied here except, the magnitude of suppression increases with decreasing $\sqrt{s_{NN}}$, implying more annihilation of $\bar{\Lambda}$ and \bar{p} at lower $\sqrt{s_{NN}}$. Similarly, the effect of $B\bar{B}$ annihilation on rapidity dependence of $\bar{\Lambda}$ and \bar{p} yields are studied and plotted in Fig. 5.8. The annihilation effect is most significant at mid-rapidity in low $\sqrt{s_{NN}}$ for both $\bar{\Lambda}$ and \bar{p} ,

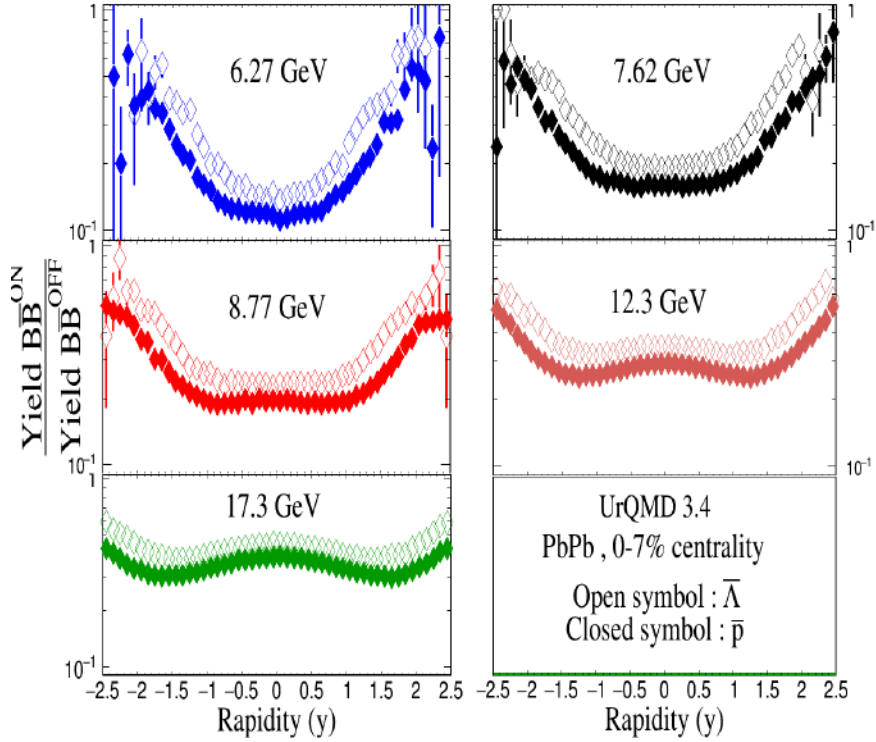


Figure 5.8: The rapidity dependence of ratios of yields of $\bar{\Lambda}$'s (open marker) and \bar{p} 's (closed marker), with and without incorporating $B\bar{B}$ annihilation calculated from UrQMD in central Pb+Pb collisions at $\sqrt{s_{NN}} = 6.27$ to 17.3 GeV.

characterized by a large suppression of ratio of yields obtained from model calculations with and without $B\bar{B}$ annihilation. As energy increases, the overall magnitude of suppression start to decrease however, the maximum suppression now occurs at forward rapidity instead of mid-

rapidity. This happens because with increasing energy baryon stopping is less and the high baryon density region gradually move from mid to forward rapidity. As a result, the effect of $B\bar{B}$ annihilation at higher $\sqrt{s_{NN}}$ becomes more significant at forward rapidity.

5.3.4 Estimation of annihilation fraction

Next we summarize the effect of $B\bar{B}$ annihilation on $\bar{\Lambda}$ and \bar{p} yields as a function of $\sqrt{s_{NN}}$ for low and inclusive p_T in Fig. 5.9. In this figure we quantify the magnitude of annihilation in terms of a quantity called annihilation fraction which is defined as relative difference in yields with and without $B\bar{B}$ annihilation ($Y^{B\bar{B}-on} - Y^{B\bar{B}-off}$) scaled by the yield obtained without incorporating $B\bar{B}$ annihilation.

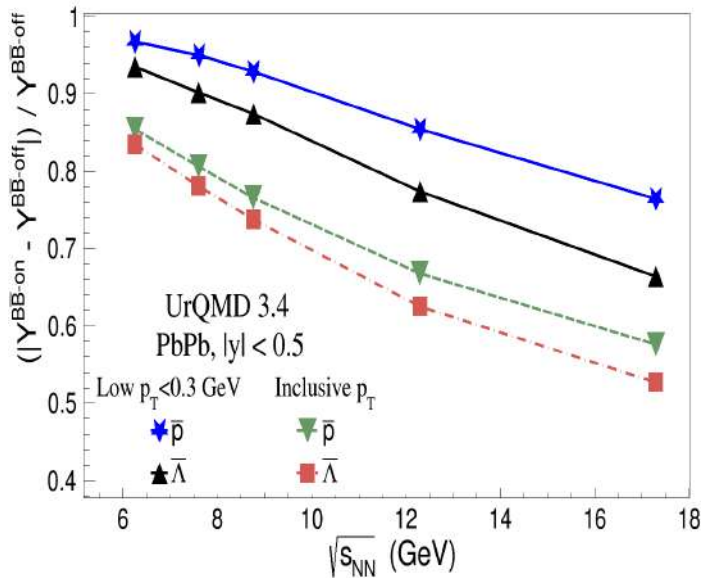


Figure 5.9: Annihilation fraction of \bar{p} and $\bar{\Lambda}$ as a function of $\sqrt{s_{NN}}$ for low and inclusive p_T from UrQMD.

From Fig. 5.9 it is clear that at low $\sqrt{s_{NN}}$, say at 6.27 GeV, more than 95% of the initially produced low- p_T \bar{p} are annihilated whereas, for $\bar{\Lambda}$ the annihilation fraction is about 92% to 94%. For inclusive p_T , annihilation fraction is below 90% for both the particles. As the energy increases annihilation fraction drops, i.e lesser number of initially produced baryons are annihilated. It is seen that for $\bar{\Lambda}$, annihilation fraction as a function $\sqrt{s_{NN}}$ drops faster than \bar{p} for both inclusive and low- p_T .

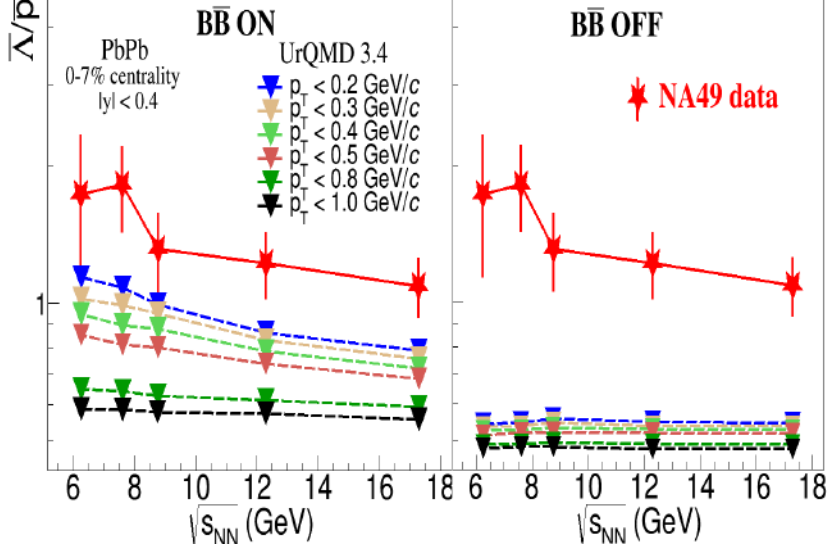
5.3.5 Effect of $B\bar{B}$ annihilation on $\bar{\Lambda}/\bar{p}$ ratios

Figure 5.10: The $\bar{\Lambda}/\bar{p}$ ratio at mid-rapidity as a function of collision energy at $\sqrt{s_{NN}} = 6.27$ to 17.3 GeV with (left) and without (right) $B\bar{B}$ -annihilation from UrQMD. Also shown the effect of different p_T cut on the ratio. Model calculation is compared with NA49 [131] data (feed-down uncorrected) at same $\sqrt{s_{NN}}$.

Finally, we calculate $\sqrt{s_{NN}}$ dependence of $\bar{\Lambda}/\bar{p}$ ratios with and without $B\bar{B}$ annihilation, as shown in Fig. 5.10, where NA49 data points are also included. We find that $\bar{\Lambda}/\bar{p}$ ratios are indeed sensitive to $B\bar{B}$ annihilation and its impact depend strongly on the kinematic selection, in particular, to the choice of p_T -range. We observe that in low p_T range ($p_T < 0.2$ GeV/c) $\bar{\Lambda}/\bar{p}$ ratios achieve maximum and it exceeds unity for the lowest collision energy. This trend for $\bar{\Lambda}/\bar{p}$ enhancement in the UrQMD model is qualitatively similar to data and somehow expected, because, annihilation cross-sections of $\bar{\Lambda}$ is less than \bar{p} which result in more suppression of \bar{p} yield in the final state compared to $\bar{\Lambda}$, leading to an enhancement in $\bar{\Lambda}/\bar{p}$ ratios. The effect is certainly more pronounced in low- p_T as we have already seen in Fig. 5.7 that annihilation probability increases with decrease in p_T . It is also interesting to note when UrQMD calculations are done without incorporating $B\bar{B}$ -annihilation, irrespective of the choice of p_T range no enhancement can be seen in $\bar{\Lambda}/\bar{p}$ ratios. Here we want to draw attention on a fact that the first report on $\bar{\Lambda}/\bar{p}$ ratios from NA49, as shown in Fig. 5.10 [131] are calculated from feed-down un-corrected $\bar{\Lambda}$ yields [126] and we speculate this could be a main reason for quantitative disagreement

between data and model calculation. Therefore to verify our speculation we now calculate $\bar{\Lambda}/\bar{p}$ ratios from the feed-down corrected data. Since feed-down corrected yields are not directly available for different p_T range, we extract feed-down corrected yields for both $\bar{\Lambda}$ and \bar{p} using Blast-wave fit [140] to feed-down corrected p_T spectra [127] and integrating it over desired p_T range. Results for the feed-down corrected $\bar{\Lambda}/\bar{p}$ ratios are shown in Fig. 5.11 for low and inclusive p_T at $\sqrt{s_{NN}} = 8.77, 12.3$ and 17.3 GeV together with the results from UrQMD model calculations including $B\bar{B}$ annihilation at same $\sqrt{s_{NN}}$ and in same p_T -range.

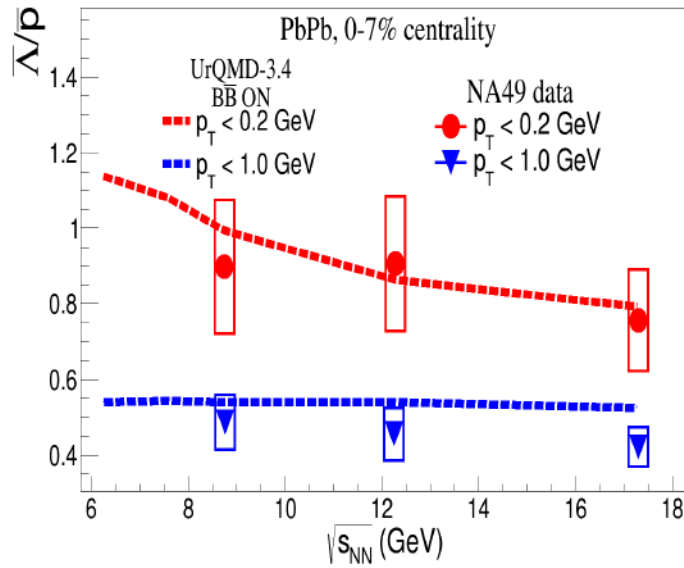


Figure 5.11: Dependence of $\bar{\Lambda}/\bar{p}$ ratios as a function of $\sqrt{s_{NN}}$ with $B\bar{B}$ annihilation in UrQMD and compared it with feed-down corrected NA49 data points at low p_T and inclusive p_T for central (0-7%) PbPb collisions.

After the feed-down correction, $\bar{\Lambda}/\bar{p}$ ratios in data and model calculations show very good agreement, although with large uncertainty on data. It is to be noted that the enhancement in $\bar{\Lambda}/\bar{p}$ ratios both in data and model calculation is only observed at low- p_T but for inclusive p_T ratios are almost flat with $\sqrt{s_{NN}}$. Therefore, it may be inferred that the observed enhancement in $\bar{\Lambda}/\bar{p}$ ratios in data could be an effect of $B\bar{B}$ annihilation. We further study $\bar{\Lambda}/\bar{p}$ ratios as function of centrality both from data and UrQMD at $\sqrt{s_{NN}} = 17.3$ GeV. The ratios in data are extracted from feed-down corrected yields using same procedure mentioned above and compared with UrQMD calculation with $B\bar{B}$ annihilation in Fig. 5.12. The above comparison between data and model indicate that for inclusive p_T , $\bar{\Lambda}/\bar{p}$ ratios remain nearly flat as a

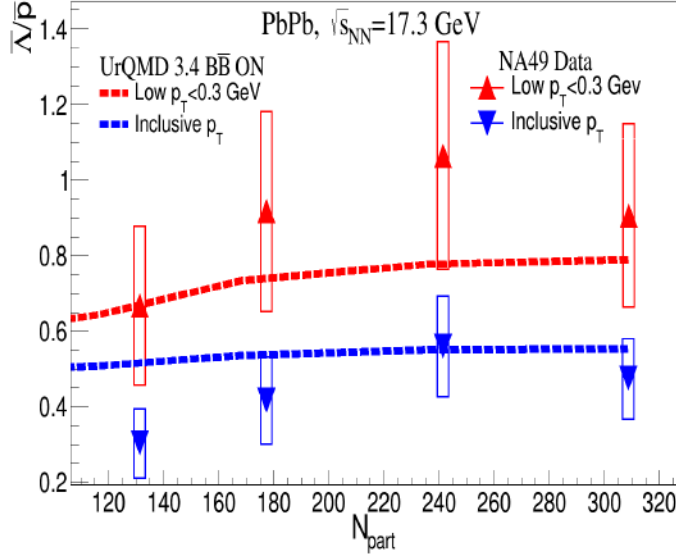


Figure 5.12: $\bar{\Lambda}/\bar{p}$ ratios as a function of N_{part} or centrality both from UrQMD ($\bar{B}\bar{B}$ ON) and feed-down corrected NA49 data at $\sqrt{s_{NN}} = 17.3$ GeV at low p_T and inclusive p_T .

function of centrality for both in data and model. For low- p_T , ratio increases from peripheral to central collision in UrQMD as well as in data although, uncertainties on data points are quite large. This systematic agreement between feed-down corrected data and UrQMD model including $\bar{B}\bar{B}$ annihilation further suggests that there is a strong impact of $\bar{B}\bar{B}$ annihilation on $\bar{\Lambda}/\bar{p}$ ratios and the enhancement in $\bar{\Lambda}/\bar{p}$ ratios may not be a necessary indication for strangeness enhancement in data [141].

5.4 Summary

$\bar{\Lambda}/\bar{p}$ ratios have been measured at RHIC AGS and CERN SPS as a probe of strangeness enhancement. A large enhancement in the ratios were reported around 6-8 GeV collision energy, apparently consistent with the expectation of strangeness enhancement and hence to the onset of partonic deconfinement. However, at lower $\sqrt{s_{NN}}$, where baryon density is large, hadronic interactions like $\bar{B}\bar{B}$ annihilation can significantly influence the individual spectra and yields of $\bar{\Lambda}$ and \bar{p} . In this work, we therefore studied whether $\bar{B}\bar{B}$ annihilation has any role in enhancement of $\bar{\Lambda}/\bar{p}$ ratios. To do so, we used the UrQMD hadronic transport model taking into account $\bar{B}\bar{B}$ annihilation in the final state.

As a first step we established that $B\bar{B}$ annihilation effects are significant at the SPS energy range by studying its effect on the average transverse mass spectra, $\langle m_T \rangle - m_0$ for Λ and $\bar{\Lambda}$ as a function of $\sqrt{s_{NN}}$ and compared it with NA49 and STAR data. It is seen that despite the same mass of Λ and $\bar{\Lambda}$, the $\langle m_T \rangle - m_0$ for Λ and $\bar{\Lambda}$ are different in magnitude, in particular $\langle m_T \rangle - m_0$ for $\bar{\Lambda}$ is higher than Λ , and the difference is large at low $\sqrt{s_{NN}}$ and gradually reduces with increasing $\sqrt{s_{NN}}$. UrQMD can qualitatively reproduce the trend in $\langle m_T \rangle - m_0$ when $B\bar{B}$ annihilation is included. As a function of centrality, $\langle m_T \rangle - m_0$ for Λ and $\bar{\Lambda}$ exhibits an interesting feature, at small N_{part} $\langle m_T \rangle - m_0$ for Λ is higher than $\bar{\Lambda}$ and then the trend becomes opposite i.e, $\bar{\Lambda}$ has higher $\langle m_T \rangle - m_0$ than Λ for $N_{part} > 100$. This "switch over" can also be understood as a consequence of $B\bar{B}$ annihilation because in UrQMD calculation without $B\bar{B}$ annihilation, $\langle m_T \rangle - m_0$ for Λ is systematically higher than $\bar{\Lambda}$ at all N_{part} .

Finally we studied the effect of $B\bar{B}$ annihilation on $\bar{\Lambda}/\bar{p}$ ratios by comparing NA49 data with UrQMD calculations with $B\bar{B}$ annihilation. In this case UrQMD could reproduce the qualitative trend in $\bar{\Lambda}/\bar{p}$ enhancement in data as a function $\sqrt{s_{NN}}$. Subsequently we realize that $\bar{\Lambda}$ yields used for calculating the ratios in data are not feed-down corrected. Thus, we extract yields for $\bar{\Lambda}$ and \bar{p} from the feed-down corrected spectra using a Blast-Wave fit to the corrected spectra and then used corrected yields to compute the $\bar{\Lambda}/\bar{p}$ ratios for low and inclusive p_T . The feed-down corrected $\bar{\Lambda}/\bar{p}$ ratios show enhancement as a function of $\sqrt{s_{NN}}$ and centrality only for low- p_T whereas, for inclusive p_T no such enhancement is observed. The systematic of feed-down corrected $\bar{\Lambda}/\bar{p}$ ratios are seen to be in good agreement with UrQMD calculations including $B\bar{B}$ annihilation. This suggests that the observed enhancement $\bar{\Lambda}/\bar{p}$ ratios is not necessarily related to strangeness enhancement but can also be interpreted as $B\bar{B}$ annihilation effect. However, these findings can be concluded firmly from the measurements at the future facilities like FAIR where several orders of magnitude more data are foreseen to be collected.

Chapter 6

Searching for initial state fluctuations in heavy ion collisions using Principal Component Analysis at FAIR energy

6.1 Initial conditions in heavy ion collisions

Besides understanding the properties of quark gluon plasma, one of the major goals of hot QCD research program is to pin down the initial condition that prevails during the first few instants when two hadrons or nuclei collide at relativistic energies. The initial distributions of the colliding nucleons or of the partons are of particular interest because the subsequent stages of the evolution of the medium are controlled by initial conditions. In fact the interpretation of observables that are based on the final state particles [106, 107] depends to a large extent on the initial conditions. For example, extraction of medium properties like η/s or ξ/s or jet quenching parameter \hat{q} can only be done reliably provided the knowledge of initial condition are well constrained. Depending on the energy of the collisions, various types of models like Glauber model [142, 143], colour glass condensate (CGC) [144] are frequently being used to describe the initial states of the collisions. Conclusions about the correct descriptions of the

initial state configurations are made based on the model that describes the data well [145]. However, there is no established unique method which could be applied to probe solely the initial state of the collisions. It has been shown that the structures in the initial nucleonic or partonic states might be carried over by some observables that remain unaffected by the evolution of the medium. One type of such observables is the flow coefficients of various orders that reflect the momentum anisotropy in the final state particles as representatives of the initial state spatial anisotropies [146–148]. Extensive studies have been done in this area in heavy ion collisions spanning over a range of colliding energies and collision species. The prominent feature of the initial state configurations in such cases is that the arrangements of the colliding nucleons over a large number of events could be described as the convolution of several geometrical shapes like ellipse, triangle etc [149]. These geometries appear where the models like Monte-Carlo Glauber [150] with Woods-Saxon potential is used to describe the geometry of the collision. These asymmetries are studied experimentally with the help of the Fourier decomposition of the azimuthal distributions with respect to the reaction plane [151]. By now, it is well known that the initial conditions in heavy ion collisions are not smooth rather, they fluctuate from event to event. This event-by-event fluctuation of the collision geometry is a result of random fluctuations in the nucleon positions within the overlap region of two colliding nuclei. Such fluctuations may sometime cause large energy density in the localized regions known as the hot spots [147, 152, 153]. In a hydrodynamic picture, these hot spots are also transported to the final state which might cause large fluctuations in the final state observables. It is important to understand how these hot spots in the initial condition get reflected in the final state observables like anisotropic flow and flow fluctuations in-order to constrain both the initial model and transport properties of the produced medium.

In this work we have explored the sensitivity to these event wise initial state fluctuations by adopting a generalized approach where the phase-space momentum distributions of the final state particles are decomposed by using the Principal Component Analysis (PCA) technique [154]. This technique reduces the dimension of the correlated space and the eigenvalues of the prominent components represent the variance along that component. As the initial fluctuations could be imprinted in the distributions of any particular or in all final state variables, for a systematic study, we first implemented a spatial rearrangement of the nucleons on top of the

Woods-Saxon distribution so that hot spot like local regions could be created in the initial state. Subsequently, we study the PCA eigenvalues of the final state particles under various initial conditions as inputs. We have worked at an intermediate energy ($\sqrt{s_{NN}} = 6.27$ GeV) Pb+Pb collisions, which is likely to be accessible at the beam energy scan programme of RHIC [155] or at the upcoming FAIR facility [156] and at this energy, the initial state could be well described using nucleons and therefore we have introduced the hot spots like initial configurations at the nucleonic level. We have used UrQMD [135, 136] as the model for the transportation of the colliding nuclei, evolution of the medium and the production of the final state particles. At this energy, UrQMD describes most of the available data quite well. The chapter is organised as follows, the UrQMD model and its applicability at this energy has been already been discussed in chapter 5, section 5.2. So, we skip discussion on UrQMD here. We start by discussing PCA and its implementation in the present study in the section 2. The implementation of hot spots in the initial configuration has been discussed in the section 3, followed by results in section 4 and summary in the section 5.

6.2 Principal Component Analysis (PCA)

PCA is a technique being used widely in machine learning for pre-processing as it removes the correlated features in the input variables and reduces the running time [157]. This technique reduces a multi-dimensional feature space into lower dimension keeping the essential features nearly intact. This is an unsupervised statistical method by which the inter-relations between the input variables are examined and newer variables called principal components (PCs) are extracted. The new variables are represented by orthogonal eigenvectors and eigenvalues giving the variables and the corresponding variance respectively. It is seen that a large fraction of the total eigenvalues are contained in the first few components thereby reducing the original dimension of the data space into only those few dimensions. It should be noted that even though the original input variables have physical interpretations, the newer variables (PCs) being a combination or derived from the input variables might not be physically interpretable. Proper combinations might be attempted to obtain physically meaningful variables from the PCs [158]. The main advantage is to reduce the computing complexity and extract the desired

features. In this exercise, two steps are extremely important, first the construction of matrix representing the variables and then process to obtain the eigenvalues and eigenvectors. In our application, ROOT-based implementation TPrincipal [159] has been used for the decomposition using the matrices as described below.

In high energy heavy ion collisions, PCAs have been used primarily in analysing azimuthal correlation data first in [160], where the potential of the components in obtaining the finer structures of the azimuthal correlations was mentioned and was followed by an analysis of the CMS data using the PCA technique [161]. A connection between the PCA eigenvalues with the event-averaged flow coefficients was attempted in [162, 163]. The sensitivity in exploring the PCA eigenvalues to the initial partonic cluster structures at the initial phase was made in [164]. In this work, we have studied the PCA sensitivity to the initial nucleonic arrangements in a colliding nucleus which is responsible for hot spot like structures in heavy ion collisions. Here, for the PCA analysis the columns of the input matrix in a row is constructed by binning the distributions of the input variables in an event. All the events analysed are then form all such rows forming the entire matrix. As per PCA analysis, the PC1 represents the variance of the 1st decomposed component. The introduction of the grouping in the nucleonic structure is likely to cause hot spots in the initial state affecting the corresponding variance to be seen in the PCA eigenvalues.

6.3 Implementation of hot spot at the nucleon level in UrQMD

In the present study, we have implemented a rearrangement of nucleon positions to create hot spot like structures in the projectile (Pb) and target (Pb) nuclei in UrQMD transport model as described below. A nucleon is selected as a seed at random and the seed is taken as the center of the hot spot. All nucleons whose inter-nucleonic distance with respect to the seed nucleon on the transverse plane lie within a certain radial distance (parameter R), are brought closer to the seed nucleon by reducing the radial distances of the nucleons by a certain factor (parameter dR).

When the formation of one such localized group or say hot spot is completed, another unassigned nucleon is taken as the seed and the process continues till all nucleons are exhausted.

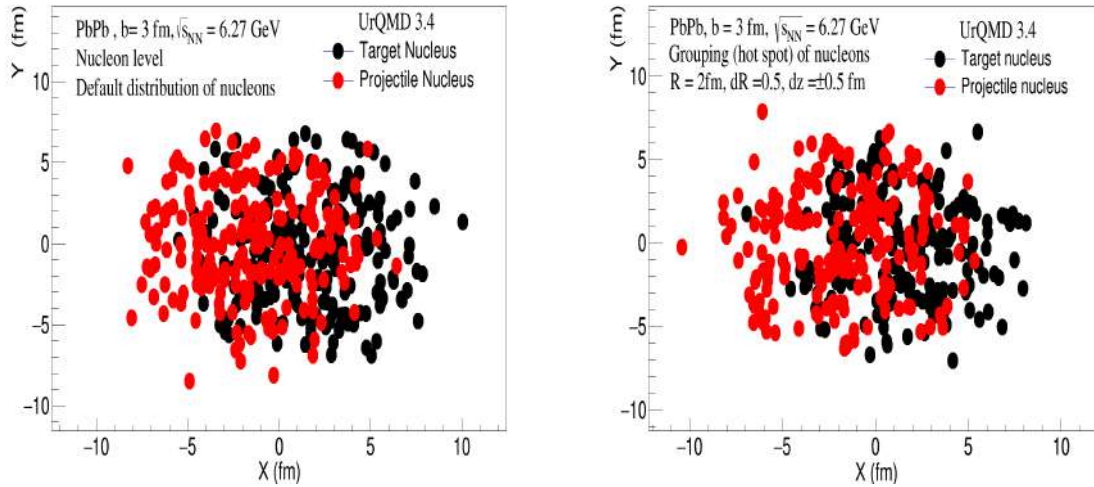


Figure 6.1: The XY distributions of the nucleons in projectile and target Pb nucleus in the transverse plane with the impact parameter $b = 3$ fm before hot spot creation (left) and after hot spot creation (right) with parameters $R=2$ fm, $dR=0.5$ and $dz=\pm 0.5$ fm.

The nucleons which are already a member of one hot spot are not considered in other hot spot. We perform the grouping of nucleons lying within ± 0.5 fm in the longitudinal (Z) direction (dZ) with respect to the seed nucleons. Fig. 6.1 shows the XY distributions of the centre of the nucleons in an event in the projectile and the target nuclei in the transverse plane with the impact parameter $b = 3$ fm before hot spot creation (left) and after hot spot creation (right) with parameters $R=2$ fm, $dR=0.5$ and $dz=\pm 0.5$ fm. We can see that before spatial rearrangement is done to create hot spots there is nearly uniform distribution of the nucleons in the colliding region and after the hot spot creation, we can see modifications in the spatial arrangements of the nucleons with some local domains created in the X-Y plane. In Fig. 6.2, we have shown the average number of nucleons per hot spot with parameters $R = 2$ fm, $dR = 0.5$ and $dZ = \pm 0.5$ fm for a colliding nucleus and we can see that mostly there are single-nucleons and groups of 2 to 3 nucleons. In the present case, the grouping with $R = 2$ fm, $dR = 0.5$ corresponds to a group with maximum 1 fm radius ($R \times dR$). It is seen that in the original distribution, mostly there are 1 or 2 nucleons within radius of 1 fm.

It is to be noted that multiplicity distribution from default distributions of nucleons in UrQMD and for different hot spot conditions with different radius parameters, $R = 1, 1.5, 2, 3$ fm, $dR = 0.5$ are nearly same. We have first studied the distributions of η , ϕ and p_T of the

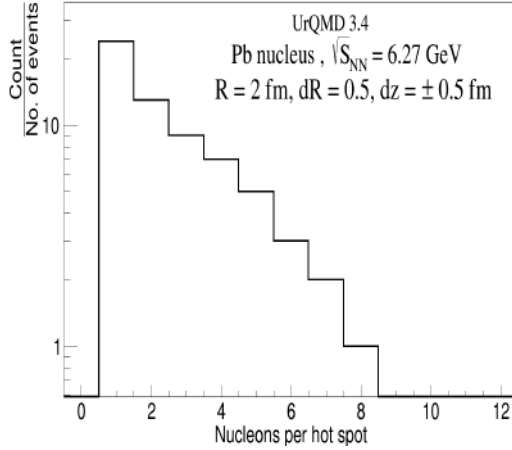


Figure 6.2: The number of nucleons per hot spot with parameters $R = 2 \text{ fm}$, $dR = 0.5$ and $dZ = \pm 0.5 \text{ fm}$ for one colliding Pb nucleus.

produced pions as obtained from UrQMD in one (1-D) and two (2-D [$\eta - \phi$, $\eta - p_T$ and $\phi - p_T$]) dimensional spaces under various conditions of nucleonic hot spots and then compared them with the original results. It should be mentioned that the implementation of the hot spots in the initial configuration is expected to cause fluctuations in the final state momentum variables of the produced particles. These fluctuations are then expected to be observed also in the variance of the principal components as represented by the corresponding eigenvalues. In the present case, hot spots are introduced in the transverse plane is expected to be primarily reflected in the azimuthal distributions of the produced particles. However, other momentum components might also get affected. We have therefore investigated both 1-D and 2-D distributions.

6.4 Results

In this work we have performed simulations using the UrQMD hadronic transport model with Pb+Pb collisions at $\sqrt{s_{NN}} = 6.27 \text{ GeV}$. We have generated 1 million central events (0-10%) to ensure that the resultant statistical errors on the event-averaged eigenvalues are not significant. We have used the produced positive and negative pions for this study.

For the PCA analysis, we have obtained the PCA eigenvalues for both the 1-D and the 2-D distributions of the produced pions under different initial conditions characterized by the R-parameter, so that the sensitivity of PCs to the rearrangements of nucleons in the initial

configurations could be tested. For the 1-D distributions, we have used η , ϕ and p_T variables dividing each event wise distributions into 20 bins and the event by event bin wise count form the columns of the matrix for each variable. We then obtained the PCA decompositions taking all the events in the sample as rows. We have then extended the study by taking the 2-D bins of $\eta - \phi$, $\eta - p_T$ and $\phi - p_T$ divided in each case into linearized 16 bins in each event as columns of the matrix and the number of events as rows. The regions covered under this study for p_T , η and ϕ are 0 to 3 GeV/c, -1 to 1 and $-\pi$ to π respectively.

Fig. 6.3 shows the eigenvalue distributions from the decomposition of the 1-D and 2-D distributions respectively for different values of the R parameter. It is seen that for all three cases of the 1-D distributions, the eigenvalues reduce drastically after that of the 1st component (PC1) and remains nearly flat for the higher order components. In case of the 1-D and 2-D distributions, the first component (PC1) is highest and changes with the parameter R, the higher components, although non-zero, does not show appreciable change with the rearrangements in the initial configurations of the nucleon positions. We have therefore analysed the PC1 only for both the 1-D and the 2-D distributions for further study. It is to be noted that the exclusion of the remaining eigenvalues might result in loss of some information [165].

We have studied the PC1 values for different initial configurations generated by varying the R parameter, i.e, R = 1 fm, 1.5 fm, 2 fm and 3 fm and compared with that for the unmodified condition for the p_T , η and ϕ distribution as shown in the Fig. 6.3. From Fig. 6.3, it is also clear that 1st PC component which contains the maximum information is very much sensitive to the R-parameter or in other words to the size of the hot spot.

To evaluate the relative sensitivity we have taken ratios of the PC1 corresponding to different R-values with respect to the unmodified distribution. Fig. 6.4 shows the variation of the PC1 ratio with respect to the radius parameter (R) for all three 1-D cases superposed with each other. In the figures, R = 0 corresponds to unmodified original UrQMD distribution. It is seen that up to R = 2 fm, the eigenvalues increase up to 10% with somewhat less separation between η , ϕ , p_T and then rises up to 20% for R parameter of 3 fm with wider separation for three variables.

It is also observed that the azimuthal distribution shows higher sensitivity in terms of the relative increase in PC1, which is more prominent at the higher R. This could be due to

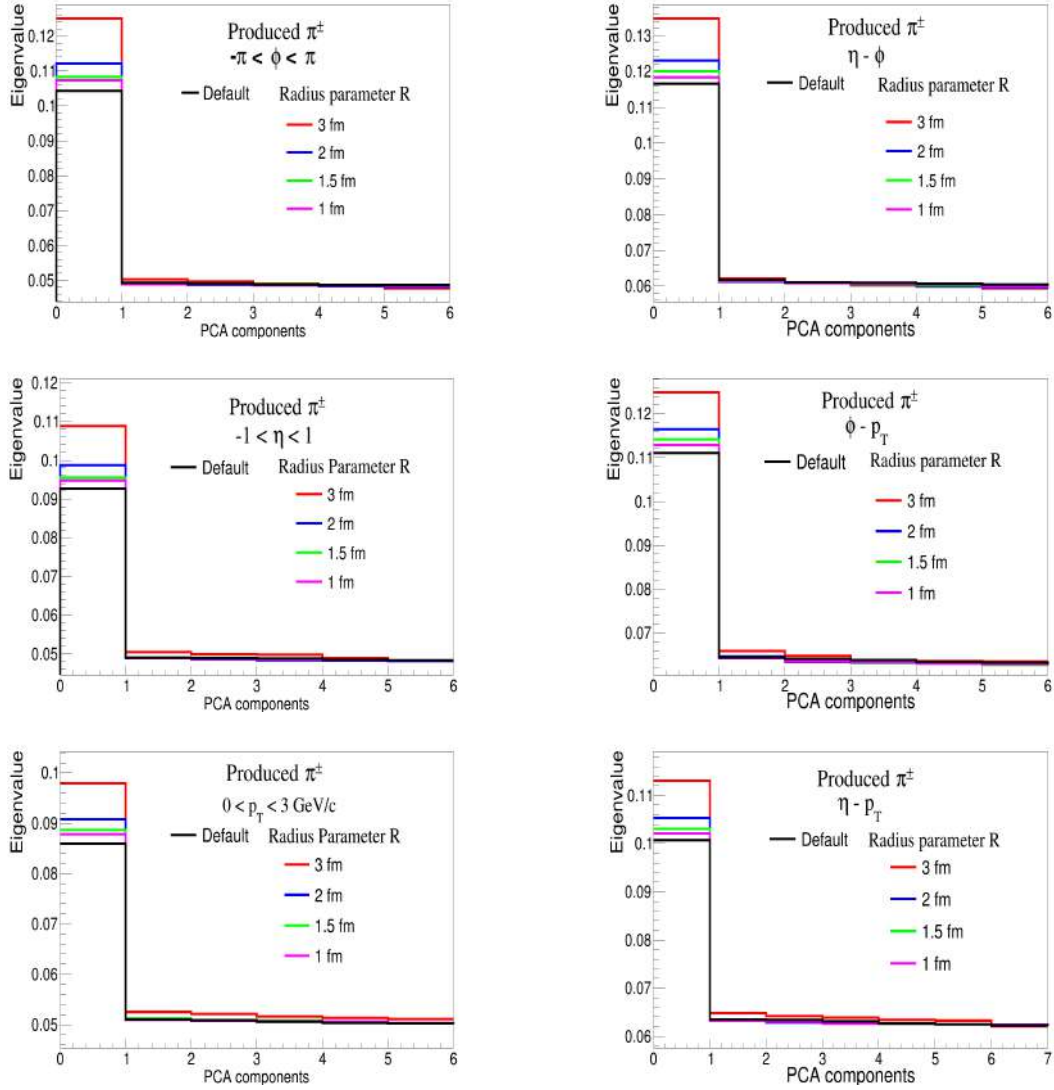


Figure 6.3: Eigenvalues in PC decomposition in 1-D distributions of ϕ , η and p_T bins (left) and for 2-D distributions for $(\eta-\phi)$, $(\phi-p_T)$, $(\eta-p_T)$ bins (right) of produced π^\pm for default UrQMD and with different hot spot conditions with radius parameters, $R = 1, 1.5, 2, 3 \text{ fm}$, $dR = 0.5$ and $dz = \pm 0.5 \text{ fm}$.

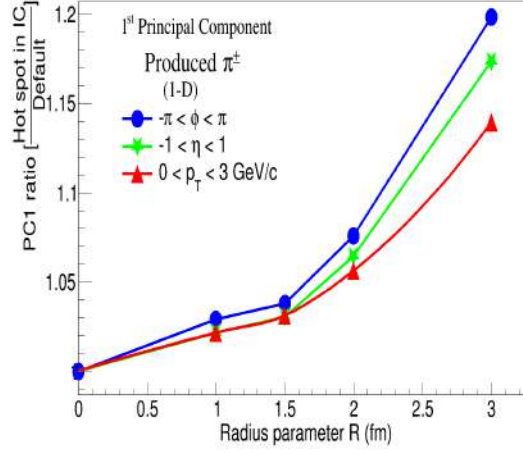


Figure 6.4: First eigenvalue (PC1) ratio of hot spot condition to the default UrQMD condition of produced π^\pm with radius parameter R for ϕ , η and p_T (1-D) distributions.

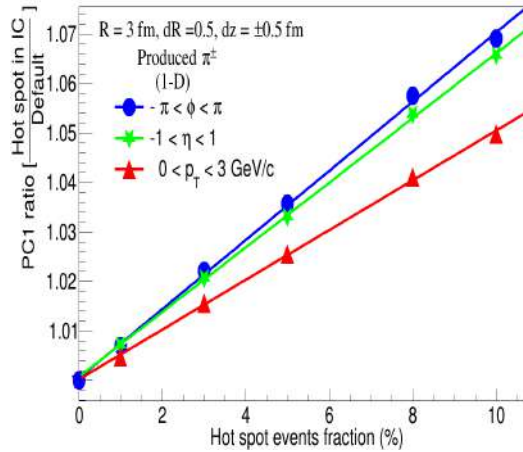


Figure 6.5: Variation of the first eigenvalue (PC1) ratio of hot spot to the default condition with the event fraction having hot spot like events in ϕ , η and p_T 1-D distributions.

the reason that the implementation of the grouping of nucleons is primarily on the azimuthal plane. It is however clear that the azimuthal nucleonic grouping affect the other momentum components i.e., η and p_T of the final state particles as well.

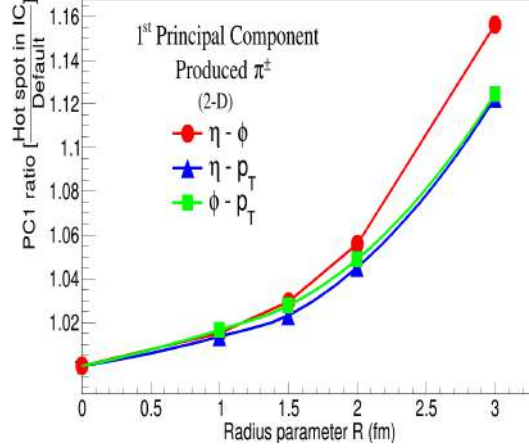


Figure 6.6: First eigenvalue (PC1) ratio of hot spot condition to the default UrQMD condition of produced π^\pm with radius parameter R for the decomposition of the 2-D distributions of $\eta-\phi$, $\eta-p_T$ and $\phi-p_T$.

In the study so far, modifications to the initial nucleon position distribution with specific parameters was introduced in every event. However, it is likely that the events with such hot-spot-like nucleon distribution will not occur in every event. In view of that, we have introduced nucleonic hot spots randomly in a varying fraction of events. Figure 6.5 shows the variation of PC1 ratio with respect to the percentage of event with hot-spot with radius parameter $R = 3$ fm, $dR = 0.5$ and $dz = \pm 0.5$ fm. It is seen that for an increase in an event fraction with hot-spot up to 10%, the event averaged PC1 increases linearly for all three distributions. The slope shows somewhat slower increase for the η and p_T distributions as compared to that for the azimuthal distributions.

The relative variation of the PC1 with respect to that unmodified configuration for the 2-D distributions is similar to those observed in 1-D cases as shown by the variation of the PC1 ratio with respect to R and the fraction of events with hot spot in initial configuration in Fig. 6.6 and Fig. 6.7 respectively. In the case of 2-D distributions, as expected from the 1-D results, the sensitivity is higher for the $(\eta - \phi)$ space. This variation is similar as that observed in case of 1-D distributions suggesting that the sensitivity does not improve much due to finer

structures.

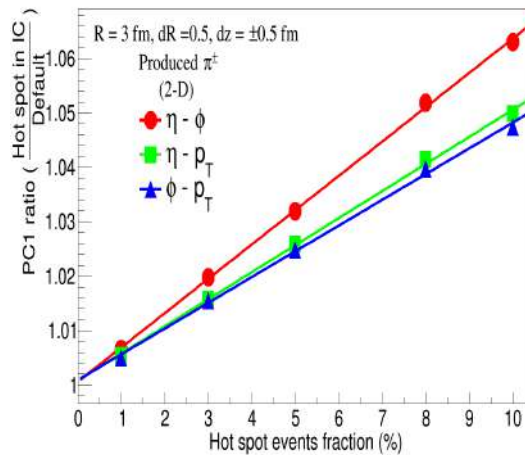


Figure 6.7: Variation of the first eigenvalue (PC1) ratio of hot spot to the default condition with the event fraction having hot spot like events in decomposition of the 2-D distributions in η - ϕ , η - p_T and ϕ - p_T .

From the results so far, the sensitivity of the PC1 is highest for the ϕ distribution which is likely to be connected to the azimuthal asymmetry of the produced particles. From the results of the asymmetric flow studies, it is observed that the asymmetry is higher for the mid-central collisions. Keeping this in mind, it is expected that the present observables should have similar response to the centrality of the collisions. We have therefore studied the eigenvalues for three different centralities i.e., $b=0$ - 3 fm, 5-7 fm and 8-10 fm for Pb+Pb collisions. In this study modifications to the initial nucleon positions have been introduced in all events. It is found that the eigenvalues for all the 1-D distributions increase with reduced centralities. As a specific example, we have shown in Fig. 6.8 the PC1 results for the azimuthal distributions at 3 different centralities in which the values increase by a factor of three from 0.1 at the most central to 0.3 at the mid-central events. The increase of PC1 for the ϕ -distribution towards lower centrality is a reflection of the higher azimuthal asymmetry coefficients towards more non-central collisions.

Figure 6.9 shows the 1st and 2nd eigenvectors obtained after the PCA decomposition of ϕ -distributions for events where hot spots are implemented with radius parameter $R = 3$ fm. In heavy ion collisions, azimuthal distributions are represented in terms of Fourier harmonics [151]

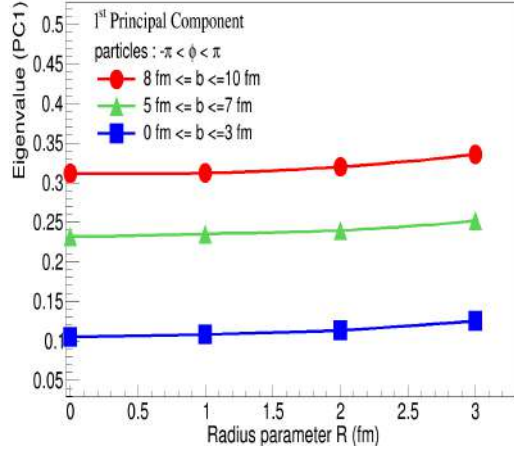


Figure 6.8: Variation of the first eigenvalue (PC1) with hot spot radius parameter R ($R = 0$ corresponds to default condition of UrQMD) for three different centralities $b = 0 - 3$ fm, $5 - 7$ fm and $8 - 10$ fm for Pb+Pb collisions in ϕ distribution.

as,

$$\frac{dN}{d\phi} = \frac{1}{2\pi} \left(1 + 2 \sum_n v_n \cos(n\phi) + 2 \sum_n a_n \sin(n\phi) \right). \quad (6.1)$$

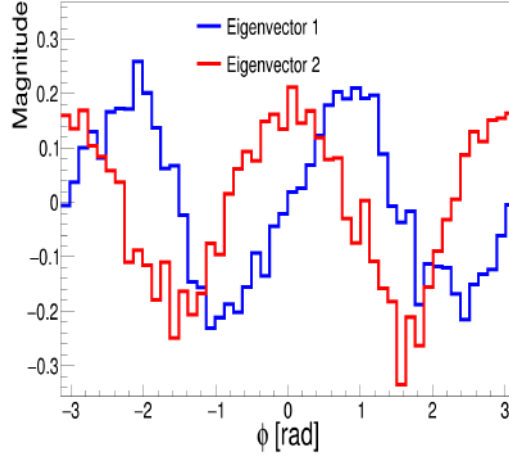


Figure 6.9: The 1st and 2nd eigenvectors obtained from PCA decomposition of ϕ -distributions for events where hot spots are implemented.

One can immediately identify the 1st and 2nd eigenvectors from PCA with Fourier decomposition bases of $\sin(2\phi)$ and $\cos(2\phi)$, respectively. We have also checked other higher components but they do not show any definite pattern which is likely to be due to smaller contributions of the higher order flow components. It is however, clear that PCA can extract the appropriate

basis set that allows a more meaningful representation of a distribution.

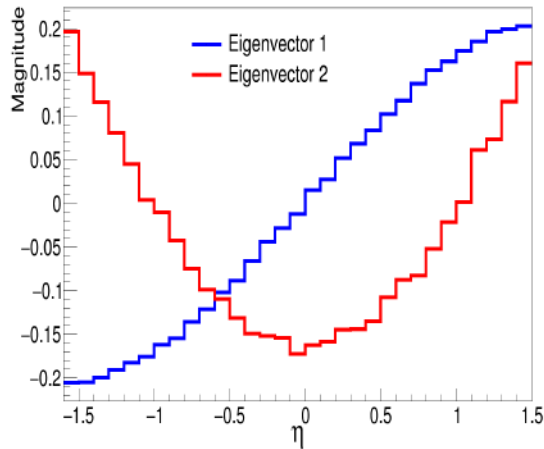


Figure 6.10: The first two eigenvectors obtained from PCA decomposition of η distribution for events where hot spots are implemented.

It may be noted that after hot spots implementation in the initial state the eigenvectors obtained from the PC decomposition of ϕ -distribution shows more prominent cosine and sine modulation. This may be because that hot spots in the initial state induce more anisotropic flow or flow fluctuations as has been reflected by PCA results. Similarly optimal basis set to represent η -distribution can also be obtained via its PCA decomposition. Fig 6.10 shows the first two eigenvectors obtained from PC decomposition of η distributions. The eigenvectors are similar to that of Legendre's polynomial with minor distortions. This means the optimal basis set to represent η distribution are Legendre polynomials [163],

$$\frac{dN}{d\eta} \approx c_1\eta + c_2\left(\frac{3}{2}\eta^2 - \frac{1}{2}\right). \quad (6.2)$$

Use of these basis vectors on extracting other observables like flow components, or components representing fluctuations will be investigated in the subsequent studies.

6.5 Summary

In high energy heavy ion collisions, the initial nucleonic configurations of the colliding nuclei play a major role in deciding the properties of the created medium. For understanding the

evolution of the colliding system through the finally produced particles, it is extremely important to understand the imprints of each of the phases through which the medium evolves. One stage which is least understood so far is the initial state of the nucleons or partons. It has been demonstrated that during the evolution of the medium the initial spatial configurations get transferred to the final state momentum configurations of the produced particles. In this chapter, we have employed the technique of the Principal Component Analysis on the η , ϕ and p_T distributions of the produced particles and examined the eigenvalues of the first principal component which represent the variance of the lower dimension observable. The aim was to study the sensitivity of these eigenvalues to the initial state fluctuations in nucleon positions. We have introduced a spatial rearrangement of nucleonic configurations at the incoming nuclei to mimic hot spot like energy deposition in UrQMD and compared the PCA results on the distributions of produced pions with and without the implementing the modification. It has been observed that for the analyses of the 1-D distributions i.e., (η, ϕ, p_T) and the 2-D $(\eta-\phi, \phi-p_T)$ and $(\eta-p_T)$ distributions obtained by making combinations of the variables, the eigenvalues increase with the size of the hot spots. The increase in eigenvalue is more prominent in the azimuthal distributions due to the nature of the hot spot implemented in the transverse plane. We have also observed that the eigenvalues increase towards the peripheral collisions showing more prominent effect on the azimuthal distributions. For studying a realistic scenario, we have seen that the eigenvalues increase with the increase in the fraction of the events with initial nucleonic hot spots. These observations can be used to filter the events based on PC eigenvalues and then study other observables like the flow coefficients and flow fluctuations in the events with relatively higher eigenvalues. These events are likely to have hot spots in the initial configurations and its effect is likely to be prominently reflected in the final state observables mentioned above. We have also obtained the eigenvectors from the PCA decomposition of ϕ and η distributions. The 1st and 2nd eigenvectors from the ϕ -distribution can be identified with $\sin(2\phi)$ and $\cos(2\phi)$ Fourier bases, respectively. Similarly, orthonormal basis set for η distribution are seen to be associated to distorted Legendre polynomials. It is however important to understand the sensitivity of the variables to the structures likely to be formed at intermediate stages other than or in addition to the initial stage of the collisions. These investigations are currently beyond the scope of this work and will be followed up in subsequent

studies.

Chapter 7

Summary & Conclusions

The phase transition from ordinary nuclear matter to the quark-gluon plasma (QGP) phase is being studied extensively by colliding heavy nuclei at relativistic energies. QGP is predicted to be formed under extreme conditions of temperatures or pressures and this deconfined medium of quarks and gluons is believed to have existed a few micro-second after the Big-Bang and still exists at the core of neutron stars. Quantum Chromodynamics (QCD), the theory for strong interactions, predict a smooth cross-over transition from hadronic matter to QGP at the energy available at CERN-LHC and at the top RHIC energy where the medium formed in heavy ion collisions is mostly net-baryon free. Whereas at the high net-baryon density region, the transition from normal nuclear matter to QGP is predicted to be a first order phase transition. The RHIC beam energy scan program and the LHC have so far explored the QCD phase diagram covering the region from very small to intermediate net-baryon densities (μ_B). However, region of very high net-baryon density (going up to 10 times of the normal nuclear matter density) remains to be unexplored. At the Facility for Anti-proton and Ion Research (FAIR) situated at GSI, Darmstadt, Germany this high net-baryon density region of the QCD phase diagram will be explored.

FAIR at GSI, is an international accelerator facility which is being developed for the accelerator based research in nuclear physics, atomic physics, hadron therapy, biological sciences, among others. The Compressed Baryonic Matter (CBM) experiment is a forthcoming fixed target nuclear physics experiment at FAIR, which aims to explore the phases of nuclear matter and their properties in the region of very high net-baryon density at the beam energy range

2-12 AGeV in the first phase [56]. The model calculations predict that a density of $\sim 5-6$ times the normal nuclear density can be achieved at the core of the fireball at this CBM experiment. The main physics goals for CBM are focused on the followings: the search for the equation of states (EOS) of high net-baryon density nuclear matter and its connection to that of the neutron stars, relevant degrees of freedom at such high net-baryon densities and search for the critical end point in QCD phase diagram, including experimental signatures for the chiral symmetry restoration. The uniqueness of the CBM experiment is, that the above physics objectives will be addressed by measuring relevant observables using rare and diagnostic probes like charmonia, low mass vector mesons, multi-strange hadrons, such that unambiguous evidence of those phenomena are obtained. In order to achieve such a goal, CBM has to operate at an unprecedented interaction rate, reaching up to 10 MHz. Thus, the detectors participating in CBM have to be high-rate capable, withstand high radiation dose and equipped with triggerless free-streaming DAQ systems [56]. In chapter 2 of this thesis, all sub-detectors, which are to be used in CBM experiment in SIS100 setup are discussed in details. A central part of the CBM physics program is dilepton measurement because dileptons are not or negligibly affected by the strong interactions and therefore carry information from their point of origin almost unperturbed. Thus, CBM has two dedicated detectors for dilepton measurements - Muon Chamber or MuCh for muon identification and Ring Imaging Cherenkov Detector (RICH) for electrons. The MuCh detector for CBM is one of the major in-kind Indian contributions for the CBM experiment. The novel feature of the CBM muon detector system is that it has segmented absorbers, which are alternated between three layers of detectors (called a station). This particular design allows efficient detection of muon tracks over a broad momentum range. The CBM-MuCh has several configurations that differ from one another in terms of number of detector layers and absorber segments, in order to meet the requirement of efficient muon identification over a wide energy range. As the interaction rate in CBM is expected go up to 10 MHz, the CBM detectors including MuCh have to sustain high particle density and radiation doses. The first two stations of MuCh will face maximum particle rates and thus, a high rate capable gaseous detector based on Gas Electron Multiplier (GEM) technology is chosen for the first two stations. In the following third and fourth stations, where particle density is relatively lower, the Resistive Plate Chamber (RPC) detectors have been proposed as a base-line

option [79].

Prior to actual detector building, it is necessary to determine an optimized version of MuCh detector which would make muon identification highly efficient and subsequent detection of low mass vector mesons (LMVMs) and of J/ψ from their dimuon decay channels feasible. The optimizations have been done on the overall, as well as, the individual thicknesses & materials of hadrons absorbers in MuCh, absorber sizes & shapes, detector size, beam pipe & shielding material within the MuCh region. The details of the simulation procedures are discussed in chapter 3. A dedicated software package called, the CBMROOT, was used to simulate the response of MuCh performance to any changes in those above mentioned design parameters and study its effect on the point-density (a measure of particle rate) & occupancy at each detector station and, whether such a change is feasible or acceptable was judged based on the overall detection efficiencies and the signal-over-background ratios for the signal candidates, that could be either LMVMs or J/ψ decaying into a muon pair. The signal candidates are generated using PLUTO event generator and embedded into background particles obtained from UrQMD event generator. Till date, the optimised version of CBM-MuCh for SIS100B setup has four absorbers and four detector stations. The first absorber layer has two parts, the inner part which is inside the magnet is made out of carbon of thickness 28 cm and the other half is built from concrete of thickness 30 cm. Rest of the three absorbers are made from iron of thicknesses 20 cm, 20 cm and 30 cm, respectively. The geometry of RPC has been implemented and detector responses for RPCs are also simulated using the same CBMROOT software package by integrating RPC geometry in the simulation chain [79]. Also the effect of different RPC detector segmentation angles and the charge thresholds on the muon pair reconstruction efficiency and signal over background have been studied [84]. The optimized MuCh setup is used to study the performance of dimuon detection decaying from low mass vector mesons (ρ, ω, ϕ, η). These studies have been done in central Au+Au collisions at 8 - 12 AGeV beam energy which corresponds to SIS100B geometry. For signal particle generation, PLUTO [66] and for background events UrQMD [38] event generators are used. The signal particles are embedded into the background events and then transported through the CBM setup using GEANT3/GEANT4 [67] transport engine in CBMROOT [98] software framework. The track propagation and reconstruction is performed using Kalman Filter technique [53].

Then the reconstructed global tracks are selected as the muon candidate tracks after applying some suitable selection cuts on the χ^2 with respect to the primary vertex and on the global tracks. Cuts are also applied on the number of associated hits with the tracks i.e on the length of the tracks. After selecting the muon candidates, invariant mass of the mother particle is calculated using the four momenta of the muon candidate tracks. Total signal along with the background invariant mass distribution is fitted with a Gaussian + pol2 function, and from it the signal is extracted from the Gaussian area after subtracting the background around $\pm 2\sigma$ in the Gaussian mean position. The invariant mass distribution of the low mass vector meson cocktails have been extracted and the efficiency of LMVM with respect to the transverse momentum and rapidity has been calculated.

In chapter 4, we discuss the performance of the MuCh-GEM detector modules in high particle density environment in heavy ion collisions in the mini CBM (mCBM) experiment at Darmstadt, Germany [87]. This mCBM at SIS18 facility is a part of the FAIR phase-0 program, where pre-series productions of CBM detectors including their electronics were tested to analyse the performance of individual detectors as well as, their integrated response. The primary aim of mCBM is to install, commission and test the different detectors with the trigger-less data acquisition system in high particle density environment. It also aims to reconstruct the online event selection and reconstruction [88]. In mCBM experiment, two real size GEM modules of dimensions corresponding to the module size of the first station were installed as a part of mini-MuCh (mMuCh) setup, downstream from the target with an offset angle of 25° away from the beam axis. The detector performance in terms of spills and digi correlations have been studied. The performance of mMuCh modules were characterized by studying the response of GEM detectors to varying beam intensity, which was found to be mostly linear in the measured range. Also, the timing response of the GEM detectors, quantified by the time resolution, were found to be of the order (roughly 20 ns). The spatial uniformity of the time resolutions over the full detector area, are studied at different FEB positions. A time based event reconstruction technique, which will be actually used in CBM, was applied to the free streaming data for the first time in mCBM, by grouping timestamped hits from different sub-detectors within a time window of 200 ns. Events reconstructed from these free streaming data were used further to calculate spatial correlations between GEM1 hits & mTOF-tracks projected onto the GEM1

plane. A clear spatial correlation was observed between the two different detector sub-systems despite of different detector technologies [100]. This clearly indicates an effectiveness of event reconstruction with free streaming of data in mCBM along with the time synchronous behaviour of two detector systems with different detector technologies and read-out electronics. Finally, efficiency of GEM1 detector was measured relative to mTOF-tracks projected on GEM1 plane. Uniformity of GEM efficiency has been studied with time. Systematics of GEM efficiency have been performed with GEM high voltage and particle's velocity (β) and it is showing consistent result with β and GEM high voltage, i.e. GEM efficiency increases with lower β and higher GEM high voltage [101, 102]. The results are close to the expectations with the standalone measurement of the detectors in the laboratory with radiation sources.

In chapter 5 and 6 of thesis two physics problems have been studied. It is known for long that the strangeness enhancement is a signature for partonic deconfinement, which is also a topic of physics interest in CBM. A non-monotonic increase in energy dependence of K^+/π ratios was first observed at the CERN SPS and eventually attributed to a possible signature for the strangeness enhancement. Similar observation was made in the baryon sector, where ratios of $\bar{\Lambda}$ to \bar{p} were also found to be enhanced when studied as a function of collision energy. Since $\bar{\Lambda}$ and \bar{p} are both anti-particles, which can only be produced in a collision, it was thought to be an unambiguous evidence in favour of strangeness enhancement due to partonic deconfinement. However, at high net-baryon density, hadronic interactions, in particular the interactions between baryons and anti-baryons dominate, and their role in strangeness enhancement may not be completely ruled out. In chapter 5, it was particularly investigated using UrQMD hadronic transport model [135, 136] that the baryon-anti-baryon annihilation, which is an important hadronic interaction channel in the region of high baryon density, affect the production of $\bar{\Lambda}$ and \bar{p} , among others. It was found that the $B\bar{B}$ -annihilation is responsible for splitting of the mean transverse mass of Λ and $\bar{\Lambda}$. The mean transverse mass is a measure of the effective temperature of the medium that include both thermal energy and kinetic energy due to radial boost. For particles of same mass, which is the case for Λ and $\bar{\Lambda}$, it was expected to be same. Experimental measurements from NA49 and STAR however, exhibit a splitting in the mean transverse mass as a function of collision energy with mean transverse mass of $\bar{\Lambda}$ greater Λ . Splitting is prominent at lower collision energy, where the baryon density is large and hence

the $B\bar{B}$ -annihilation probability is more. The magnitude of splitting gradually decreases with increase in collision energy. UrQMD model calculation have shown that $B\bar{B}$ -annihilation can reproduce the trend in splitting of mean transverse mass of Λ and $\bar{\Lambda}$ reasonably well and thus established that impact of $B\bar{B}$ -annihilation on ordinary and strange baryons production can not be ignored. Another important observation made in this study was, that even without $B\bar{B}$ -annihilation, the split in mean transverse mass of Λ and $\bar{\Lambda}$ exist and trend is now reverse, that is Λ is higher than $\bar{\Lambda}$. Subsequently it was found that Λ s are mainly produced in the associated production channel together with kaons has a lower threshold (~ 700 MeV) than $\bar{\Lambda}$ which are produced primarily via pair-production channel that has a threshold of ~ 2200 MeV. As a result, kinetic energy available to Λ is more than $\bar{\Lambda}$ therefore, the mean transverse mass of Λ is also higher than $\bar{\Lambda}$ [141].

Furthermore, it was found that the enhancement in $\bar{\Lambda}/\bar{p}$ ratios observed at SPS and AGS energies can also be explained invoking $B\bar{B}$ -annihilation. UrQMD calculations with $B\bar{B}$ -annihilation could reproduce the qualitative trend in $\bar{\Lambda}/\bar{p}$ ratios in data at the first place. Taking into account the feed-down contribution in data, it was found that ratios obtained from the UrQMD model calculation and that from the data are consistent with the limits of uncertainties in data point. Agreement between data and model calculation suggests that $B\bar{B}$ -annihilation and different annihilation fraction for $\bar{\Lambda}$ & \bar{p} together with its strong kinematic dependence is the root cause for the observed $\bar{\Lambda}/\bar{p}$ enhancement in data [141]. Nevertheless, for more confirmation uncertainties in data have to be reduced significantly, which can be achieved when FAIR and CBM become operational.

In chapter 6, an attempt was made to identify initial conditions and fluctuation in initial conditions by using principal component analysis (PCA) technique. The PCA technique involve reduction of correlated space to a smaller dimension at the same time keeping the information loss minimal. Sensitivity of PCA technique was tested by implementing hot-spot like initial conditions in the UrQMD model. The hot-spot are generally created when there is a large energy deposition in a localized region. Such an initial condition was produced by bringing the nucleons in the incoming nuclei closer in the coordinate space. The degree of closeness was controlled by a free parameter, which was varied in a way such that the inter-nucleon separation can be varied from 1 fm to maximum 3 fm. This initial condition was then fed into the UrQMD

model, which then evolved in the usual manner. The final state pions were then selected to construct transverse momentum, rapidity and ϕ -distributions which were then decomposed into several bins and fed as input to the Principal Component Analysis algorithm. Changes in first few Principal Components were observed on varying the hot spot sizes. Since, it is unlikely that every event will have hot-spot(s), so to emulate such a scenario we introduced hot-spots in 1% to 10 % of the total simulated events and studied its effect on Principal Components, even then some sensitivity was observed in first few Principal Components. Thus it indicates that PCA may serve as a suitable tool to discern the nature of initial condition and small localized fluctuations.

The main purpose of this thesis work is to design, simulate and test the detector system for the CBM muon system in the upcoming CBM experiment at FAIR, Germany. With an extensive all-round simulation work, a suitable design has been obtained and the detector system are being developed. The development work is also highly motivated by the high net-baryon density physics of the strongly interacting matter, two topics of which have been studied in detail, i.e. strangeness enhancement and a method to find any fluctuations in the initial geometry of the collisions which might lead to the preprints in the final particles.



Bibliography

- [1] S. L. Glashow. *Nuclear Physics*, 22:579–588, 1961.
- [2] S. Weinberg. *Phys. Rev. Lett.*, 19:1264–1266, 1967.
- [3] P. W. Higgs. *Phys. Rev. Lett.*, 13:508–509, 1964.
- [4] G. Hooft. *Adv. Ser. Direct. High Energy Phys.*, 26:1–27, 2018.
- [5] F. Wilczek. *Rev. Mod. Phys.*, 71:S85–S95, 1999.
- [6] G. Aad and et al. (ATLAS Collaboration). *Phys. Lett. B*, 716(1):1–29, 2012.
- [7] S. Chatrchyan and et al. (CMS Collaboration). *Phys. Lett. B*, 716(1):30–61, 2012.
- [8] D. J. Gross. *Proc. Nat. Acad. Sci*, 102:9099–9108, 2005.
- [9] H. D. Politzer. *Phys. Rev. Lett.*, 30:1346–1349, 1973.
- [10] B. L. Ioffe, V. S. Fardin, and L. N. Lipatov. *Quantum chromodynamics: Perturbative and nonperturbative aspects*. Cambridge Univ. Press, 2010.
- [11] D. J. Gross. *Rev. Mod. Phys.*, 77:837–849, 2005.
- [12] Szabolcs Borsanyi, Zoltan Fodor, Christian Hoelbling, Sandor D. Katz, Stefan Krieg, and Kalman K. Szabo. *Phys. Lett. B*, 730:99–104, 2014.
- [13] A. Bazavov et al. *Phys. Rev. D*, 90:094503, 2014.
- [14] Eemeli Annala, Tyler Gorda, Alekski Kurkela, Joonas Nättilä, and Alekski Vuorinen. *Nature Phys.*, 16(9):907–910, 2020.

- [15] T. D. Lee and G. C. Wick. *Phys. Rev. D*, 9:2291–2316, 1974.
- [16] T. D. Lee. *Rev. Mod. Phys.*, 47:267–275, 1975.
- [17] J Glauber and G. Matthiae. *Nucl. Phys. B*, 21:135–157, year =.
- [18] David d’Enterria and Constantin Loizides. *Ann. Rev. Nucl. Part. Sci.*, 71:315–344, 2021.
- [19] Huan Z. Huang. *J. Phys. G*, 30:S401–S410, 2004.
- [20] Jaroslav Adam et al. *Phys. Rev. C*, 102(3):034909, 2020.
- [21] Jaroslav Adam et al. *Phys. Lett. B*, 766:212–224, 2017.
- [22] A. Adare et al. *Phys. Rev. C*, 84:054912, 2011.
- [23] T. Matsui and H. Satz. *Phys. Lett. B*, 178:416–422, 1986.
- [24] Serguei Chatrchyan et al. *Eur. Phys. J. C*, 72:1945, 2012.
- [25] S. Voloshin and Y. Zhang. *Z. Phys. C*, 70:665–672, 1996.
- [26] M. S. Abdallah et al. *Phys. Lett. B*, 831:137152, 2022.
- [27] J. Adam et al. *Phys. Rev. Lett.*, 126(9):092301, 2021.
- [28] Frank Geurts and Ralf-Arno Tripolt. *Prog. Part. Nucl. Phys.*, 128:104004, 2023.
- [29] Masayasu Harada and Chihiro Sasaki. *Phys. Rev. D*, 73:036001, 2006.
- [30] R. Arnaldi et al. *Eur. Phys. J. C*, 61:711–720, 2009.
- [31] Ralf Rapp and Hendrik van Hees. *Phys. Lett. B*, 753:586–590, 2016.
- [32] J. Eschke. *J. Phys. G.: Nucl. Part. Phys.*, 31:S967, 2005.
- [33] P. Senger, for CBM Collaboration. *J. Phys.: Conf. Ser.*, 50:357–360, 2006.
- [34] Yu. B. Ivanov and et al. *Phys. Rev. C*, 74:044904, 2006.
- [35] P. V. Konchakovski and et al. *Phys. Rev. C*, 90:014903, 2014.
- [36] G. Bureau and et al. *Phys. Rev. C*, 71:054905, 2005.

-
- [37] M. Wagner. *Phys. Rev. C*, 71:034910, 2005.
- [38] S. A. Bass and et al. *Prog. Part. Nucl. Phys.*, 41:255, 1998.
- [39] H H Gutbrod and et al. FAIR - Baseline technical report Executive summary, 2006.
- [40] W. Erni and et al (The PANDA Collaboration). 2012.
- [41] Guenther Rosner. Future Facility: FAIR at GSI. *Nuclear Physics B Proceedings Supplements*, 167:77–81, May 2007.
- [42] P Spiller. FAIR AT GSI. *Proceedings of HB2006*, pages 24–28, 2006.
- [43] N. Herrmann and for The CBM Collaboration. *EPJ Web of Conferences*, 259(09001), 2022.
- [44] The Cbm Physics Book, ISBN : 978-3-642-13292-6, Volume 814. 2011.
- [45] T. Ablyazimov and et al. Challenges in QCD matter physics -The scientific programme of the Compressed Baryonic Matter experiment at FAIR. *European Physical Journal A* **53**, 60, 2017.
- [46] W. Cassing, E. L. Bratkovskaya, and A. Sibirtsev. Open charm production in relativistic nucleus-nucleus collisions. *Nucl. Phys. A*, 691:753–778, 2001.
- [47] I. Kiesel. *Nucl. Inst. Meth. A*, 566:85–88, 2006.
- [48] M. Deveaux and et al. *Nucl. Inst. Meth. A*, 958:162653, 2020.
- [49] U. Frankenfeld and et al. *CBM Progress Report*, page 22, 2012.
- [50] P. Larionov and for The CBM Collaboration. *J. Phys.: Conf. Ser.*, 599(012025), 2015.
- [51] H. R. Schmidt and for the CBM Collaboration. *Nucl. Inst. Meth. A*, 936:630–633, 2019.
- [52] J. Heuser et al., editors. *Technical Design Report for the CBM Silicon Tracking System (STS)*. GSI, Darmstadt, 2013.
- [53] S. Gorbunov and et al. *Comp. Phys. Comm.*, 178:374–383, 2008.

- [54] R. Frühwirth. *Nucl. Inst. Meth. A*, 262:444–450, 1987.
- [55] C. Höhne. *Technical Design Report for the CBM Ring Imaging Cherenkov Detector*. 2013.
- [56] S. Chattopadhyay and et al. *Technical Design Report for the CBM : Muon Chambers (MuCh)*. GSI, 2015.
- [57] C. Blume, C. Bergmann, and D. Emschermann. *Technical Design Report for the CBM Transition Radiation Detector (TRD)*. Darmstadt, 2018.
- [58] F. Roether and for the CBM Collaboration. *J. Phys.: Conf. Ser.*, 1024(012040), 2018.
- [59] P. Kähler, F. Roether, and for the CBM Collaboration. *Nucl. Inst. Meth. A*, 958(162727), 2020.
- [60] P. Senger. *Int. J. Mod. Phys. E*, 29:2030001, 2020.
- [61] N. Herrmann. *Technical Design Report for the CBM Time-of-Flight System (TOF)*. GSI, Darmstadt, 2014.
- [62] I. Deppner, N. Herrmann, and for the CBM Collaboration. *JINST*, 14(C09020), 2019.
- [63] F. Guber and I. Selyuzhenkov. *Technical Design Report for the CBM Projectile Spectator Detector (PSD)*. GSI, Darmstadt, 2015.
- [64] The Green IT Cube. <https://ttsp-hwp.de/projects/green-it-cube/>.
- [65] O. Singh et al. CBM Progress Report 2019. pages 95–96, 2020. <https://repository.gsi.de/record/228172>.
- [66] I. Fröhlich. *PoS ACAT*, 50:076, 2007.
- [67] R. Brun. *CERN Program Library Long Writeup W5013*, 1993.
- [68] FLUKA. <http://www.fluka.org/fluka.php>.
- [69] Valentina Akishina. *Four-dimensional event reconstruction in the CBM experiment*. PhD dissertation, Goethe-Universität, 2016.
- [70] C. Amsler. *Phys. Lett. B*, 667:1–6, 2000.

-
- [71] R. Frühwirth and et al, editors. *Data Analysis Techniques for High-Energy Physics*. Cambridge University Press, 2000.
- [72] Design and performance simulation of a segmented-absorber based muon detection system for high energy heavy ion collision experiments. *Nuclear Instruments and Methods in Physics Research Section A: Accelerators, Spectrometers, Detectors and Associated Equipment*, 775:139–147, 2015.
- [73] P. Senger and V. Friese. CBM Progress Report 2020. Technical Report 2021-00421, 2021.
- [74] CBM Progress Report 2019. Technical Report CBM-PR-2019, 2020.
- [75] CBM Progress Report 2018. Technical Report CBM Progress Report 2018, 2019.
- [76] CBM Progress Report 2017. Technical Report CBM Progress Report 2017, 2018.
- [77] I. Selyuzhenkov and A. Toia, editors. *CBM Progress Report 2016*. GSI, 2017.
- [78] Partha Bhaduri. *Thesis on "Charmonium Production and Detection in High Energy Nuclear Collisions at FAIR"*. PhD dissertation, Homi Bhabha National Institute, 2014.
- [79] Ekata Nandy et al. CBM Progress Report 2018. pages 163–164, 2019. <https://repository.gsi.de/record/220128>.
- [80] E. Nandy et al. CBM Progress Report 2015. page 68, 2016. <https://repository.gsi.de/record/186952>.
- [81] Ekata Nandy et al. CBM Progress Report 2017. pages 66–67, 2018. <https://repository.gsi.de/record/209729>.
- [82] Ekata Nandy, Subhasis Chattopadhyay, and Shabir Ahmad. Performance Study of MUCH Beam Pipe and Shielding for CBM Experiment. *DAE Symp. Nucl. Phys.*, 60:806–807, 2015.
- [83] S. Ahmad et al. CBM Progress Report 2015. page 69, 2016. <https://repository.gsi.de/record/186952>.

- [84] Ekata Nandy et al. CBM Progress Report 2019. pages 76–77, 2020. <https://repository.gsi.de/record/228172>.
- [85] CBM Collaboration wiki page, Thermal FIST model. <https://cbm-wiki.gsi.de/foswiki/bin/view/PWG/CbmDileptonInfoFilesAuAu11000>.
- [86] *Particle Data Book (PDG)*. <https://pdg.lbl.gov/>.
- [87] mCBM@SIS18. Technical Report CBM, Darmstadt, 2017.
- [88] <https://indico.gsi.de/event/10698/>, mcbm@sis18 2021/22 a cbm full system test-setup for high-rate nucleus-nucleus collisions at gsi/fair. Technical report, 2021.
- [89] K. Kasinski et al. *Nucl. Instrum. Meth. A*, 908:225 – 235, 2018. <https://doi.org/10.1016/j.nima.2018.08.076>.
- [90] Rafal Kleczek. *Journal of Instrumentation*, 12:C01053–C01053, 2017. <https://doi.org/10.1088/1748-0221/12/01/C01053>.
- [91] Rama Prasad Adak et al. *Nucl. Instrum. Meth. A*, 846:29 – 35, 2017. <https://doi.org/10.1016/j.nima.2016.12.004>.
- [92] Ajit Kumar et al. *DAE Symp. Nucl. Phys.*, 62:1006–1007, 2017. <https://cds.cern.ch/record/2674709>.
- [93] A. Kumar, A. Agarwal, S. Chatterjee, S. Chattopadhyay, A.K. Dubey, C. Ghosh, E. Nandy, V. Negi, S.K. Prasad, J. Saini, V. Singhal, O. Singh, G. Sikder, J. de Cuveland, I. Deppner, D. Emschermann, V. Friese, J. Frühauf, M. Gumiński, N. Herrmann, D. Hutter, M. Kis, J. Lehnert, P.-A. Loizeau, C.J. Schmidt, C. Sturm, F. Uhlig, and W. Zabolotny. Commissioning and testing of pre-series triple gem prototypes for cbm-much in the mcbm experiment at the sis18 facility of gsi. *Journal of Instrumentation*, 16(09):P09002, sep 2021.
- [94] S. K. Kundu et al. *CBM Progress Report*, pages 102–103, 2020. https://repository.gsi.de/record/228172/files/cbm_pr2019_final.pdf.

-
- [95] Ajit Kumar. *Development and performance studies of GEM based tracking detectors for the Compressed Baryonic Matter (CBM) experiment at FAIR*. PhD dissertation, Homi Bhabha National Institute, 2021.
- [96] K. Kasinski et al. *Journal of Instrumentation*, 11(11):C11018–C11018, 2016.
- [97] K. Kasinski et al. *Journal of Instrumentation*, 12(03):C03023–C03023, 2017.
- [98] The CbmRoot Framework. <http://computing.gitpages.cbm.gsi.de/cbmroot/>.
- [99] A. Agarwal et al. CBM Progress Report 2020. page 89, 2021. <https://repository.gsi.de/record/237432>.
- [100] Ekata Nandy et al. CBM Progress Report 2019. page 105, 2020. <https://repository.gsi.de/record/228172>.
- [101] Ekata Nandy et al. CBM Progress Report 2021. pages 103–104, 2022. <https://repository.gsi.de/record/246663>.
- [102] Ekata Nandy et al. CBM Progress Report 2020. pages 90–91, 2021. <https://repository.gsi.de/record/237432>.
- [103] M. Cheng et al. *Phys. Rev. D*, 77:014511, 2008.
- [104] I. Arsene et al. *Nucl. Phys. A*, 757:1–27, 2005.
- [105] B. B. Back et al. *Nucl. Phys. A*, 757:28–101, 2005.
- [106] K. Adcox et al. *Nucl. Phys. A*, 757:184–283, 2005.
- [107] John Adams et al. *Nucl. Phys. A*, 757:102–183, 2005.
- [108] Berndt Muller, Jurgen Schukraft, and Boleslaw Wyslouch. *Ann. Rev. Nucl. Part. Sci.*, 62:361–386, 2012.
- [109] Johann Rafelski and Berndt Muller. *Phys. Rev. Lett.*, 48:1066, 1982. [Erratum: *Phys.Rev.Lett.* 56, 2334 (1986)].
- [110] Zi-wei Lin and C. M. Ko. *Phys. Rev. Lett.*, 89:202302, 2002.

- [111] Denes Molnar and Sergei A. Voloshin. *Phys. Rev. Lett.*, 91:092301, 2003.
- [112] Rudolph C. Hwa and C. B. Yang. *Phys. Rev. C*, 67:064902, 2003.
- [113] R. J. Fries, Berndt Muller, C. Nonaka, and S. A. Bass. *Phys. Rev. Lett.*, 90:202303, 2003.
- [114] V. Greco, C. M. Ko, and P. Levai. *Phys. Rev. Lett.*, 90:202302, 2003.
- [115] Jun Song, Xiao-Feng Wang, Hai-Hong Li, Rui-Qin Wang, and Feng-Lan Shao. *Phys. Rev. C*, 103(3):034907, 2021.
- [116] Michael K. Mitrovski et al. *J. Phys. G*, 32:S43–S50, 2006.
- [117] Salah Hamieh, Krzysztof Redlich, and Ahmed Tounsi. *Phys. Lett. B*, 486:61–66, 2000.
- [118] A. Tounsi and K. Redlich. *J. Phys. G*, 28:2095–2102, 2002.
- [119] B. I. Abelev et al. *Phys. Rev. C*, 81:024911, 2010.
- [120] M. M. Aggarwal et al. *Phys. Rev. C*, 83:024901, 2011.
- [121] J. L. Klay et al. *Phys. Rev. C*, 68:054905, 2003.
- [122] L. Adamczyk et al. *Phys. Rev. C*, 96(4):044904, 2017.
- [123] W. Cassing, A. Palmese, P. Moreau, and E. L. Bratkovskaya. *Phys. Rev. C*, 93:014902, 2016.
- [124] F. Antinori et al. *Eur. Phys. J. C*, 11:79–88, 1999.
- [125] F. Antinori et al. *J. Phys. G*, 32:427–442, 2006.
- [126] C. Alt et al. *Phys. Rev. Lett.*, 94:192301, 2005.
- [127] C. Alt et al. *Phys. Rev. C*, 78:034918, 2008.
- [128] B. B. Back et al. *Phys. Rev. Lett.*, 87:242301, 2001.
- [129] G. S. F. Stephans and Y. Wu. *J. Phys. G*, 23:1895–1901, 1997.
- [130] T. A. Armstrong et al. *Phys. Rev. C*, 59:2699–2712, 1999.

-
- [131] C. Alt et al. *arXiv:nucl-ex/0512033*, 2005.
- [132] P. Koch, Berndt Muller, and Johann Rafelski. *Phys. Rept.*, 142:167–262, 1986.
- [133] E. Seifert and W. Cassing. *Phys. Rev. C*, 97(4):044907, 2018.
- [134] Fuqiang Wang, Marlene Nahrgang, and Marcus Bleicher. *Phys. Rev. C*, 85:031902, 2012.
- [135] M. Bleicher et al. *J. Phys. G*, 25:1859–1896, 1999.
- [136] S. A. Bass and et al. *Prog. Part. Nucl. Phys.*, 41:255–369, 1998.
- [137] Jorgen Randrup and Jean Cleymans. *Phys. Rev. C*, 74:047901, 2006.
- [138] L. Ahle et al. *Phys. Lett. B*, 476:1–8, 2000.
- [139] L Ahle et al. *Phys. Lett. B*, 490:53–60, 2000.
- [140] Ekkard Schnedermann, Josef Sollfrank, and Ulrich W. Heinz. *Phys. Rev. C*, 48:2462–2475, 1993.
- [141] Ekata Nandy and Subhasis Chattopadhyay. *Eur. Phys. J. A*, 58(10):199, 2022.
- [142] W. Broniowski, M. Rybczynski, and P. Bozek. *Comput. Phys. Commun.*, 180:69–83, 2009.
- [143] D. d’Enterria and C. Loizides. *Ann.Rev.Nucl.Part.Sci.*, 71:315–344, 2021.
- [144] FRANÇOIS G. *International Journal of Modern Physics A*, 28.
- [145] Giacalone G. and et. al. *Phys. Rev. C*, 100(2):024905, 2019.
- [146] J. Y. Ollitraut. *Phys. Rev. D*, 229, 1992.
- [147] B. Alver and Roland G. *Phys. Rev. C*, 82, 2010.
- [148] R. BhaleraoS., M. Luzum, and J.-Y Ollitraut. *Phys. Rev. C*, 84.
- [149] K. Aamodt et al. *Phys. Lett. B*, 708:249–264, 2012.
- [150] L. M. Miller. *Annual Review of Nuclear and Particle Science*, 57:205–243, 2007.

- [151] S. Voloshin and Y. Zhang. *Z. Phys. C*, 70:665, 1996.
- [152] R. Snyder, M. Byres, S. H. Lim, and J. L. Nagle. *Phys. Rev. C*, 103:024906, 2021.
- [153] Sruthy J. Das. *Longitudinal Fluctuations in Ultra-Relativistic Heavy-Ion Collisions*. MS thesis, IISER Pune, 2019.
- [154] I. T. Jolliffe and J. Cadima. *Philosophical Transactions of Royal Society A*, 374(2065), 2016.
- [155] D. Tlusty. *arXiv:nucl-ex/1810.04767*, 2018.
- [156] S. Chattopadhyay. *Eur. Phys. J. ST*, 230(3):689–696, 2021.
- [157] T. Howley and et al. *DOI:10.1007/1-84628-224-1-16*.
- [158] H.-w. Ma, L. Yizhou, and Z. Nie. *International Journal of Structural Stability and Dynamics*, 165:1950109, 2019.
- [159] R. Brun. <https://root.cern.ch/doc/master/classTPrincipal.html>.
- [160] R. S. Bhalerao, J.-Y. Ollitrault, S. Pal, and D. Teaney. *Phys. Rev. Lett.*, 114(15):152301, 2015.
- [161] A. M. et al. Sirunyan and (CMS Collaboration). *Phys. Rev. C*, 96(6):064902, 2017.
- [162] Z. Liu, W. Zhao, and H. Song. *Eur. Phys. J. C*, 79(10):870, 2019.
- [163] I Altsybeev. *Physics of Particles and Nuclei*, 51:314–318, 2020.
- [164] S. Acharya and S. Chattopadhyay. *Phys. Rev. C*, 103(3):034909, 2021.
- [165] I. M. Johnstone and A. Y. Lu. *Journal of the American Statistical Association*, 104:682–693, 2012.

List of Figures

1.1	Depiction of the elementary particles and forces in the Standard model.	2
1.2	QCD running coupling constant α_S as a function of momentum transfer (Q). Solid and open symbols are experimental values overlaid on QCD prediction shown is yellow band. In the limit of large momentum transfer, strong coupling tends to vanish asymptotically.	4
1.3	A schematic representation of how QGP can be produced in laboratories by subjecting ordinary nuclear matter to high temperature and/or high compression (pressure).	5
1.4	Lattice QCD calculations for pressure, energy density, entropy density nor- malised to 4^{th} or 3^{rd} power of temperature, showing a rapid change with temperature- an indication for phase transition. Vertical yellow band corresponds to cross-over transition region. Solid lines represent predictions from Hadron Resonance Gas (HRG) model and horizontal black dashed line is for energy density in weakly interacting ideal gas limit. The y-axis in the plot corresponds to number of degrees of freedom in the system, which is a dimensionless quantity.	6
1.5	Phases of QCD matter under different conditions of temperature and baryon chemical potential. Also shown the experimental facilities that probe different regions of the phase diagram.	7
1.6	Stages in the evolution of heavy ion collision.	10

1.7	Evidence for strangeness enhancement. (Top) K/π ratio at midrapidity as a function of $\sqrt{s_{NN}}$ from RHIC beam energy scan data for most central 0-5% Au-Au collisions. Also shown are the results from the previous experiments at AGS, SPS. (Bottom) Yields of hyperons normalised by number of wounded nucleons in Pb-Pb collision at $\sqrt{s_{NN}} = 17.3$ GeV relative to pBe yields at same energy.	14
1.8	J/Ψ suppression in heavy ion collisions quantified by nuclear modification factor as a function of centrality represented by N_{part} . Red solid markers represent $J/\Psi R_{AA}$ measurement in Pb-Pb collisions at $\sqrt{s_{NN}} = 2.76$ TeV [21] at forward rapidity and black open markers are PHENIX measurements for Au-Au collisions at $\sqrt{s_{NN}} = 200$ GeV [22].	15
1.9	A compilation of R_{AA} measurements in central heavy ion collisions at SPS ($\sqrt{s_{NN}} = 17.3$ GeV), RHIC ($\sqrt{s_{NN}} = 200$ GeV) and LHC ($\sqrt{s_{NN}} = 2.76$ TeV) energies. Also shown are the predictions from different model calculation. Figure adapted from [24].	17
1.10	A schematic representation of how initial anisotropy is converted in to momentum space azimuthal anisotropy.	18
1.11	Elliptic flow (v_2) normalised by initial eccentricity ϵ_2 as a function of particle density.	18
1.12	Constituent quark number scaling of v_2 as a function of (top) p_T and (bottom) $m_T - m_0$.	19
1.13	Higher moments of net-proton distributions as function of collision energy measured in Au-Au collisions; (left) $S\sigma$ and (right) $\kappa\sigma^2$. A non-monotonic energy dependence observed for $\kappa\sigma^2$ as a function of $\sqrt{s_{NN}}$.	20
1.14	Dimuon invariant mass spectra from In-In collisions in SPS at $\sqrt{s_{NN}} = 17.3$ GeV compared with theoretical model calculation that include; in-medium modification of spectral functions of ρ and ω along with chiral mixing and dimuons from QGP.	22
1.15	$\sqrt{s_{NN}}$ dependence extracted temperature, T , from dilepton mass spectra in the intermediate mass region. Yellow hatched region indicates phase transition temperature at zero baryon chemical potential.	22

2.1	Evolution of net baryon density with time at different collision energies, calculated from UrQMD and PHSD [35,38].	26
2.2	Interaction rate with collision energy has been shown for different experiments.	27
2.3	The existing GSI facilities are shown in blue which includes UNILAC , ESR and SIS18 accelerator. Planned FAIR facilities are shown in red. FAIR has four major experiments APPA, PANDA, NUSTAR and CBM [39]. Experiments are shown in black [40].	28
2.4	different stages of heavy ion collisions from UrQMD has been shown for U+U at 23 AGeV. At different stages different particles are emitted at different time.	29
2.5	Multiplicity times branching ratio for various particles at 25 AGeV Au+Au collisions as calculated from HSD [46]. For vector mesons (ρ , ω , ϕ , J/ψ) their decay through dilepton channels have been considered. For D meson their decay to hadronic channels in pions and kaons have been assumed.	30
2.6	CBM experimental setup with all its sub detectors.	33
2.7	A view of STS with MVD housed inside magnet is shown [49].	35
2.8	Tracks passing through STS detectors of 8 layers from central Au+Au collisions at 12 AGeV using GEANT simulation.	35
2.9	Momentum threshold for pion and kaon production for cherenkov light in RICH detector [55].	37
2.10	TRD consisting of drift chamber and radiator is used for pion and electron identification by the principle of transition radiation is shown by the schematic diagram [57].	38
2.11	The reconstructed TOF m^2 versus momentum for the charged hadrons at 10 AGeV Au+Au interaction by simulation [60].	40
2.12	Schematic diagram of dilepton/dimuon sources from different invariant mass regions.	42
2.13	Invariant mass distribution of dimuon spectra from NA60 data in In+In collisions at 158 AGeV and compared with theoretical calculations including in medium vector spectral functions.	43

3.1	Different modular versions of MuCh geometry depending on beam energy and physics criteria. SIS100-A (left), which consists of 3 stations and 3 absorbers, SIS100-B (middle) with 4 stations and 4 absorbers and SIS100-C (right) with 5 stations and 5 absorbers along with Magnet, Silicon Tracking Stations (STS), Transition Radiation Detector (TRD) and Time of Flight (TOF) detectors. . .	47
3.2	Simulation steps for track reconstruction in MuCh.	49
3.3	Schematic representation of track propagation and track finding process in detector stations [69]	52
3.4	Particle count as a function of distance travelled in iron absorber for muons from omega, J/ψ and other hadrons like pions and protons. The muons that result from the decay of J/ψ and omega mesons are produced by the PLUTO event generator, while the remaining particles are produced by the UrQMD event generator.	56
3.5	The variation in particle multiplicity with C and Fe absorber thickness at 10 AGeV (top) and 25 AGeV (bottom) central Au+Au collisions [72].	57
3.6	The ratio of reconstructed tracks to the accepted tracks has been shown with the iron absorber thickness.	58
3.7	The reconstructed background tracks invariant mass distribution for different iron absorber thickness of 40 cm (green), 30 cm (blue), 20 cm (red) and 10 cm (black line) for the first absorber.	59
3.8	Ratio of reconstructed to acceptable input MC tracks for absorber material thickness of C and Fe.	60
3.9	The sketch diagram of SIS100-B muon setup which consists of four stations and four absorbers along with TRD and TOF detectors.	60
3.10	Invariant mass distribution of reconstructed background tracks for different gaps of 15 cm, 30 cm, 45 cm and 60 cm in between absorbers.	61
3.11	The detector layers are of circular profile. The total active area in a layer is divided in trapezoidal sector shape modules with overlapping with each other to avoid dead region.	62

3.12	The MC point density (points/cm ² /event) distribution of different stations in MuCh with radius from the beam pipe at 8 AGeV central Au+Au collisions [79].	63
3.13	Schematic view of projective pad segmentaion in Much detector layers.	63
3.14	Modification of first absorber shape from biconical (left) to trapezoidal + parallelopiped (right). Rest all absorbers are made of parallelopiped shape.	64
3.15	Ratio of the point density in first station of modified trapezoidal + parallelopiped shape of the first absorber to that of the biconical absorber.	65
3.16	MC point density distribution of the detector stations with the reduced size of second station (green colour) compared with default size of second station (purple colour).	66
3.17	Initial configuration of beampipe and shielding where gaps were present (left) and modified shielding and beampipe with the gaps filled with shielding material (right) [82, 83].	66
3.18	Reduction of point density in first station by $\sim 10\%$ with the filled up shielding materials as shown in the red color, whereas black color is the point density for the default initial configuration of beampipe and shielding [82].	67
3.19	Schematic layout of the MuCh geometry with two GEM detectors in first and second station and two RPC detectors in third and fourth station in SIS100B geometry along with TRD and TOF detectors.	68
3.20	Arrangement of modules in staggered manner on both sides of a support structure (top left). Single RPC module structure (top right) and total modules making circular detector profile (bottom).	70
3.21	5° (left fig) & 6° (right fig) azimuthal segmentation in station 3 & station 4 respectively.	71
3.22	Schematic representation of generation of the primary electrons inside RPC gas volume along the track.	71
3.23	Number of primary electrons distribution within RPC drift volume.	72
3.24	The event averaged charge distribution in station 3 (left) and station 4 (right) at 8 AGeV central Au+Au collisions.	74

3.25	The point density distributions for primary (left) and secondary particles (right) has been shown for 2 GEM + 2 RPC configuration and all 4 GEM configurations in the third station.	74
3.26	The point density distribution for primary (left) and secondary particles (right) has been shown for 2GEM + 2 RPC configuration and all 4 GEM configurations in the fourth station.	75
3.27	The hit density distribution for 2GEM + 2 RPC configuration and all 4 GEM configurations in third (left) and fourth station (right).	76
3.28	Points per cluster, digis per cluster and hits per cluster info for station 3 and 4.	77
3.29	The invariant mass distribution of signal ω and background. Signal omega is embedded into the background events.	78
3.30	RPC detector segmentation with different azimuthal angle 1° , 2° in 3^{rd} and 4^{th} station and 5° in 3rd and 6° in 4th station.	78
3.31	Occupancy distribution for the 3^{rd} & 4^{th} station with different segmentation angles.	79
3.32	Invariant mass distribution of ω embedded in background at different segmentation angles for third and fourth stations.	80
3.33	Invariant mass distribution of ω embedded in background at 1° and 5° segmentation for different charge threshold.	81
3.34	TOF m^2 vs momentum distribution of the reconstructed global tracks for signal muon candidates (left) from ω and right plot is background + signal tracks (right).	87
3.35	The invariant mass distribution of ω at 12 AGeV central Au+Au collisions. The total signal+background fitted with Gaussian (signal) + pol-2 (background). .	88
3.36	The invariant mass distribution of reconstructed cocktails along with the signal to background ratio at 12 AGeV central Au+Au collisions.	90
3.37	p_T and rapidity of reconstructed ω at 12 AGeV central Au+Au collisions. . . .	90
3.38	Pair reconstruction efficiency of ω and ϕ meson with respect to p_T (top) and rapidity (bottom) at 12 AGeV central Au+Au collisions.	91
3.39	Phase space acceptance y - p_T of ω and ϕ from input PLUTO (top) and after reconstruction (bottom) at 12 AGeV central Au+Au collisions.	92

4.1	A conceptual layout of mCBM setup.	97
4.2	CBMROOT Simulation generated setup for mCBM 2020.	97
4.3	Actual photograph of mCBM setup 2020.	99
4.4	Two real size GEM modules for prototype of MuCh-first station have been installed in March-May 2020 beamtime (top). And the Al cooling plate support structure (bottom).	100
4.5	The readout chain for mCBM operated in May 2020, based on the DPB and FLIB.	102
4.6	Spills in GEM1 including noise.	103
4.7	The channels counts have been shown for a FEB in GEM1 including the noisy channels.	104
4.8	Ratio of difference of channel counts in ON spill and OFF spill to the summation of channel counts in ON spill and OFF spill for all the channels have been plotted.	105
4.9	After rejecting noisy channels the good channels are shown in blue lines.	105
4.10	After rejecting noisy channels the spill structure in GEM1.	106
4.11	The spill distribution for all the sub-detectors in mCBM at low intensity (left) $2 \times 10^6/9s$ spill and high intensity (right) of $1 \times 10^8/9s$ spill for $Pb_{67+}^{208} + Au$ collisions with thin 0.25 mm gold target.	106
4.12	The digi correlations between GEM1-T0, GEM1-TOF and GEM1-GEM2 at low intensity $2 \times 10^6/9s$ spill (upper row) and at high intensity $1 \times 10^8/9s$ spill (lower row) for $Pb_{67+}^{208} + Au$ collisions with thin 0.25 mm gold target.	107
4.13	The number of digis per time slice with respect to the normalized beam intensity for GEM1 (top) and GEM2 (bottom) for two different GEM's high voltages of 4500 V and 4600 V [99].	108
4.14	Time correlation between GEM1-T0, GEM1-TOF (upper row) and GEM2-T0, GEM2-TOF (lower row) at intensity of $2 \times 10^6/9s$ spill for $Pb_{67+}^{208} + Au$ collisions with thin 0.25 mm gold target.	109
4.15	This time correlation width σ has been calculated across different FEBs in GEM, to study to spatial uniformity of GEM detectors.	110
4.16	The time correlation mean for different FEBs before time offset correction. Different FEB has different offset.	110

4.17	The time correlation mean for different FEBs after time offset correction. The mean is around zero for all the FEBs.	111
4.18	The schematic of the Fixed Time Window algorithm of 200 ns time window in event reconstruction from the raw mCBM data.	112
4.19	The number of reconstructed events per time slice from the raw mCBM data. .	112
4.20	The event by event distribution of digis, hits and cluster multiplicity in mMuCh system from the raw mCBM data.	113
4.21	The XY coverage of hits in GEM1 and GEM2 from mCBM data.	113
4.22	Event by event distribution of TOF track multiplicity (left). The number of TOF hits per TOF tracks (middle) and the XY distribution of the reconstructed TOF hits in mTOF detector.	114
4.23	The XY projection of mTOF tracks at the origin (0,0,0). The X projection and Y projection are shown separately.	114
4.24	Spatial correlations XX and YY between mMUCH and mTOF detectors using reconstructed mMUCH hits and mTOF tracks projected at GEM1 plane [102].	115
4.25	The XX and YY spatial correlation coefficient with different mTOF track multiplicity has been studied. XX and YY spatial correlations have been plotted for three regions in mTOF tracks multiplicity (a) $N_{TOFtracks} \leq 4$ (top row) (b) $4 < N_{TOFtracks} < 10$ (middle row) and (c) $N_{TOFtracks} \geq 10$ (bottom row). The correlation coefficient R for XX correlation is 0.3, 0.17, 0.10 and for YY correlation 0.51, 0.29 and 0.18 for the cases of (a), (b) and (c) respectively.	116
4.26	The XY distribution of GEM1 hits and the mTOF tracks projected at GEM1 plane. The common acceptance between GEM1 and the projected mTOF tracks is shown in blue colour (left). Simulation plot of the pads in a GEM module (right).	117
4.27	The residual X and Y distributions taking the spatially nearest GEM1 hit w.r.to the projected mTOF tracks.	118

4.28	The variation of x and y residuals of GEM1 hits w.r.t projected mTOF tracks at GEM1 plane within the common acceptance of GEM1 and mTOF with different pad sizes : small pads $5 < y < 20$ cm (top), middle pad sizes $-5 < y < 5$ cm (middle) and large pads sizes $-20 < y < -5$ cm (bottom) [101].	119
4.29	Common acceptance of GEM1 hits and mTOF tracks shown in black boundary, blue points are the fired pads centers.	120
4.30	Efficiency with time for GEM HV of 4700 V, at low intensity 2×10^6 /9s spill, thick target.	121
4.31	GEM HV of 4700 V, at low intensity 2×10^6 /9s spill, thick target.	121
4.32	GEM efficiency has been calculated for different range of velocity β . We have taken four ranges of β ; $0.2 < \beta < 0.6$, $0.4 < \beta < 0.8$, $0.8 < \beta < 1.2$ and inclusive β for GEM HV of 4700 V, at low intensity 2×10^6 /9s spill, s thick target.	122
4.33	Dependence of GEM1 efficiency with GEM1 high voltage (HV) for two values of GEM1 HV 4700 V and 4800 V for inclusive β , at low intensity 2×10^6 /9s spill, thin and thick gold target respectively.	123
5.1	[Color online] Collision energy dependence of $\Lambda, \bar{\Lambda}$ and \bar{p} yields (dN/dy) at mid-rapidity ($ y < 0.5$) in central Au+Au/Pb+Pb collision from UrQMD with $B\bar{B}$ annihilation (solid line) and without $B\bar{B}$ annihilation (dashed line) from $\sqrt{s_{NN}} = 4.7$ to 17.3 GeV. Also shown a comparison with available data from AGS [128] , NA49 [127] and STAR BES [20].	131
5.2	[Color online] Beam energy dependence of Λ and $\bar{\Lambda}$ to pions ($1.5(\pi^+ + \pi^-)$) at mid-rapidity ($ y < 0.5$) in central Au+Au/Pb+Pb collision from UrQMD with $B\bar{B}$ annihilation (solid line) and without $B\bar{B}$ annihilation (dashed line) from $\sqrt{s_{NN}} = 4.7$ to 17.3 GeV. UrQMD results are compared with available data from AGS [128,138,139] , NA49 [127] and STAR BES [20,122].	132

5.3	[Color online] Beam energy dependence of Λ/K^+ and $\bar{\Lambda}/K^-$ at mid-rapidity ($ y < 0.5$) in central Au+Au/Pb+Pb collision from UrQMD with $B\bar{B}$ annihilation (solid line) and without $B\bar{B}$ annihilation (dashed line) from $\sqrt{s_{NN}} = 4.7$ to 17.3 GeV. UrQMD results are compared with available data from AGS [128, 138, 139], NA49 [127] and STAR BES [20, 122].	133
5.4	Energy dependence of mean transverse mass, $\langle m_T \rangle - m_0$, at mid-rapidity ($ y < 0.4$) for Λ and $\bar{\Lambda}$ in central Pb+Pb collisions at $\sqrt{s_{NN}} = 6.27$ to 17.3 GeV from UrQMD with $B\bar{B}$ annihilation and without $B\bar{B}$ annihilation. UrQMD calculations are compared with existing results from central Pb+Pb collisions at $\sqrt{s_{NN}} = 6.27$ to 17.3 from NA49 [127] and STAR results from central Au+Au collisions at $\sqrt{s_{NN}} = 7.7$ and 11.5 GeV [20].	134
5.5	The $\langle m_T \rangle - m_0$ spectra for Λ and $\bar{\Lambda}$ as a function of N_{part} as obtained from the STAR data for Au+Au collisions at $\sqrt{s_{NN}} = 11.5$ GeV (left) [20] and compared it with UrQMD calculations including $B\bar{B}$ annihilation at the same $\sqrt{s_{NN}}$ (right).	135
5.6	$\langle m_T \rangle - m_0$ for Λ and $\bar{\Lambda}$ w.r.to N_{part} at $\sqrt{s_{NN}} = 11.5$ GeV, AuAu collision, mid rapidity $ y < 0.5$ in UrQMD without including $B\bar{B}$ annihilation.	135
5.7	The p_T dependence of ratios of yields of $\bar{\Lambda}$'s (open marker) and \bar{p} 's (closed marker), with and without incorporating $B\bar{B}$ annihilation calculated from UrQMD in central Pb+Pb collisions at $\sqrt{s_{NN}} = 6.27$ to 17.3 GeV.	137
5.8	The rapidity dependence of ratios of yields of $\bar{\Lambda}$'s (open marker) and \bar{p} 's (closed marker), with and without incorporating $B\bar{B}$ annihilation calculated from UrQMD in central Pb+Pb collisions at $\sqrt{s_{NN}} = 6.27$ to 17.3 GeV.	138
5.9	Annihilation fraction of \bar{p} and $\bar{\Lambda}$ as a function of $\sqrt{s_{NN}}$ for low and inclusive p_T from UrQMD.	139
5.10	The $\bar{\Lambda}/\bar{p}$ ratio at mid-rapidity as a function of collision energy at $\sqrt{s_{NN}} = 6.27$ to 17.3 GeV with (left) and without (right) $B\bar{B}$ -annihilation from UrQMD. Also shown the effect of different p_T cut on the ratio. Model calculation is compared with NA49 [131] data (feed-down uncorrected) at same $\sqrt{s_{NN}}$	140

5.11	Dependence of $\bar{\Lambda}/\bar{p}$ ratios as a function of $\sqrt{s_{NN}}$ with $B\bar{B}$ annihilation in UrQMD and compared it with feed-down corrected NA49 data points at low p_T and inclusive p_T for central (0-7%) PbPb collisions.	141
5.12	$\bar{\Lambda}/\bar{p}$ ratios as a function of N_{part} or centrality both from UrQMD ($B\bar{B}$ ON) and feed-down corrected NA49 data at $\sqrt{s_{NN}} = 17.3$ GeV at low p_T and inclusive p_T	142
6.1	The XY distributions of the nucleons in projectile and target Pb nucleus in the transverse plane with the impact parameter $b = 3$ fm before hot spot creation (left) and after hot spot creation (right) with parameters $R=2$ fm, $dR=0.5$ and $dz=\pm 0.5$ fm.	149
6.2	The number of nucleons per hot spot with parameters $R = 2$ fm , $dR = 0.5$ and $dZ = \pm 0.5$ fm for one colliding Pb nucleus.	150
6.3	Eigenvalues in PC decomposition in 1-D distributions of ϕ , η and p_T bins (left) and for 2-D distributions for $(\eta-\phi)$, $(\phi-p_T)$, $(\eta-p_T)$ bins (right) of produced π^\pm for default UrQMD and with different hot spot conditions with radius parameters, $R = 1, 1.5, 2, 3$ fm, $dR = 0.5$ and $dz = \pm 0.5$ fm.	152
6.4	First eigenvalue (PC1) ratio of hot spot condition to the default UrQMD condition of produced π^\pm with radius parameter R for ϕ , η and p_T (1-D) distributions.	153
6.5	Variation of the first eigenvalue (PC1) ratio of hot spot to the default condition with the event fraction having hot spot like events in ϕ , η and p_T 1-D distributions.	153
6.6	First eigenvalue (PC1) ratio of hot spot condition to the default UrQMD condition of produced π^\pm with radius parameter R for the decomposition of the 2-D distributions of $\eta-\phi$, $\eta-p_T$ and $\phi-p_T$	154
6.7	Variation of the first eigenvalue (PC1) ratio of hot spot to the default condition with the event fraction having hot spot like events in decomposition of the 2-D distributions in $\eta-\phi$, $\eta-p_T$ and $\phi-p_T$	155

6.8	Variation of the first eigenvalue (PC1) with hot spot radius parameter R ($R = 0$ corresponds to default condition of UrQMD) for three different centralities $b = 0 - 3$ fm, $5-7$ fm and $8-10$ fm for Pb+Pb collisions in ϕ distribution.	156
6.9	The 1^{st} and 2^{nd} eigenvectors obtained from PCA decomposition of ϕ -distributions for events where hot spots are implemented.	156
6.10	The first two eigenvectors obtained from PCA decomposition of η distribution for events where hot spots are implemented.	157

List of Tables

2.1	Accessible beam kinetic energy are listed for SIS100 for different Z/A of ion species.	29
3.1	Different configurations of MuCh geometry for SIS100	48
3.2	Characteristics of different absorber materials for hadron absorption.	55
3.3	Digitization parameters for GEM and RPC.	73
3.4	Comparison of efficiency and S/B of signal ω for 2GEM and 2RPC and 4 GEM case geometry.	76
3.5	Details of different segmentation angles.	79
3.6	comparison of final efficiency and S/B of ω at 8 AGeV central Au+Au collision for different segmentation angles.	80
3.7	Efficiency and S/B of ω for different segmentation angles and different charge threshold values.	80
3.8	Input parameters for different beam energies and temperature in PLUTO.	85
3.9	The multiplicity and branching ratios for the LMVM cocktails at 12 AGeV Au+Au collisions.	89
4.1	Run details for mCBM campaign March- May 2020.	102